Ab Initio Modelling of Magnetoelectric Materials

Natalie Tillack

The Queen's College

University of Oxford

A thesis submitted for the Degree of

Doctor of Philosophy



Oxford

July 12, 2016

natalie.tillack@gmail.com

(This page is intentionally left blank)

Ab Initio Modelling of Magnetoelectric Materials

Natalie Tillack

The Queen's College

University of Oxford

A thesis submitted for the Degree of

Doctor of Philosophy

The search for magnetoelectric materials, *i.e.* materials that respond with a polarisation (magnetisation) when an external magnetic (electric) field is applied, has become more important in recent years—both for the standalone magnetoelectricity and as part of the cross-coupling in modern multiferroics. To date, applications of magnetoelectrics (MEs) in technology are hampered by either small coupling strengths or low operating temperatures. In the present work, the linear magnetoelectric coupling is examined by means of density functional theory with the aim to understand the physics of the coupling, and in turn open up pathways in the search for improved coupling properties.

The spin part of the ME coupling tensor was shown to be the sum of the electronic and the lattice contribution. Recently developed first-principles frameworks allow us to gain insights into the microscopic mechanisms of the coupling and are applied to compute the response in modifications of the prototypical ME Cr_2O_3 and isostructural compounds. We find that strains at ambient pressures influence the lattice contribution significantly. At higher pressures, a magnetic phase transition is shown to destabilise magneto-active phonon modes and lead to a divergence of the longitudinal lattice response due to *magnetic softness*, with a coupling strength 650 times larger than its zero-pressure value. Equivalently, a divergence of the electronic response is measured at the transition from insulator to metal—previously suggested in literature, but to date not measured. The largest value of the electronic response is shown to be $31.4\,\mathrm{ps\,m^{-1}}$, which is larger than the ambient value by a factor of 70, and also large in terms of the absolute value. We exemplify both the magnetic softness and band-gap alterations by doping the Cr_2O_3 parent structure with Fe and Ti. We show that doping provides a powerful way to include magnetic frustration resulting in a ten-fold increase of magnetic contributions to the lattice response. When the dopants lower the Cr_2O_3 band gap, the electronic response is measured to be ten times larger than reported for pure Cr_2O_3. Finally, the high-symmetry configurations of the spinflop phase of Cr_2O_3 are modelled. A combined phenomenological and group-theoretical analysis reveals a novel ME coupling mechanism only present in the spinflop phases. Akin to the ferroaxial mechanism in multiferroics, a chiral in-plane transverse coupling term is observed, whose Landau invariant is of 5^{th} order.

(This page is intentionally left blank)

Acknowledgements

First of all, I want to thank my supervisor Jonathan Yates, who gave me the opportunity to come to Oxford, supported the project, and always helped me pursuing scientific collaborations and extracurricular activities.

I would like to show my gratitude to Paolo Radaelli. With his profound knowledge and extensive experience, he helped moving our project further, and motivated me throughout the process. Roger, Francis, and Noah are also gratefully acknowledged for their patience and discussions.

Also, I am immensely grateful to David Vanderbilt for welcoming me at Rutgers, and not only providing me with a place to work, but also for the many fruitful discussions that immersed during our collaboration. Meng Ye is gratefully acknowledged. Her willingness to share her knowledge of magnetoelectrics and code development is really appreciated, as well as her efforts to introduce me to the incredibly knowledgeable and fun group at Rutgers.

I have the pleasure of thanking Eric Bousquet for all the valuable discussions. He always pointed me in the right direction and asked the right questions when discussing results.

My "three-and-a-half" years in Oxford are full of many, many great experiences. I am thankful to have studied in such a breathtaking environment. Many friends in London and at The Queen's College made my time here special, but above all, I want to show my gratitude to Daniel "Daniel" Yin. So many laughters, arguments, nights out, discussions, eye-openers, cries, and rants have brought me through the PhD and made the time in Oxford special. I cannot express how much I have learned from you (and your proofreadings). Best house mate.

Nina and Maya count to the friends "back home", who I never want to miss, and who provide me with laughter and wisdom, long chats and love, and everything I could wish for.

Furthermore, I would like to send my best thanks to my other chapter-wise proofreaders: Marina, Hannes, Bi-Ching, Tilmann, Samuel, Olli, Martin, Isabel, George, Fabio, Miguel (in no particular order). Thanks also to the rest of the MML!

Finally, my parents and my family deserve the deepest appreciation. I cannot put into words how much I love you. You are the backbone for everything I did: you listened, when I thought I will give up, you joked when I haven't laughed in ages, you lifted the weight off my shoulders when my head was over-occupied, and you supported me physically with house-moves and financially during my degree. Everything I do is dedicated to you, "Mamo" and "Papo".

The work was funded by EPSRC grants, number EP/J003557/1, entitled "New Concepts in Multiferroics and Magnetoelectrics" and number EP/M020517/1, entitled "Oxford Quantum Materials Platform Grant", and the Scatcherd European Scholarship. This work used the ARCHER UK National Supercomputing Service (http://www.archer.ac.uk), for which access was obtained via the UKCP consortium and funded by EPSRC grant ref EP/K013564/1. All structures in this thesis are plotted using VESTA [1].

(This page is intentionally left blank)

Publications

The results of two chapters are described in the following publications:

Accepted N. Tillack, J. R. Yates, P. G. Radaelli, "*Ab Initio* Cycloidal and Chiral Magnetoelectric Responses in Cr_2O_3", Physical Review B.
ArXiv: http://arxiv.org/abs/1603.00665

In submission N. Tillack, J. R. Yates, P. G. Radaelli, "Strain Dependence and Giant Linear Magneto-Electric Response at the Metal-Insulator Transition in Cr_2O_3 from First Principles"

Nomenclature

Experimental

MIT	Metal insulator transition
NPD	Nitrogen-phosphorus detector
SQUID	Superconducting quantum interference device

Computational

AE	All-electron
APW	Augmented plane wave
DFPT	Density functional perturbation theory
DFT	Density functional theory
FD	Finite differences
FLAPW	Full-potential linearised augmented-plane wave
GGA	Generalised gradient approximation
LAPW	Linearised augmented plane wave
NC	Norm-conserving
NN/NNN	Nearest neighbour / Next-nearest neighbour
PAW	Projector augmented-wave
PBE	Perdew-Burke-Ernzerhof functional
PES	Potential energy surface
PP	Pseudopotential
PZ	Perdew-Zunger parametrisation

RMM-DIIS	Residual minimization method—direct inversion in the iterative subspace
L(S)DA	Local (spin) density approximation
US	Ultra-soft
VWN	Vosko-Wilk-Nusair parametrisation
xc	Exchange correlation

Magnetism

AFM	Antiferromagnetic/Antiferromagnetism
CS	Centrosymmetric/Centrosymmetry
EB	Exchange bias
FM	Ferromagnetic/Ferromagnetism
ME	Magnetoelectric/-ity
PE	Piezoelectric/-ity
PM	Paramagnetic/Paramagnetism

Quantities

BEC	Born effective charges
DOS	Density of states
ϵ/μ	Electric/magnetic permittivity
e	Elementary charge
E/H	Electric/magnetic field
$\hbar$	Reduced Planck constant
IFC	Interatomic force constant
MC	Magnetic charges
P/M	Spontaneous polarisation/magnetisation
SOC	Spin-orbit coupling

Contents

Nomenclature 8

List of Figures 17

List of Tables 20

1 Magnetoelectricity 21

1.1 Introduction and Basics . . . 21

1.1.1 Heuristic Picture . . . 21

1.1.2 Historical Background . . . 24

1.1.3 Possible Applications . . . 25

1.1.4 Exchange Bias . . . 27

1.1.5 Thesis Outline . . . 29

1.2 Theoretical Background . . . 30

1.2.1 Magnetic Symmetry . . . 31

1.2.2 Thermodynamic Interactions . . . 32

1.2.3 Tensorial Properties . . . 37

1.2.4 Microscopic Theory . . . 39

1.3 Magnetoelectric Materials . . . 47

1.3.1 Experimental Techniques . . . 47

1.3.2 Cr_2O_3 . . . 48

1.3.3 AFM and Cycloidal Arrangements . . . 50

2 Ab Initio Theory **57**

2.1 Many-Body Systems . . . 57

2.1.1 Born-Oppenheimer Approximation . . . 59

2.1.2 Rayleigh-Ritz Variational Principle . . . 61

2.2 Density Functional Theory . . . 62

2.2.1 Hohenberg-Kohn Theorems . . . 62

2.2.2 Kohn-Sham Theory . . . 64

2.2.3 Exchange-Correlation Functionals . . . 67

2.2.4 Bloch's Theorem . . . 71

2.2.5 Plane Waves . . . 71

2.2.6 Pseudopotentials . . . 73

2.2.7 Projector Augmented-Wave Method . . . 78

2.3 Materials Properties . . . 81

2.3.1 Interatomic Force-Constant Matrix . . . 81

2.3.2 Polarisation and Berry Phases . . . 82

2.3.3 Born-Effective Charges . . . 85

2.3.4 Spin Polarised Density Functional Theory . . . 86

2.3.5 Orbital Magnetisation . . . 89

2.3.6 Relativistic Effects . . . 89

3 Magnetoelectricity in the $\bar{3}'m'$ Phase of Cr_2O_3 **91**

3.1 Preliminaries . . . 92

3.1.1 Group-Theory Analysis . . . 92

3.1.2 Existing Methodology . . . 95

3.1.3 Implemented Formalism . . . 100

3.2 Results . . . 103

3.2.1 Ground-State Properties . . . 103

3.2.2 Interatomic Force-Constant Matrix . . . 106

3.2.3 Born Effective Charges . . . 106

3.2.4 Magnetic Charges . . . 109
3.3 Analysis . . . 111
3.3.1 Lattice Response . . . 111
3.3.2 Electronic Response . . . 117
3.3.3 *XC*-Functionals . . . 118
3.4 Summary . . . 130

4 Pressure Dependence of the ME Effect 133
4.1 Preliminaries . . . 134
4.1.1 Theoretical Background . . . 134
4.1.2 First-Principles Formalism . . . 135
4.2 Results . . . 136
4.2.1 Ground-State Properties . . . 136
4.2.2 Electronic Properties . . . 139
4.3 Analysis . . . 141
4.3.1 Lattice Response . . . 141
4.3.2 Electronic Response . . . 145
4.3.3 Discussion . . . 147
4.4 Summary . . . 149

5 Compounds Based on the Cr_2O_3 Corundum Phase 151
5.1 Preliminaries . . . 152
5.1.1 The Impurity Atoms . . . 152
5.1.2 Group-Theory Analysis . . . 156
5.1.3 First-Principles Formalism . . . 158
5.2 Results . . . 160
5.2.1 Ground-State Properties . . . 160
5.2.2 Magnetoelectric Response . . . 164
5.3 Analysis . . . 169

5.3.1 Magnetoelectric Tensor . . . 169
5.3.2 Interpretation and Discussion . . . 170
5.4 Summary . . . 173

6 Spinflop Phase of Cr_2O_3 **175**
6.1 Preliminaries . . . 175
6.1.1 Theoretical Background . . . 175
6.1.2 Group-Theory Analysis . . . 177
6.2 Results . . . 182
6.2.1 Ground-State Properties . . . 182
6.2.2 Magnetoelectric Response . . . 183
6.3 Analysis . . . 186
6.3.1 Microscopic Contributions . . . 186
6.3.2 Landau Invariants . . . 192
6.4 Summary . . . 194

7 Conclusion and Perspective **197**
7.1 Summary . . . 197
7.2 Outlook . . . 202

Bibliography **205**

List of Figures

1.1 Hysteresis loop. 22

1.2 Relationship between electric, magnetic, and elastic properties. . 23

1.3 Groups of magnetoelectric and multiferroic materials. 24

1.4 Mechanistic origin of the exchange bias effect at an AFM/FM interface. 28

1.5 Schematic explanation of stereographic projections. 32

1.6 Symmetry transformations for axial vectors. 33

1.7 Transformation properties of the ferroic orders, including the toroidal moment. 37

1.8 Magnetic point groups and their corresponding tensor form of the ME coupling tensor. 40

1.9 Effect on the induced polarisation by different collinear and non-collinear spin structures. 42

1.10 Symmetric exchange inducing a polarisation. 43

1.11 Direct and inverse effects of the Dzyaloshinskii-Moriya interaction. 44

1.12 A left- and right-handed proper-screw structure. 46

1.13 Rhombohedral primitive cell of Cr_2O_3. 48

1.14 Temperature-dependent magnetoelectric response of Cr_2O_3. . . . 49

1.15 Multiferroicity in $HoMnO_3$. 51

1.16 Magnetic structures of rare-earth manganites. 53

2.1 Schematic representation of the self-consistency cycle to solve the Kohn-Sham equations. 70

2.2 Ultra-soft, norm-conserving, and all-electron $3d$ radial wave-function for iron. 75

2.3 The multi-valuedness of the net-polarisation in the Berry-phase approach. 83

3.1 The stereographic projection of the Cr_2O_3 crystallographic point group $\bar{3}m$. 93

3.2 Visualisation of the two symmetry elements of AFM-G Cr_2O_3 (magnetic point group $\bar{3}'m'$). (**a**) Trigonal point group $\bar{3}'$, (**b**) monoclinic mirror transformation m'. 93

3.3 Polarisation change in Cr_2O_3 through lattice and electronic mediated responses. 98

3.4 Cr_2O_3 bandstructure comparison of VASP, Quantum Espresso, and Elk. 105

3.5 Influence of spin-orbit coupling on the Cr_2O_3 conduction and valence sets of bands. 106

3.6 Nonlinear behaviour of the ionic forces upon application of an external magnetic field in Cr_2O_3. 111

3.7 Linear behaviour of the ionic forces in Cr_2O_3 with respect to an external magnetic field with PBE. 112

3.8 Linear behaviour of the ionic forces in Cr_2O_3 with respect to an external magnetic field within the LDA. 113

3.9 LDA change in polarisation over an applied magnetic field in Cr_2O_3. 118

3.10 Tilting of the Cr magnetic moment for LDA and LDA+U calculations under a strong magnetic field. 121

3.11 Convergence of the Cr magnetic moment for LDA and LDA+U calculations under a strong magnetic field. 121
3.12 Difference in charge densities for LDA and LDA+U calculations with a strong magnetic field in x direction. 122
3.13 LDA and LDA+U density of states of Cr_2O_3. 129
3.14 Effect of the Hubbard U on the band gap and the transverse electronic ME response. 130

4.1 Pressure dependence of magnetic and electric properties in Cr_2O_3. 137
4.2 Pressure dependence of the structural properties in the AFM and PM phase of Cr_2O_3. 138
4.3 Pressure dependence of the structural properties in the AFM and PM phase of Cr_2O_3. 138
4.4 Density of states in the AFM and PM phase of Cr_2O_3 under pressure. 140
4.5 Eigenvalues, BEC, and the magnetic charges of Cr_2O_3 under pressure. 142
4.6 Lattice response α^{latt} in Cr_2O_3 under pressure. 144
4.7 Electronic response α^{latt} and dielectric tensor in Cr_2O_3 under pressure. 146
4.8 Comparison of strengths of ME coupling tensors. 148

5.1 Structures of $(Cr_{1-x}M_x)_2O_3$ in the substituted $\bar{3}'m'$ corundum phase of Cr_2O_3. 153
5.2 Tensor forms of the Born effective charges, magnetic charges, and the magnetoelectric coupling tensor in the compound phases of Cr_2O_3. 158
5.3 Differential charge density distributions of $(Cr_{1-x}M_x)_2O_3$ in the substituted $\bar{3}'m'$ corundum phase of Cr_2O_3. 165

6.1 Low-field and spinflop magnetic structures of Cr_2O_3. 177
6.2 Stereographic projection of the crystallographic point group of the spinflop phase of Cr_2O_3. 178
6.3 Tensor forms of the Born effective charges, magnetic charges, and the magnetoelectric coupling tensor in the low-field and spinflop phases of Cr_2O_3. 181
6.4 Dzyaloshinskii-Moriya, longitudinal, and chiral mechanism for the magnetisation response to an external magnetic field. 187

List of Tables

1.1 Symmetry properties of electric and magnetic quantities. 35

1.2 Transformation laws for polar and axial tensors. 38

1.3 A list of magnetoelectric materials. 56

3.1 Transformation matrices for $\bar{3}$ and m. 94

3.2 Structural, electronic, and magnetic properties of Cr_2O_3 104

3.3 Comparison of IR active mode frequencies for Cr_2O_3. 107

3.4 Transformation matrices for 2 and 3. 107

3.5 Tensor forms of the BEC tensor and the magnetic charge tensor for the Cr and the O atom. 108

3.6 Born effective charges of Cr in Cr_2O_3. 109

3.7 Born effective charges of O in Cr_2O_3. 109

3.8 Dynamical magnetic charges Z^m of Cr in Cr_2O_3. 111

3.9 Dynamical magnetic charges Z^m of O in Cr_2O_3. 113

3.10 Comparison of mode decomposition of the Born effective charges for Cr_2O_3 with PBE. 116

3.11 Comparison of mode decomposition of the dynamical magnetic charges for Cr_2O_3 with PBE. 116

3.12 Mode contribution to α for Cr_2O_3 using the PBE functional. . . 117

3.13 Born effective charges Z^e of Cr in Cr_2O_3 for different xc-functionals. 123

3.14 Born effective charges Z^e of O in Cr_2O_3 for different xc-functionals. 123

3.15 Comparison of IR active mode eigenvalues for Cr_2O_3. 124
3.16 Dynamical magnetic charges Z^m of Cr in Cr_2O_3 for different xc-functionals. 124
3.17 Dynamical magnetic charges Z^m of O in Cr_2O_3 for different xc-functionals. 125
3.18 Comparison of the mode contribution to α for Cr_2O_3 with a relaxed unit cell. 126
3.19 Comparison of the mode contribution to α for Cr_2O_3 with a fixed lattice parameter. 127
3.20 Comparison of values for α^{latt} and α^{el} from the present work and literature. 128

5.1 Transformation matrices for $3 \parallel z$, $m \perp x$, and $2 \parallel x$. 157
5.2 Wyckoff positions and respective symmetries in the substituted compound phases of Cr_2O_3. 159
5.3 Structural, electronic, and magnetic properties of $\uparrow\downarrow\downarrow\uparrow$ Fe_2O_3 and PM Ti_2O_3 161
5.4 Ground-state properties of the Fe- and Ti-substituted Cr_2O_3. . . 163
5.5 Born effective charges of Cr in M-substituted Cr_2O_3. 167
5.6 Magnetic charges of Cr in Fe-substituted Cr_2O_3. 168
5.7 Magnetic charges of O in Fe-substituted Cr_2O_3. 169
5.8 ME coupling tensors in Fe-substituted Cr_2O_3. 171
5.9 Comparison of the mode contribution to α for Cr_2O_3 and Fe_2O_3. 172

6.1 Wyckoff positions and respective symmetries in the low-field and spinflop phases of Cr_2O_3. 179
6.2 Change in lattice properties between the $\bar{3}'m'$ and the SF phases. 183
6.3 Magnetic charges for the low-field and spinflop phases of Cr_2O_3. 184

6.4 Magnetoelectric coupling tensors for the low-field and spinflop phases of Cr_2O_3. 185
6.5 Invariant polynomials of the space group $R\bar{3}c$ up to 5^{th} order that give rise to terms in the ME tensor. 193
6.6 Tensor forms of the ME tensor for Cr_2O_3 in its low-field and spinflop phases expressed in terms of invariant polynomials. . . 194

1 Magnetoelectricity

The present chapter serves as an overview about magnetoelectricity (ME) and magnetoelectric materials. Section 1.1 will introduce magnetoelectricity on the basis of its historical discovery and will motivate the research behind it. The theoretical concepts to describe magnetoelectricity will be discussed in Section 1.2 and exemplified in Section 1.3, where common families of MEs will be reviewed.

1.1 Introduction and Basics

In the following section, the concept of magnetoelectricity, its historical discovery, and its practical applications will be discussed. The background for multiferroicity, its similarities and differences to magnetoelectricity will also be outlined briefly, as a co-existence between the two phenomena ("magnetoelectric multiferroics") is often desired. The section covers aspects relevant for the present thesis. For more detailed reviews of the topic, the interested reader is referred to Refs. [2–4].

1.1.1 Heuristic Picture

Ferromagnetism is a type of magnetic long-range ordering. It shows a spontaneous magnetisation, which can be reversed by an external magnetic field. The time-dependent magnetisation in response to a magnetic field is described by

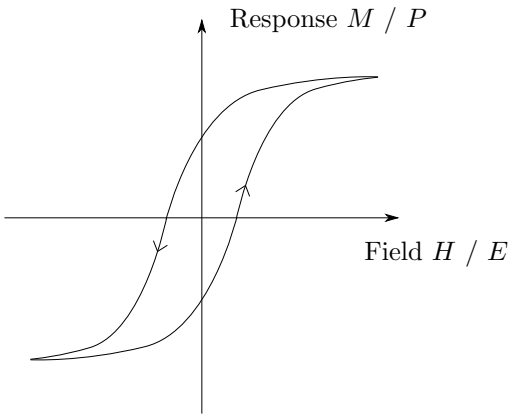


Figure 1.1: Hysteresis loop for ferromagnetic or ferroelectric materials. If a field is applied, magnetic or electric dipole moments adjust according to the material and *remain*, even if the field is turned off, thus resulting in a net-magnetisation or net-polarisation. Fields in opposite direction reverse the net-moments.

a "hysteresis" loop (Fig. 1.1). Ferroelectricity is the electric equivalent of ferromagnetism, exhibiting a net-polarisation without an external electric field, and is also described by a hysteresis [5].

Magnetoelectric coupling describes the response of the polarisation (magnetisation) of a material to an external magnetic (electric) field. In classic electromagnetism, the electric field $\mathbf{E}$ controls the polarisation $\mathbf{P}$, the magnetic field $\mathbf{H}$ influences the magnetisation $\mathbf{M}$, and the strain $\boldsymbol{\epsilon}$ depends on the stress $\boldsymbol{\sigma}$. The triangle in Fig. 1.2 sketches different materials properties and how they are induced. The cross-coupling indicated by the dashed arrows is called "magnetoelectricity" (ME).

The linear ME response is quantified by the ME coupling tensor α_{ij}:

$$\alpha_{ij} = \mu_0 \left(\frac{\partial M_j}{\partial E_i} \right) = \left(\frac{\partial P_i}{\partial H_j} \right), \tag{1.1}$$

with M and P, H and E being the spontaneous magnetisation and polarisation, and the external magnetic and electric field, respectively. μ_0 is the vacuum permeability.

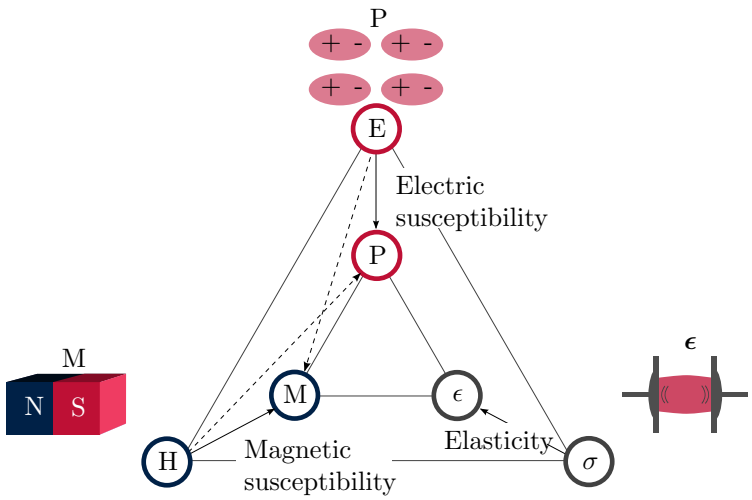


Figure 1.2: Relationship between electric, magnetic, and elastic properties, modified from Ref. [6]. Where normally the magnetic field H, electric field E, and stress σ control the magnetisation M, polarisation P, and strain ϵ, respectively, the cross-couplings are of high interest. Piezoelectricity (piezomagnetism) is the coupling of elastic and electric (magnetic) properties; magnetoelectricity describes the coupling between magnetic and electric properties.

Multiferroicity (MF) defines the co-existence of two or more ferroic order parameters, such as spontaneous long-range magnetic and dipolar order [7]. Currently, the set of materials that are both ferromagnetic and ferroelectric are mostly referred to as multiferroic. Of major interest are MFs that not only exhibit a co-existence, but also a *coupling* of their magnetic and electric properties. It is important to note that it is neither sufficient nor necessary for MFs to be ME or *vice versa* [8]; there can be magnetoelectric and non-magnetoelectric MFs, as well as non-MF MEs (Fig. 1.3). Because of the complex interplay between these material properties and because an exhaustive theory for the mechanistic reasons for magnetoelectricity and multiferroicity is still lacking, the search for a deeper understanding of ME, both as part of the cross-coupling in multiferroics and as a standalone property, has become ever more important in recent years.

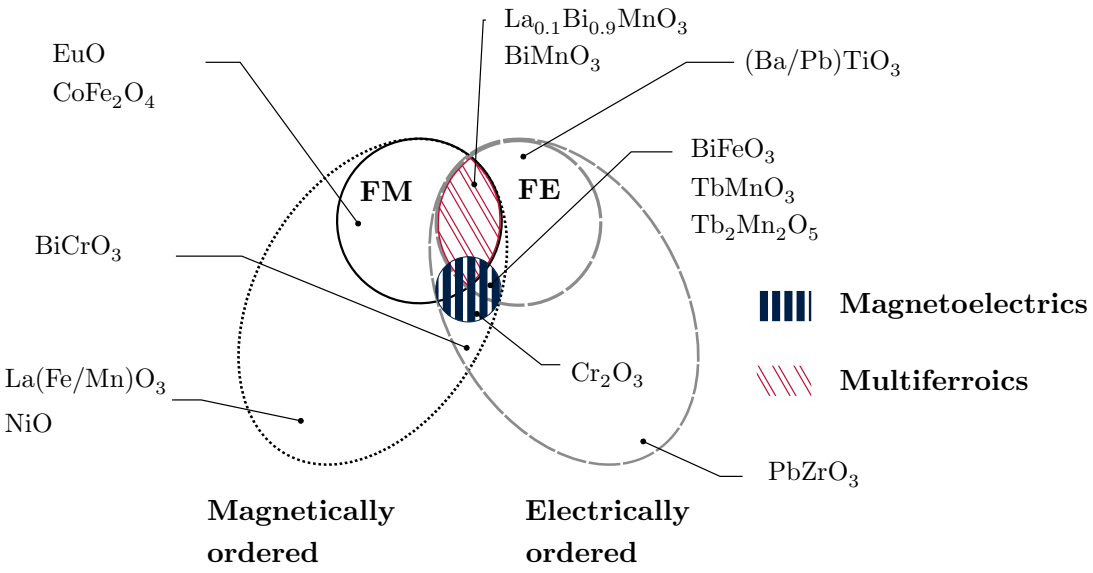


Figure 1.3: Groups and subgroups of magnetoelectric (ME) and multiferroic (MF) materials, adapted from Ref. [8, 9]. The exemplary oxides are reported in Ref. [10]. The dotted black and dashed grey ellipses denote magnetically and electrically ordered materials, respectively, with black and grey circles for ferromagnets (FMs) and ferroelectrics (FEs) as respective subgroups. The overlap of these circles are—in the modern sense—MF materials, showing both spontaneous polarisation and magnetisation in the same phase, and are represented by the diagonally hatched region. ME materials, the striped circle, are both magnetically and electrically polarisable. *Their* overlap in turn are MF MEs—when spontaneous magnetisation and polarisation co-exist and couple. The lower part of the ME circle includes materials that are magnetically ordered but do not exhibit FE, such as Cr_2O_3. The AFM FE MEs include $TbMnO_3$ and $BiFeO_3$. MFs on the other hand that are not ME, where magnetic and electric order co-exists independently, are, *e.g.* $BiMnO_3$ or $La_{0.1}Bi_{0.9}MnO_3$. The remaining part of the ellipses are other magnetically/electrically ordered materials, such as antiferroelectrics, antiferromagnets, or ferrimagnets.

1.1.2 Historical Background

The discovery of an induced magnetisation in a dielectric material moving in an electric field dates back to Wilhelm Conrad Röntgen [11], but Pierre Curie was the first one to discuss an intrinsic correlation between electric and magnetic properties in 1894 [12].[1] In 1926, Peter Debye coined the term "magnetoelectricity" when he described the induction of a magnetic response upon an electric field and *vice versa* [14]. The actual investigation of ME and its

[1] In fact, it was also Pierre Curie and his brother Jacques Curie, who discovered the coupling of elasticity and electricity in 1880, later known as "piezoelectricity" [13].

symmetry requirements took place in the 1950s and 1960s. L. Landau and E. Lifshitz proved with their symmetry analysis that ME only occurs in magnetic, *i.e.* time-reversal odd, materials [15]. Two years later the first theoretical prediction of a ME material was published by I. Dzyaloshinskii for Cr_2O_3 [16, 17]. The experimental proof followed soon thereafter, when it was first observed that it exhibits a *magnetisation* upon application of an external *electric* field [18–20], complemented by experiments revealing a spontaneous *polarisation* upon application of a *magnetic* field [21, 22]. Cr_2O_3 became the prototypical ME.

The interest in ME materials greatly increased and reached its first peak in 1973 with the first "Magnetoelectric Interaction Phenomena In Crystals" conference, only to plummet shortly after, as the coupling remained too small to be useful in any applications. Renewed interest in recent years was sparked, however, with the rise of modern multiferroics [3, 9, 23–25].

1.1.3 Possible Applications

The magnitude of their response is crucial for the actual implementation of ME materials in technical applications. In earlier studies, the coupling tensor α was reported in the rationalised Gaussian unit system; more recently SI units are used and α is given in $\mathrm{ps\,m^{-1}}$. The relation is [26]:

$$c\alpha_{\mathrm{SI}} = 4\pi\alpha_{\mathrm{rG}}, \tag{1.2}$$

with c being the vacuum speed of light. Multiferroicity is quantified by the magnitude of induced ferroelectricity in a material with a magnetic order parameter. The induced polarisation is usually reported in $\mu\mathrm{C\,cm^{-2}}$.

MEs have hitherto not been used in many applications. Low operating temperatures or high magnetic fields are often required to keep the material in its ME state. In addition, most of the presently known MEs have a small coupling tensor of a few $\mathrm{ps\,m^{-1}}$, making them impractical to use. This limitation is partly attributed to the upper bound [27]

$$\alpha_{ij} \leq \sqrt{\epsilon_{ii}\mu_{jj}}, \tag{1.3}$$

where ϵ and μ are the dielectric and magnetic permeabilities. In fact, the actual values for α are usually well below the upper bound: the coupling strength of the prototypical ME Cr_2O_3 reaches values of 0.1 % its upper bound [27].

There are numerous technologies that would benefit or even be possible when utilising magnetoelectrics [28, 29]; particularly the rise of antiferromagnetic spintronics is worth noting [30]. The advantage to switch a magnetic state with a voltage input is of huge interest for modern technology. These switches should be quick and persist after switching when being used in storage devices. Magnetoelectric MFs in memory devices should ideally be insulating and maintain a high polarisation of $\geq 1\,\mathrm{\mu C\,cm^{-2}}$ after the switch. This is challenging, as when a material meets one of these requirements, it performs poorly on the others. Take, *e.g.* CuO, which is MF with a Curie temperature of 230 K [31, 32], but has a polarisation that is too small to be read by a sense amplifier for a switched-capacitor RAM, a digital data-storage device. Also in other cases polarisations are usually in the order of magnitude of a few $\mathrm{nC\,cm^{-2}}$ or $\mathrm{\mu C\,cm^{-2}}$ [8, 32]. Hexaferrites, *i.e.* iron oxides with hexagonal crystal structures, have recently been observed to show ME behaviour at room temperature and only under a small magnetic field [33–36]. Most of them still exhibit a very small polarisation, but their discovery is a big step toward finding suitable MF materials.

In addition to their use in multiferroic devices, materials that provide a voltage output (magnetisation) due to a magnetic (electric) field are very useful on their own, *viz.* for the replacement of SQUIDs (Superconducting quantum interference devices) [37]. Sandwich structures are a possible alternative for these applications. Ref. [8] mentions military applications for such technology, as well as portable magnetic detectors for field work, and medical applications such as MRIs. Moreover, voltage driven phase shifters may be implemented in phased-array radar devices.

1.1.4 Exchange Bias

Due to its room-temperature ME response, a renewed interest in the prototypical Cr_2O_3 has emerged through recent efforts directed towards the ME switching of exchange bias (EB) in Cr_2O_3 interfaces [38–41]. EB is a coupling phenomenon that occurs at interfaces of ferromagnetic (FM) and antiferromagnetic (AFM) layers,[2] causing a shift in the FM hysteresis loop along the magnetic-field axis. EB is based on the alignment of magnetic moments in the AFM material along the FM spin direction upon cooling. It was first discovered in 1956, where it was observed as "exchange anisotropy" in fine particles of cobalt and cobaltous oxide [44]. The FM cobalt spins interacted with the AFM CoO spins below the Néel temperature of CoO. The mechanism is sketched in Fig. 1.4. If an external magnetic field is applied in the low-temperature state, or the field direction is changed, the spins of the FM material try to realign, while the AFM configuration remains. The magnetic exchange "pins" the FM spins to their initial position, so that the initial configuration is the most stable, making the anisotropy unidirectional.

EB systems are already used in permanent magnets, magnetic recording media, and recording heads. With EB materials, states of readback heads of

[2] The same mechanism holds generally true for interfaces of magnetically-ordered materials [42, 43].

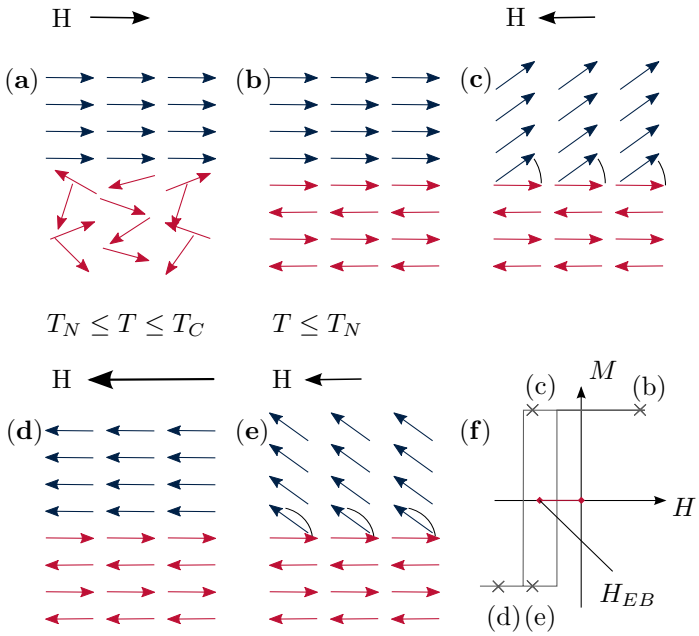


Figure 1.4: Mechanism for the exchange bias effect at an antiferromagnetic (magenta)/ferromagnetic (blue) interface, adapted from Ref. [45]. From (**a**) to (**b**) the sample is cooled under a magnetic field H ("magnetic field cooling") from a temperature $T_C > T > T_N$ to $T < T_N$ causing the antiferromagnet (AFM) to align along the ferromagnetic (FM) layer. Depending on the exchange interaction between the atomic species in the layers, the they align either ferromagnetically or antiferromagnetically (depicted here is the former). Upon application of a magnetic field in the other direction, the FM spins cannot switch as easily as without the AFM layer: it is *pinned* to the AFM layer (**c**). The magnetic field required to reverse the FM direction is higher with the AFM layer, (**d**), and a smaller field is required to bring the spins in the FM layer back to their original position, (**e**). This "unidirectional" anisotropy leads to a shift of the magnetic hysteresis loop of H_{EB}, as summarised in (**f**).

hard-disk drives can be pinned at their point of maximum sensitivity. Without the pinning, the magnetic domain state of the readback head could become unstable thus unpredictable. It was also observed that the saturation fields in giant magnetoresistance are reduced if EB systems are used [46]. The magnetoresistive random-access memory (MRAM) circuits and spin valve readback heads that utilise the magnetic tunneling or giant magnetoresistance effect, also make use of the pinning mechanism of EB systems [47]. For a more exhaustive background on the EB effect, the reader is referred to Ref. [48].

Within the last decade, AFM magnetoelectrics have been investigated to serve in the EB bilayers. The key advantage is to change the AFM state by an external electric field and therefore change the sign of the EB field H_{EB} [39, 49–52]. The possibility to control the EB via voltage inputs leads to an easier switching [41], efficiency increase, and cost reduction in all the aforementioned EB applications. Again, the archetypical Cr_2O_3 proves itself to be extremely useful: not only the room temperature magnetoelectricity, but also its uniaxiality allowing for only two different 180° magnetic or polar domains, make Cr_2O_3 of "unprecedented" value [23, 38, 53].

1.1.5 Thesis Outline

One crucial step towards actual applications and improved performance of ME driven technologies is to gain a deeper understanding of the mechanisms behind ME. Besides the discovery of more families of materials with ME behaviour, and of MF magnetoelectrics, to date researchers have not derived a trend to systematically predict new MEs, or design materials with a stronger coupling, higher polarisation and operating temperature, and the other properties of interest. This is the area the present DPhil project attempts to delineate. In this thesis, state-of-the-art *ab initio* methods are used, developed, and tested, in order to study magnetoelectric (ME) materials under different influences with the aim to get a better understanding of the underlying mechanisms of ME.

The previous section 1.1 introduced the basic principles of ME and MF and motivated the research on these materials with their possible applications. Sections 1.2 and 1.3 will outline the origin behind ME and MF on the basis of key experimental, group-theoretical, and computational studies. To investigate magnetoelectricity, we combined group-theoretical and computational models. In order to describe the subtle effects of the studied mechanisms, we employed

and implemented modern additions to conventional density functional theory (DFT) codes. These will be covered in Chapter 2, where DFT with its implementations of noncollinear magnetism, the modern theory of polarisation, and the application of external electric or magnetic fields in the self-consistent cycle will be discussed. How the first-principles techniques were applied to model the quantities of interest and how different computational parameters affect the results will be covered in Chapter 3. Subsequently, a focus will be given on the cases studied in the present work: in Chapter 4, we will report on the effect of pressure on the ME coupling. The impact of the crystallographic, magnetic, and electronic structure will be examined in detail. We modelled the effect of doping by substituting single atoms in a Cr_2O_3 matrix, which will be covered in Chapter 5. The isolated effect of the magnetic structure on the ME coupling was modelled and will be reported in Chapter 6, where we show a novel ME coupling in the spinflop case of Cr_2O_3. Finally, a conclusion is given in Chapter 7, together with an outlook on how future studies can complement the present findings and bring the field of magnetoelectrics one step closer to real-life applications.

1.2 Theoretical Background

Physical properties describe, in terms of general condensed matter physics, how a material reacts to an external influence. This section serves as an overview about the origin behind magnetoelectricity and multiferroicity on the basis of group-theoretical, thermodynamic, and microscopic principles, as well as about the experimental background. As magnetoelectricity is a direction-dependent response, symmetry and anisotropy in magnetic crystals must be understood in great detail. An introduction of magnetic properties will hence be given first. Group-theory conventions, followed by symmetry considerations that classify a material as a possible ME will be outlined, as well as the thermodynamic

framework in which ME can be explained with respect to the free energy of a material. The microscopic mechanisms that allow for a coupling between magnetic and electric properties will be derived on the basis of Cr_2O_3 and significant work on the other types of MEs and MFs.

1.2.1 Magnetic Symmetry

3-dimensional infinite materials are described by 14 lattice types and 7 crystal systems. 32 crystallographic point groups and 230 space groups are required to characterise the systems by their invariance to symmetry elements such as translations, reflections, proper and improper rotations, screw axis operations, and glide plane operations [54]. In this thesis, the Hermann-Mauguin notation, or "international notation", will be used to label space and point groups. To visualise the 3-dimensional symmetry operations of a crystal in 2 dimensions, we will use stereographic projections, illustrated in Fig. 1.5.

In magnetic materials, magnetic moments on crystallographic positions need to be taken into account and each symmetry operation needs to be re-examined on the basis of time reversal symmetry. As opposed to *polar* vector quantities, such as a force or a polarisation, which are invariant under time reversal or improper rotations, magnetic moments originate from a moving charge and therefore transform differently under symmetry operations. Such vector quantities are represented by *axial* vectors or *pseudovectors* [58]. Fig. 1.6 visualises their main differences and shows how positions can become inequivalent under a spatial symmetry operation if magnetisation is taken into account. Combining the crystallographic point and space groups with magnetic configurations, their numbers add up to 122 magnetic point groups and 1651 magnetic space groups [59].

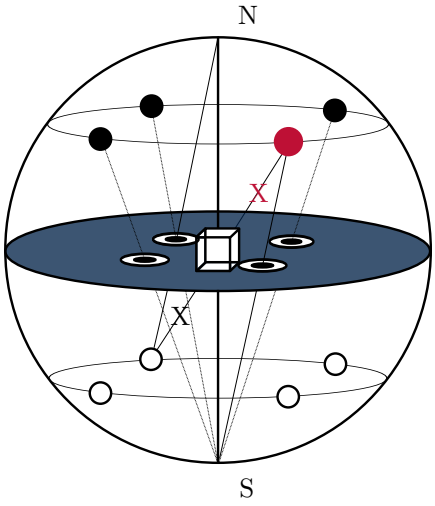


Figure 1.5: A stereographic projection maps 3-dimensional objects onto a 2-dimensional plane and is used to visualise crystallographic point groups and their generating elements. If a crystal is placed at the centre of a sphere, the horizontal plane cutting through it is defined as the "equatorial plane", which defines the north (N) and south (S) pole. A point of interest (X) is projected onto the sphere (•) and connected to the pole in the other hemisphere. Its stereographic projection is the point where the connecting line intersects the equatorial plane. It is convention that open (closed) circles describe points originating from the southern (northern) hemisphere. The empty circles in the southern hemisphere show the equivalent positions of their northern projections. Displayed here is the stereogram for a crystal with four equivalent positions linked by 90° rotations, such as point group 4, modified from Refs. [55–57].

1.2.2 Thermodynamic Interactions

The phenomenological *ansatz* for magnetoelectric exchange can be derived on the basis of thermodynamics by expanding the Gibbs free energy into a series of coupling terms [61]. To derive the ME coupling tensor, one expands with respect to an external E- and H-field [25]:

$$\begin{aligned} F(E,H) = F_0 - P_i^s E_i - M_i^s H_i - \frac{\epsilon_0 \epsilon_{ij}}{2} E_i E_j - \frac{\mu_0 \mu_{ij}}{2} H_i H_j \\ - \alpha_{ij} E_i H_j - \frac{\beta_{ijk}}{2} E_i H_j H_k - \frac{\gamma_{ijk}}{2} H_i E_j E_k - \cdots , \end{aligned} \tag{1.4}$$

with s denoting the spontaneous order parameters, ϵ_0 and μ_0 being the electric and magnetic vacuum permittivity, respectively; their relative equivalents are

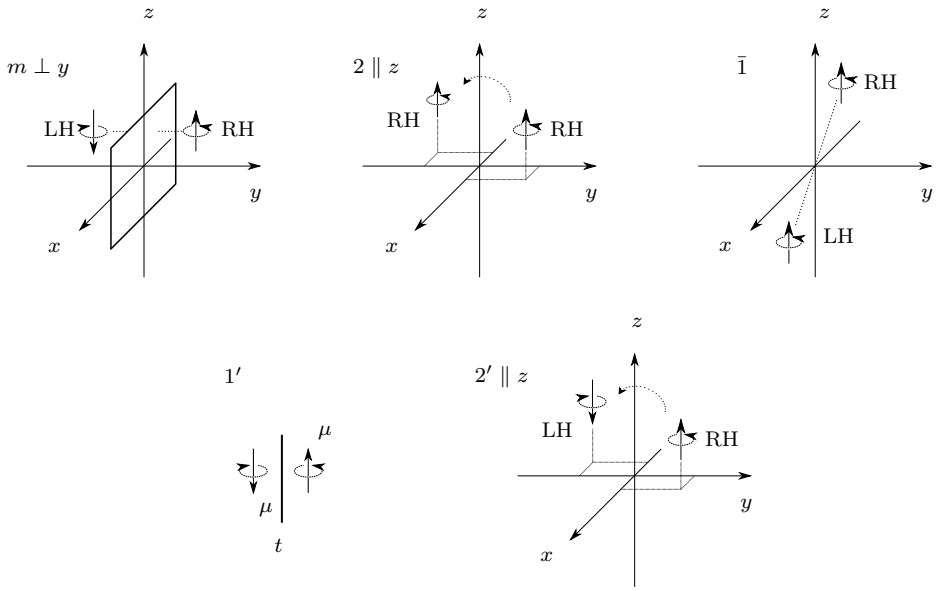


Figure 1.6: Symmetry transformations for axial vectors, adapted from Ref. [60]. The magnetic moment is displayed as a current flow. It transforms differently under symmetry operations than a polar quantity. For instance, the mirror operation shown in panel one reverses the direction of the current flow, hence the handedness of the pseudovector is changed, but would not affect the direction of a polar vector. Proper rotations, such as the one by 180° around z, do not affect the handedness of an axial vector, nor does point inversion ($\bar{1}$). Symmetry operations can be coupled to time reversal, denoted by primed quantities, and change the direction of the current flow (bottom panels). A polarisation, which originates from the spatial distance of two charges, is invariant under time reversal.

the second-rank tensors ϵ_{ij} and μ_{ij}. Einstein summation is implied. It follows that

$$\begin{aligned} P_i(E,H) &= -\frac{\partial F}{\partial E_i} = P_i^s + \epsilon_0\epsilon_{ij}E_j + \alpha_{ij}H_j + \frac{\beta_{ijk}}{2}H_jH_k + \gamma_{ijk}H_iE_j + \cdots \\ M_i(E,H) &= -\frac{1}{\mu_0}\frac{\partial F}{\partial H_i} = M_i^s + \mu_0\mu_{ij}H_j + \alpha_{ij}E_i + \beta_{ijk}E_iH_j + \frac{\gamma_{ijk}}{2}E_jE_k + \cdots . \end{aligned} \tag{1.5}$$

One can see the first-order coupling of the magnetic and electric properties through the ME coefficient

$$\alpha_{ij} = \mu_0\left(\frac{\partial M_j}{\partial E_i}\right) = \left(\frac{\partial P_i}{\partial H_j}\right). \tag{1.6}$$

The middle (right) term in Eq. 1.6 stands for the direct (converse) ME ef-

fect. Furthermore, β and γ describe higher-order coupling effects. Similarly, expanding the thermodynamic potential by the electric field E and stress σ, one can obtain the response coefficients for the piezoelectric coupling:

$$d_{nij} = -\left(\frac{\partial^2 F}{\partial \sigma_{ij} \partial E_n}\right) = \left(\frac{\partial P_n}{\partial \sigma_{ij}}\right) = \left(\frac{\partial \epsilon_{ij}}{\partial E_n}\right). \tag{1.7}$$

Here, d_{nij} is the piezoelectric (PE) coupling tensor and ϵ_{ij} the strain. Again, the middle (right) term in Eq. 1.7 denotes the direct (converse) PE effect. We can see how expanding the Gibbs energy by the stress and the magnetic field yields the direct and converse piezomagnetic relations:

$$Q_{nij} = -\left(\frac{\partial^2 F}{\partial \sigma_{ij} \partial H_n}\right) = \left(\frac{\partial M_n}{\partial \sigma_{ij}}\right) = \left(\frac{\partial \epsilon_{ij}}{\partial H_n}\right) \tag{1.8}$$

Examples for higher-order coupling in piezoelelectric and piezomagnetic responses are electrostriction and magnetostriction, respectively [60]: the electrostriction (magnetostriction) coefficient is proportional to the strain dependence on the electric (magnetic) field squares; or to the electric (magnetic) field dependence of the piezoelectric (piezomagnetic) coefficient.

The Landau theory of phase transitions is a symmetry-based approach [62, 63], which describes the equilibrium behaviour of materials close to a phase transition. A phase transition is defined by an "order parameter", which—like in the case of magnetic ordering—becomes finite when the temperature is lowered from a high-symmetry structure (such as a paramagnetic phase) to a structure of lower symmetry (such as an AFM phase). In order to arrive at an expression linking the order parameters, the free energy of Eq. 1.4 can be expanded in terms of and minimised with respect to order parameters such as $\mathbf{M}$, $\mathbf{P}$, or the AFM order parameter $\mathbf{L}$. We can expand according to

Table 1.1: Symmetry properties of electric and magnetic quantities. "+" and "-" stand for even and odd transformation properties.

Quantity	Space	Time
E, **P**	-	+
M, **H**	+	-

$$
\begin{aligned}
F(P,M) = F_0 + &\frac{1}{2}\alpha_{ij}P_iP_j + \frac{1}{3}\beta_{ijk}P_iP_jP_k + \frac{1}{4}\gamma_{ijkl}P_iP_jP_kP_l + \ldots - a_{ij}P_iE_j \\
&+\frac{1}{2}\alpha'_{ij}M_iM_j + \ldots - a'_{ij}M_iH_j \\
&+\frac{1}{2}\alpha''_{ij}P_iM_j + \ldots \frac{1}{4}\gamma''_{ijkl}P_iP_jM_kM_l + \ldots,
\end{aligned}
$$

and identify the phenomenological Landau-Devonshire coefficients α, β, γ, *etc.*, and a_{ij} and a'_{ij} are the electric susceptibility and magnetic permittivity, respectively. Which terms are allowed depends on the space group of the crystal; they must be invariant under all symmetry operators of the group *above* the phase transition, the so-called "parent phase". In order to exhibit linear magnetoelectricity, the space group must contain bilinear terms, since these are invariant to both space and time inversion and we differentiate F with respect to the order parameter to get an expression for its value. Combinations of even powers of both **P** and **M** are allowed in every space group [3] and do not necessarily represent a linear coupling between both parameters.

Non-trivial coupling terms are linear in P and can be derived considering the symmetry arguments from Section 1.2.1. Table 1.1 summarises the symmetry properties of magnetic and electric quantities: **E** and **P** change sign under inversion of all their coordinates $\mathbf{r} \rightarrow -\mathbf{r}$ but are invariant under time inversion $t \rightarrow -t$, while the magnetic quantities **M** and **H** are space-even and time-odd.

Familiar examples are of the order $\mathbf{PM}^2$, where $\mathbf{M}^2$ transforms as a polar vector. The Lifshitz invariants derived by Mostovoy [64] and Sosnowska *et*

al. [65] are examples of how polarisation can be induced by an inhomogeneous magnetic order:

$$F(\mathbf{P}) \propto \mathbf{P} \cdot [\mathbf{M}(\nabla \cdot \mathbf{M}) - (\mathbf{M} \cdot \nabla \mathbf{M})] \tag{1.9}$$

and

$$F(\mathbf{P}) \propto \mathbf{P} \cdot [\mathbf{L}(\nabla \cdot \mathbf{L}) + \mathbf{L} \times (\nabla \times \mathbf{L})]. \tag{1.10}$$

Another example is the coupling of the form

$$F(\mathbf{P}) \propto \mathbf{P} \cdot (\mathbf{L} \times \mathbf{M}), \tag{1.11}$$

which is described by the spin-current mechanism [66] and the inverse Dzyaloshinskii-Moriya interaction [16, 67]. Details on how these terms can be induced microscopically follow in Section 1.2.4.

New switching mechanisms are frequently proposed, the most recent ones being by Benedek *et al.* [68], Johnson *et al.* [69], and Yang *et al.* [70]. The background for the most common microscopic mechanisms providing for the phenomenological coupling terms is given in Section 1.2.4.

In addition to the polarisation, magnetisation, and strain, corresponding to, respectively, ferroelectric, ferromagnetic, and ferroelastic properties of materials, the concept of another order parameter was recently defined. A spontaneous "toroidal moment" can be induced according to $\mathbf{T} = \mathbf{E} \times \mathbf{H}$, complementing the transformation properties of the aforementioned ferroic orders by being space- and time-odd, Fig. 1.7. It contributes to the total free energy [71]:

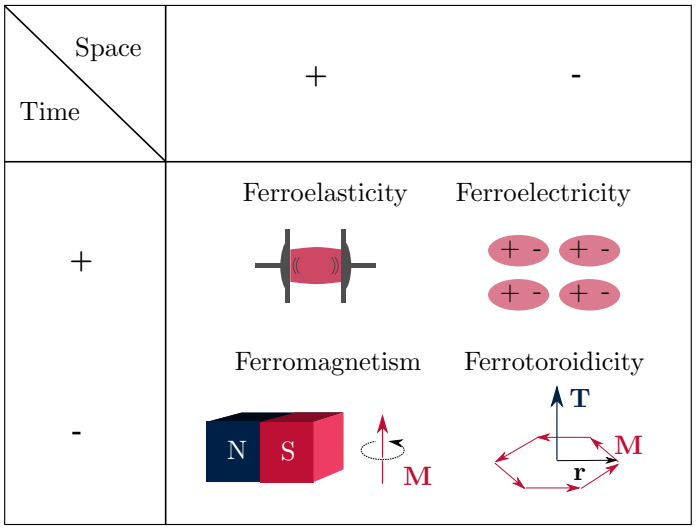


Figure 1.7: Transformation properties of the ferroic orders, including the toroidal moment. "+" and "-" stand for even (invariant) and odd transformation properties. Modified from Ref. [72].

$$F(\mathbf{P}) \propto \mathbf{T} \cdot (\mathbf{P} \times \mathbf{M}). \tag{1.12}$$

The toroidal moment is of magnetoelectric nature and is proportional to the antisymmetric part of the ME coupling tensor [73]. The importance and the impact of toroidal moments are unclear: they have been successful in describing some magnetoelectrics, whereas they cannot explain the magnetoelectric effects in, *e.g.* Cr_2O_3, and are subject of current research [74].

1.2.3 Tensorial Properties

In the last section, α was introduced as a 3×3 matrix. More generally, "tensors" describe physical properties of a system. They are described by their rank (or "degree") and their transformation properties with respect to space-time coordinate transformations. Scalars are tensors of rank 0, vectors tensors of rank 1, matrices are of rank 2, and a tensor of rank n has n indices and 3^n components. The concept of polar and axial vectors was already introduced in relation to magnetic symmetries of crystals. In the most general sense, Table 1.2 shows a summary of polar and axial tensors of different ranks and

Table 1.2: Polar and axial tensors A of different ranks after transformation from one coordinate system $\mathbf{e}_i$ into another one $\mathbf{e'}_i$ by a transformation T. The Einstein summation is implied, $\|T\|$ describes the determinant of the transformation matrix, and $i, \ldots, u = 1, 2, 3$.

Rank	Polar Tensor	Axial Tensor
0	$A'_{ij} = A_{kl}$	
1	$A'_i = T_{ij}A_j$	$A'_i = \|T\|T_{ij}A_j$
2	$A'_{ij} = T_{ik}T_{jl}A_{kl}$	$A'_{ij} = \|T\|T_{ik}T_{jl}A_{kl}$
3	$A'_{ijk} = T_{il}T_{jm}T_{kn}A_{lmn}$	$A'_{ijk} = \|T\|T_{il}T_{jm}T_{kn}A_{lmn}$
n	$A'_{ijk\ldots n} = T_{ip}T_{jq}T_{kr}\ldots T_{nu}A_{pqr\ldots u}$	$A'_{ijk\ldots n} = \|T\|T_{ip}T_{jq}T_{kr}\ldots T_{nu}A_{pqr\ldots u}$

their transformations. The handedness change for axial vectors is described by including the determinant of the transformation matrix.

Ginzburg-Landau analysis can be used to determine which elements of the coefficients (such as the elements of ϵ, μ, α, β, and γ in Eq. 1.4) in the order-parameter polynomials (such as P and M) can be nonzero for a given crystal symmetry. It follows, for example, that α can only be finite in space- and time-odd systems: from Eq. 1.6 one can write

$$M_i = \alpha_{ij}E_j \tag{1.13}$$

and see that α must be an axial tensor of rank 2, since E is polar with rank one and M is a first-rank axial tensor. In order for α to be nonzero, the crystal symmetry needs to break both inversion and time symmetry. If spatial inversion I was a generating element, a tensor A of that group would transform as $T(I)A \to A$, in turn leading to

$$\begin{aligned} & T(I)M_i = T(I)(\alpha_{ij}E_j) \\ \Leftrightarrow & T(I)M_i = (T(I)\alpha_{ij})(T(I)E_j) \\ \Leftrightarrow & M_i = \alpha_{ij}(-E_j) \\ \Rightarrow & \alpha = 0. \end{aligned} \tag{1.14}$$

In a time-reversal (R) even system, $T(R)A \rightarrow A$ holds true, leading to

$$\begin{aligned} & T(R)M_i = T(R)(\alpha_{ij}E_j) \\ \Leftrightarrow & T(R)M_i = (T(R)\alpha_{ij})(T(R)E_j) \\ \Leftrightarrow & -M_i = \alpha_{ij}E_j \\ \Rightarrow & \alpha = 0. \end{aligned} \tag{1.15}$$

For α to be finite, both space inversion and time reversal must thus be broken.

In the same way, the tensor form of α itself can be determined by applying the generating elements of the crystal to α. An overview about which magnetic point groups allow ME coupling, together with the corresponding form of α are given in Fig. 1.8. Detailed symmetry analyses for different magnetic phases of Cr_2O_3 are given in Chapters 3, 5, and 6.

1.2.4 Microscopic Theory

To derive a microscopic theory for the induction of a polarisation by certain magnetic arrangements, we will consider terms that appear in an effective Hamiltonian for a magnetic crystal. Emphasis is put on the three main contributions: symmetric exchange striction, antisymmetric Dzyaloshinskii-Moriya interaction, and chiral coupling, all of which can provide for the magnetic term in the free energy. This section is by no means exhaustive; for more details on the microscopic mechanisms behind ME the reader is referred to Refs. [75, 76].

Magnetoelectricity and multiferroicity are closely related. A material is considered MF when long-range magnetic and electric order co-exist. Especially the co-existence of FM and FE is of interest, so that this special case is often referred to as MF. Both properties seemed to be exclusive for a long time [77, 78] because of their contrary requirements: where an electronic d^0 configuration is required for FE, it precludes magnetism, requiring partially filled d shells. In symmetry terms, FE can occur in time-reversal even sys-

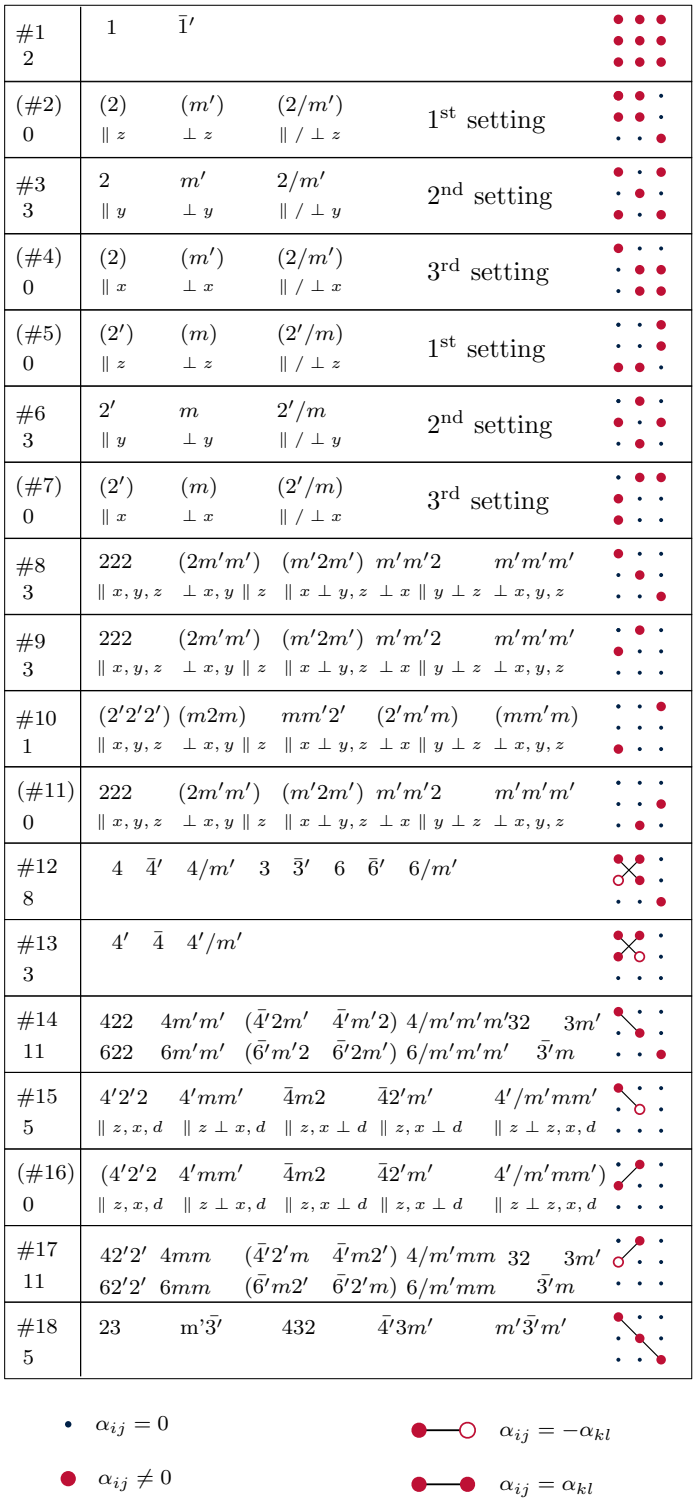


Figure 1.8: Magnetic point groups (in Hermann-Mauguin notation) and their corresponding tensor form of α, adapted from Ref. [26]. The monoclinic groups are specified by the orientation of their binary axes (along the x-, y-, or z-direction of their crystallographic coordinate system). Parentheses define the non-standard crystallographic groups. Only 58 magnetic point groups can show linear ME behaviour.

tems, but requires broken space-inversion symmetry. Polarisation thus cannot occur in centrosymmetric crystals. On the other hand, magnetism, as was pointed out for the ME symmetry considerations, only occurs in time-reversal odd systems. Most conventional magnetic materials are also invariant under space inversion.[3] When a certain spin arrangement leads to a polarisation, the magnetic and an electric order co-exist and couple, so that we speak of a magnetoelectric multiferroic. For this reason, the following interactions play a role in both magnetoelectric and multiferroic materials. A schematic view of exemplary magnetic structures is shown in Fig. 1.9: the collinear ferro- and antiferromagnets as well as more complex structures.

Symmetric exchange

The exchange interaction is the main driver for magnetic ordering in a material, due to the magnitude of its response. The important term is of the isotropic Heisenberg type and adds to the effective Hamiltonian:

$$H_{\mathrm{ex}} = -\sum J_{ij}^{\mathrm{ex}}(\mathbf{S}_i \cdot \mathbf{S}_j). \tag{1.16}$$

$J_{ij}^{\mathrm{ex}}(\mathbf{r}_{ij})$ denotes the exchange constant of the two neighbouring ions on positions i and j and decreases rapidly with their distance $\mathbf{r}_{ij}$. $\mathbf{S}_{i,j}$ is their respective spins. In case of a positive (negative) exchange interaction, the spin alignment is parallel (antiparallel) resulting in a FM (AFM) spin arrangement. Due to the distance dependence of J^{ex}, nearest-neighbour (NN) interactions play the biggest role in determining the overall magnetic structure.[4]

In the Landau theory, the magnetic term can induce a local polarisation in Eq. 1.4 of $\mathbf{P} \propto \mathbf{r}_{ij}(\mathbf{S}_i \cdot \mathbf{S}_j)$ [82], which can lead to a net-polarisation. This

[3] In fact, only 13 magnetic point groups allow for the simultaneous occurrence of FE and FM and even out of these not all exhibit MF behaviour [79].

[4] In fact, if this was strictly the case, the symmetric exchange would only lead to collinear FM or AFM magnetic structures.

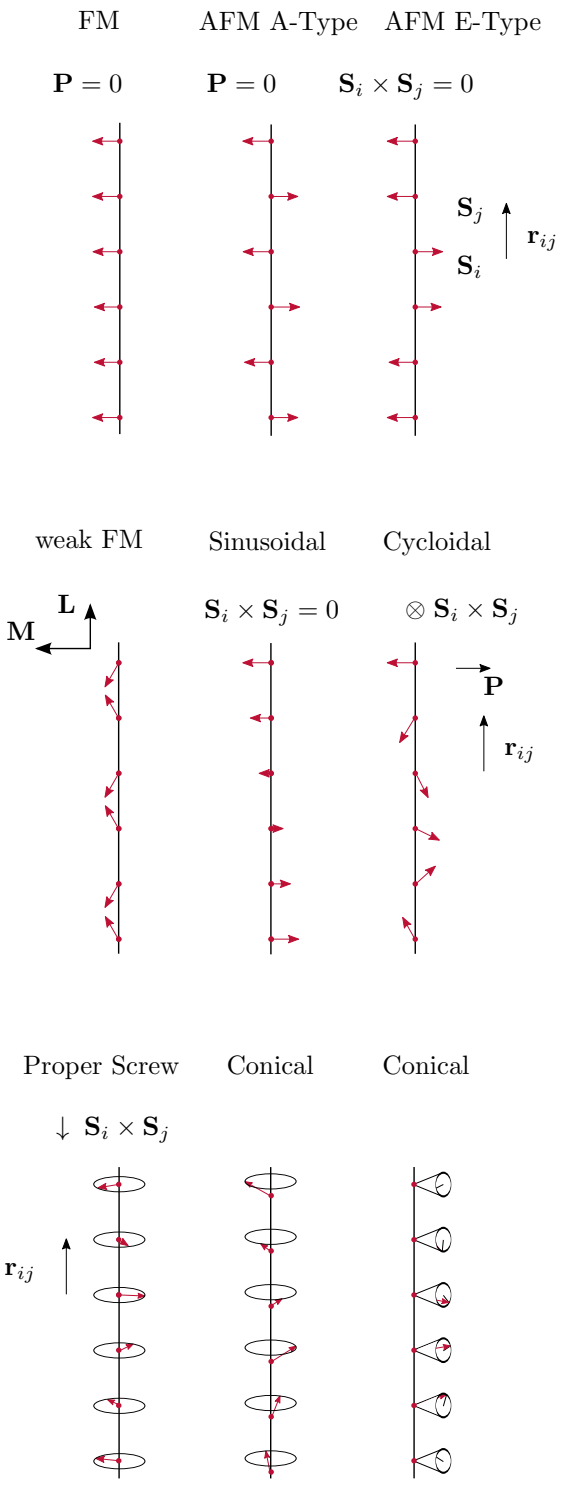


Figure 1.9: Different collinear and noncollinear spin structures, visualisation of their respective parameters, and their possible effect on the induced polarisation, adapted from Refs. [60, 80]. S, L, and M denote the individual spins, the antiferromagnetic order parameter, and the magnetic moment, respectively. P is the net polarisation and r_{ij} connects ions i and j.

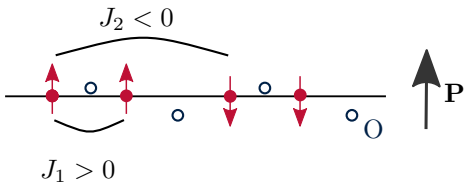


Figure 1.10: Effect of the symmetric exchange interaction on the polarisation [81]. For a magnetic configuration with competing spin interactions, one possible ground state is the frustrated ↑↑↓↓ spin chain (for example when the nearest-neighbour interaction in a material is FM ($J_1 > 0$) and the next-nearest neighbour interaction is AFM ($J_2 < 0$)). In the case of a positive nearest-neighbour interaction the energy is lowered if the FM (AFM) aligned atoms move closer (further away), making the charged oxygen atoms move down and inducing a net-polarisation. Similarly, upon application of an external magnetic field, bonds between ions with parallel (antiparallel) spins will be shortened (stretched) due to exchange striction. Inversion symmetry is broken and—if the ions are differently charged—a polarisation induced.

exchange can therefore account for a coupling of electric and magnetic properties,[5] or for an induced polarisation in a magnetically ordered material (see Fig. 1.10). When a nonmagnetic ion is used as an exchange medium for two magnetic ions, one speaks of "superexchange" [83].

Antisymmetric exchange

In spin systems that are not fully collinear an additional term adds to the exchange energies and integrals. The so-called "Dzyaloshinskii-Moriya" interaction was proposed as a microscopic mechanism and provides for the invariant of Eq. 1.12 to be finite [79]. It involves the antisymmetric part of the anisotropic superexchange [16, 67] and is of relativistic nature. The phenomenological picture will be explained on the basis of the top panel of Fig. 1.11: two ions are magnetically coupled via superexchange, *i.e.* mediated by ligands such as an oxygen atom. They are connected by $\mathbf{r}_{ij}$ and the shift of O from $\mathbf{r}_{ij}$ is called $\mathbf{x}$. The additional term that contributes to the Hamiltonian is

$$H_{\mathrm{DM}} = -\sum \mathbf{D}_{ij}(\mathbf{S}_i \times \mathbf{S}_j), \tag{1.17}$$

[5] When, for example, a magnetic field causes the magnetic moments to change and therefore induces the polarisation term.

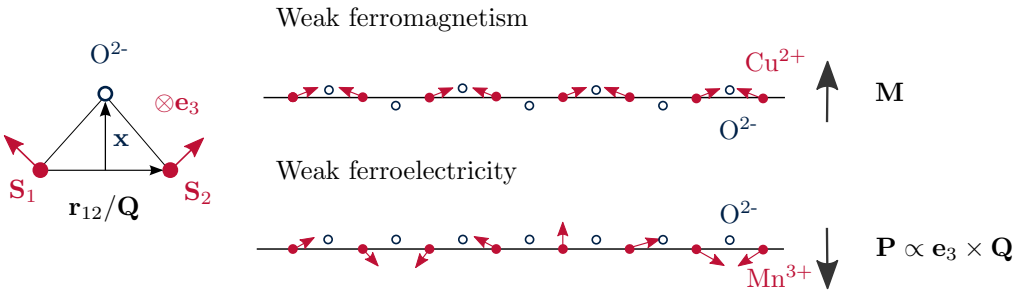


Figure 1.11: Direct and inverse effects of the Dzyaloshinskii-Moriya (DM) interaction, modified from Ref. [3]. The left panel explains the notation used in the text. The top configuration describes weak ferromagnetism in an atomic chain, which is the case for La_2CuO_4 [84]. The oxygen ions are shifted in between the transition metal ions—*i.e.* a finite $\mathbf{x}$ exists—inducing a spin canting on the transition metal ions. The bottom panel shows a cycloidal magnetic structure for $RMnO_3$. $\mathbf{r}_{12}$ connects ions 1 and 2 and also describes the spin chain direction $\mathbf{Q}$. $\mathbf{S}_i \times \mathbf{S}_j \propto \mathbf{e}_3$ is the axis, around which the spins rotate. Due to the inverse DM interaction, the O^{2-} are pushed along $\mathbf{r}_{12} \times \mathbf{e}_3$ and thus induce a net-polarisation.

where the so-called "Dzyaloshinskii vector" $\mathbf{D}_{ij}$ is proportional to the spin-orbit coupling and to $\mathbf{x} \times \mathbf{r}_{ij}$. The Dzyaloshinksii-Moriya (DM) interaction thus induces a canting of the spins, *i.e.* it induces a finite $\mathbf{S}_i \times \mathbf{S}_j$, hence a small local *magnetisation*. Weak ferromagnetism is a result (see the top panel of Fig. 1.11). Fe_2O_3 was the first material studied with respect to its weak FM based on the DM interaction.

The spin-current mechanism or the "inverse" DM interaction explain ferroelectricity in canted spin structures or spin cycloids [66, 82]. It produces a finite $\mathbf{x} \times \mathbf{r}_{ij}$ when a finite and non-oscillating $\mathbf{S}_i \times \mathbf{S}_j$ exists. In this model, charged atoms are shifted perpendicular to $\mathbf{r}_{ij}$ inducing a net-*polarisation* according to $\mathbf{P} \propto \mathbf{r}_{ij} \times (\mathbf{S}_i \times \mathbf{S}_j)$. The effect is sketched in the bottom panel of Fig. 1.11.

As the antisymmetric exchange originates from relativistic effects, it is usually weaker than the symmetric Heisenberg exchange at higher temperatures. However, if we consider the *change* of the exchange terms when the symmetry is broken by an external field, the effects can be comparable.

Chiral Coupling

In addition to an induced polarisation in collinear or cycloidal spin structures, an additional term accounts for polarisation in chiral proper-screw systems (bottom left panel of Fig. 1.9). Proper screws are space-odd, as any other helical structure, and time-even [80] (Fig. 1.12). Proper screws therefore do not allow for a first-order ME effect, unless time reversal symmetry is broken, *e.g.* by applying a magnetic field and making the magnetic structure conical. In such case higher-order coupling terms can occur.

A polarisation, however, can be induced by chiral coupling, as first proposed in Ref. [69]. The DM vector $\mathbf{D}_{ij}$ is decomposed into a part parallel and perpendicular to $\mathbf{r}_{ij}$ via $\mathbf{D}_{ij} = \mathbf{P}_{ij} \times \mathbf{r}_{ij} + \sigma_{ij} \cdot \mathbf{r}_{ij}$. Here, $\mathbf{P}_{ij}$ is a polar vector, such as the local polarisation $\mathbf{P} = \sum_{ij} \mathbf{P}_{ij}$ (compare to $\mathbf{x}$ in Fig. 1.11). Just from symmetry arguments, σ_{ij} must be a pseudoscalar (space-odd and time-even, like the polarisation), which defines the macroscopic "chirality" of the system $\sigma = \sum_{ij} \sigma_{ij}$ with the local chiral moments $\sigma_{ij} = \mathbf{r}_{ij} \cdot (\mathbf{S}_i \times \mathbf{S}_j)$. The first term corresponds to the inverse DM interaction, which can induce a polarisation in itself. The second term introduces chiral coupling, which can provide for the magnetic term in Eq. 1.9 by coupling to an order parameter $\mathbf{A}$ supported by the high-symmetry (paramagnetic) phase: $\mathbf{P} \propto \gamma \sigma \mathbf{A} \Leftrightarrow \mathbf{P} \propto \gamma \mathbf{r}_{ij} \cdot (\mathbf{S}_i \times \mathbf{S}_j) \cdot \mathbf{A}$. Coupling to $\mathbf{A}$ means coupling to the crystal structure; $\mathbf{A}$ must be a macroscopic axial vector. It represents a collective rotation of parts of the crystal. Materials, which allow for the structural axial vector on the basis of their point group, are called "ferroaxial".

Further Interactions

Further mechanisms that change magnetic properties by electric influences or *vice versa* are single-ion anisotropy and Zeeman and dipolar interactions.

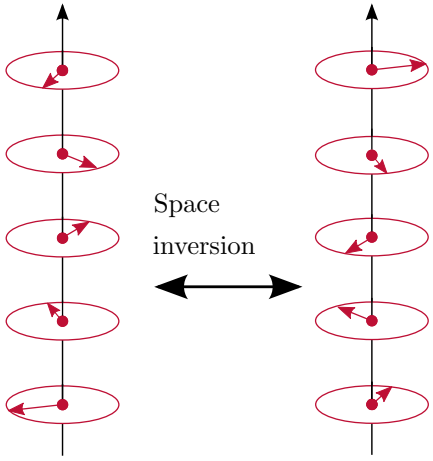


Figure 1.12: A left- and right-handed proper-screw structure from Ref. [80]. The structures are chiral, meaning that none of them can be obtained by a mirror image of the other. Only space inversion transforms one into the other.

Single-ion anisotropy occurs when a magnetic ion is placed in a crystalline field, so that a quenching of its orbitals will occur according to the symmetry of the surrounding crystal. The additional term is $\propto \mathbf{S}_i^2$, although higher-order even powers can occur, which are usually much weaker. Single-ion anisotropy mainly leads to a pinning of the spin direction along the "easy axis" in the crystal field. If an external field is applied, surrounding ions could move and therefore change this direction, producing ME behaviour.

Dipolar interactions in magnetic materials manifest in the Hamiltonian as a term proportional to $3\ (\mathbf{m}_i \cdot \mathbf{r}_{ij})(\mathbf{m}_j \cdot \mathbf{r}_{ij}) - \mathbf{m}_i \cdot \mathbf{m}_j$, where $\mathbf{m}_i$ is the magnetic dipole moment of ion i. The interaction is anisotropic but symmetric, and under an electric field piezoelectric distortions can lead to nonuniform magnetic-ion movements, which in turn modifies the dipolar energy contribution.

The Zeeman energy is $\propto \mathbf{B}\mathbf{g}_i\mathbf{S}_i$. Here, $\mathbf{g}_i$ is a tensor that characterises the direction and size of the magnetic moment of atom i. The g-factor also depends on the ground-state wave function. This means, an external field can either change the wave function of the system directly or can create local

distortions of the crystal field and therefore change the wave function. In turn, these effects can lead to a change in the g-value and subsequently in the Zeeman energy.

1.3 Magnetoelectric Materials

In the last two sections, the theoretical background and the microscopic mechanisms to understand the occurrence of magnetoelectricity and multiferroicity were outlined. This section answers practical questions: how is magnetoelectricity measured and what are some magnetoelectric or multiferroic materials? What materials show which sort of mechanism and how strong are the respective polarisations and/or couplings?

1.3.1 Experimental Techniques

Experimentally, the ME coupling tensor is determined by applying an external electric or magnetic field to a crystal and measuring the magnetic or electric response, respectively. X-ray analyses can be performed to orient the crystal. In order to prevent restructuring of the sample such as twinning upon cooling, techniques like magnetic annealing can be used. Electrodes are used to detect or to apply an electric field, *e.g.* by painting or spraying surfaces with conducting materials [26, 85]. The material can be held in a sample holder with conducting pressure contacts serving as electrodes. To measure the magnetically-induced "ME_H" effect, a magnetic field can be applied along a chosen direction. By measuring the voltage induced between the electrodes, or integrating the current per unit area over time, the induced polarisation can be measured. Alternatively, when applying an electric field, the magnetic moments can be obtained by measuring a voltage change within the sample, which is called the "ME_E" effect. To minimise the risk of an electrical breakdown, the ME_H is the method of choice [86]. It is worth noting that ME experiments

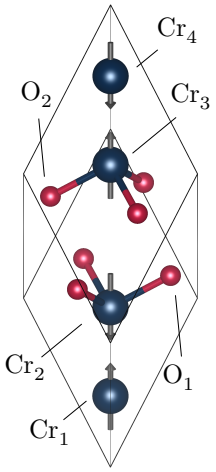


Figure 1.13: The rhombohedral primitive cell of Cr_2O_3 features two structural units, each containing two Cr and three O atoms. The arrows indicate the antiferromagnetically coupled Cr magnetic moments in one of the two $\bar{3}'m'$ AFM phases. The labels define the notation used later in the thesis.

often complement data gathered by other methods in order to determine magnetic or crystallographic symmetries; if x-ray or neutron diffraction data do not suffice to clarify which magnetic structure a material has, the form of the ME coupling tensor gives information about its symmetry according to Fig. 1.8.

1.3.2 Cr_2O_3

As mentioned in Section 1.1, the first experiments on measuring the ME coupling tensor α in Cr_2O_3 were conducted by Astrov [18, 19]. Its magnetic ground state is the G-type AFM configuration shown in Fig. 1.13, where the spin direction is that of the rhombohedral [111] axis. Two 180° domains are possible and can be transformed into each other by time reversal. Astrov demonstrated that a magnetisation of the Cr atoms occurred upon application of an external electric field. Shortly thereafter, the coupling strengths parallel ($\alpha_\parallel$) and perpendicular ($\alpha_\perp$) to the applied field were studied in order to determine the direction dependence of the response [20]. Via semi-empirical one- and two-ion models, symmetric exchange was proposed as one mechanism for ME for Cr_2O_3 at elevated temperatures [21, 22, 87–89]. In addition,

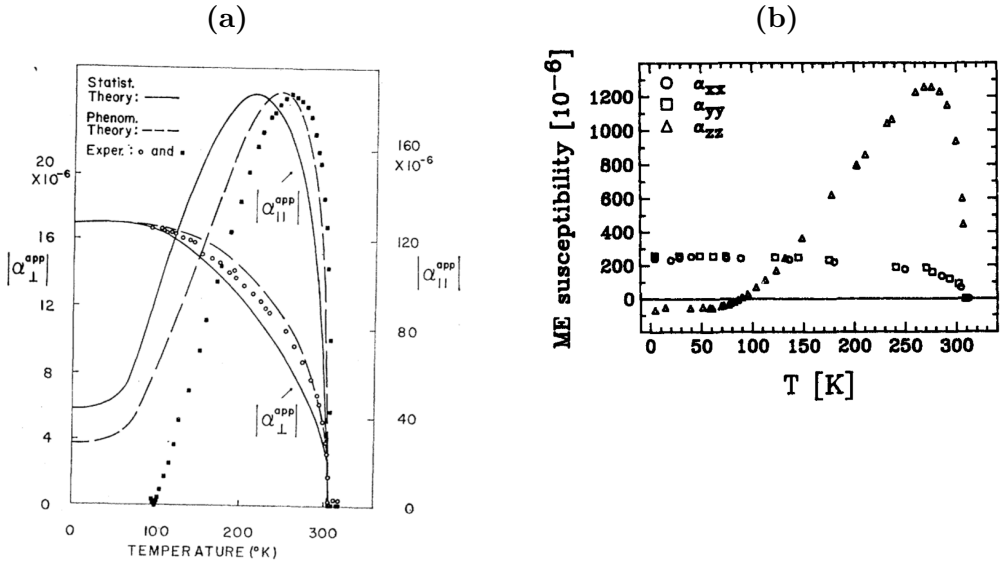


Figure 1.14: The magnetoelectric coupling tensor of Cr_2O_3 throughout the temperature range. One can see the anisotropy of the ME coupling, the nonzero response at $T = 0\,\mathrm{K}$ and the vanishing ME coupling above the Néel temperature at $\simeq 307\,\mathrm{K}$. (**a**) Experiments at $T \leq 100\,\mathrm{K}$ show the anisotropy of the linear ME coupling tensor α (circles) [20]. The experiments did not capture the nonzero components for $\alpha_\parallel$ at $0\,\mathrm{K}$ predicted by the microscopic theory by Rado [21, 22, 87] (solid lines). (**b**) Experimental evidence of nonzero components at low temperatures for both contributions $\alpha_\parallel$ and $\alpha_\perp$ [90].

spin-orbit coupling accounts for a significant part of the ME coupling for $\alpha_\perp$ (Fig. 1.14a). Due to lowering the symmetry upon applying an external field, the electric-field induced inverse Dzyaloshinskii-Moriya interaction allows for its ME response at low temperatures.

The corresponding experiments followed shortly thereafter (Fig. 1.14b). In agreement with Astrov, it was found that the response is direction- and temperature dependent. Fig. 1.14 shows the temperature behaviour of α: $\alpha_\parallel$ peaks at room temperature with a value of $4.14\,\mathrm{ps\,m^{-1}}$. It seems to vanish below $97\,\mathrm{K}$, but rises immediately below that temperature. Later studies revealed that the response at $0\,\mathrm{K}$ is nonzero—again, first theoretically [88], then experimentally [91]. $\alpha_\perp$ is about a magnitude smaller throughout the measured temperature range. It decreases upon increasing the temperature, until

both responses become zero when the Néel temperature[6] is reached and Cr_2O_3 becomes paraelectric. The actual value of the ME tensors might be larger than the ones given in literature [18–20, 87], since Cr_2O_3 can exhibit two degenerate AFM domains in a sample that has not been magnetically annealed upon cooling. More recent measurements therefore exhibit slightly larger values of α [90, 91] and the zero-temperature responses were determined to be $\|\alpha_\perp(4.2\,\mathrm{K})\| = 0.73\,\mathrm{ps\,m^{-1}}$ and $\|\alpha_\parallel(4.2\,\mathrm{K})\| = 0.23\,\mathrm{ps\,m^{-1}}$.

1.3.3 AFM and Cycloidal Arrangements

Noncollinear perovskites are of interest in the field of magnetoelectricity and multiferroicity, as they present a vast array of the microscopic interactions introduced in Section 1.2.4 [24]. They belong to different groups and subgroups of the Venn diagram shown in Fig. 1.3, some being multiferroic with AFM, FM, or cycloidal spin arrangements, some being magnetoelectric. Hence, MF perovskites will be discussed in the following, as well as other structures exhibiting ME and/or MF behaviour attributed to their competing spin interactions.

Two distinct mechanisms can produce ferroelectricity for MF materials. Firstly, one speaks of "proper ferroelectricity" when different atoms in the material are responsible for magnetism and FE, so that only the polarisation changes in the phase transition from paraelectric to FE. This is the case for $BiMnO_3$ [95–97], with Mn providing the magnetism whereas the stereochemically active lone-pairs of Bi^{3+} (Pb^{2+} ions have the same effect) make the cations "off-centre". Because the ferroic orders are the contributions of different ions, there is no ME coupling [98]; the transition temperatures for the ferroelectric and ferromagnetic transitions are $T_{\mathrm{FE}} = 750\,\mathrm{K}$ and $T_{\mathrm{N}} = 105\,\mathrm{K}$, respectively. Secondly, "improper FE" is induced as a by-product of symmetry-

[6] The magnetic structure and Néel temperature of Cr_2O_3 are investigated until today [92], demonstrating the ongoing interest in Cr_2O_3. First shown in Ref. [93] and re-confirmed in 2013 [94], the latter is measured as $T_N \simeq 307\,\mathrm{K}$.

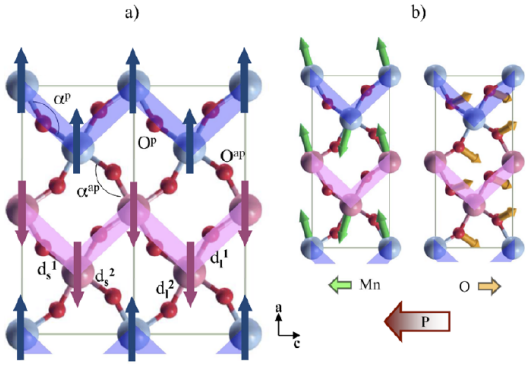


Figure 1.15: Structure and multiferroicity of the orthorhombic collinear E-type antiferromagnet $HoMnO_3$ (with a doubled lattice vector along the *a*-direction due to the magnetic structure) from Ref. [102]. Red (blue) atoms correspond to Mn (O). Along the *ac*-diagonal the structure is ↑↑↓↓ . The *ac*-plane of MnO_2 in a) shows FM zigzag spin chains (highlighted in blue and pink for up and down chains, respectively), which are AFM coupled to adjacent chains and to chains along the *b*-direction [103]. Inequivalent oxygen atoms bonded to Mn atoms with parallel spin (O^p) with respect to those with antiparallel spins (O^{ap}) lead to an asymmetry of their electronic structure [99]. The symmetric superexchange makes the Mn and O atoms shift: because AFM coupling between the Mn atoms is energetically favourable, the oxygen atoms minimise (maximise) the distance to the ↑↓ (↑↑) atoms. Due to exchange-striction the net shift of Mn (O) ions along the negative (positive) *c*-direction induces a net-polarisation, displayed in b).

breaking mechanisms in otherwise centrosymmetric (CS) systems. In electronic or magnetic MFs, the primary order parameter is related to spin, charge, or orbital order [3, 99], followed by a rearrangement of the polar electronic charge and in turn leading to a non-CS shift of the ions as a secondary phase transition. The advantages of electronic MFs compared to the standard ones are faster switching times and reduced fatigue problems [81, 100, 101], as—phenomenologically—one compares "faster and lighter" electrons to "slower and heavier" nuclei. Because of the origin of their ferroelectricity, magnetic MFs are expected to show a ME coupling. These materials are therefore classified as magnetoelectric multiferroics.

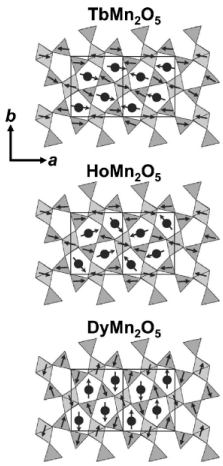
AFM multiferroics, where the spin pattern breaks inversion symmetry via exchange striction, are, *e.g.* the orthorhombic rare-earth manganites RMn_2O_5 (R=Y, Tb−Ho, but also Bi) and $RMnO_3$ (R=Y, Sr, La, Ho−Lu). Similar rare-

earth compounds such as (Tb/Dy/La/Sr)MnO_3 also exhibit MF behaviour, but due to their cycloidal spin structure [3]. To the group of AFM MFs further belong other perovskite-like structures such as $LaTiO_3$ and $YTiO_3$, and other materials such as Ln_2CuTiO_6 (Ln=Y, Dy, Ho, Er, Yb), $Bi_2Fe_2O_9$, and $Ca_3(Co,Mn)_2O_6$.

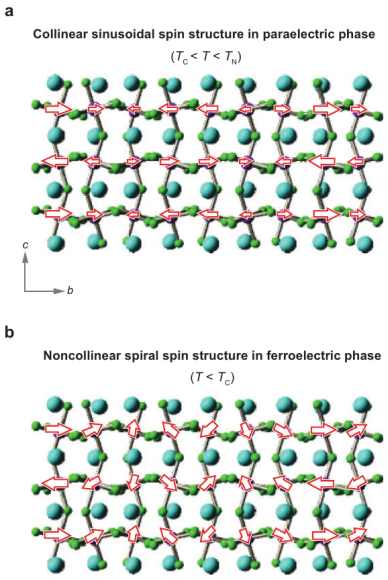
Fig. 1.15 shows how ferroelectricity can be induced in the orthorhombic collinear $RMnO_3$ [102]. Its space group is *Pbnm* and the spin configuration is of the AFM-E type, where zigzag chains of FM spins in the MnO_2 planes are AFM coupled to chains in- and out-of-plane [103]. Symmetric superexchange leads to a shift of differently charged ions breaking atomic CS and contributing to the total FE polarisation.

Other orthorhombic rare-earth manganite compounds with MF and ME[7] behaviour belong to the RMn_2O_5 family [105–110]. Fig. 1.16a shows the crystallographic and magnetic structures for selected AFM compounds of this family. Their complex magnetic structures range from sinusoidal above 42 K to 45 K to AFM upon cooling, to an incommensurate state and finally to an ordering of the rare-earth spins upon further cooling [3, 111]. The onset of the commensurate AFM phase gives rise to FE via breaking of CS due to symmetric exchange [98]. Single-crystal measurements on RMn_2O_5 (R= Y, Ho, Bi) show additional nonzero moments in *c*-direction [106, 107], which resemble a cycloidal structure and give rise to FE through DM interaction (Fig. 1.16a). Its influence should be comparably small: although $BiMn_2O_5$ has similar polarisation values as the other compounds, it does not exhibit a large *c*-axis component of the magnetic moments. It was shown that the dielectric properties of the rare-earth compounds have a magnetic origin and that the colossal

[7] The electric polarisation in, *e.g.* $TbMn_2O_5$ can be reversed by an external magnetic field [104].



(a) Sketch of the magnetic structure of three RMn_2O_5 compounds [105].



(b) Paraelectric AFM phase at room temperature and FE AFM noncollinear phase of $TbMnO_3$ from Ref. [80].

Figure 1.16: Magnetic structures of rare-earth manganites such as the AFM $TbMn_2O_5$, $HoMn_2O_5$, and $DyMn_2O_5$, and the sinusoidal and cycloidal spin structure of $TbMnO_3$ by neutron diffraction measurements of polycrystalline samples at different temperatures.

ME effect is interpreted as a phenomenon of the phase transition induced by an external magnetic field [107].

Other materials that exhibit MF due to the inverse DM interaction are, amongst others, $Ni_3V_2O_8$, $LiCu_2O_2$, $LiCuVO_4$, $MnWO_4$, or $CsCuCl_3$. The magnetic structure of $TbMnO_3$ is presented in Fig. 1.16b. It shows a sinusoidal structure below the Néel temperature of $T_N \simeq 43\,\mathrm{K}$ where it is paraelectric and undergoes another phase transition to a cycloidal state at 28 K (bottom panel of Fig. 1.16b), where it becomes FE.

Screws and Higher-Order Coupling

Eq. 1.4 shows further ME coupling terms besides the linear α_{ij}. For example, β_{ijk} (γ_{ijk}) links the ME response linear in E (H) and bilinear in H (E). These coupling terms are responsible for ME effects in materials that do not allow for

a linear ME effect [112, 113]. For non-helical systems, this was first observed in 1965 as the "paramagnetoelectric" effect, where an external magnetic field was applied to the paramagnetic state of piezoelectric $NiSO_4 \cdot 6\,H_2O$ [114]. An external electric field was also shown to lower the symmetry of yttrium iron garnet as an example for the rare-earth garnets RFe_5O_{12} (R=Gd, Y, or Dy) and therefore to induce ME. Due to its magnetic point group $\bar{3}m'$, it should, however, not allow for a first-order ME effect [115].

$ZnCr_2Se_4$ exhibits a helical magnetic structure and was shown to become conical by application of an external magnetic field [116]. Again, a linear ME effect is not observed. For application purposes, it is of interest to modify the ME response and the polarisation vector by low magnetic fields instead of field magnitudes of some Tesla, which was recently achieved [36]. A magnetic field of $\sim \pm 30\,\mathrm{mT}$ was applied to the helical magnet $Ba_2Mg_2Fe_{12}O_{22}$ and a ME response was observed, whose direction could be tuned by the direction of H.

MF behaviour in *proper* screws is only a recent discovery. Following the introduction of ferroaxial $Cu_3Nb_2O_8$, several other proper-screw MFs were found, including $CaMn_7O_{12}$ and $RbFe(MoO_4)_2$ [69, 117, 118].

Recently, hexaferrites of type Y, such as $Ba_2Mg_2Fe_{12}O_{22}$, were reported to be ME under moderate magnetic fields, which induce a conical screw structure [35, 36]. The search for room-temperature MEs with high coupling tensors led to the investigation of helimagnetic $Ba_{0.5}Sr_{1.5}Zn_2(Fe_{1-x}Al_x)_{12}O_{22}$ exhibiting the giant ME effect with $\alpha = 2 \times 10^4\,\mathrm{ps\,m^{-1}}$ at room temperature at low magnetic fields [34, 119]. The Z-type $Sr_3O_2Fe_{24}O_{41}$ shows similar properties: as a magnetically induced MF, it is ME at low magnetic fields and room temperature [33].

To summarise the broad range of magnetically induced MFs and non-MF magnetoelectrics, a list of prototypical linear MEs is given in Table 1.3, together with their coupling strength and Néel or Curie temperature. To illustrate how fast-moving the field is, it is worth noting that the list, published in 2006 [120], included the materials with the largest coupling coefficients or highest operating temperatures. Equally, the 2005 review in Ref. [25] mentioned the largest coupling measured to be $36.7\,\mathrm{ps\,m^{-1}}$. The aforementioned hexaferrite exhibits a response that is two orders of magnitude larger. A less "complex" material, $Fe_2Mo_3O_8$, was reported in 2015 to have a coupling coefficient of $\sim 5000\,\mathrm{ps\,m^{-1}}$, the largest measured to date, with an operating temperature of 60 K.

This chapter explored the materials background required for the present thesis: the theoretical framework was covered with an overview about what mechanisms are known to date to induce magnetoelectricity and/or multiferroicity. The distinct mechanisms were exemplified on the basis of representative materials. The next chapter will cover *how* the magnetoelectric response is modelled.

Table 1.3: A list of some ME materials, adapted from Refs. [26, 120]. The corresponding Néel / Curie temperature and maximum coupling constant α are given. Units converted from the original source according to Eq. 1.2.

Compound	T_N or T_C [K]	Maximum α_{obs} [ps m^{-1}]
Fe_2TeO_6	219	1.3
$DyAlO_3$	3.5	84
$GdAlO_3$	4.0	4.2
$TbAlO_3$	4.0	42
$TbCoO_3$	3.3	1.3
Cr_2O_3	318	4.2
$Nb_2Mn_4O_9$	110	0.08
$Nb_2Co_4O_9$	27	0.84
$Ta_2Mn_4O_9$	104	0.42
$Ta_2Co_4O_9$	21	4.2
$LiMnPO_4$	35	0.84
$LiFePO_4$	50	4.2
$LiCoPO_4$	22	29
$LiNiPO_4$	23	1.7
$GdVO_4$	2.4	13
$TbPO_4$	2.2	730
$DyPO_4$	3.4	42
$HoPO_4$	1.4	8.4
$Mn_3B_7O_{13}I$	26	0.08
$Co_3B_7O_{13}Cl$	12	13
$Co_3B_7O_{13}Br$	17	84
$Co_3B_7O_{13}I$	38	42
$Ni_3B_7O_{13}I$	61.5	8.4
$Ni_3B_7O_{13}Cl$	9	12.6
$Cu_3B_7O_{13}Cl$	8.4	0.13
$FeGaO_3$	305	16.8
TbOOH	10.0	16.8
DyOOH	7.2	4.19
ErOOH	4.4	21
Gd_2CuO_4	6.5	4.2
$MnNb_2O_6$	4.4	0.13
$MnGeO_3$	16	0.08
$CoGeO_3$	31	4.2
$CrTiNdO_5$	13	0.42

2 Ab Initio Theory

The following chapter is devoted to the first-principles frameworks required for modelling the magnetoelectric response. It covers the quantum-mechanical basics of many-body systems, introduces density functional theory (DFT) as a computational approach to solve the many-body equations, and gives an overview about how DFT can be used to model certain materials properties. It is, however, by no means exhaustive; if more detail about a topic is needed, the reader is encouraged to explore Refs. [121–123] for an overview about the topic, or, for in-depth coverage, the references given in the text.

2.1 Many-Body Systems

The approach used in this work is a quantum mechanical *ab initio* or first-principles *ansatz*, which means that no experimental assumptions or data reduced to the specific material are used. One of the main principles of quantum mechanics is that the properties of microscopic particles such as their position, velocity, and interaction have to be described in a probabilistic way. Wavefunctions describe a quantum state with probability densities and a phase factor and can be calculated by solving the Schrödinger equation. In the present work, only equilibrium properties are considered, which are described by stationary states. As a result, the time-independent many-body Schrödinger equation can be applied. For a given material with wavefunctions $\Psi_n = \Psi_n\left(\{\mathbf{r}_i\}, \{\mathbf{R}_I\}\right)$

belonging to energy levels n, it reads:

$$E_n \Psi_n = \hat{H} \Psi_n, \tag{2.1}$$

with lower- (upper-)case indices running over the number of electrons (nuclei), N_e (N_N) and the Hamilton operator

$$\hat{H} = \hat{T}^{\text{nuc}} + \hat{T}^{\text{el}} + \hat{V}^{\text{nuc-nuc}} + \hat{V}^{\text{el-el}} + \hat{V}^{\text{nuc-el}}. \tag{2.2}$$

The kinetic-energy operators of the nuclei and electrons, $\hat{T}^{\text{nuc}}$ and $\hat{T}^{\text{el}}$, respectively, and the nucleus-nucleus, electron-electron, and nucleus-electron interactions, $\hat{V}^{\text{nuc-nuc}}$, $\hat{V}^{\text{el-el}}$, and $\hat{V}^{\text{nuc-el}}$, respectively, are described by:

$$\hat{T}^{\text{nuc}}(\{\mathbf{R}_I\}) = -\sum_{I}^{N_N} \frac{\hbar^2}{2M_I} \nabla_I^2, \tag{2.3}$$

$$\hat{T}^{\text{el}}(\{\mathbf{r}_i\}) = -\sum_{i}^{N_e} \frac{\hbar^2}{2m_e} \nabla_i^2, \tag{2.4}$$

$$\hat{V}^{\text{nuc-nuc}}(\{\mathbf{R}_I\}) = \frac{1}{2} \sum_{I}^{N_N} \sum_{J \neq I}^{N_N} \frac{Z_I Z_J e^2}{4\pi\epsilon_0 \left|\mathbf{R}_I - \mathbf{R}_J\right|}, \tag{2.5}$$

$$\hat{V}^{\text{el-el}}(\{\mathbf{r}_i\}) = \frac{1}{2} \sum_{i}^{N_e} \sum_{j \neq i}^{N_e} \frac{e^2}{4\pi\epsilon_0 \left|\mathbf{r}_i - \mathbf{r}_j\right|}, \tag{2.6}$$

$$\hat{V}^{\text{nuc-el}}(\{\mathbf{r}_i\}, \{\mathbf{R}_I\}) = -\sum_{i}^{N_e} \sum_{I}^{N_N} \frac{Z_I e^2}{4\pi\epsilon_0 \left|\mathbf{r}_i - \mathbf{R}_I\right|}, \tag{2.7}$$

e (m_e) denoting the elementary charge (mass) and Z_I (M_I) the proton number (mass) of nucleus I. $\hbar$ and ϵ_0 are the reduced Planck constant and the electric constant, respectively. Solving the Schrödinger equation and calculating the properties of the investigated system from Ψ is essentially the most basic first-principles idea. In practice, when system sizes of more than two particles

are considered, it cannot be solved exactly.[1] Several approximations have been developed within the last decades to approach that problem: the most important ones for the present work will be illustrated in the following sections.

2.1.1 Born-Oppenheimer Approximation

The Born-Oppenheimer approximation, also referred to as the "adiabatic approximation", is a perturbation approach, which arises due to the large differences between nuclear and electronic masses. The starting point is the ratio of nuclear to electronic masses ($M_N/m_e \geq 10^4$), resulting in ionic and electronic processes living on different time scales.[2] Electrons thus have sufficient time to relax to their according ground state depending on the nuclear potential. Electronic and nuclear wavefunctions can therefore be decoupled, so that the former can be treated quantum mechanically, the latter classically.

The mathematical formulation of the Born-Oppenheimer approximation is made up of three steps, of which the first one is to treat the $\frac{1}{M_N}$ term as a perturbation and set it to zero, which sets the kinetic energy of the nuclei to zero and makes their interaction constant. With that, the electronic Schrödinger equation with an electronic Hamiltonian and electronic wavefunctions can be written as [124]

$$\hat{H}^{\text{el}} := \hat{H} - \hat{T}^{\text{nuc}} = \hat{T}^{\text{el}} + \hat{V}^{\text{el-el}} + \hat{1}E^{\text{nuc-nuc}}\left(\{\mathbf{R}_I\}\right) + \hat{V}^{\text{nuc-el}}\left(\{\mathbf{R}_I\}\right), \tag{2.8}$$

with

$$\hat{H}^{\text{el}}\Psi_\nu\left(\mathbf{r}_1 \dots \mathbf{r}_{N_e}\right) = E_\nu^{\text{el}}\left(\{\mathbf{R}_I\}\right)\Psi_\nu\left(\mathbf{r}_1 \dots \mathbf{r}_{N_e}\right), \tag{2.9}$$

[1] In fact, when $N = N_e + N_N$ is the total number of particles in a system, it has to be described by a $3N$-dimensional wavefunction depending on N variables, leading to a factorial scaling of N^N.

[2] In solids and molecules the ionic vibrations have eigenfrequencies of 10^{12} Hz, whereas the radiation emitted by the electronic transitions are in the order of magnitude of 10^{17} Hz to 10^{18} Hz.

where ν denotes the electronic state. As the ionic coordinates $\mathbf{R}_I$ only act as a set of external parameters,[3] an eigenvalue equation can be solved separately for every nuclei configuration to obtain the full solution to Eq. 2.9. The re-introduction of the nuclear kinetic-energy operator is the second step of the Born-Oppenheimer approximation and leads to the definition of a nuclear Hamiltonian:

$$\hat{H}_\nu^{\text{nuc}} = \hat{T}^{\text{nuc}} + \hat{1} E_\nu^{\text{el}} \left(\{\mathbf{R}_I\} \right). \tag{2.10}$$

The nuclear Hamilton operator has no coupling terms in ν so that its eigenvalues E^{nuc} and its eigenfunctions Λ can be labelled by ν and an index μ running for a fixed ν over all eigenfunctions:

$$\begin{aligned} \hat{H}_\nu^{\text{nuc}} \left(\{\mathbf{R}_I\} \right) \Lambda_{\nu,\mu} \left(\{\mathbf{R}_I\} \right) = \\ [\hat{T}^{\text{nuc}} \left(\{\mathbf{R}_I\} \right) + \hat{1} E_\nu^{\text{el}} \left(\{\mathbf{R}_I\} \right)] \Lambda_{\nu,\mu} \left(\{\mathbf{R}_I\} \right) = E_{\nu,\mu}^{\text{nuc}} \Lambda_{\nu,\mu} \left(\{\mathbf{R}_I\} \right). \end{aligned} \tag{2.11}$$

An important observation of the nuclear Schrödinger equation 2.11 is that the nuclei move in a potential field, which consists of the energy of the electrons in the nuclear potential $E_\nu^{\text{el}} \left(\{\mathbf{R}_I\} \right)$. In other words, every $E_\nu^{\text{el}} \left(\{\mathbf{R}_I\} \right)$ describes a potential energy surface (PES) in which the nuclei move. The nucleus-electron interaction $\hat{V}^{\text{el-nuc}}$ and the electron-electron interaction $\hat{V}^{\text{el-el}}$ are thus often referred to as the external potential $\hat{V}^{\text{ext}}$ and internal potential $\hat{V}^{\text{int}}$, respectively.

The third and final step is to decouple the original Schrödinger equation 2.1 by assuming that its eigenvalues E_n can be approximated by the eigenvalues of the nuclear Schrödinger equation, $E_{\nu,\mu}^{\text{nuc}}$ (Eq. 2.11):

$$E_n \approx E_{\nu,\mu}^{\text{nuc}}. \tag{2.12}$$

[3] In the same way that the effect of the nuclei on the electrons is treated as an external potential, other external influences, such as electric or magnetic fields, can be introduced easily [121].

Using the Born-Oppenheimer approximation provides the ability to decouple the eigenvalue problems for electrons and nuclei. Therefore, the wavefunction can be determined in two computationally less time-demanding steps, where the electrons have to be treated quantum mechanically, the nuclei can be considered classically. The number of electrons is larger than the number of nuclei in the investigated systems, so that the scaling can be reduced to $N_e^{N_e}$. Since the calculations are still too large to be solved directly, further approximations have to be performed, but can be now derived separately for nuclei and electrons.

2.1.2 Rayleigh-Ritz Variational Principle

The variational principle is a useful tool to approximate the energy and wavefunction of a Hamiltonian. It states that the expectation value of a Hamiltonian $\hat{H}$ for any wavefunction Ψ is always larger or equal to the true ground-state energy. The variational principle reads as

$$E[\Psi] = \frac{\langle \Psi | \hat{H} | \Psi \rangle}{\langle \Psi | \Psi \rangle} \geq E_0, \tag{2.13}$$

where E_0 is the ground-state energy and $\frac{\langle \Psi | \hat{H} | \Psi \rangle}{\langle \Psi | \Psi \rangle}$ is defined as the "Rayleigh ratio", which is only equal to E_0 if Ψ is identical to the ground-state wavefunction [122, 123]. This powerful statement implies that one can obtain an upper bound for the ground-state energy of a system. The Rayleigh-Ritz variation principle provides the user with the directions on how to find this upper bound: a test wavefunction is described by a linear combination of basis functions with variable coefficients. The latter can in turn be varied to minimise the energy of the given wavefunction until a minimum energy is obtained. The variational principle can be applied to solve the eigenvalue equations in DFT in an iterative, self-consistent manner, as illustrated in Section 2.2.2.

2.2 Density Functional Theory

Density functional theory (DFT) maps the information of the coupled many-body wavefunction on the—as the name suggests—electronic *charge density*. The following section provides the framework of DFT up until a point where a computation of the total energy of a system becomes possible.

2.2.1 Hohenberg-Kohn Theorems

The important step towards modern density functional theory was made by Hohenberg and Kohn in 1964. In order to obtain the ground state of a given system (referring to the energetically lowest state with energy E_0^{el} at $T = 0\,\mathrm{K}$), it was proven that its ground-state energy is a unique functional of its electronic charge density $\rho(\mathbf{r})$. Together with the description on how to obtain the density, they form the basis of the two *Hohenberg-Kohn theorems*, which apply to any system of electrons moving in an external potential [125, 126]. The first theorem reads as:

Theorem 1 ***Existence Theorem***

The total energy of a non-degenerated ground state of a many-electron system in an external potential $\hat{V}^{\mathrm{ext}}$ *is a unique functional of its electronic charge density* $\rho(\boldsymbol{r})$.

For this reason, the special case of the ground-state electronic wavefunction Ψ_0 is also unique for a given external potential:

$$\Psi_n = \Psi_n[\rho], \tag{2.14}$$

and

$$E_n = E_n[\rho\,(\mathbf{r})] = \int d\mathbf{r}\rho(\mathbf{r})V^{\mathrm{ext}}(\mathbf{r}) + F[\rho(\mathbf{r})], \tag{2.15}$$

where

$$\rho(\mathbf{r}) := N_e \int \dots \int d\mathbf{r}_2 d\mathbf{r}_3 \dots d\mathbf{r}_{N_e} \left|\Psi_\nu(\{\mathbf{r}_i\})\right|^2 . \tag{2.16}$$

The first term in Eq. 2.15 describes the interaction with the external potential and $F[\rho(\mathbf{r})]$ stands for the kinetic and electron-electron interaction energies [127]:

$$F[\rho(\mathbf{r})] = \min_{\Psi\to\rho} \langle\Psi|\hat{T} + \hat{V}_{\text{el-el}}|\Psi\rangle. \tag{2.17}$$

Eq. 2.16 implies that $\rho(\mathbf{r})$ is a function of only three spatial variables as compared to $\Psi_\nu(\{\mathbf{r}_i\})$, a function of $3N_e$ variables. Furthermore, $\Psi_\nu(\{\mathbf{r}_i\})$ has to be obtained solving an eigenvalue problem instead of a central equation.

Applying the Rayleigh-Ritz variational principle (Section 2.1.2) to the energy functional $E_n[\rho\,(\mathbf{r})]$ from Eq. 2.15 shows that this energy is always larger or equal to the ground-state energy E_0:

$$E_n[\rho\,(\mathbf{r})] \geq E_0. \tag{2.18}$$

The second Hohenberg-Kohn theorem utilises this behaviour and extends the proof of the *existence* of an energy $E[\rho(\mathbf{r})]$ with a description of *how to obtain it* [125, 127]:

Theorem 2 ***Variational Principle***

The functional $E[\rho(\boldsymbol{r})]$ is minimal for the density $\rho_0(\boldsymbol{r})$ corresponding to the ground state:

$$E_0 = E[\rho_0(\mathbf{r})] = \min_{\rho(\mathbf{r})} \langle\Psi[\rho]|\hat{T}^{\text{el}} + \hat{V}^{\text{ext}} + \hat{V}^{\text{el}}|\Psi[\rho]\rangle. \tag{2.19}$$

The external potential usually refers to the electron-nuclei interaction. Now, the ground-state electron density of a system instead of its complete many-body wavefunction can be determined.

2.2.2 Kohn-Sham Theory

The formulation of the Kohn-Sham approach [128] makes the actual computation of the ground state of a system possible and therefore provides the groundwork for the implementation of DFT codes. It combines the Lagrangian method of undetermined multipliers with the parametrisation of the density $\rho(\mathbf{r})$ into one-electron orbitals, from where the functional $F[\rho(\mathbf{r})]$ from Eq. 2.15 and 2.17 can be determined.

The main step forward is the Kohn-Sham construction of mapping the problem of an interacting electron system onto an auxiliary system of independent electrons of equal density $\rho(\mathbf{r})$. The non-interacting electrons move in an effective potential that mimics the dependency of the other particles. The key is to express the density in Eq. 2.15 by the solutions ϕ to a non-interacting system and to minimise the energy functional with respect to these solutions. For the single-electron equations we can write:

$$E_S[\rho] = \langle \phi_S[\rho] | \hat{T}_S + \hat{V}^{\text{eff}} | \phi_S[\rho] \rangle. \tag{2.20}$$

Here, the subscript S enumerates the single-electron equations, $\hat{T}_S$ describes the kinetic energy of the non-interacting electrons, and $\hat{V}^{\text{eff}}$ is the local, so-called "effective" (or "Kohn-Sham"), potential. The operators can be expressed by [129]

$$\hat{T}_S[\rho] = \min_{\phi \to \rho} \langle \phi | \hat{T} | \phi \rangle, \tag{2.21}$$

and

$$\hat{V}^{\text{eff}} = \hat{V}^{\text{ext}} + \hat{V}^{\text{el}} + (\hat{T}^{\text{el}} - \hat{T}_S). \tag{2.22}$$

Setting up the effective single-particle Schrödinger equations results in the "Kohn-Sham equations":

$$[\hat{T}_S + V^{\text{eff}}(\mathbf{r})]\phi_i(\mathbf{r}) = [-\frac{\hbar^2}{2m}\nabla^2 + V^{\text{eff}}(\mathbf{r})]\phi_i(\mathbf{r}) = \epsilon_i\phi_i(\mathbf{r}). \tag{2.23}$$

ϕ_i are the orthogonal single-electron Kohn-Sham orbitals with the corresponding orbital energy ϵ_i. They reproduce $\rho_0(\mathbf{r})$ of the interacting many-body system and also yield the electronic density of the non-interacting system by

$$\rho(\mathbf{r}) = \sum_i f_i \left|\phi_i(\mathbf{r})\right|^2, \tag{2.24}$$

where f_i describes the Fermi-Dirac function

$$f_i = \frac{1}{1 + e^{(\epsilon_i - \mu)}/(k_B T)}, \tag{2.25}$$

and μ the Fermi level. The Kohn-Sham equations therefore describe electrons moving in an effective one-electron potential V^{eff}, which can be derived by applying the variational principle from Section 2.1.2 to Eq. 2.20:

$$\frac{\delta E_S[\rho]}{\delta\rho(\mathbf{r})} = \frac{\delta\hat{T}_S}{\delta\rho(\mathbf{r})} + \hat{V}^{\text{ext}} + \frac{\delta\hat{V}^{\text{el}}}{\delta\rho(\mathbf{r})} + \frac{\delta E^{xc}[\rho(\mathbf{r})]}{\delta\rho(\mathbf{r})}, \tag{2.26}$$

or, alternatively, by adding and subtracting $\hat{V}^{\text{el}}$ and $\hat{T}_S$ to Eq. 2.15:

$$\begin{aligned} E_n[\rho\,(\mathbf{r})] =& \hat{V}^{\text{el}} - \hat{V}^{\text{el}} + \hat{T}_S - \hat{T}_S + \int d\mathbf{r}\rho(\mathbf{r})V^{\text{ext}}(\mathbf{r}) + F[\rho(\mathbf{r})] \\ =& \hat{T}_S + \int d\mathbf{r}\rho(\mathbf{r})V^{\text{ext}}(\mathbf{r}) + \hat{V}^{\text{el}} + E^{xc}[\rho(\mathbf{r})]. \end{aligned} \tag{2.27}$$

In both cases, we see that a new "exchange-correlation energy" E^{xc} was defined as $E^{xc} = F[\rho(\mathbf{r})] - \hat{T}_S - \hat{V}^{\text{el}}$, *i.e.* as the difference between the exact expectation value of the kinetic energy and electron-electron interaction of the interacting system and the expectation value of the kinetic energy and electron-electron interaction of the non-interacting system. The term therefore represents the "physics" of the full interacting system and leads to the effective potential

$$V^{\text{eff}}(\mathbf{r}) = V^{\text{ext}}(\mathbf{r}) + \int d\mathbf{r}' \frac{e^2\rho(\mathbf{r}')}{|\mathbf{r} - \mathbf{r}'|} + V^{xc}[\rho(\mathbf{r})], \tag{2.28}$$

where the exchange-correlation potential is obtained from the variational derivation of the exchange-correlation energy:

$$V^{xc}[\rho(\mathbf{r})] = \frac{\delta E^{xc}[\rho(\mathbf{r})]}{\delta\rho(\mathbf{r})}. \tag{2.29}$$

Since the Kohn-Sham equations are a set of single-particle equations, they are considerably easier to solve than the coupled Schrödinger equation, particularly for system sizes with a large number of electrons. The Kohn-Sham orbitals and their eigenenergies are not eigenfunctions and eigenvalues, respectively, of the actual system. In order to determine the *actual* total electronic ground-state energy of the system, one evaluates the density given by the Kohn-Sham eigenfunctions (Eq. 2.24) and inserts it in Eq. 2.27. Multiplying the complex conjugate of ϕ_i, ϕ_i^*, to the Kohn-Sham equation (2.23) and integrating leads to

$$E = \sum_i \epsilon_i - \int d\mathbf{r}d\mathbf{r}' \frac{e^2\rho(\mathbf{r})\rho(\mathbf{r}')}{|\mathbf{r} - \mathbf{r}'|} + E^{xc} - \int d\mathbf{r}\rho(\mathbf{r})V^{xc}(\mathbf{r}). \tag{2.30}$$

It is worth noting that the Kohn-Sham equations are *exact* and yield the exact density, because the problem of the interacting electron system has so far

only been mapped onto a non-interacting one with an additional term. The approximations take place when an expression for the exchange-correlation functional is derived, which will be covered in the next section.

2.2.3 Exchange-Correlation Functionals

Let us introduce the approach to arrive at a description for the exchange-correlation (xc-) functional. The two most popular approaches are the local density approximation (LDA) and the generalised-gradient approximation (GGA), which are the subjects of the present section [129].

Local density approximation Introduced by Kohn and Sham, the earliest functional-approach assumes that the exchange-correlation energy can be locally approximated by the exchange-correlation energy density of the uniform electron gas $\epsilon^{xc}_{\mathrm{UEG}}$. In other words, it is assumed that the exchange-correlation energy of an inhomogeneous system can be at each point approximated by the energy of a uniform, *i.e.* homogeneous, electron gas with that density. This reads as [128]:

$$E^{xc}_{\mathrm{LDA}}[\rho(\mathbf{r})] = \int d\mathbf{r}\rho(\mathbf{r})\epsilon^{xc}_{\mathrm{UEG}}[\rho(\mathbf{r})]. \tag{2.31}$$

The most basic functional is the Slater expression for the exchange potential, where only one parameter α is used and adjusted to the properties of the modelled system. It is therefore often called the "X_α-functional" [130]. The correlation part can not be determined exactly; quantum Monte Carlo methods can be used to determine an expression for it on the basis of an homogeneous electron gas, as suggested by Ceperley and Alder [131]. Two common parametrisations for the data are named after Perdew and Zunger [132] (PZ81) and after Vosko, Wilk and Nusair [133] (VWN), which use different analytical forms for E^c.

The expressions for the exchange and the correlation part add up to the exchange-correlation functional.

In solid state physics, the LDA functional has been the standard approximation since the early 1970s. It was shown that it provides reasonable molecular data but strongly overestimates atomisation energies [134], and was thus never popular within the quantum-chemistry community [132, 133, 135, 136].

Generalised gradient approximation To account for the inhomogeneous charge-density distributions that exist in a real system, the density *gradient* is considered in the calculation of the exchange-correlation energy in addition to the electron density itself:

$$E^{xc}_{\mathrm{GGA}}[\rho(\mathbf{r})] = \int d\mathbf{r} f(\rho(\mathbf{r}), \nabla\rho(\mathbf{r})). \tag{2.32}$$

The approach is known as the "generalised-gradient approximation" (GGA). The construction of GGA functionals is based on fitting to *ab initio* materials properties. The most popular implementation of a GGA functional is the one by Perdew, Burke, and Ernzerhof (PBE) [136]. It was observed that the errors in the predicted LDA atomisation energies could be reduced [137], leading to the adoption of GGAs as a standard quantum-chemical method [138]. Where LDA potentials are widely used in solid state physics, binding properties are usually better represented by GGA functionals. In some cases, the LDA overbinding effect results in shorter bond lengths and leads to worse predictions of ground-state properties, in other cases the structural softness of PBE predicted materials are more pronounced [134, 139].

One way to include exchange interactions in the functionals is to screen the interaction onto the *xc*-functional; the B3LYP and HSE functionals are examples for such "hybrid" functionals, with the former being fitted to empirical parameters, the latter being fully *ab initio*. Hybrids are usually the most accurate, yet computationally most demanding functionals for energetic DFT calculations.

On-site Coulomb interaction It is possible to include the on-site Coulomb interaction, which is particularly strong for localised *d*- and *f*-electrons and is not treated well in LDA or GGA *xc*-functionals. One way to mimic the effect of the Coulomb interaction of localised electrons is to shift the localised orbitals relative to the others by introducing a Hubbard-like term to the potential [140]. The term is added for highly localised atomic-like orbitals on the same atomic site and quantified by the on-site Coulomb interaction U and the on-site exchange J.

Liechtenstein [141] and Dudarev [142] implemented the two most popular "flavours" to treat the Coulomb interaction. The former adds the on-site interaction by a Hartree-Fock term and subtracts the double counting ("*dc*") term according to

$$E^{dc}(\hat{f}) = \frac{U}{2}\hat{f}^{\mathrm{tot}}(\hat{f}^{\mathrm{tot}} - 1) - \frac{J}{2}\sum_{\sigma}\hat{f}_{\sigma}^{\mathrm{tot}}(\hat{f}_{\sigma}^{\mathrm{tot}} - 1), \tag{2.33}$$

where f_σ are the orbital occupancies. Dudarev's approach treats only one parameter, the effective $U_{\mathrm{eff}} = U - J$, leading to a "penalty" term in the energy, which forces the on-site occupation matrix f_σ to fully occupied or unoccupied states:

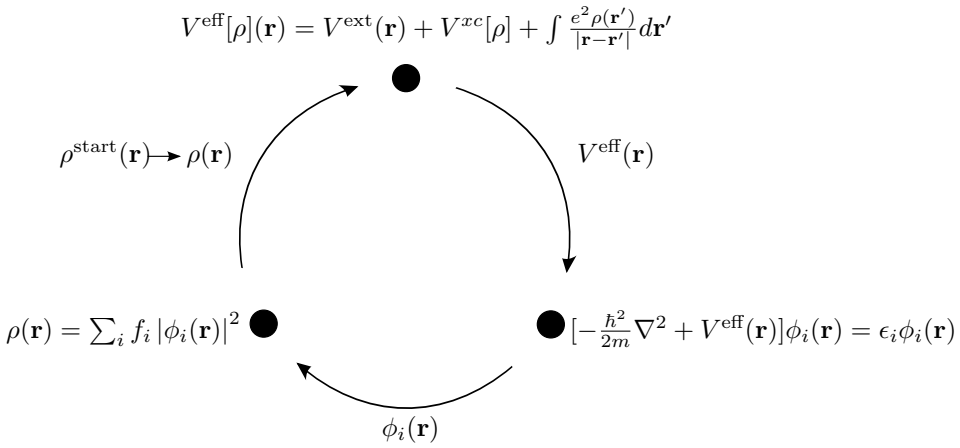


Figure 2.1: Schematic representation of the self-consistency cycle to solve the Kohn-Sham equations. If the energy difference between two successive steps falls below a predefined value, the iteration is stopped.

$$E^{\text{tot}}(f,\hat{f}) = E^{\text{DFT}}(f) + \sum_{\sigma} \frac{U_{\text{eff}}}{2} \left[\left(\sum_{m_1} f_{\sigma}^{m_1,m_2} - \sum_{m_1,m_2} f_{\sigma}^{m_1,m_2} f_{\sigma}^{m_1,m_2} \right) \right], \tag{2.34}$$

where σ and m are the spin index and state index, respectively. In both versions, the parameters U and J (or U_{eff}) need to be adjusted to fit to empirical data.

Usually, different *xc*-functionals are tested to be the most suitable for the quantity in question.

For a given functional, the Kohn-Sham equations can be solved in a self-consistent manner, as shown schematically in Fig. 2.1. One starts with an initial guess of the electronic charge density ρ^{start}. The effective potential is calculated and with that the Kohn-Sham equation can be solved. With the new wavefunction, a new charge density can be determined. If the self-consistency criterion is reached, output quantities like the energy, forces, stresses, or eigenvalues can be obtained.

2.2.4 Bloch's Theorem

An important property of materials is their periodicity on small scales. The translational symmetries can be used to describe whole crystals with primitive cells and periodic boundary conditions [143]. Wavefunctions of periodic systems can be expressed as a function

$$\Psi_{n\mathbf{k}}(\mathbf{r}) = u_{n\mathbf{k}}(\mathbf{r})e^{i\mathbf{kr}}, \tag{2.35}$$

where $u_{n\mathbf{k}}(\mathbf{r}) = u_{n\mathbf{k}}(\mathbf{r}+\mathbf{R})$ exhibits the periodicity of the crystal with $\mathbf{R}$ being a lattice vector. The exponential term is a plane wave commensurate with the entire system. The wave-vector $\mathbf{k}$ is constrained to the first Brillioun zone, which introduces the band index n linking a certain $\mathbf{k}$ to an energy value. In principle, an infinite system has an infinite number of wave-vectors, which accounts for the infinite number of electrons in the truly periodic system. The wave-vector can thus be used to classify any excitation of a periodic crystal. However, the change in $u_{n\mathbf{k}}$ for close k-points becomes negligible if $\Psi_{n\mathbf{k}}$ is smooth in $\mathbf{k}$. The first Brillouin zone is thus sampled with a finite grid of k-points, that is commonly described by an equidistant mesh, *e.g.* as introduced by Monkhorst and Pack [144].

2.2.5 Plane Waves

The plane-wave approach makes use of the fact that every function can be expanded in a basis set. When periodic systems are described, it is convenient to expand the wavefunctions in a set of Fourier components representing plane waves. An advantage of using a plane-wave basis set over Gaussian orbitals or minimal basis sets is the use of the reciprocal lattice vectors $\mathbf{G}$: because of the cell periodicity, the basis then exhibits the periodicity of the lattice. The wavefunctions from the Kohn-Sham equations (Eq. 2.23) can be expanded in

a Fourier basis applying periodic boundary conditions:

$$\Psi_{n\mathbf{k}} = \frac{1}{\sqrt{\Omega}} \sum_{\mathbf{G}} u_{n\mathbf{k}}(\mathbf{G}) e^{i(\mathbf{G}+\mathbf{k})\mathbf{r}}, \tag{2.36}$$

where $\Omega = N_{\text{cell}}\Omega_{\text{cell}}$. If an infinite set of reciprocal lattice vectors $\{\mathbf{G}\}$ was chosen, the full wavefunction would be represented exactly. However, the sum reaches convergence as more Fourier terms are included, since the coefficients become smaller with a higher plane-wave number. A criterion for a finite number of $\mathbf{G}$-vectors in Eq. 2.36 can be defined by an energy cut-off E_{cut}, which determines the vectors $\mathbf{G}$ that are accounted for in the Fourier expansion:

$$\frac{\hbar^2}{2m} |\mathbf{G} + \mathbf{k}|^2 \leq E_{\text{cut}}. \tag{2.37}$$

The Kohn-Sham equations are split up into N_k equations by applying the concept of periodicity, N_k being the number of k-points. The equations can be solved one by one, since they are only linked through the electron density $\rho(\mathbf{r})$. This is a considerable improvement of the computational effort compared to solving the coupled Schrödinger equation or to the infinite number of Kohn-Sham equations. The overall scaling is N_e^3, where the cubic dependence comes from the required orthogonalisation of the electronic orbitals.[4]

Strongly localised valence electrons that need to be orthogonal to the core wavefunctions close to the nuclei are usually heavily oscillating. They require a large number of plane waves to be accurately described, hence a high cut-off energy, and therefore lead to computationally demanding calculations. To avoid this problem, various approaches have been established based on dividing the system into core and valence regions. Close to the nuclei, the

[4]The Hamiltonian has a dimensionality proportional to N_e and diagonalisation methods have a scaling of n^3, where n is the number of dimensionality of the diagonalisable matrix.

atomic-like features vary quickly and therefore have to be described efficiently and accurately. Outside these regions, valence functions vary smoothly, which reduces the computational effort.

The augmented plane wave (APW) method, which was introduced by Slater in 1937 [145], represents the outside states as plane waves and the core states as radial wavefunctions. The eigenstates of the independent-particle Schrödinger equation are expanded in basis functions that are represented differently within and outside the core region. Matching the functions at the sphere boundary becomes infeasible as it leads to non-linear equations [146]. The linearised augmented plane wave (LAPW) [147] method accounts for that issue. As a result, it is one of the most accurate approaches but also more time demanding than other approximations [121].

The plane-wave expansion of the wavefunction (Section 2.2.5) is feasible for free-electron-like systems. However, if one wants to describe the wavefunction near atomic cores, they will be far from free-electron like: due to the strong Coulomb potential, the core electrons are tightly bound to the nucleus and strongly localised, leading to strong oscillations in that region for energy levels $n > 1$. Secondly, the valence wavefunctions are required to be orthogonal to the core-electron states, which in turn leads to strongly oscillating wavefunctions near the core.

2.2.6 Pseudopotentials

Another way of approaching the wavefunctions within and outside the region around the nuclei is the pseudopotential (PP) method. Pseudopotentials replace the effect of the core electrons on the valence electrons by an effective potential. The valence wavefunctions are smoothened and need a smaller number of plane waves in their expansion. An outline of the PP method will be given in the next section.

Because most material properties are determined by bonds that are formed by valence electrons, bonds are not affected by the details of the valence wavefunction near atomic nuclei. Additionally, core orbitals are mostly independent of changes in the chemical environment as the different orbitals from different sites do not overlap. The use of PPs can therefore often be a powerful tool to perform accurate and less time-demanding calculations.

Pseudopotentials replace both the core electrons and the atomic nucleus by an effective potential. The potential is created in a way that it is smooth compared to the original potential leading to less-curved valence wavefunctions compared to the true wavefunctions. The potential aims to reproduce the orthogonality and the effects of the nuclear potential. The smoothing is performed within a certain region—the core region—which is defined by a radius r_c.

To construct a pseudopotential, an all-electron (AE) DFT calculation is carried out on an isolated atom. Within the core region, the AE wavefunction is pseudised, *i.e.* smoothened, to construct wavefunctions that are node-less. Solving the Schrödinger equation for the pseudised wavefunctions leads to the pseudopotential. There are several requirements to the effective potential: firstly, the eigenvalues of the valence orbitals should be as close to the AE eigenvalues as possible. Secondly, it has to produce wavefunctions that are continuous and differentiable at the core-region boundaries.

One approach requires both the pseudised and the AE wavefunctions to represent the same charge within the core region, leading to "norm-conserving" (NC) PPs [148, 149]. A comparison of the $3d$-wavefunctions of iron generated by a NC PP together with the corresponding all-electron wavefunction can be seen in Fig. 2.2. The AE and the pseudised wavefunction converge quickly for larger radii and are identical by construction outside the cut-off radius r_c.

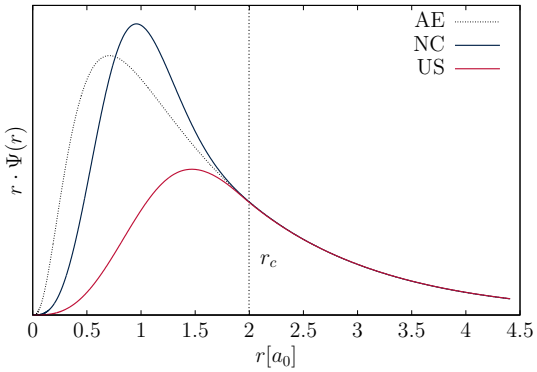


Figure 2.2: $3d$-radial wavefunction $r \cdot \phi(r)$ for iron as modelled in an all-electron (AE) calculation, with a norm-conserving (NC) pseudopotential (PP), and an ultra-soft (US) PP. A cut-off radius of $r_c = 2.0\,\mathrm{a\,u}$ is chosen for all calculations. For Fe, as well as for other transition-metal elements, the NC PP is very similar to the AE wavefunction. This yields in a high number of plane waves necessary to model the NC wavefunction. The US PP smoothens the wavefunction to a greater extend leading to faster calculations. The PPs were generated with CASTEP [152].

Localised atom-centred augmentation charges can be introduced [150, 151] to account for the charge deficit, when the restriction of norm-conservation is lifted. The comparison between a so-called "ultra-soft" (US) PP, a norm-conserving PP and the original Coulomb potential together with their corresponding wavefunctions can be seen in Fig. 2.2 for the $3d$-radial wavefunction of iron.

The new, non-norm-conserving smooth atomic function $\widetilde{\phi}$ is numerically connected to the AE atomic function ϕ by accounting for the charge deficit within the core region. A charge augmentation function was introduced, which represents the difference of charge of the AE wavefunction and the pseudised wavefunction:

$$Q_{ij}(\mathbf{r}) = \phi_i(\mathbf{r})\phi_j^*(\mathbf{r}) - \widetilde{\phi}_i(\mathbf{r})\widetilde{\phi}_j(\mathbf{r}). \tag{2.38}$$

Together with the Hermitian overlap operator

$$\hat{S} = \hat{1} + \sum_{i,j} q_{ij} \left|\beta_j\right\rangle\left\langle\beta_i\right|, \tag{2.39}$$

where $q_{ij} = \int d\mathbf{r} Q_{ij}(\mathbf{r})$, and a non-local Hermitian pseudopotential operator

$$\hat{V}^{NL} = \sum_{i,j} D_{ij} \, |\beta_j\rangle\langle\beta_i| \, . \tag{2.40}$$

The smooth functions $\widetilde{\phi}$ are obtained for each reference-atom state i as the solutions of the generalised eigenvalue problem [121]

$$(\hat{H} - \epsilon\hat{S})|\widetilde{\phi}\rangle = (\hat{T} + \hat{V}^{\text{loc}} + \hat{V}^{NL} - \epsilon\hat{S})|\widetilde{\phi}\rangle = 0. \tag{2.41}$$

For norm-conserving PPs, q_{ij} equals zero and therefore yields an overlap operator that reduces to the unity operator [153]. In Eq. 2.40, D_{ij} is given by

$$D_{ij} = \langle\phi_j| - (\hat{T} + \hat{V}^{\text{loc}} - \epsilon)|\phi_i\rangle \tag{2.42}$$

and the β_i act as a new basis, which is dual to the pseudo wavefunctions $|\widetilde{\phi}_j\rangle$ of the system:

$$\langle\beta_i|\widetilde{\phi}_j\rangle = \delta_{ij}. \tag{2.43}$$

Due to the relaxation of the norm-conservation, the new wavefunctions obey a generalised orthonormality condition

$$\langle\widetilde{\phi}_i|\hat{S}|\widetilde{\phi}_j\rangle = \delta_{ij}. \tag{2.44}$$

Finally, the total energy can be obtained by minimising

$$E_{\text{tot}} = \sum_{i}^{\text{occ}} \langle\widetilde{\phi}_i| \left(\hat{T} + \hat{V}^{\text{loc}} + \sum_{n,m} D_{nm} |\beta_n\rangle\langle\beta_m| \right) |\widetilde{\phi}\rangle + \iint d\mathbf{r'} d\mathbf{r} \frac{\rho(\mathbf{r'})\rho(\mathbf{r})}{|\mathbf{r} - \mathbf{r'}|} + E^{\text{ion-ion}} + E^{xc}. \tag{2.45}$$

The transition to the generalised eigenvalue problem follows in a new electron density [154]:

$$\rho(\mathbf{r}) = \sum_{n}^{\text{occ}} |\widetilde{\Psi}_n(\mathbf{r})|^2 + \sum_{n,i,j} \langle \widetilde{\Psi}_n | \beta_j \rangle \langle \beta_i | \widetilde{\Psi}_n \rangle Q_{ij}(\mathbf{r}). \tag{2.46}$$

The charge distribution given in Eq. 2.46 could be exact if the second part, namely the augmentation part $Q_{ij}(\mathbf{r})$, would be represented exactly. The approach that is taken in the ultra-soft scheme is to pseudise $Q_{ij}(\mathbf{r})$ again. Together with increasing the accuracy by decreasing the cut-off radius of the pseudised wavefunction, another factor in yielding more accurate results is to reduce the core region of the core-augmentation charge, which is also distinguished by a cut-off radius. Both pseudised quantities, namely the wavefunction and the core-augmentation charge, are modelled on grids for the fast-Fourier transforms, leading to an efficient numerical way of simulating three-dimensional distributions.

Compared to the AE calculation, the pseudisation of the two quantities results in much more efficient computational performance. Pseudopotentials are therefore a very popular approach to model materials with first-principles methods, also because of their formal simplicity as compared to "more accurate" AE approaches.

Combining ideas of the PP approach with the accuracy of all-electron calculations has been established by Blöchl [153]. It makes use of several pseudisation assumptions of the PP method but describes the wavefunctions in the core region with all-electron wavefunctions. The core calculations are transferred to a projector basis which accounts for the name of the method, the projector augmented-wave method (PAW).

2.2.7 Projector Augmented-Wave Method

The results obtained by pseudopotential approaches are sufficient for properties weighted outside the nucleus. If that is not the case, another way to treat the core-augmentation charge $Q_{ij}(\mathbf{r})$ is implemented in the projector augmented-wave method. It makes use of smoothening the wavefunction of the crystal as well but also accounts for the details of the core wavefunction by computing the core-augmentation charge with all-electron calculations.

There exist two ways of introducing the PAW scheme. In the following, the historic way is outlined, which is based on one atom, and which introduces the projector formalism on which the PAW method is based. The idea is to model the AE wavefunction with a smooth function that accounts for the whole crystal and with an exact function close to the nuclei by projecting out parts of the smooth pseudised wavefunction and replacing them with the AE wavefunctions. The approach follows Ref. [121], to which the reader is referred to if a more detailed derivation is required.

A transformation maps the set of pseudo-wavefunctions $\widetilde{\Psi}_i^v(\mathbf{r})$ to the AE *valence* wavefunctions $\Psi_i^v(\mathbf{r})$, $\Psi^v(\mathbf{r}) = \mathfrak{T}\widetilde{\Psi}^v$. For simplicity, the superscript v and the label i are omitted in the following. Once again, each smooth function $|\widetilde{\Psi}\rangle$ is expanded into atomic-like states expressed as partial waves $|\widetilde{\phi}_m\rangle$ within each sphere:

$$|\widetilde{\Psi}\rangle = \sum_m c_m |\widetilde{\phi}_m\rangle, \tag{2.47}$$

where c_m are coefficients, m stands for the atomic site, the angular momentum quantum numbers $L = (l, m)$, and an additional index to label different partial waves for the same atomic site and angular momentum. The AE wavefunction in Eq. 2.47 relates to the partial waves through

$$|\Psi\rangle = \mathfrak{T}|\widetilde{\Psi}\rangle = \sum_m c_m |\phi_m\rangle, \tag{2.48}$$

making it possible to express the AE wavefunction by [155]

$$|\Psi\rangle = |\widetilde{\Psi}\rangle + \sum_m c_m \{|\phi_m\rangle - |\widetilde{\phi}_m\rangle\}. \tag{2.49}$$

The c_m can be obtained by a projection in each sphere, as $\mathfrak{T}$ is required to be linear:

$$c_m = \langle \beta_m | \widetilde{\Psi} \rangle \tag{2.50}$$

for a set of projection operators β. The projector functions obey an orthonormality condition with the partial waves:

$$\langle \beta_i | \phi_j \rangle = \delta_{ij}. \tag{2.51}$$

With the projectors, the transformation operator can be written as

$$\mathfrak{T} = \mathbb{1} + \sum_m \{|\phi_m\rangle - |\widetilde{\phi}_m\rangle\} \langle \beta_m |. \tag{2.52}$$

An important observation is the fact that $\mathfrak{T}$ is still a function of the AE wavefunction, as opposed to the transformation taking place within the PP *ansatz*.

To arrive at an expression for the AE *charge density* via the smooth wavefunctions, operators can be transformed according to $\mathfrak{T}$, so that they act only on the smooth wavefunction [153]. The following equation holds true for any operator; for the particular case of the Hamilton operator $\hat{H}$, it reads as[5]

[5] Neglecting cross terms between atomic sites.

$$\widetilde{H} = \mathfrak{T}^{\dagger}\hat{H}\mathfrak{T} = \hat{H} + \sum_{n,m} |\beta_n\rangle\{\langle\phi_n|\hat{H}|\phi_m\rangle - \langle\widetilde{\phi}_n|\hat{H}|\widetilde{\phi}_m\rangle\}\langle\beta_m|. \tag{2.53}$$

Letting $\hat{H}$ act on the valence functions, it follows that

$$\widetilde{H} = \hat{T} + V^{\mathrm{loc}} + \sum_{n,m} |\beta_n\rangle\{\epsilon_m Q_{nm}(\mathbf{r}) + \langle\widetilde{\phi}_n|\epsilon_m - \hat{T} - V^{\mathrm{loc}}|\widetilde{\phi}_m\rangle\}\langle\beta_m|. \tag{2.54}$$

Until now, no assumption was made that contradicts the PP scheme. Comparing the Hamiltonian in Eq. 2.54 and the PP energy given in Eq. 2.45 shows that they match—so far, only another formalism has been used to derive an energy correlation depending on $Q_{ij}(r)$ [156]. As opposed to the ultra-soft scheme, however, where the core-augmentation charge is pseudised again, the PAW approach takes the charge density derived from Eq. 2.54 as

$$\rho(\mathbf{r}) = \widetilde{\rho}(\mathbf{r}) + \rho^{c}(\mathbf{r}) - \widetilde{\rho}^{c}(\mathbf{r}), \tag{2.55}$$

where

$$\widetilde{\rho}(\mathbf{r}) = \sum_{i}^{occ} |\widetilde{\Psi}_i(\mathbf{r})|^2, \tag{2.56}$$

$$\rho^{c}(\mathbf{r}) = \sum_{i}^{occ} \sum_{m,n} \langle\widetilde{\Psi}_i|\widetilde{\phi}_m\rangle \phi_m^{\dagger}(\mathbf{r})\phi_n(\mathbf{r})\langle\widetilde{\phi}_n|\widetilde{\Psi}_i\rangle, \tag{2.57}$$

$$\widetilde{\rho}^{c}(\mathbf{r}) = \sum_{i}^{occ} \sum_{m,n} \langle\widetilde{\Psi}_i|\widetilde{\phi}_m\rangle \widetilde{\phi}_m^{\dagger}(\mathbf{r})\widetilde{\phi}_n(\mathbf{r})\langle\widetilde{\phi}_n|\widetilde{\Psi}_i\rangle. \tag{2.58}$$

Treating the difference between the smooth $\widetilde{\Psi}^{c}$ wavefunction and the AE core wavefunction Ψ^{c} as one property makes it possible to expand the wavefunction with a more efficient basis. As the valence electrons experience the strong Coulomb potential screened by the core electrons, a basis for the valence electron wavefunctions can be built from the atomic wavefunctions. AE calculations are performed for the core part. The time-consuming core calcu-

lations are thus transferred to the PAW basis. This results in a much lower cut-off energy required, making the PAW scheme as popular as it is.

We have just explored how the ground-state energy of a system can be computed, which is a powerful way to derive quantities of solid states, and the subject of the next section.

2.3 Materials Properties

By calculating the ground-state energy of a system, useful properties inherent to the material can be derived. The following section addresses the theoretical and computational frameworks used to model quantities that are needed to determine the magnetoelectric response.

2.3.1 Interatomic Force-Constant Matrix

The interatomic force constant (IFC) matrix consists of the second derivatives of the total energy with respect to the atomic positions, and is a necessary component in determining the final magnetoelectric response. A more exhaustive overview about the theory and implementation work behind vibrational properties of crystals is given in Refs. [157, 158]; the current section only serves to define the terminology briefly.

The Hellman-Feynman forces F_n [159, 160] for an atom n are defined by the energy change with their respective displacement u_n:

$$F_n = -\partial E/\partial u_n. \tag{2.59}$$

One—intuitive—way to arrive at an expression for the IFC matrix is the so-called "finite-difference method", in which atoms are *displaced*: the induced force on an atom n is calculated, when another atom m moves. The

$3N$-dimensional vector of Eq. 2.59 is differentiated once more leading to the $3N \times 3N$ IFC matrix. Each configuration needs to be examined in an own self-consistent calculation, leading to high computational efforts [161].[6]

Another option is to employ density functional perturbation theory (DFPT) [157, 162, 163]. The displacements are treated as perturbations with a wave-vector and the first-order response can be determined. One advantage of the DFPT approach is that generating supercells becomes redundant and even incommensurate wave-vectors can be treated in the primitive unit cell.

2.3.2 Polarisation and Berry Phases

Although ways have been found to calculate certain magnetoelectric (ME) coupling responses without the actual application of external fields (Ref. [164] and Section 3.1.2) computing the macroscopic polarisation or applying an external electric field is necessary to calculate dielectric, ferroelectric, or piezoelectric properties, as well as the electronic part of the ME coupling. The "modern theory of polarisation" redefines the formal polarisation from a single-valued vector to a multi-valued vector quantity on a *lattice*. The quantum-mechanical approach uses Berry phases to calculate the *change* in polarisation. Refs. [121, 165, 166] and the sources referenced throughout this section provide further detail if necessary.

The problem with the polarisation becomes apparent when considering the classic definition of a polarisation in a one-dimensional atomic chain. In the Clausius-Mossotti model, solids are divided into polarisable units with polarisation centres [167, 168], in which the polarisation is defined as the sum of localised dipole moments divided by the unit volume. We can see the physical

[6] Using symmetry considerations the amount of distinct displacements can, however, be reduced.

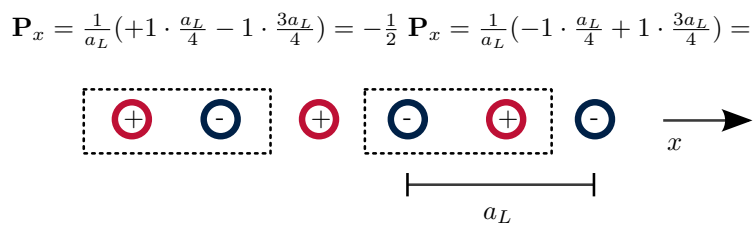


Figure 2.3: Sketch of a one-dimensional chain of differently charged ions, modified from Ref. [166]. Depending on the unit cell, the calculated polarisation could vary from -1/2 to 1/2 (in arbitrary units).

problem of "multi-valuedness" in Fig. 2.3: depending on the choice of cell, the polarisation is defined differently and could even point in opposite directions. In bulk materials however, where we assume periodic boundary conditions, the charge density $\rho(\mathbf{r})$ is a continuous function of $\mathbf{r}$. In an attempt to classically define the polarisation of the cell $\mathbf{P}_{\text{cell}}$, we would therefore define [165]

$$\mathbf{P}_{\text{cell}} = \frac{1}{V_{\text{cell}}} \int_{\text{cell}} d\mathbf{r}\ \mathbf{r}\rho(\mathbf{r}), \tag{2.60}$$

yet we arrive at the same problem [166]: $\mathbf{r}\rho(\mathbf{r})$ is nonperiodic, incompatible with Bloch's theorem, and leads to runaway solutions by an ill-defined ground state [169].

Considering the *change* in polarisation rather than the absolute value is the basis of the modern theory of polarisation. Only recently, R. D. King-Smith and D. Vanderbilt interpreted $\Delta\mathbf{P}$ as the unique polarisation *current* flowing through the bulk [170]. Periodicity can thus be preserved [171]:

$$\Delta\mathbf{P} = \mathbf{P}(\Delta t) - \mathbf{P}(0) = \int_0^{\Delta t} dt\mathbf{j}(t) = \int_0^{\Delta t} dt \left(\frac{d\mathbf{P}}{dt}\right). \tag{2.61}$$

t can be understood as the time to progress from the nonpolarised to the polarised state. However, Berry phases are required to prove that ΔP in Eq. 2.61 is independent of the path integral. We can take advantage of periodicity in k-space and describe physical properties as integrals over occupied

bands [121]. Starting from the independent-particle Kohn-Sham approach (Section 2.2.2), the eigenfunctions are written in terms of the Bloch functions $u_{n\mathbf{k}}$ (Eq. 2.35): $\Psi_{n\mathbf{k}}(\mathbf{r}) = u_{n\mathbf{k}}(\mathbf{r})e^{i\mathbf{kr}}$, obeying $H|\Psi_{n\mathbf{k}}\rangle = E_{n\mathbf{k}}|\Psi_{n\mathbf{k}}\rangle$ with the Hamiltonian $H_{\mathbf{k}} = \frac{(\mathbf{p}+\hbar\mathbf{k})^2}{2m} + V$. Substituting t by λ, an adiabatic perturbation to $\mathbf{P}$, leads to the first-order correction

$$\frac{d\mathbf{P}_n}{d\lambda} = \frac{ie}{(2\pi)^3}\int_{\mathrm{BZ}} d\mathbf{k}\left\langle \nabla_{\mathbf{k}} u_{n\mathbf{k}} \middle| \frac{\partial}{\partial\lambda} u_{n\mathbf{k}} \right\rangle + \text{c.c.}, \tag{2.62}$$

where "c.c." stands for the complex conjugate, yielding the perturbation of the polarisation *per band*. If we insert Eq. 2.61 with $t = \lambda$ into Eq. 2.62, sum over all bands, and integrate with respect to λ, the electronic contribution to the polarisation results:

$$\mathbf{P}_{\mathrm{el}}(\lambda) = \frac{e}{(2\pi)^3}\,\mathbb{Im}\left\{\sum_n^{\mathrm{occ}}\int_{\mathrm{BZ}} d\mathbf{k}\,\langle u^{\lambda}_{n\mathbf{k}}|\nabla_{\mathbf{k}}|u^{\lambda}_{n\mathbf{k}}\rangle\right\}. \tag{2.63}$$

$\mathbb{Im}\{X\}$ is the imaginary part of X. The adiabatic condition demands the system to be insulating for every λ along the path, so that the result is independent of the path and only depends on the start and end point. We can therefore write for the effective polarisation, where we add the ionic part and the polarisation difference between the polar and centrosymmetric state:

$$\mathbf{P}_{\mathrm{eff}} = \Delta\mathbf{P}_{\mathrm{ion}} + \left[\mathbf{P}_{\mathrm{el}}(\lambda = 1) - \mathbf{P}_{\mathrm{el}}(\lambda = 0)\right]. \tag{2.64}$$

The ionic contribution is

$$\mathbf{P}_{\mathrm{ion}} = \frac{e}{\Omega}\sum_I Z_I^{\mathrm{ion}}\mathbf{r}_I, \tag{2.65}$$

where Ω is the cell volume and a sum is implied over all ions at position $\mathbf{r}_I$.

The integrand of Eq. 2.63 is a "Berry phase" [172], characterised by the form of a Berry connection $\mathbf{A}(\mathbf{k}) = i\langle u_{n\mathbf{k}}|\nabla_{\mathbf{k}}|u_{n\mathbf{k}}\rangle$. Being a phase, the Berry phase is only well defined $\pmod{2\pi}$, leading to the conclusion that $\mathbf{P}_n$ is only well defined *modulo* a "polarisation quantum" $\frac{e\mathbf{R}}{\Omega}$, $\mathbf{R}$ being a lattice vector. This is in line with the initially introduced multivaluedness of the polarisation. For an integral with infinitesimal steps from one point along the path to another, this does not affect the results, as we are talking about a *change* in polarisation. In practise, because the Brillouin zone in modelled on a grid (Section 2.2.4), Eq. 2.63 involves a sum over a discrete set of k-points rather than an integral, known as the "polarisation lattice". Care needs to be taken that the choice of branch is consistent; each point of the Brillouin zone has an infinite number of polarisation values separated by $\frac{e\mathbf{R}}{\Omega}$.

With the modern theory of polarisation, it became possible to apply external electric fields according to $-\mathbf{r}\cdot\mathbf{E}$ to the Hamiltonian in DFT simulations.[7] Responses like the Born effective charges and the piezoelectric effect can be determined [169, 173, 174]; their concepts will be introduced in the next section.

2.3.3 Born-Effective Charges

It was demonstrated in the last section that in the computational approach of implementing a finite polarisation into DFT codes, the polarisation itself cannot be seen as the product of a formal ionic charge (such as $1+$ for Na^{1-} or $2-$ for ions like O^{2-}) with its displacement. Considering Wannier centres instead, which are localised in space, the picture of "displacement times charge" can be validated again [166]. The contribution of charges from the positively and negatively charged ions centred at the centre of each Wannier function

[7] It is obvious that $-\mathbf{r}\cdot\mathbf{E}$ shows the same problems as the polarisation: it is nonperiodic, causing difficulties to apply Bloch's theorem, and unbounded from below, leading to runaway solutions by an ill-defined ground state [169].

is the equivalent to the previously mentioned formal charge—so the Wannier centres can move by a different amount than the ion cores. When both move in different directions, the induced polarisation during this displacement is larger than the formal charges and *vice versa*. With the displacement and the corresponding polarisation, *effective charges* can be introduced. The so-called "Born effective charge" (BEC) tensor of an atom i is defined as

$$Z^*_{i\beta\gamma} = \frac{\Omega}{e}\frac{dP_\beta}{du_{i\gamma}} = -e\frac{dF_{i\gamma}}{d\epsilon_\beta} = e\frac{d^2E}{du_{i\gamma}d\epsilon_\beta}. \tag{2.66}$$

The two equivalent definitions present alternative routes to determine the BECs: via the change in $\mathbf{P}_\beta$ after a displacement of atom i by $\mathbf{u}_{i\gamma}$ and via the change in forces in γ-direction on atom i upon application of an electric field ϵ along β. The concept of the BECs is crucial to compute important responses based on electronic interactions, such as the dielectric or ME coupling tensor.

2.3.4 Spin Polarised Density Functional Theory

So far, only the electron density has been introduced in the DFT formulation of Section 2.2. In order to include magnetism, the Kohn-Sham equations of Eq. 2.23 can be solved separately for "up" and "down" Kohn-Sham orbitals $\phi_{i\uparrow}(\mathbf{r})$ and $\phi_{i\downarrow}(\mathbf{r})$ corresponding to up and down spin densities $\rho_\uparrow(\mathbf{r})$ and $\rho_\downarrow(\mathbf{r})$, respectively. Substituting arrows by the spin index σ yields

$$\left[-\frac{\hbar^2}{2m_e}\nabla^2 + V^{\text{ext}}(\mathbf{r}) + \int d\mathbf{r}'\frac{e^2\rho(\mathbf{r}')}{|\mathbf{r}-\mathbf{r}'|} + V^{xc}(\mathbf{r})\right]\phi_{i\sigma}(\mathbf{r}) = \epsilon_{i\sigma}\phi_{i\sigma}(\mathbf{r}). \tag{2.67}$$

In the "Local Spin Density Approximation" (LSDA), Eq. 2.31 becomes

$$E^{xc}_{\text{LSDA}}[\rho_\uparrow(\mathbf{r}),\rho_\downarrow(\mathbf{r})] = \int d\mathbf{r}\rho(\mathbf{r})\epsilon^{xc}_{\text{UEG}}[\rho_\uparrow(\mathbf{r}),\rho_\downarrow(\mathbf{r})]. \tag{2.68}$$

Instead of using up and down densities, one can redefine the total electronic density $\rho(\mathbf{r}) = \rho_\uparrow(\mathbf{r}) + \rho_\downarrow(\mathbf{r})$ and introduce the local spin magnetisation $m(\mathbf{r}) = \mu_e[\rho_\uparrow(\mathbf{r}) - \rho_\downarrow(\mathbf{r})]$, with μ_e being the magnetic moment of an electron.

Effectively, the Kohn-Sham equations keep their form by using the total electron density and introducing a local magnetic field $B^{xc}(\mathbf{r}) = -\frac{\delta E^{xc}}{\delta m(\mathbf{r})}$:

$$\left[-\frac{\hbar^2}{2m_e}\nabla^2 + V^{\text{ext}}(\mathbf{r}) + \int d\mathbf{r}' \frac{e^2\rho(\mathbf{r}')}{|\mathbf{r}-\mathbf{r}'|} + \hat{V}^{xc}(\mathbf{r}) \mp \mu_e B^{xc}(\mathbf{r})\right] \phi_{i\uparrow/\downarrow}(\mathbf{r}) = \epsilon_{i\uparrow/\downarrow}\phi_{i\uparrow/\downarrow}(\mathbf{r}), \tag{2.69}$$

leading to the total energy

$$E = \sum_i \epsilon_i - \int d\mathbf{r} d\mathbf{r}' \frac{e^2\rho(\mathbf{r})\rho(\mathbf{r}')}{|\mathbf{r}-\mathbf{r}'|} + E^{xc} - \int d\mathbf{r}\rho(\mathbf{r})\hat{V}^{xc}(\mathbf{r}) + \int d\mathbf{r} B^{xc}(\mathbf{r})m(\mathbf{r}). \tag{2.70}$$

If the full spin-density matrix $\rho_{\sigma\sigma'}(\mathbf{r})$—instead of just considering "up" and "down" spins—the same substitution leads to the corresponding Kohn-Sham equations: $\rho_{\sigma\sigma'}(\mathbf{r})$ becomes $\rho(\mathbf{r}) = \text{Tr}[\rho_{\sigma\sigma'}(\mathbf{r})]$ with $\mathbf{m}(\mathbf{r}) = \mu_e \sum_{\sigma_1\sigma_2} \boldsymbol{\sigma}_{\sigma_1\sigma_2}\rho_{\sigma_1\sigma_2}(\mathbf{r})$, $\boldsymbol{\sigma}$ being a vector of the three Pauli matrices

$$\sigma_1 = \begin{bmatrix} 0 & 1 \\ 1 & 0 \end{bmatrix}, \quad \sigma_2 = \begin{bmatrix} 0 & -i \\ i & 0 \end{bmatrix}, \text{ and } \sigma_3 = \begin{bmatrix} 1 & 0 \\ 0 & -1 \end{bmatrix}, \tag{2.71}$$

resulting in

$$\left\{\left[-\frac{\hbar^2}{2m_e}\nabla^2 + V^{\text{ext}}(\mathbf{r}) + \int d\mathbf{r}' \frac{e^2\rho(\mathbf{r}')}{|\mathbf{r}-\mathbf{r}'|} + \hat{V}^{xc}(\mathbf{r})\right]\delta_{\sigma\sigma'} - \mu_e \mathbf{B}^{xc}(\mathbf{r})\boldsymbol{\sigma}_{\sigma\sigma'}\right\}\phi_{i\sigma'}(\mathbf{r}) = \epsilon_i\phi_{i\sigma}(\mathbf{r}). \tag{2.72}$$

Again, $\mathbf{B}^{xc}(\mathbf{r}) = -\frac{\delta E^{xc}}{\delta \mathbf{m}(\mathbf{r})}$ and $\hat{V}^{xc}(\mathbf{r}) = \frac{\delta E^{xc}}{\delta \rho(\mathbf{r})}$. A sum over σ' is implied and V^{xc} can have off-diagonal components. The total energy follows:

$$E = \sum_i \epsilon_i - \int d\mathbf{r} d\mathbf{r}' \frac{e^2 \rho(\mathbf{r})\rho(\mathbf{r}')}{|\mathbf{r}-\mathbf{r}'|} + E^{xc} - \int d\mathbf{r}\rho(\mathbf{r})\hat{V}^{xc}(\mathbf{r}) + \int d\mathbf{r}\mathbf{B}^{xc}(\mathbf{r})\mathbf{m}(\mathbf{r}). \tag{2.73}$$

A theory for noncollinear magnetism in plane-wave pseudopotentials was developed in the 1990s [175], where the magnetisation was allowed to relax as well as the atomic structures in a self-consistent manner. Further theories to model noncollinear magnetism in DFT codes have been developed for different schemes, such as for pseudopotentials or PAW approaches [176]. Within the atomic-sphere approach, the direction of the magnetic moment can be fixed for every sphere [177, 178]. In the full-potential linearised augmented-plane wave (FLAPW) scheme, the magnetisation density and exchange field are free to move and are described as vector fields, whereas within the almost-touching "muffin-tin" spheres, the axes are fixed [179, 180]. In the early 2000s, a vector-field like treatment of the magnetisation in PAW was developed [180–183].

The *xc*-functionals have been developed for collinear systems. Because the noncollinear implementations require a local reference frame at each spatial coordinate to render the magnetisation density and the *xc*-magnetic field collinear [177], only *local* functionals such as the LDA are properly suited to describe noncollinear magnetism. GGA functionals or other "semi-local" functionals were studied with respect to their applicability to noncollinear structures [184]; proper theories, however, are still in the development phase. Additions to the *xc*-functionals, such as exact-exchange functionals have been suggested [185], but require high computational effort. More elaborate theories have been proposed, but have yet to be implemented in modern DFT codes [186–188].

2.3.5 Orbital Magnetisation

The magnetic response of a material can originate from both spin and orbital magnetisation. The full orbital magnetisation is defined as the orbital moment per unit volume [189]:

$$\mathbf{M}^{\mathrm{orb}} = -\frac{e}{2cV}\sum_{i}^{\mathrm{occ}}\langle\Psi_i|\mathbf{r}\times\mathbf{v}|\Psi_i\rangle. \tag{2.74}$$

Here, $\mathbf{r}\times\mathbf{v}$ can be denoted as the circulation operator, and poses problems when dealing with periodic boundary conditions due to the unbounded $\mathbf{r}$ operator. In Refs. [190–193], it is demonstrated that the magnetisation can be expressed in terms of Bloch states, so that the nonperiodic nature of $\mathbf{M}$ in Eq. 2.74 can be handled [189, 194, 195].

In 2011, Coh *et al.* implemented one part of the orbital magnetisation in DFT and tested its influence on the ME coupling for different materials [196]. The complete approach to compute the orbital magnetisation was published in 2012 [197–199] (Chapter 3). The magnitude of the orbital contribution varies between the materials, but is negligible for, *e.g.* Cr_2O_3.

2.3.6 Relativistic Effects

Relativistic effects in solids, particularly for heavier atoms, manifest themselves, amongst others, in screening effects [200], spin-orbit coupling (SOC), and magneto-crystalline anisotropy. To get an understanding of SOC, one can imagine a change in radius of the electrons due to the relativistic mass increase according to

$$m = \frac{m_0}{\sqrt{1-(v^2/c^2)}}, \tag{2.75}$$

with m_0 being the rest mass, c being the speed of light, and v the speed of the electron. The mass changes the effective Bohr radius a_0:

$$a_0 = 4\pi\epsilon_0 \frac{\hbar^2}{me^2}. \tag{2.76}$$

In the case of Hg, the radius decreases by 23 %. Because of orthogonality constraints, the higher shells will also be effected by that change. Due to the contraction of the inner orbits, the effective potential for higher d- and f-electrons will be screened more efficiently.

The SOC is a relativistic effect, in which the electrons generate a magnetic field due to their radial motion, which in turn interacts with their magnetic spin. SOC leads to a shift in the energy levels of the atoms, and therefore, in solids, to a splitting of otherwise degenerate bands. The "Dirac" equation, the relativistically covariant form of the Schrödinger equation, uses four-component single-particle wavefunctions describing spin-$^1/_2$ particles, which can be decomposed into two-component spinors. Most effected though are the core electrons, so that an indirect treatment via pseudopotentials is possible [201–204]. These can be generated by solving the Dirac equation on single atoms [205, 206] and used when solving the non-relativistic Schrödinger equation for the whole solid.

Because spinors are required to include relativistic effects, calculations are performed using noncollinear magnetism. On the other hand, it is possible to employ the noncollinear formalism without the treatment of relativistic effects.

In this chapter, we have explored what first-principles models are used in the present thesis. How they are applied to model magnetoelectricity will be exemplified on the basis of Cr_2O_3, which will be covered in the next chapter.

3 Magnetoelectricity in the $\bar{3}'\mathrm{m}'$ Phase of Cr_2O_3

In the following chapter, the procedure to determine the full magnetoelectric (ME) tensor (the lattice and electronic part) in the ground-state $\bar{3}'m'$ phase of Cr_2O_3 will be explained. Firstly, the chapter serves as a validation for the remainder of the present thesis: the approaches employed in previous studies and in the present work will be discussed, the results compared, and the rationale behind the *ansatz* we chose outlined. We will show how symmetry analyses on grounds of group theory determine the form of the ME coupling tensor, the atomic Born effective charges, and the magnetic charges. The implemented first-principles routines will be illustrated and the methodology to obtain each ingredient of the ME response will be presented. In this chapter, the prototypical magnetoelectric Cr_2O_3 is used as a model material.

Secondly, possibilities and limitations of employing modern density functional theory (DFT) methods to model the ME response are examined on the basis of present results. The convergence behaviour of the most common local and semi-local exchange-correlation (*xc*-)functionals is discussed. Particularly interesting is the limit of tight convergence criteria for magnetic moments when noncollinear magnetism is employed. The results raise the question if the use of non-local functionals is valid when noncollinear magnetism is included in

the computation. In addition to numerical instabilities, we find predictions of different physical behaviours, such as higher-order coupling under strong magnetic fields. The choice of computational parameters turns out to be critical to predict the linear ME coupling tensor with quantitative accuracy. Correlations between the choice of the cell volume and the lattice-mediated part are revealed, as well as between the electronic band gap and the electronic part of the ME tensor.

3.1 Preliminaries

3.1.1 Group-Theory Analysis

As first mentioned in Section 1.2.1, only 58 out of the 122 magnetic point groups can show linear magnetoelectric responses due to symmetry considerations [59]. In this section, the actual form of the ME coupling tensor for Cr_2O_3 will be determined by analysing how its point group elements symmetrise the coupling tensor α. The theoretical introduction is to be found in Section 1.2.3. The analysis brings two insights: it can verify the results obtained by the DFT calculations and can give information about other magnetic point groups that could exhibit ME properties.

As a first step in the group-theory analysis, the magnetic point group needs to be determined from the combined *crystallographic* and *magnetic* structure. Time-reversal symmetry must be considered when transforming axial vectors to leave the magnetic symmetry invariant. Secondly, the transformation matrices of the magnetic point group are employed to define the structure of the magnetoelectric tensor.

Cr_2O_3 crystallises in the corundum-type structure shown in Fig. 1.13 and belongs to the crystallographic space group $R\bar{3}c$, which counts a 3- and

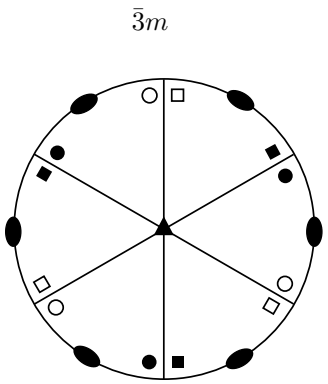
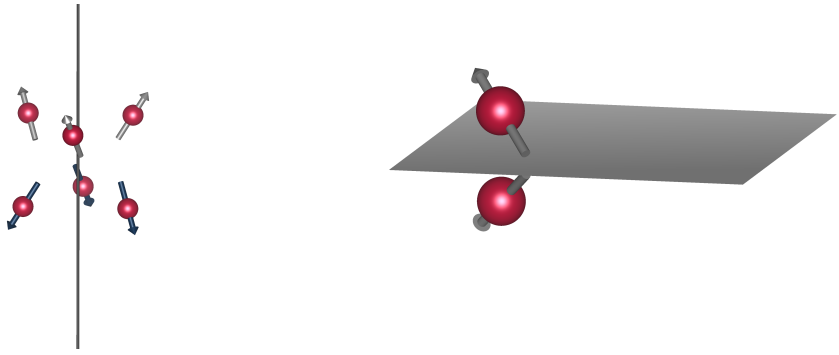


Figure 3.1: The stereographic projection of the Cr_2O_3 crystallographic point group $\bar{3}m$, modified from Refs. [57, 207]. In this point group, the two generating elements are $m \perp x$ and $\bar{3} \parallel z$.



(a) **(b)**

Figure 3.2: Visualisation of the two symmetry elements of AFM-G Cr_2O_3 (magnetic point group $\bar{3}'m'$). (**a**) Trigonal point group $\bar{3}'$, (**b**) monoclinic mirror transformation m'.

2-fold rotation, inversion, and a glide plane to its symmetry elements. The stereographic representation of its point group $\bar{3}m$ is shown in Fig. 3.1. When its AFM-G spin structure is taken into account, time reversal needs to be combined with both generating elements $\bar{3} \parallel z$ and $m \perp x$ in order to leave the configuration invariant, which is visualised in Fig. 3.2. Their corresponding transformation matrices are given in Table 3.1. The *magnetic* point group of Cr_2O_3 is thus $\bar{3}'m'$.

Let us now symmetrise the coupling tensor $\alpha = \alpha(\bar{3}'m')$ by applying the generating elements of $\bar{3}'m'$. Because the transformation should leave α invariant, the resulting matrix equals the one before the symmetrisation: $\alpha'_{ij} = \alpha_{ij}$.

Table 3.1: Transformation matrices T for the $\bar{3}$ and m operations, which are the symmetry elements of the AFM-G magnetic point group $\bar{3}'m'$ of Cr_2O_3.

$T(\bar{3} \parallel z)$	$T(m \perp x)$
$\begin{pmatrix} 1/2 & -\sqrt{3}/2 & 0 \\ \sqrt{3}/2 & 1/2 & 0 \\ 0 & 0 & -1 \end{pmatrix}$	$\begin{pmatrix} -1 & 0 & 0 \\ 0 & 1 & 0 \\ 0 & 0 & 1 \end{pmatrix}$

Because α is an axial tensor of rank two, it transforms as $\alpha'_{ij} = \pm\|T\|T_{ik}T_{jl}\alpha_{kl}$ (Section 1.2.3), taking into account time reversal and the determinant of the transformation matrix T. The first symmetry operation $m' \perp x$ transforms α in the following way:

$$\begin{aligned}
&\begin{pmatrix} \alpha'_{11} & \alpha'_{12} & \alpha'_{13} \\ \alpha'_{21} & \alpha'_{22} & \alpha'_{23} \\ \alpha'_{31} & \alpha'_{32} & \alpha'_{33} \end{pmatrix} \\
&= (-1)(-1) \begin{pmatrix} -1 & 0 & 0 \\ 0 & 1 & 0 \\ 0 & 0 & 1 \end{pmatrix} \begin{pmatrix} \alpha_{11} & \alpha_{12} & \alpha_{13} \\ \alpha_{21} & \alpha_{22} & \alpha_{23} \\ \alpha_{31} & \alpha_{32} & \alpha_{33} \end{pmatrix} \begin{pmatrix} -1 & 0 & 0 \\ 0 & 1 & 0 \\ 0 & 0 & 1 \end{pmatrix} \\
&= \begin{pmatrix} \alpha_{11} & -\alpha_{12} & -\alpha_{13} \\ -\alpha_{21} & \alpha_{22} & \alpha_{23} \\ -\alpha_{31} & \alpha_{32} & \alpha_{33} \end{pmatrix} \equiv \begin{pmatrix} \alpha_{11} & \alpha_{12} & \alpha_{13} \\ \alpha_{21} & \alpha_{22} & \alpha_{23} \\ \alpha_{31} & \alpha_{32} & \alpha_{33} \end{pmatrix},
\end{aligned} \tag{3.1}$$

where the first (second) sign-change is attributed to time reversal (the determinant of $T(m)$). The "$\equiv$" re-defines that the symmetrised tensor is equal to the original. The set of linear equations can only be true if $\alpha_{12} = \alpha_{13} = \alpha_{21} = \alpha_{31} = 0$. For the second symmetry operation, the new tensor is symmetrised under $\bar{3}' \parallel z$:

$$\begin{aligned}
&\begin{pmatrix} \alpha''_{11} & \alpha''_{12} & \alpha''_{13} \\ \alpha''_{21} & \alpha''_{22} & \alpha''_{23} \\ \alpha''_{31} & \alpha''_{32} & \alpha''_{33} \end{pmatrix} \\
&= (-1)(-1) \begin{pmatrix} 1/2 & \sqrt{3}/2 & 0 \\ -\sqrt{3}/2 & 1/2 & 0 \\ 0 & 0 & -1 \end{pmatrix} \begin{pmatrix} \alpha_{11} & 0 & 0 \\ 0 & \alpha_{22} & \alpha_{23} \\ 0 & \alpha_{32} & \alpha_{33} \end{pmatrix} \begin{pmatrix} 1/2 & -\sqrt{3}/2 & 0 \\ \sqrt{3}/2 & 1/2 & 0 \\ 0 & 0 & 1 \end{pmatrix}
\end{aligned}$$

$$= \begin{pmatrix} \left(\frac{1}{4}\alpha_{11} + \frac{3}{4}\alpha_{22}\right) & \left(-\frac{\sqrt{3}}{4}\alpha_{11} + \frac{\sqrt{3}}{4}\alpha_{22}\right) & \frac{\sqrt{3}}{2}\alpha_{13} \\ \left(\frac{\sqrt{3}}{4}\alpha_{11} - \frac{\sqrt{3}}{4}\alpha_{22}\right) & \left(\frac{3}{4}\alpha_{11} + \frac{1}{4}\alpha_{22}\right) & -\frac{1}{2}\alpha_{23} \\ \frac{\sqrt{3}}{2}\alpha_{32} & -\frac{1}{2}\alpha_{32} & \alpha_{33} \end{pmatrix} \equiv \begin{pmatrix} \alpha_{11} & 0 & 0 \\ 0 & \alpha_{22} & \alpha_{23} \\ 0 & \alpha_{32} & \alpha_{33} \end{pmatrix}.$$

In order for the last equation to be true, $\alpha_{11} = \alpha_{22}$ and $\alpha_{23} = \alpha_{32} = 0$. Therefore, the final ME coupling tensor for Cr_2O_3 has only two independent components and has the following shape:

$$\alpha = \begin{pmatrix} \alpha_{11} & 0 & 0 \\ 0 & \alpha_{11} & 0 \\ 0 & 0 & \alpha_{33} \end{pmatrix}, \tag{3.2}$$

in alignment with the tensor form for $\bar{3}'m'$ shown in Fig. 1.8 on page 40.

3.1.2 Existing Methodology

The approach in the previous chapter is purely phenomenological based on symmetry relations. In order to describe *how* the coupling can occur and be computed, we turn to the physical considerations used to study the coupling. There are various contributions to the ME response. One way to decompose the response is to split it into four parts: the lattice and the electronic response, α^{latt} and α^{el}, respectively, and the spin and orbital response. The former distinction represents the mechanism that makes the external field couple to the system, the latter represents the characteristics of the magnetic properties. Each part can be treated separately, and in the case of lattice-mediated response, can in turn be expressed by different microscopic contributions.

Most of the previous numerical work on the ME response has been done by two groups [164, 196, 197, 208–211]. In 2008, Iñíguez [164] modelled the lattice-mediated spin response to an external electric (magnetic) field via the infrared active phonon modes by means of their dielectric (magnetic) polarity. Bousquet *et al.* implemented an external Zeeman field and determined the

polarisation change via Berry phases, hence expanding α into the polarisation change with respect to the applied magnetic field and computing the gradient $^{\Delta\mathbf{P}}/_{\Delta\mathbf{H}}$ [210]. In 2012, all four contributions were determined via finite displacements through an external magnetic field by Malashevich *et al.* [197]. Ye *et al.* combined the first two approaches in 2014 and defined and computed the dynamical magnetic charges (MCs) as a factor of the lattice contribution, including the spin and orbital magnetisation for Cr_2O_3 [211].

Because the formalisms employed in the present thesis build on different parts of the aforementioned theories, it is important to outline the approaches in more detail. The "convenient" notation of bold vectors when forming derivatives, such as $^{\partial\mathbf{P}}/_{\partial\mathbf{u}} = {}^{\partial P_i}/_{\partial u_j}$, is commonly used in literature and in this thesis. For clarity, the present section introduces this notation by repeating key equations in both notations.

Íñiguez computed the spin-lattice response in Cr_2O_3 by calculating its behaviour under an electric field in terms of its of infrared (IR) modes [164].[1] The author determined the spin-lattice contribution via the dielectric polarity $\mathbf{p}_n^d$ of each IR mode n (the mode-decomposed Born effective charges), their magnetic analogue $\mathbf{p}_n^m$, and the mode eigenvalue C_n:

$$\alpha_{ij}^{\text{latt}} = \frac{1}{\Omega_0} \sum_{n=1}^{N_{IR}} \frac{p_{ni}^d p_{nj}^m}{C_n}, \tag{3.3}$$

where Ω_0 is the cell volume. The dielectric (magnetic) polarity of the n^{th} mode is defined by its induced polarisation (magnetisation):

[1] The author used VASP with the LDA+U scheme by Dudarev with $U_{\text{eff}} = 2\,\text{eV}$. Non-collinear magnetism and spin-orbit coupling (SOC) were considered for the response values, collinear structures for ground-state calculations. Orbital magnetism was not included.

$$\begin{aligned}\mathbf{P}^{\text{latt}} &= \frac{1}{\Omega_0}\sum_{n=1}^{N_{IR}} \mathbf{p}_n^d u_n, \\ \mathbf{M}^{\text{latt}} &= \frac{1}{\Omega_0}\sum_{n=1}^{N_{IR}} \mathbf{p}_n^m u_n,\end{aligned} \tag{3.4}$$

with u_n as the amplitude of mode n. In order to determine the $\alpha_\perp = \alpha_{11} = \alpha_{22}$ ($\alpha_\parallel = \alpha_{33}$) response, the modes active in the xy-plane (polarised along z) had to be taken into account. The results of $\alpha_\perp = 0.43\,\text{ps}\,\text{m}^{-1}$ matched the experimental results that range from $0.7\,\text{ps}\,\text{m}^{-1}$ to $1.56\,\text{ps}\,\text{m}^{-1}$ [21, 22, 87, 90, 91] (converted here from Gaussian to SI units); the longitudinal value however could not be reproduced (0.00, contrary to the experiments). The author concluded that the missing contribution to the ME coupling might be the electronic response to the field.

Indeed, a 2011 study from Bousquet *et al.*, in which the electronic contribution to α for Cr_2O_3 was determined [210], showed that it accounts for $1/4$ of the total value of $\alpha_\perp$ in Cr_2O_3. The authors implemented an external Zeeman magnetic field.[2] The polarisation was determined using the Berry phase approach whilst a magnetic field H was applied. α^{el} was obtained within clamped-ion calculations, α^{latt} as the resulting polarisation change when relaxation was allowed:

$$\boldsymbol{\alpha}^{\text{tot}} = \boldsymbol{\alpha}^{\text{el}} + \boldsymbol{\alpha}^{\text{latt}} = \left(\frac{\partial \mathbf{P}}{\partial \mathbf{H}}\right)\Big|_u + \left(\frac{\partial \mathbf{P}}{\partial \mathbf{H}}\right). \tag{3.5}$$

The corresponding coupling constants were determined (see Fig. 3.3), to be $\alpha^{\text{latt}} = 1.11\,\text{ps}\,\text{m}^{-1}$ and $\alpha^{\text{el}} = 0.34\,\text{ps}\,\text{m}^{-1}$, which agrees with experiments. The authors suggested to increase the spin-lattice coupling by non-relativistic

[2] The authors used the Dudarev implementation of LDA+U in VASP with $U_{\text{eff}} = 2\,\text{eV}$; SOC and noncollinear magnetism were included. The orbital contribution to the magnetisation was not taken into account. The lattice constant was fixed to the experimental value.

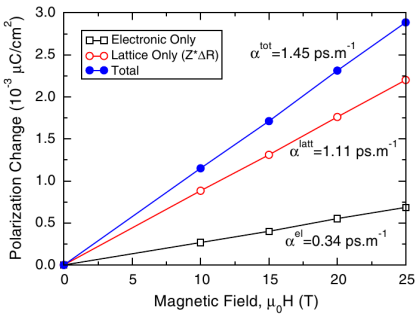


Figure 3.3: Polarisation change in Cr_2O_3 through lattice and electronic mediated responses. The electronically mediated polarisation makes up 1/4 of the total value [210].

mechanisms, in addition to the suggestion in Ref. [164] to destabilise the lattice to enhance soft polar modes.

With the theory developed by Coh *et al.* to include one part of the orbital ME response, namely the Chern-Simons orbital ME polarisability (CSOMP), the authors were able to apply their method to Cr_2O_3 [196].[3] The results were, as expected, negligible (the orbital contribution to $\alpha_\perp$ was less than 4 %) for the case of Cr_2O_3.[4] The authors concluded that topological insulators, with, *e.g.* gapped surfaces, could exhibit large orbital ME coupling.

The same group determined all four permutations, the spin-lattice, orbital-lattice, spin-electronic, and orbital-electronic part to α and hence computed the *full* ME response in Cr_2O_3 in 2012 [197]. For the lattice response, they used linear-response techniques to calculate the Born effective charges (BECs) and the interatomic force-constant (IFC) matrix to determine the atomic displacements with an electric field E applied:

[3] The LDA *xc*-potential was used, noncollinear magnetism included, and different strengths of SOC modelled.

[4] Other materials modelled were $BiFeO_3$, $GdAlO_3$, and Bi_2Se_3. The orbital part was similarly small for all but the $\mathbf{Z}_2$ topological insulator Bi_2Se_3.

$$(\alpha^{\text{latt}})^T = \mu_0 \frac{\partial \mathbf{M}}{\partial \boldsymbol{\epsilon}} = \mu_0 \frac{\partial \mathbf{M}}{\partial \mathbf{u}} \frac{\partial \mathbf{u}}{\partial \mathbf{F}} \frac{\partial \mathbf{F}}{\partial \boldsymbol{\epsilon}} = -\mu_0 \Omega_0 \frac{\partial \mathbf{M}}{\partial \mathbf{u}} \left(\frac{\partial^2 E}{\partial \mathbf{u} \partial \mathbf{u}} \right)^{-1} \left(\frac{\partial \mathbf{P}}{\partial \mathbf{u}} \right)^T,$$

$$\alpha^{\text{latt}}_{\nu\beta} = \mu_0 \frac{\partial M_\beta}{\partial \epsilon_\nu} = \mu_0 \frac{\partial M_\beta}{\partial u_i} \frac{\partial u_i}{\partial F_j} \frac{\partial F_j}{\partial \epsilon_\nu} = -\mu_0 \Omega_0 \frac{\partial M_\beta}{\partial u_i} \left(\frac{\partial^2 E}{\partial u_j \partial u_i} \right)^{-1} \frac{\partial P_\nu}{\partial u_j},$$

where the energy was substituted by the force derivative over the ionic positions and the Born effective charges by their equivalent definition $(\partial \mathbf{F}/\partial \boldsymbol{\epsilon})^T = \Omega_0 \partial \mathbf{P}/\partial \mathbf{u}$ according to Eq. 2.66. Field-induced displacements were calculated by an arbitrary, yet small enough to remain in the linear regime, electric field: $\Delta \mathbf{u} = (\partial \mathbf{u}/\partial \boldsymbol{\epsilon})\, \Delta \boldsymbol{\epsilon}$. Under this displacement, the change in magnetisation (spin and orbital) could be determined. For the electronic response α^{el}, an external electric field was coupled to the electrons, with fixed ions. The authors chose a finite-field approach and obtained $\Delta \mathbf{M}^{\text{spin}} + \Delta \mathbf{M}^{\text{orb}}$ with an applied electric field.[5]

The results showed that the orbital contribution to the transverse response $\alpha_\perp$, being of relativistic origin, is less than 2 %, whereas it makes up for half of the longitudinal response $\alpha_\parallel$, where the Heisenberg exchange is responsible for coupling at elevated temperatures. $\alpha_\parallel$ was predicted by experiments to be two orders of magnitude larger.

Following the work of Ref. [211], in which the lattice-mediated ME response for Cr_2O_3 was determined, the alternative definition of the ME tensor (see Eq. 1.6 on page 33) was expanded in the following way:

$$\alpha^{\text{latt}}_{\beta\nu} = \frac{\partial P_\beta}{\partial H_\nu} = \frac{\partial P_\beta}{\partial u_i} \frac{\partial u_i}{\partial H_\nu} = \frac{\partial P_\beta}{\partial u_i} \frac{\partial u_i}{\partial F_j} \frac{\partial F_j}{\partial H_\nu} = \frac{\partial P_\beta}{\partial u_i} \left(\frac{\partial u_j \partial u_i}{\partial^2 E} \right) \frac{\partial F_j}{\partial H_\nu}, \tag{3.6}$$

with F_j and E being the field-induced forces and total energy, respectively; β and $\nu \in \{1, 2, 3\}$; and the compound indices $i,\ j \in \{1x, 1y, 1z, 2x, ..., Nz\}$,

[5] SOC was considered and the PBE functional used, as opposed to the aforementioned studies, where LDA+U functionals were used, imposing the experimental lattice structure [164, 210].

with N being the number of atoms in the unit cell. The authors defined the "magnetic charges" Z^m in analogy to the Born effective charges and used the alternative definition, $Z^m_{j\nu} = \frac{\partial F_j}{\partial B_\nu} = \frac{\partial M_\nu}{\partial u_j}$, similar to the equivalent definitions of the Born effective charges. The changes of the magnetic moments with respect to ionic displacements were hence determined.

3.1.3 Implemented Formalism

The formalism employed in the present thesis makes use of Eq. 3.6 to compute the lattice-mediated ME tensor. The magnetic charges, however, are determined via $Z^m_{j\nu} = \frac{\partial F_j}{\partial B_\nu}$. The definitions read as

$$\begin{aligned} \boldsymbol{\alpha}^{\text{latt}} &= \left(\frac{\partial \mathbf{P}}{\partial \mathbf{u}}\right)\left(\frac{\partial^2 E}{\partial \mathbf{u}\partial \mathbf{u}}\right)^{-1}\left(\frac{\partial \mathbf{F}}{\partial \mathbf{H}}\right) \\ \Leftrightarrow \alpha^{\text{latt}}_{\beta\nu} &= \left(\frac{\partial P_\beta}{\partial u_i}\right)\left(\frac{\partial^2 E}{\partial u_i \partial u_j}\right)^{-1}\left(\frac{\partial F_j}{\partial H_\nu}\right) \qquad (3.7) \\ &= {}^1\!/\!_{\Omega_0}\ \underbrace{Z^e_{i\beta}}_{\text{BECs}}\ \underbrace{K^{-1}_{ij}}_{\substack{\text{Inverse of the} \\ \text{Force Constant Matrix}}}\ \underbrace{Z^m_{j\nu}}_{\substack{\text{Magnetic equivalent} \\ \text{of the BECs}}}. \qquad (3.8) \end{aligned}$$

The ME tensor is hence described by the force response of each atom upon applying an external magnetic field, the displacement of each atom upon these forces, and the resulting polarisation due to the internal displacements.

The electronic contribution is calculated via the clamped-ion change in polarisation with the external magnetic field according to Eq. 3.5. The polarisation is determined via Berry phases (Section 2.3.2). With this method, the lattice part can be determined when the ions are relaxed; the value for α^{latt} serves as a comparison to the one obtained by Eq. 3.8.

Both approaches require the implementation of an external magnetic field $\mu_0\mathbf{H}$. A uniform Zeeman field is applied to the Hamiltonian at every step of the

self-consistent cycle.[6] Following Ref. [210], the $\mu_0 \mathbf{H}\boldsymbol{\mu}_{\mathrm{tot}}$ shift in the Hohenberg-Kohn energy functional ($\boldsymbol{\mu}_{\mathrm{tot}}$ being the total magnetic moment of the system) leads to an additional term in the Kohn-Sham potential $\Delta V_{\sigma\sigma'}$ for each of the four spin manifolds:

$$\Delta V_{\sigma\sigma'} = \frac{g}{2}\mu_B\mu_0 \begin{pmatrix} H_z & H_x + iH_y \\ H_x - iH_y & -H_z \end{pmatrix}, \tag{3.9}$$

where g is the Landé factor and the σ are defined over the noncollinear spin density matrix as $n_{\sigma\sigma'}$. The routine is implemented in VASP and Quantum Espresso, so that we are able to apply the Zeeman field in the self-consistent field (scf) cycle.

Three density-functional theory codes are employed in the present thesis, namely the projector augmented-wave (PAW) [156] code "VASP" [212], "Quantum Espresso" [213] with norm-conserving pseudopotentials [148, 149], and—as a benchmark code—the all-electron full-potential linearised augmented-plane wave (FLAPW) [147] code "Elk" [214]. Non-collinear magnetism and spin-orbit coupling (SOC) are included if not otherwise stated. Convergence of the cutoff radius of the core augmentation charge and the fine-grid scale are ensured, where applicable. Because the behaviour of interest is of magnetic nature, not only the energy, but also the magnetic moments of the Cr atoms have to be precisely converged.

Since the Elk code only serves to benchmark structural, magnetic, and electronic parameters, not to model the full magnetoelectric response, a relatively low plane-wave cutoff energy of $8.0\,E_{\mathrm{h}}$ and an automatically generated Monkhorst-Pack k-point grid of $4 \times 4 \times 4$ suffice to converge the total energy to $\Delta E_{\mathrm{tot}} \leq 0.5\,\mathrm{meV}$ per atom. Because the magnetoelectric effect is an extremely subtle response, computational parameters have to be chosen more

[6] We thank M. Ye for the help with implementing the routine in VASP.

rigorously. For Quantum Espresso, a cutoff energy of 160 Ry $\simeq$ 2200 eV with a k-point mesh of $4 \times 4 \times 4$ is necessary to converge the magnetic moments to $1 \times 10^{-5}\,\mu_B$. For VASP a PAW dataset is used, explicitly treating the $3d$- and $4s$-electrons for Cr, and the $2s$- and $2p$-electrons for O as valence. The energy and magnetic moments are converged using a cutoff energy of 550 eV and a k-point spacing of $4 \times 4 \times 4$. In all cases, the k-point grid is shifted in order to model the Brillouin zone with the Γ-point in its centre.

Blöchl's corrections for the tetrahedron smearing method are employed with a broadening width of 0.05 eV. The structures are relaxed with the residual minimization method—direct inversion in the iterative subspace (RMM-DIIS) quasi-Newton algorithm [215]; a tight convergence criterion of $5 \times 10^{-6}\,\text{eV}\,\text{Å}^{-2}$ has to be chosen to account for the sensitive answer of the forces to the magnetic field. No symmetry constraints are used in the calculations.

We test the effect of different xc-functionals and employ the local density approximation (LDA), the generalised gradient approximation (GGA) with its implementation by Perdew, Burke, and Ernzerhof (PBE) [136], and by treating localised Cr d-orbitals with a Hubbard U on the LDA functional. The DFT+U implementation by Dudarev *et al.* is used [142]. We choose the value for U_{eff} to be 2.0 eV, but also test the dependence of the ME coupling on U in a regime from 0.5 eV to 2.0 eV (from Refs. [210, 216, 217]). The "functional of choice" for subsequent calculations, such as the electronic ME response, or studies of pressure or the "spinflop" phase in Cr_2O_3[7] (Chapters 4 and 6, respectively) is the LDA, as it provides a consistent implementation with noncollinear magnetism (Section 2.3.4) and because it resembles the ground-state properties of Cr_2O_3 well (Table 3.2).

[7] The spinflop phase of Cr_2O_3, with the Cr magnetic moments oriented in the basal plane, occurs at strong magnetic fields along the rhombohedral [111] direction.

To ensure convergence of the Hellman-Feynman forces and the magnetisation for the computation of the magnetic charges, the former are calculated at every 5^{th} *scf* step, the forces are printed with a precision of $1 \times 10^{-6}\,\text{eV}\,\text{Å}^{-1}$, and the magnetisation with a precision of $1 \times 10^{-8}\,\mu_\text{B}$.

This computational procedure is applied to the system of interest. Cr_2O_3 in its $\bar{3}'m'$ phase is the model material in the present thesis, for which we test the effect of different *xc*-functionals. The results will be presented in the next section.

3.2 Results

3.2.1 Ground-State Properties

In order to reliably predict the magnetoelectric phenomena in "novel" materials or configurations, the correct treatment of the systems at the DFT level has to be guaranteed. Therefore, we compare ground-state parameters with existing literature. In particular, the structural, magnetic, and electronic properties are validated, such as the rhombohedral lattice parameter and angle, the band gap, and the magnetic moment of the Cr atom.

A comparison is given in Table 3.2, where all three DFT codes are benchmarked against literature (experimental and computational) values. The present results comply well with the ones given in literature, particularly when using the same functional.[8] Where literature LDA (PBE) calculations predict a cell volume of $89.0\,\text{Å}^3$ ($98.7\,\text{Å}^3$), the present LDA (PBE) calculations yield $89.2\,\text{Å}^3$ ($96.7\,\text{Å}^3$ to $97.7\,\text{Å}^3$). Our LDA+U calculations also compare well to literature values with a value of $95.5\,\text{Å}^3$ and literature values of $95.0\,\text{Å}^3$ to $95.4\,\text{Å}^3$. Similarly good agreements were achieved for the Cr magnetic moment and the band gap when using the same functional. As expected

[8] The volume in particular shows little deviations (in the *per mille* regime), where the results for the rhombohedral lattice parameter and angle vary slightly more.

Table 3.2: Structural, electronic, and magnetic properties of Cr_2O_3 as determined with different codes and benchmarked against literature values. Lattice parameter a^{lat}, cell angle α^{cell}, cell volume V^{cell}, Cr magnetic moment M_{Cr}, and band gap E^{gap}. Numbers in parenthesis stand for the value obtained in calculations at the experimental cell volume. Missing cell volumes/cell angles in literature are added for consistency.

Details	a^{lat} [Å]	α^{cell}[°]	V^{cell}[Å^3]	M_{Cr} [μ_B]	E^{gap} [eV]
			Present work		
PBE, QE	5.42	54.4	97.7	2.27	1.8
PBE, Elk	5.35	55.2	96.7	2.37	1.0
PBE, VASP	5.42	54.3	97.6	2.67	1.7
PBESol, VASP	5.37	53.7	93.7	2.56	1.5
LDA, VASP	5.36	52.3	89.2	2.22 (2.49)	0.8 (1.4)
LDA+U, VASP	5.34	55.1	95.5	2.79 (2.76)	2.5 (2.5)
			Literature values		
LDA, QE [196]	5.32	53.0	89.0	2.0	1.3
LDA+U, Ref. [216][1]	5.37	54.3	95.0	2.8	2.8
B3LYP, Ref. [218][2]	5.43	58.6	86.2	2.9	3.0
LDA+U, Vasp [219][3]	5.34	55.1	95.4		3.4
GGA+U [220][4]	5.40	54.7	97.5	2.56	3.2
PBE, QE [197]	5.42	54.5	98.7	2.7	
sX hybrid [221]	5.39	55.1	98.1	3.52	3.3
LDA [222]	5.37	55.2	97.1	2.76	1.5
Exp. [223][5]				2.76	
Exp. [224][6]	5.36	55.1	96.5	2.65/2.31	

[1] $U_{\text{eff}} = 3.2\,\text{eV}$; [2] 10 % Hartree-Fock exchange contribution; [3] $U_{\text{eff}} = 3.5\,\text{eV}$; [4] $U_{\text{eff}} = 4.0\,\text{eV}$; [5] Neutron powder diffraction; [6] SQUID (Superconducting quantum interference device) measurements (Osiris/GEM diffractometer)

(Section 2.2.3), the band gaps are underestimated compared to the experimental value when neglecting correlation effects. Yet, they agree with other reported LDA and PBE values. The LDA+U calculations match the hybrid-functional results, as well as other LDA+U literature values.

As introduced in Section 2.3.4, the theory of noncollinear magnetism in DFT simulations is based on local densities, hence the LDA (or LDA+U when the correct treatment of the electronic band gap must be guaranteed) is the

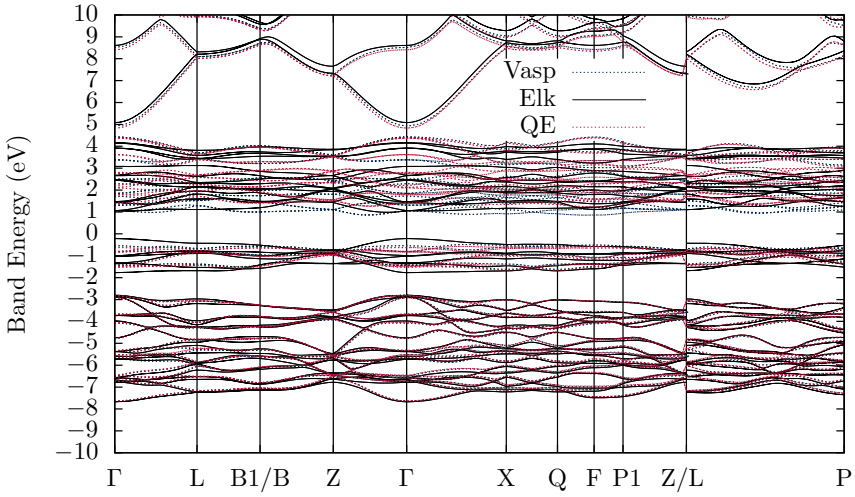


Figure 3.4: PBE bandstructure of Cr_2O_3 from VASP, Quantum Espresso (QE), and Elk calculations. Spin-orbit coupling is included.

functional of choice in the present thesis. However, as a benchmark to the PBE results in Ref. [211], we compare selected properties with our PBE calculations. A more thorough analysis of the influence of different *xc*-functionals will be given in Section 3.3.3.

To further ensure that the electronic properties of Cr_2O_3 are modelled correctly, the bandstructures and density of states (DOS) are determined and the effect of SOC studied (Figs. 3.4 and 3.5). Spin-orbit (scalar relativistic) pseudopotentials are employed to simulate the crystal with (without) SOC. All codes predict similar bandstructures. Fig. 3.5 shows close-ups of the conduction and valence states of Cr_2O_3 revealing the influence of SOC. A splitting of the energy levels can be seen; the global shift, however, remains small.

In order to compute the lattice-mediated response α^{latt} according to Eq. 3.8, we can now determine the three contributions: the interatomic force-constant matrix, the Born effective charges, and the magnetic charges.

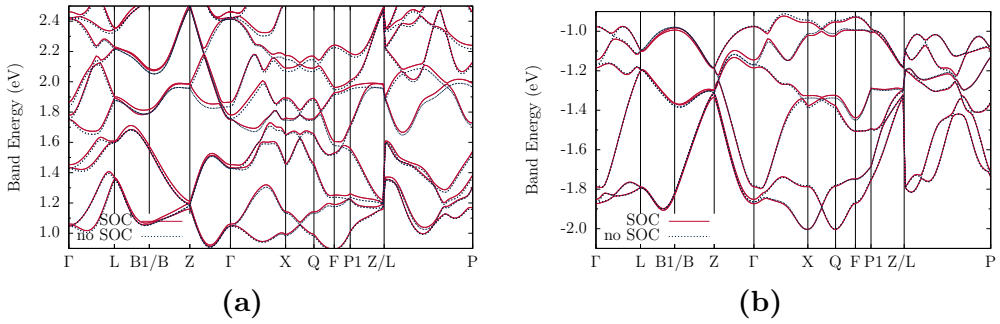


Figure 3.5: Influence of spin-orbit coupling on the Cr_2O_3 bandstructure. Close-ups of two sets of bands, the (**a**) conduction and (**b**) valence states, are shown. The dotted lines represent the calculations without spin-orbit coupling (using a scalar-relativistic pseudopotential and collinear magnetism), the solid lines correspond to calculations with SOC (using a spin-orbit pseudopotential and noncollinear magnetism).

3.2.2 Interatomic Force-Constant Matrix

The interatomic force-constant (IFC) matrix is determined via finite differences (FD) and via density functional perturbation theory (DFPT) (Section 2.3.1) to check numerical accuracy. VASP and Quantum Espresso results for the eigenfrequencies of the 6 IR active phonon modes (Section 3.1.1) are shown in Table 3.3.[9] The frequencies are in excellent agreement with each other: between different codes, methods, and literature values. In the remainder of this thesis, finite differences are used for phonon calculations.

3.2.3 Born Effective Charges

The shape of the Born effective charge (BEC) tensor can be obtained from the on-site symmetry of the respective atom. Because the BEC tensors are polar quantities, only the crystal symmetry—rather than the magnetic symmetry—has to be taken into account for the symmetrisation thereof. Polar tensors of rank two transform as $Z^{e'}_{ij} = T_{ik}T_{jl}Z^{e}_{kl}$ [60]. In the $\bar{3}m$ point group, the Wyckoff position of Cr is $4c$ with site symmetry 3 (a three-fold rotation around z).

[9] The IFC matrix of the 10-atomic unit cell of Cr_2O_3 consists of $(3 * 10) \times (3 * 10) = 900$ entries. A sufficient comparison is based on selected phonon frequencies, since the eigenvalues of the dynamical matrix are mapped onto the frequencies.

Table 3.3: Comparison of the IR active mode frequencies for Cr_2O_3, from finite differences (FD) calculations in VASP, and density functional perturbation theory (DFPT) in Quantum Espresso (QE) and VASP. Literature values are based on Ref. [211]. The frequencies are given in cm^{-1}.

Code and method	E_u modes	A_{2u} modes
QE (DFPT)	289, 416, 496, 586	395, 498
VASP (DFPT)	288, 418, 494, 592	382, 504
VASP (FD)	289, 418, 494, 592	382, 504
QE (FD), Ref. [211]	297, 427, 510, 610	388, 522

Table 3.4: Transformation matrices T for the 2 and 3 operations, which are the symmetry elements of the 6e and 4c general positions of Cr_2O_3, respectively.

$T(2 \parallel x)$	$T(3 \parallel z)$
$\begin{pmatrix} 1 & 0 & 0 \\ 0 & -1 & 0 \\ 0 & 0 & -1 \end{pmatrix}$	$\begin{pmatrix} -1/2 & \sqrt{3}/2 & 0 \\ -\sqrt{3}/2 & -1/2 & 0 \\ 0 & 0 & 1 \end{pmatrix}$

The O atom is located at Wyckoff position 6e with site symmetry 2 (two-fold rotation around x). The transformation matrices are given in Table 3.4. Let us symmetrise the BEC tensor of Cr in Cr_2O_3, Z^e(Cr) (conveniently expressed as "Z"):

$$\begin{pmatrix} Z'_{11} & Z'_{12} & Z'_{13} \\ Z'_{21} & Z'_{22} & Z'_{23} \\ Z'_{31} & Z'_{32} & Z'_{33} \end{pmatrix} = \begin{pmatrix} -1/2 & -\sqrt{3}/2 & 0 \\ \sqrt{3}/2 & -1/2 & 0 \\ 0 & 0 & 1 \end{pmatrix} \begin{pmatrix} Z_{11} & Z_{12} & Z_{13} \\ Z_{21} & Z_{22} & Z_{23} \\ Z_{31} & Z_{32} & Z_{33} \end{pmatrix} \begin{pmatrix} -1/2 & \sqrt{3}/2 & 0 \\ -\sqrt{3}/2 & -1/2 & 0 \\ 0 & 0 & 1 \end{pmatrix}$$

$$= \begin{pmatrix} \frac{1}{4}\left(Z_{11}+3Z_{22}+\sqrt{3}Z_{21}+\sqrt{3}Z_{12}\right) & \frac{1}{4}\left(Z_{12}-3Z_{21}-\sqrt{3}Z_{11}+\sqrt{3}Z_{22}\right) & -\frac{1}{2}\left(Z_{13}-\sqrt{3}Z_{23}\right) \\ \frac{1}{4}\left(Z_{21}-3Z_{12}-\sqrt{3}Z_{11}+\sqrt{3}Z_{22}\right) & \frac{1}{4}\left(Z_{22}+3Z_{11}-\sqrt{3}Z_{12}-\sqrt{3}Z_{21}\right) & \frac{1}{2}\left(\sqrt{3}Z_{13}-Z_{23}\right) \\ -\frac{1}{2}\left(Z_{31}-\sqrt{3}Z_{32}\right) & \frac{1}{2}\left(\sqrt{3}Z_{31}-Z_{32}\right) & Z_{33} \end{pmatrix}$$

$$\equiv \begin{pmatrix} Z_{11} & Z_{12} & Z_{13} \\ Z_{21} & Z_{22} & Z_{23} \\ Z_{31} & Z_{32} & Z_{33} \end{pmatrix}. \tag{3.10}$$

Table 3.5: Tensor forms of the BEC tensor and the magnetic charge tensor for Cr at Wyckoff position 4*c* (left panel) and O at position 6*e* (right panel).

Cr	O
$\begin{pmatrix} Z_{11} & Z_{12} & 0 \\ -Z_{12} & Z_{11} & 0 \\ 0 & 0 & Z_{33} \end{pmatrix}$	$\begin{pmatrix} Z_{11} & 0 & 0 \\ 0 & Z_{22} & Z_{23} \\ 0 & Z_{32} & Z_{33} \end{pmatrix}$

Solving the nine equations results in $Z_{13} = Z_{31} = Z_{23} = Z_{32} = 0$, $Z_{21} = -Z_{12}$, and $Z_{22} = Z_{11}$, in turn leading to the final form of the BEC tensor for Cr, shown in the left panel of Table 3.5.

The same procedure is used to symmetrise the BEC for the O atom with site symmetry 2, $Z^e(\mathrm{O})$ (in the following again "Z"):

$$\begin{pmatrix} Z'_{11} & Z'_{12} & Z'_{13} \\ Z'_{21} & Z'_{22} & Z'_{23} \\ Z'_{31} & Z'_{32} & Z'_{33} \end{pmatrix} = \begin{pmatrix} -1 & 0 & 0 \\ 0 & 1 & 0 \\ 0 & 0 & 1 \end{pmatrix} \begin{pmatrix} Z_{11} & Z_{12} & Z_{13} \\ Z_{21} & Z_{22} & Z_{23} \\ Z_{31} & Z_{32} & Z_{33} \end{pmatrix} \begin{pmatrix} -1 & 0 & 0 \\ 0 & 1 & 0 \\ 0 & 0 & 1 \end{pmatrix}$$

$$= \begin{pmatrix} Z_{11} & -Z_{12} & -Z_{13} \\ -Z_{21} & Z_{22} & Z_{23} \\ -Z_{31} & Z_{32} & Z_{33} \end{pmatrix} \equiv \begin{pmatrix} Z_{11} & Z_{12} & Z_{13} \\ Z_{21} & Z_{22} & Z_{23} \\ Z_{31} & Z_{32} & Z_{33} \end{pmatrix}, \tag{3.11}$$

which can only hold true if $Z_{12} = Z_{13} = Z_{21} = Z_{31} = 0$, leading to the symmetrised tensor shown in the right panel of Table 3.5.

The actual calculation of the BECs is based on the theory described in Section 2.3.3. Both the $\frac{\partial \mathbf{P}}{\partial \mathbf{u}}$ and $\frac{\partial \mathbf{F}}{\partial \boldsymbol{\epsilon}}$ approaches are employed and compared to literature values. The Quantum Espresso and VASP results are given in Tables 3.6 and 3.7, for the Cr and O atom at Wyckoff position 4*c* and 6*e*, respectively. The $\frac{\partial \mathbf{P}}{\partial \mathbf{u}}$ and $\frac{\partial \mathbf{F}}{\partial \boldsymbol{\epsilon}}$ approaches lead to identical results considering the precision given and are therefore only printed once. The results are in excellent agreement with each other and with literature values, as well as with the symmetry constraints from Table 3.5.[10]

[10]The correct Wyckoff positions of the atoms and the shape and size of the modelled unit

Table 3.6: Born effective charges of the Cr atom in Cr_2O_3. Quantum Espresso (QE) and VASP results are compared to the QE results from Ref. [211] (the zero-by-symmetry elements in Ref. [211] are all reported as 0). All tensors given in e.

QE	VASP	Ref. [211]
$\begin{pmatrix} 3.00 & -0.31 & 0.00 \\ 0.31 & 3.00 & 0.00 \\ 0.00 & 0.00 & 3.21 \end{pmatrix}$	$\begin{pmatrix} 2.92 & -0.36 & 0.00 \\ 0.36 & 2.92 & 0.00 \\ 0.00 & 0.00 & 3.18 \end{pmatrix}$	$\begin{pmatrix} 3.02 & -0.30 & 0 \\ 0.30 & 3.02 & 0 \\ 0 & 0 & 3.18 \end{pmatrix}$

Table 3.7: Born effective charges of the O atom in Cr_2O_3. Quantum Espresso (QE) and VASP results are compared to the QE results from Ref. [211] (the zero-by-symmetry elements in Ref. [211] are all reported as 0). All tensors given in e.

QE	VASP	Ref. [211]
$\begin{pmatrix} -2.33 & 0.00 & 0.00 \\ 0.00 & -1.60 & -1.01 \\ 0.00 & -0.87 & -2.10 \end{pmatrix}$	$\begin{pmatrix} -2.36 & 0.00 & 0.00 \\ 0.00 & -1.53 & -1.05 \\ 0.00 & -0.92 & -2.12 \end{pmatrix}$	$\begin{pmatrix} -2.36 & 0 & 0 \\ 0 & -1.66 & -1.00 \\ 0 & -0.88 & -2.12 \end{pmatrix}$

3.2.4 Magnetic Charges

The third term in the ME coupling tensor expansion is the dynamical-magnetic charge tensor. As introduced in Eq. 3.8, it is calculated by the forces induced on each atom (polar rank-one tensor with $3N$ elements, where N is the number of atoms) with respect to the applied magnetic field (axial rank-one tensor with 3 elements for the Cartesian directions). The magnetic charges Z^m are thus axial rank-two tensors with $3 \times 3N$ elements, and therefore transform as $Z_{ij}^{m'} = \pm\|T\|T_{ik}T_{jl}Z_{kl}^{m}$ [60] under a transformation T, accounting for time reversal with $\pm$. Because the generating elements of $\bar{3}'m'$ ($\bar{3}'$ and m') are improper rotations that couple to time-reversal symmetry, the sign change of the determinant and

cell influence the BECs dramatically, whence we conclude that a carefully converged structure is crucial for the computation not only of the magnetic charges, but also of the Born effective charges.

time reversal cancel each other out and the transformations are equal to the ones for the BECs. The MC tensors are therefore of the same form as the BEC tensors (Table 3.5). If we label the bottom Cr in the first structural unit of Cr_2O_3 as Cr_1 and the O atom on the two-fold axis of the same unit as O_1 (see Fig. 1.13), we can derive the other magnetic charge tensors of the Cr (O) atoms by mirror or rotation operations of $Z^m(Cr_1)$ ($Z^m(O_1)$).

As expected, the PBE calculations exhibit convergence problems when a small energy threshold of 10^{-9} eV is approached. This leads to noisy force responses, so that strong magnetic fields of up to 200 T have to be applied to see a measurable response. The LDA calculations, however, are stable in all regimes. The full force response on the high-symmetry Cr atom for PBE and LDA calculations can be seen in Fig. 3.6, where a magnetic field is applied in x-direction. The following observations can be made: firstly, higher-order coupling becomes apparent and manifests itself in the quadratic F_z-responses, which is to be expected for magnetic fields of that magnitude. Secondly, the nonlinear forces occur for ΔF_z, corresponding to the zx-component in the linear magnetic charges, and which should be zero by symmetry. Thirdly, the non-linear behaviour is about an order of magnitude larger for the PBE.

A decomposition into odd and even terms separates the linear and quadratic responses. Fig. 3.7 (Fig. 3.8) shows the PBE (LDA) behaviour after the decomposition. The remaining odd terms are purely linear and zero for the terms that should be zero by symmetry. The LDA data does not exhibit any noise even at small magnetic fields. For the PBE, we choose values of $B = 200$ T to compute the magnetic-charge tensors, as the field is strong enough to get data outside the noise-regime, but still small enough that no cubic or higher-order coupling terms occur. The LDA answers are constant over the field-range.

To determine all MC tensors, a magnetic field is applied in all directions, and the change in forces is measured for all atoms. The PBE results are shown

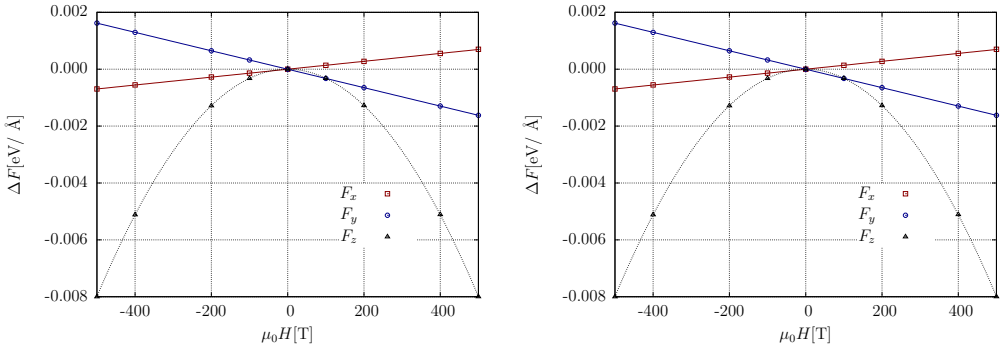


Figure 3.6: Ionic forces ΔF on the Cr atom in Cr_2O_3 at high magnetic fields $\mu_0 H$ in x-direction by (**a**) PBE and (**b**) LDA calculations. A quadratic behaviour becomes obvious, which is negligible at low fields and only arises for components whose linear part should be zero by symmetry, such as the zx-component in Cr. F_x and F_y data are joined by linear fits, F_z by a quadratic fit.

Table 3.8: Dynamical magnetic charges Z^m of the Cr atom in Cr_2O_3 with PBE compared to Ref. [211]. All tensors are given in $10^{-2}\,\mu_B/Å$. The values are in excellent agreement with the literature (the zero-by-symmetry elements in Ref. [211] are all reported as 0).

This work	Ref. [211]
$\begin{pmatrix} 5.10 & -5.12 & 0.00 \\ 5.12 & 5.10 & 0.00 \\ 0.00 & 0.00 & 0.02 \end{pmatrix}$	$\begin{pmatrix} 5.88 & -5.69 & 0 \\ 5.69 & 5.88 & 0 \\ 0 & 0 & 0.02 \end{pmatrix}$

in Tables 3.8 and 3.9 for the high-symmetry Cr and O atoms, respectively. The results can be compared on a quantitative and group-theoretical basis and correspond well to each other. A full comparison between the functionals follows in the next Section 3.3.3.

3.3 Analysis

3.3.1 Lattice Response

Now that every component of Eq. 3.6 is determined confidently, the lattice-mediated magnetoelectric coupling can be expressed in the basis of the Cr_2O_3 IR active modes, and determined via

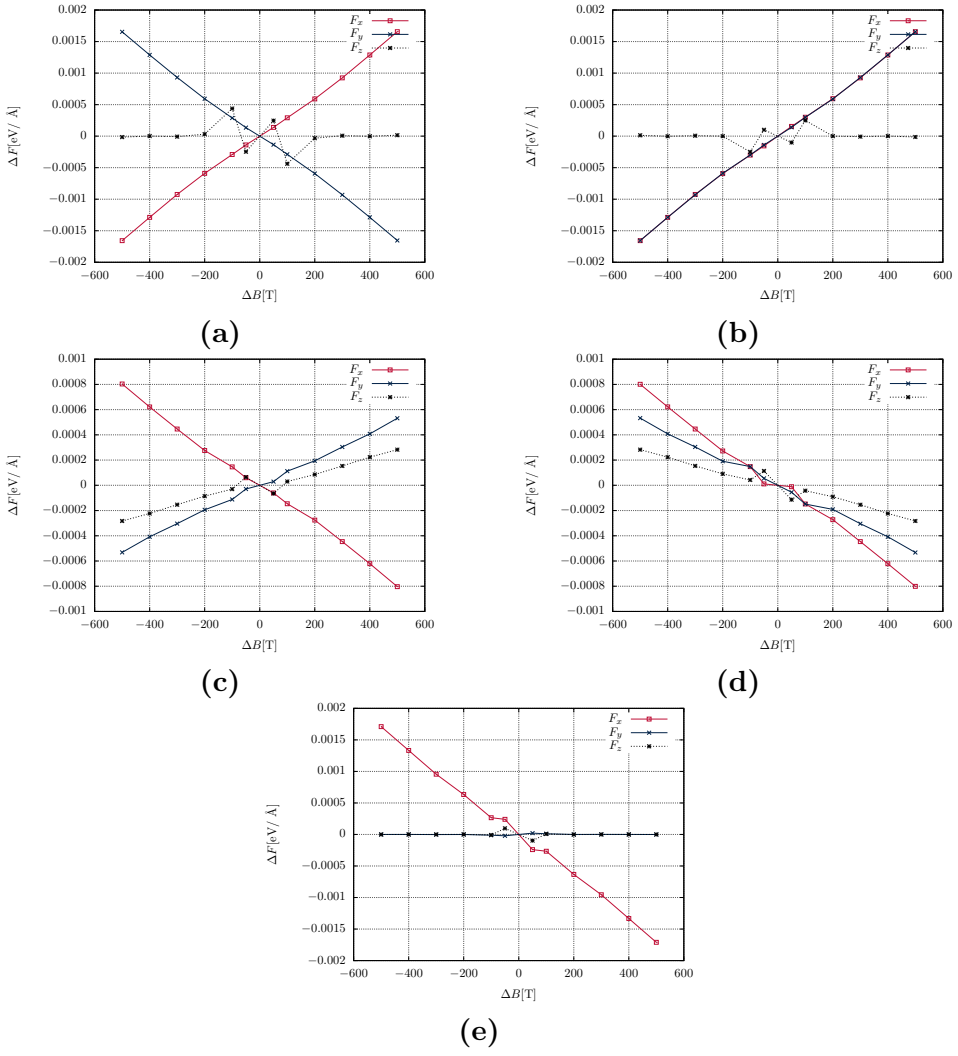


Figure 3.7: Odd decomposition of the force response in Cr_2O_3 towards a magnetic field $\mu_0 H_x$ in x-direction from PBE calculations. (**a**) shows atoms Cr_1 and Cr_4 at the high-symmetry position $4c$ (notation in Fig. 1.13), (**b**) their rotated images (linked by $2 \parallel x$), *i.e.* Cr_2 and Cr_3, (**c**) and (**d**) show the remaining two O atoms in the formula units of the high-symmetry O_1 and O_2 atoms in (**e**), and can thus be obtained by a 120° and 240° rotation around z from its tensor. The non-linear terms were purely quadratic and no cubic terms can be observed. The Z^m tensors can be determined by the gradient $\frac{\partial F_j}{\partial H_\nu}$ for each position independently, or by the symmetry operations from the high-symmetry Cr and O positions.

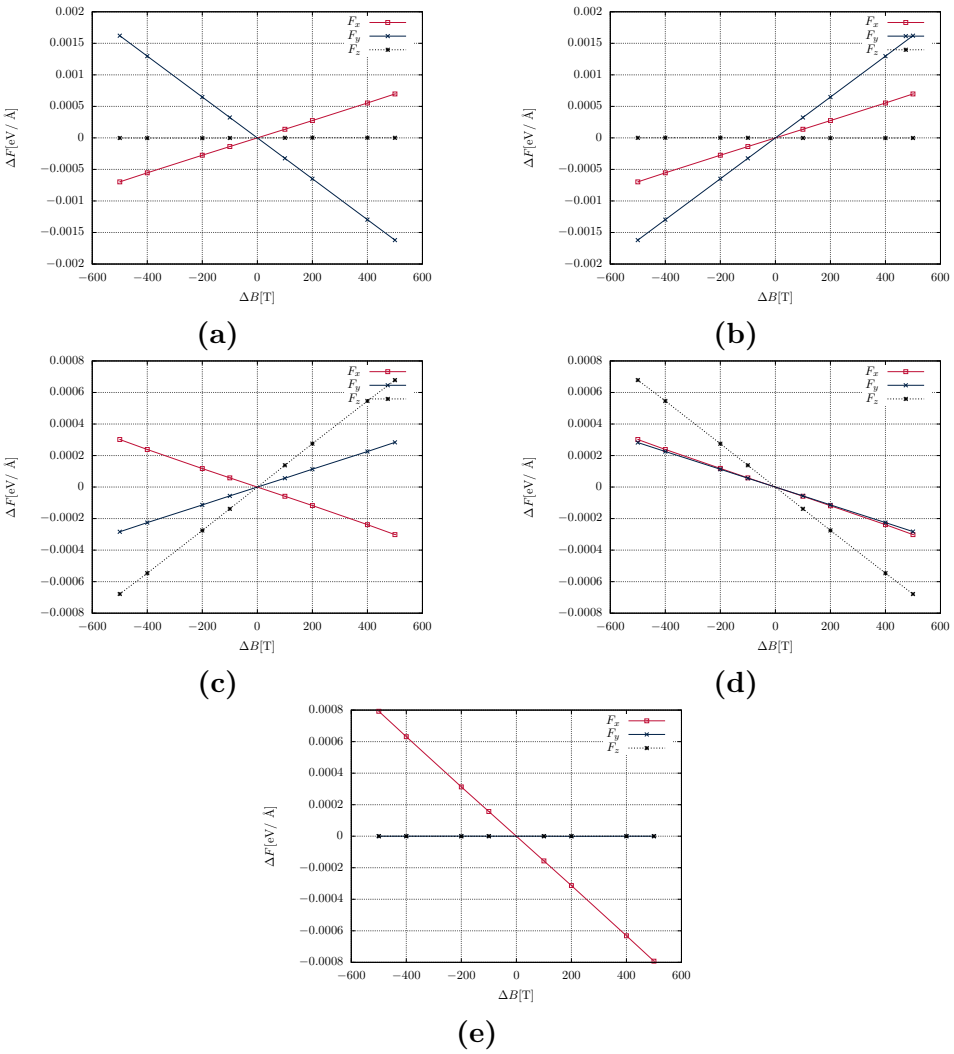


Figure 3.8: Odd decomposition of the force response in Cr_2O_3 towards a magnetic field in x-direction within the LDA. The order is equivalent to that of Fig. 3.7: Cr_1 and Cr_4 atoms at the high-symmetry position $4c$ in (**a**), Cr_2 and Cr_3 in (**b**), O atoms linked by 120° to O_1 and O_2 in (**c**), and O atoms linked by 240° in (**d**). The high-symmetry O_1 and O_2 atoms are shown in (**e**). As opposed to the PBE results in Fig. 3.7, the LDA data is stable even at low magnetic fields.

Table 3.9: Dynamical magnetic charges Z^m of the O atom in Cr_2O_3 with PBE compared to Ref. [211]. All tensors are given in $10^{-2}\,\mu_B/Å$. The values correspond well with literature (the zero-by-symmetry elements in Ref. [211] are all reported as 0).

This work	Ref. [211]
$\begin{pmatrix} -5.91 & 0.00 & 0.00 \\ 0.00 & -1.71 & 0.00 \\ 0.00 & -1.14 & -0.04 \end{pmatrix}$	$\begin{pmatrix} -5.92 & 0 & 0 \\ 0 & -1.95 & 0.00 \\ 0 & -1.10 & -0.02 \end{pmatrix}$

$$\alpha_{\perp} = \sum_{i}^{N_{\perp}} Z_i^e * Z_i^m / C_i,$$
$$\alpha_{\parallel} = \sum_{i}^{N_{\parallel}} Z_i^e * Z_i^m / C_i, \tag{3.12}$$

where the summations run over all IR active transversal and longitudinal modes, $N_{\perp}$ and $N_{\parallel}$, respectively. C_i are the corresponding eigenvalues of the IFC matrix.

Determining Φ^{-1}, the inverse of the IFC matrix, is nontrivial. The 3 acoustic and other nearly-zero modes lead to singularities when forming the inverse. The "pseudoinverse" approach, as first introduced in Ref. [225], is therefore employed. An acoustic subspace of dimension 3×3 and an optical $(3N-3) \times (3N-3)$-dimensional subspace are constructed and inverted separately, with soft modes being treated with vanishing frequencies. As a first step, the original IFC matrix is symmetrised to account for numerical inaccuracies. Next, an orthogonal $3N \times 3N$ matrix U is built from the eigenvectors of Φ, with its upper 3×3 matrix corresponding to the 3 translational modes. By forming $U^T \Phi U = \Phi'$, a pseudo matrix is constructed, with acoustic and optical subspaces: the latter can easily be inverted (by determining $\Phi^{-1} = U^T (\Phi')^{-1} U$) and the former is inverted by setting the soft-mode frequencies to zero. The two submatrices are combined into a joint matrix, called the "pseudoinverse". In the following, when we mention Φ^{-1} or the IFC matrix inverse, we construct and talk of the pseudoinverse of Φ. By identifying the mode symmetries, the corresponding eigenvalues of Φ can be mapped onto the modes of the pseudoinverse, yielding the C_i for Eq. 3.12.

Expressing the Born effective charges and the dynamical magnetic charges in the basis of the IR active modes is a powerful tool to evaluate how dipole moments and magnetic moments change under a certain vibrational mode.

The decomposition leads to the PBE results shown in Tables 3.10 and 3.11. The values for the E_u modes, the four doubly degenerate modes, are shown in the first panel (showing the change in the electric/magnetic dipole moment as a vector for each mode), the results for the two singly degenerate A_{2u} modes are given below. It can be seen that the former belong to E_u symmetry, active in the xy-plane, and the latter to A_{2u} symmetry, active in z-direction. The right panel shows the value of each mode contribution as its norm. Since a direction is yet undefined, let us define the changes in dipole moments to be positive; the magnetic charges will be given relative to the former. In this case, out of the six modes, the BECs for the ${E_u}^{1,2}$ and ${A_{2u}}^{1,2}$ modes point in the same direction as their magnetic charges, making their absolute values positive. The ${Z^e_{E_u}}^{3,4}$ and ${Z^m_{E_u}}^{3,4}$ point in opposite directions, leading to the negative sign in the magnetic answer. The results are in good agreement with literature values, particularly for the higher frequencies, which lie within $\pm 3\,\%$ ($\pm 10\,\%$) around the BEC (MC) literature values given in Ref. [211]. Fluctuations for the soft modes are due to the small magnitude of the responses, particularly for the longitudinal part of the magnetic charges. However, the deviating terms are one order of magnitude smaller, resulting in negligible effects on the coupling tensor (Table 3.12).

With the eigenvalues from Table 3.3 and the results from Tables 3.10 and 3.11, Equation 3.12 can be evaluated. The results are displayed in Table 3.12. The hard modes (${E_u}^{1,2}$) contribute most to the overall transverse part of the tensor. The softer modes lead to a small cancellation of the response of the hard modes. However, their BEC and MC contribution is about an order of magnitude smaller than for the positively contributing modes: the soft-mode BECs are $0.19\,e$ and $0.78\,e$ compared to $6.80\,e$ and $3.77\,e$; the MCs are also smaller with $-3.65 \times 10^{-2}\,\mu_\mathrm{B}/\text{Å}$ and $-0.01 \times 10^{-2}\,\mu_\mathrm{B}/\text{Å}$ compared to the hard modes $9.47 \times 10^{-2}\,\mu_\mathrm{B}/\text{Å}$ and $14.92 \times 10^{-2}\,\mu_\mathrm{B}/\text{Å}$. The cancellation is thus negligible. Both $\alpha_\perp$ and $\alpha_\parallel$ are in excellent agreement with Ref. [211].

Table 3.10: Comparison of the mode decomposition of the Born effective charges Z^e for Cr_2O_3 with PBE, excluding the acoustic modes. Literature values are based on Ref. [211]. The BECs are given in e. The values are in excellent agreement with literature values, particularly for the hard modes. The difference in the dipole response of soft modes can be ascribed to their small overall magnitude and do not have a strong impact on the overall ME tensor, as seen in Table 3.12.

Mode	Z^e vector(s)	Z^e value (Ref. [211])
${E_u}^1$	(6.76, 0.72, 0.00), (0.72, -6.76, 0)	6.80 (7.07)
${E_u}^2$	(-0.02, -3.77, 0.00), (3.77, -0.02, 0)	3.77 (3.71)
${E_u}^3$	(-0.17, -0.09, 0.00), (-0.09, 0.17, 0)	0.19 (0.39)
${E_u}^4$	(-0.03, 0.78, 0.00), (0.78, 0.03, 0)	0.78 (0.55)
${A_{2u}}^1$	(0.00, 0.00, 8.55)	8.55 (8.50)
${A_{2u}}^2$	(0.00, 0.00, 1.00)	1.00 (1.15)

Table 3.11: Comparison of the mode decomposition of the dynamical magnetic charges Z^m for Cr_2O_3 with PBE, excluding the acoustic modes. Literature values are based on Ref. [211]. The magnetic charges are given in $10^{-2}\,\mu_B/Å$. As for the BECs, the hard modes match the literature values perfectly. The deviating terms are comparatively small, leading to a negligible impact on the overall ME tensor (see Table 3.12).

Mode	Z^m vector(s)	Z^m value (Ref. [211])
${E_u}^1$	(9.42, 1.01, 0.00), (1.01, -9.42, 0)	9.47 (10.55)
${E_u}^2$	(-0.07, -14.92, 0.00), (14.92, -0.07, 0)	14.92 (16.14)
${E_u}^3$	(3.19, 1.77, 0.00), (1.77, -3.19, 0)	-3.65 (-3.97)
${E_u}^4$	(0.00, 0.01, 0.00), (0.01, 0.00, 0)	-0.01 (-0.76)
${A_{2u}}^1$	(0.00, 0.00, 0.06)	0.06 (0.05)
${A_{2u}}^2$	(0.00, 0.00, 0.04)	0.04 (0.02)

Table 3.12: Mode contribution to α^{latt} for Cr_2O_3 using the PBE functional. Acoustic modes were excluded. The Born effective charges Z^e are given in e, the magnetic charges Z^m in $10^{-2}\,\mu_B/\text{Å}$, the eigenvalues C in $\text{eV}\,\text{Å}^{-2}$, and the coupling tensor α^{latt} in $\text{ps}\,\text{m}^{-1}$.

Mode	Z^e	Z^m	C	α
${E_u}^1$	6.80	9.47	29.40	0.263
${E_u}^2$	3.77	14.92	18.70	0.361
${E_u}^3$	0.19	-3.65	15.30	-0.005
${E_u}^4$	0.78	-0.01	9.80	-0.000
$\alpha_\perp$				0.618
$\alpha_\perp$ [211]				0.633
${A_{2u}}^1$	8.55	0.06	21.40	0.003
${A_{2u}}^2$	1.00	0.02	10.30	0.001
$\alpha_\parallel$				0.004
$\alpha_\parallel$ [211]				0.0024

3.3.2 Electronic Response

In order to determine the electronic part of the ME tensor, the change in polarisation P with an external magnetic field $\mu_0 H$ is computed according to Eq. 3.5. Clamped-ion calculations lead to α^{el}; after the ionic relaxation $\partial\mathbf{P}/\partial\mathbf{H}$ yields α^{tot}. The difference in polarisation is used to determine the value for α^{latt}. We employ the local density approximation and—for comparison with the magnetic charges from Section 3.2.4—apply fields up to 200 T.

Fig. 3.9 shows the change in polarisation over the magnetic field. The transverse responses, α_{xx} and α_{yy}, are shown for fixed (α^{el}) and relaxed (α^{tot}) ionic positions. Both the total and the electronic zz parts, as well as off-diagonal terms, are zero. Again, the LDA describes the behaviour as purely linear even up to high magnetic-field strengths. The results comply with the symmetry analysis and yield $\alpha_{xx} = \alpha_{yy}$.

The gradients equal the respective values for the ME tensor components: $\alpha_\perp^{\text{el}} = 0.553\,\text{ps}\,\text{m}^{-1}$ and $\alpha_\perp^{\text{latt}} = (0.826 - 0.553)\text{ps}\,\text{m}^{-1} = 0.273\,\text{ps}\,\text{m}^{-1}$. The

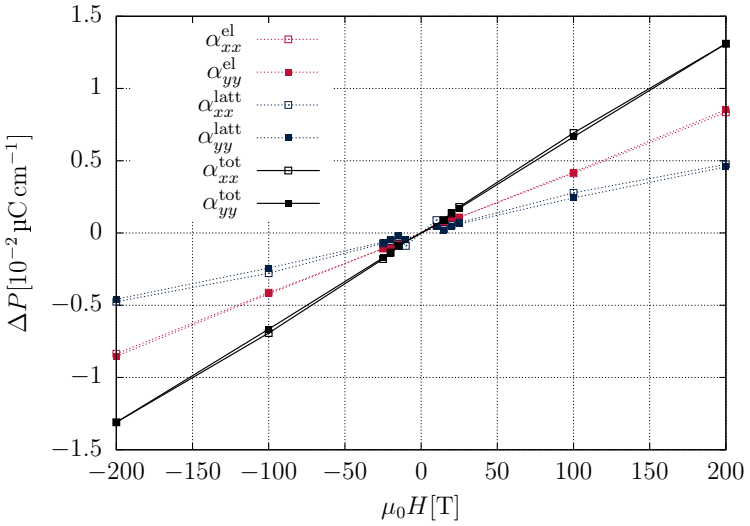


Figure 3.9: Change in polarisation P over an applied magnetic field $\mu_0 H$ within LDA calculations.

results agree remarkably well with the LDA values reported in the next section. It is also worth noting that in the setting discussed, the electronic response is *larger* than the lattice part, which is mainly attributed to the small magnitude of α^{latt}. The electronic coupling in Cr_2O_3 was described to be "unexpectedly large" in the LDA+U study in Ref. [210] with $\alpha_{\perp}^{\mathrm{el}} = 0.34\,\mathrm{ps\,m^{-1}}$, being close to the present LDA value, as compared to the reported $\alpha_{\perp}^{\mathrm{latt}} = 1.11\,\mathrm{ps\,m^{-1}}$, being significantly larger than the present value. The reasons for the discrepancy is due to the choice of *xc*-functionals, as discussed in the next section.

3.3.3 XC-Functionals

Density functional theory with its various implementations of exchange correlation functionals is known to predict slightly different ground-state properties of materials. The results of the previous section, as well as recent literature, show that DFT predicts trends related to the magnetoelectric coupling well. However, discrepancies in the quantitative values for α make a study of the impact of numerical parameters on the delicate ME tensor necessary. For this reason, the effect of *xc*-functionals on the ME coupling is investigated in the present section, and the influences are shown to be significant.

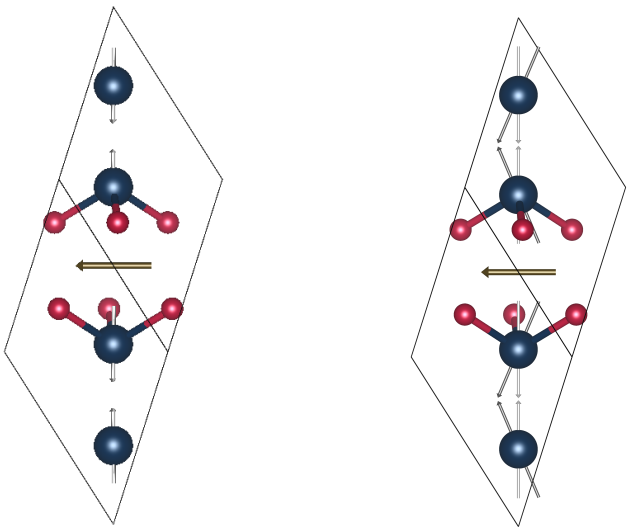
LDA (GGA) functionals are known to atomistically overbind (underbind), whereas the PBESol implementation is usually in between those predictions (Section 2.2.3). On a first level, this leads to slightly smaller (bigger) equilibrium lattice constants and smaller (bigger) vibrational frequencies. Similarly, magnetic moments and the electronic structure are predicted differently. As all four influences of the ME coupling might rely on those quantities (the equilibrium cell volume, the Born effective charges, the dynamical magnetic charges, and the IFC matrix), the analysis offers great insight of the overall effect of the functional on the ME tensor and opens pathways in the search for stronger ME coupling. We therefore repeat the calculations of the lattice-mediated coupling with PBE, LDA, PBESol, and LDA+U with $U = 2.0\,\mathrm{eV}$ descriptions. As literature approaches differ with respect to the cell shape (relaxed or experimental cell), we repeat the calculations for selected functionals, *viz.* for LDA and LDA+U, for the experimental cell parameters, and determine their electronic ME response.

Two observations are worth noting: firstly, the choice of the *xc*-parameter leads to a noticeable difference in the number of *scf* cycles and the simulation time required to reach electronic convergence. The phenomenon is only apparent when noncollinear magnetism is included. For scalar-magnetic calculations of Cr_2O_3, both the LDA and the GGA functionals converged in 21-22 *scf* steps and 150 s to 160 s on 8 cores on a Dual Quadcore E5520 with 3 GB per core to an accuracy of $\Delta E = 10^{-9}\,\mathrm{eV}$. Including noncollinear magnetism, which is necessary for the computation of the magnetic charges or the electronic response, the LDA functional convergence is achieved in ~ 20 steps and 800 s (all other parameters being equal). In the case of GGA, the number of steps and time required to reach convergence increased by *20-fold* with respect to the collinear case. This fact does not influence the results of the present work other than the convergence problems outlined in Section 3.2.4. It does,

however, highlight the need for a solution to the implementation problem of electronic charge density gradients with spinors in modern DFT codes.

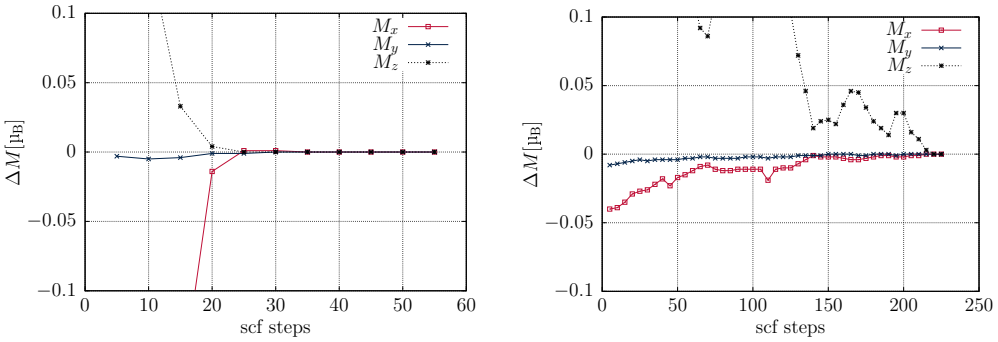
Secondly, employing the Hubbard U leads to cubic contributions to $\frac{\partial F}{\partial H}$ and $\frac{\partial F}{\partial H}$ for magnetic fields over 50 T, whereas the LDA does not exhibit any higher-order coupling for ranges up to 1000 T (Section 3.2.4). To analyse the effect of a strong magnetic field on the magnetic and electronic structure of Cr_2O_3, the changes in magnetic moment and electronic charge density, respectively, are shown in Figs. 3.10 and 3.12 for LDA and LDA+U calculations, before and after applying a magnetic field of 100 T. If using the LDA+U, the spins are more susceptible and exhibit a component in x that is 5 times larger than for the LDA. In alignment with the previous observation, the calculations require more than 5 times the scf steps to converge to an energy threshold of 10^{-8} eV; the magnetic moments still do not seem to be converged. The convergence behaviour is shown in Fig. 3.11. The LDA calculations show no localised charge accumulation, whereas including U seems to provide for a (nonlinear) bonding under strong magnetic fields. This behaviour is worth mentioning. Yet, it is beyond the scope of the present thesis to further explore the behaviour, since the magnetic-field strengths are also well above fields created in laboratories. All values presented in the remainder of this thesis are computed from the linear regime of $B \leq 20$ T, where the LDA and LDA+U description provide similar and accurate results without any higher-order coupling.

In order to compare the linear part of the ME tensor predicted by different xc-functionals, we start by comparing the BECs in their atomic basis in Tables 3.13 and 3.14. For the BECs of Cr, an interesting observation is the fact that the diagonal transverse responses increase when calculations were performed with LDA, PBESol, PBE, and LDA+U (from 2.55 e, 2.82 e, 2.92 e and 3.00 e, respectively), whereas the off-diagonal elements decrease in mag-



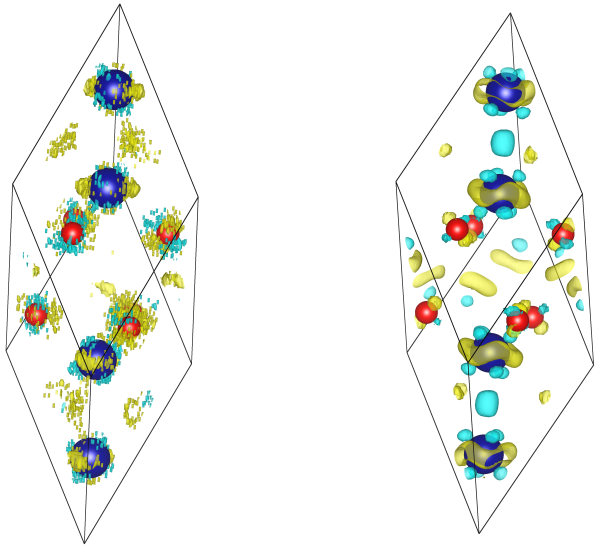
(a) **(b)**

Figure 3.10: Tilting of the Cr magnetic moment under a Zeeman magnetic field of $B = 100\,\mathrm{T}$ along x (centre arrow) within the (**a**) LDA and (**b**) LDA+U description. The influence of B is small when using LDA, whereas the nonlinear coupling becomes apparent when including a finite U. In both plots, the magnetic moment in x-direction is enlarged by a factor of 10 for better visibility.



(a) **(b)**

Figure 3.11: Convergence of the Cr magnetic moment under a Zeeman magnetic field of 100 T along x within the (**a**) LDA and (**b**) LDA+U description. Close-ups of the differences to the last data point are displayed. When including a U, the convergence of the magnetic moment becomes less smooth and the number of *scf* steps increases almost by a factor of 5 when high magnetic fields are applied.



(a) **(b)**

Figure 3.12: Difference in charge densities after a Zeeman magnetic field of 100 T is applied along the x-axis in a clamped-ion calculation within the (**a**) LDA and (**b**) LDA+U description. Yellow (cyan) isosurfaces describe positive (negative) values of 50 % the maximum value. The magnetic field leads to non-linear coupling for LDA+U, which shows in the charge densities: the influence of the field is negligible when using LDA, whereas signs of bonding appear when including a finite U.

nitude in the same functional order from 0.46 e, 0.37 e, 0.39 e and 0.24 e. The single zz-response is not influenced heavily by the choice of functional. The same holds true for O: the xx-response seems to be fairly constant with respect to the functional. Again, the symmetric elements follow the same order as for Cr (increasing values of 1.17 e, 1.44 e, 1.53 e and 1.68 e for LDA, PBESol, PBE, and LDA+U, respectively) and the off-diagonal elements display the opposite behaviour.

The eigenvalues of the IR active modes are compared in Table 3.15. It is to be expected that the LDA calculations, which predict a smaller lattice constant due to overbinding, predict higher phonon frequencies. Yet, all values are in good agreement with each other and literature values.

More interesting is the effect of the functional on the dynamical magnetic charges, Table 3.16: their magnitudes seem to be more influenced by

Table 3.13: Born effective charges of the Cr atom in Cr_2O_3, Z^e(Cr), for different xc-functionals, compared to Ref. [211]. All tensors are given in e.

PBE	PBESol	LDA
$\begin{pmatrix} 2.92 & -0.36 & 0.00 \\ 0.36 & 2.92 & 0.00 \\ 0.00 & 0.00 & 3.18 \end{pmatrix}$	$\begin{pmatrix} 2.82 & -0.37 & 0.00 \\ 0.37 & 2.82 & 0.00 \\ 0.00 & 0.00 & 3.16 \end{pmatrix}$	$\begin{pmatrix} 2.55 & -0.46 & 0.00 \\ 0.46 & 2.55 & 0.00 \\ 0.00 & 0.00 & 3.20 \end{pmatrix}$

LDA+U	Ref. [211]
$\begin{pmatrix} 3.00 & -0.24 & 0.00 \\ 0.24 & 3.00 & 0.00 \\ 0.00 & 0.00 & 3.16 \end{pmatrix}$	$\begin{pmatrix} 3.02 & -0.30 & 0.00 \\ 0.30 & 3.02 & 0.00 \\ 0.00 & 0.00 & 3.18 \end{pmatrix}$

Table 3.14: Born effective charges of the O atom in Cr_2O_3 for different xc-functionals compared to Ref. [211]. All tensors are given in e.

PBE	PBESol	LDA
$\begin{pmatrix} -2.36 & 0.00 & 0.00 \\ 0.00 & -1.53 & -1.05 \\ 0.00 & -0.92 & -2.12 \end{pmatrix}$	$\begin{pmatrix} -2.32 & 0.00 & 0.00 \\ 0.00 & -1.44 & -1.06 \\ 0.00 & -0.97 & -2.11 \end{pmatrix}$	$\begin{pmatrix} -2.24 & 0.00 & 0.00 \\ 0.00 & -1.17 & -1.16 \\ 0.00 & -1.05 & -2.14 \end{pmatrix}$

LDA+U	Ref. [211]
$\begin{pmatrix} -2.31 & 0.00 & 0.00 \\ 0.00 & -1.68 & -0.93 \\ 0.00 & -0.79 & -2.10 \end{pmatrix}$	$\begin{pmatrix} -2.36 & 0.00 & 0.00 \\ 0.00 & -1.66 & -1.00 \\ 0.00 & -0.88 & -2.12 \end{pmatrix}$

the choice of the functional than the BECs and IFC matrix. Similar to the BEC tensors, we observe an anisotropy that is smallest for the PBE functional, with an increasing difference between the diagonal and off-diagonal elements for other functionals. Using the LDA+U functional however, we observe that the magnetic charges on the Cr atoms, particularly the diagonal elements, are $\sim$ 50 % to 200 % larger than for the other functionals, yet we observe 60 % to 80 % smaller magnetic charges on the O atoms.

The decomposition into IR active phonon modes offers insights into the mechanisms behind the coupling. Table 3.18 shows our results for the Born

Table 3.15: Comparison of IR active mode eigenvalues for Cr_2O_3, as calculated by finite differences (FD) with different *xc*-functionals. Literature values are FD calculations in Quantum Espresso based on Ref. [211]. The eigenvalues are given in eV Å^{-2}; the results comply with each other and literature values. It can be seen that the LDA functionals predict higher phonon frequencies, which is due to the well-known overbinding in LDA calculations [121, 226].

Functional	E_u modes	A_{2u} modes
PBE	9.8, 15.3, 18.7, 29.4	10.3, 21.4
PBESol	9.5, 17.2, 22.6, 33.5	10.6, 25.3
LDA	10.2, 19.6, 23.2, 37.7	11.0, 29.3
LDA+U	10.8, 17.9, 24.3, 35.4	11.2, 29.2
PBE, Ref. [211]	10.2, 16.0, 20.2, 30.9	10.5, 22.5

Table 3.16: Dynamical magnetic charges of the Cr atom in Cr_2O_3 for different *xc*-functionals compared to Ref. [211]. All tensors are given in $10^{-2}\,\mu_B/Å$.

PBE

$$\begin{pmatrix} 5.10 & -5.12 & 0.00 \\ 5.12 & 5.10 & 0.00 \\ 0.00 & 0.00 & 0.02 \end{pmatrix}$$

PBESol

$$\begin{pmatrix} 4.50 & -6.85 & 0.00 \\ 6.85 & 4.50 & 0.00 \\ 0.00 & 0.00 & 0.04 \end{pmatrix}$$

LDA

$$\begin{pmatrix} 2.37 & -5.60 & 0.00 \\ 5.60 & 2.37 & 0.00 \\ 0.00 & 0.00 & 0.09 \end{pmatrix}$$

LDA+U

$$\begin{pmatrix} 7.30 & -6.26 & 0.00 \\ 6.26 & 7.30 & 0.00 \\ 0.00 & 0.00 & 0.03 \end{pmatrix}$$

Ref. [211]

$$\begin{pmatrix} 5.88 & -5.69 & 0.00 \\ 5.69 & 5.88 & 0.00 \\ 0.00 & 0.00 & 0.02 \end{pmatrix}$$

effective charges, the magnetic charges, the force-constant matrix, and for the resulting ME tensor using different functionals. Let us start by analysing the effect on the dominant transverse lattice mediated tensor. The differences for $\alpha_\perp^{\text{latt}}$ are severe, with values ranging from $0.272\,\text{ps}\,\text{m}^{-1}$ to $0.918\,\text{ps}\,\text{m}^{-1}$, resulting in a factor of 3.4, with the LDA (LDA+U) prediction at the lower (upper) boundary. The microscopic reasons are two-fold: firstly, we notice a *stronger cancellation* on a mode level, rather than decreasing values per mode. The positive contributions of the two high-frequency transverse E_u^1 and E_u^2 modes

Table 3.17: Dynamical magnetic charges of the O atom in Cr_2O_3 for different *xc*-functionals compared to Ref. [211]. All tensors are given in $10^{-2}\,\mu_B/Å$.

PBE	PBESol	LDA
$\begin{pmatrix} -5.91 & 0.00 & 0.00 \\ 0.00 & -1.71 & 0.00 \\ 0 & -1.14 & -0.04 \end{pmatrix}$	$\begin{pmatrix} -5.03 & 0.00 & 0.00 \\ 0.00 & -1.46 & -0.03 \\ 0.00 & -1.58 & -0.03 \end{pmatrix}$	$\begin{pmatrix} -2.74 & 0.00 & 0.00 \\ 0.00 & -0.48 & -0.11 \\ 0.00 & -2.70 & -0.09 \end{pmatrix}$

LDA+U	Ref. [211]
$\begin{pmatrix} -1.12 & 0.00 & 0.00 \\ 0.00 & -0.35 & 0.00 \\ 0.00 & -0.26 & 0.00 \end{pmatrix}$	$\begin{pmatrix} -5.92 & 0.00 & 0.00 \\ 0.00 & -1.95 & 0.00 \\ 0.00 & -1.10 & -0.02 \end{pmatrix}$

increase significantly from the LDA+U to the LDA results, whereas the negative contribution of the two transverse soft modes, E_u^3 and E_u^4, decreases in magnitude. Secondly, on an electromagnetic level, the BECs seem largely unaffected by the choice of the functional, and the change in $\alpha_\perp$ is attributed to the MCs and the force-constant matrix.

Table 3.18: Comparison of the mode contribution for α^{latt} in Cr_2O_3 within relaxed-cell calculations. Acoustic modes were excluded. Literature values are based on Ref. [211] and the value for U in the LDA+U calculations is 2.0 eV. The Born effective charges Z^e are given in e, the magnetic charges Z^m in $10^{-2}\,\mu_B/\text{Å}$, the eigenvalues C in $\text{eV}\,\text{Å}^{-2}$, and the coupling tensor α^{latt} in $\text{ps}\,\text{m}^{-1}$.

Mode	PBE				PBESol				LDA				LDA+U				PBE, Ref. [211]			
	Z^e	Z^m	C	α	Z^e	Z^m	C	α	Z^e	Z^m	C	α	Z^e	Z^m	C	α	Z^e	Z^m	C	α
${E_u}^1$	6.8	9.5	29	0.263	6.6	7.9	34	0.187	6.0	4.6	38	0.095	7.4	10.1	35	0.260	7.1	10.6	31	0.290
${E_u}^2$	3.8	14.9	19	0.361	3.6	16.4	22	0.313	3.4	12.3	23	0.236	2.6	11.5	24	0.153	3.7	16.1	20	0.356
${E_u}^3$	0.2	-3.7	15	-0.005	1.0	-5.1	17	-0.034	1.3	-4.5	20	-0.040	0.5	-6.2	18	-0.020	0.4	-4.0	16	-0.012
${E_u}^4$	0.8	-0.0	10	0.000	0.7	-0.8	10	-0.007	0.9	-1.6	10	-0.019	0.1	-6.4	11	-0.010	0.6	-0.8	10	-0.005
All $\perp$				0.618				0.460				0.272				0.383				0.629
${A_{2u}}^1$	8.6	0.1	21	0.003	8.5	0.2	25	0.008	8.5	0.2	29	0.006	8.5	0.1	29	0.004	8.5	0.1	23	0.002
${A_{2u}}^2$	1.0	0.0	10	0.001	1.2	-0.0	11	-0.000	1.6	0.2	16	0.002	1.0	0.3	11	0.001	1.2	0.0	11	0.000
All $\parallel$				0.004				0.007				0.008				0.005				0.003

Table 3.19: Comparison of the mode contribution for Cr_2O_3 where the cell is fixed to the experimental lattice constant. The acoustic modes were excluded. The LDA+U values are based on calculations with $U = 2.0\,\text{eV}$. The Born effective charges Z^e are given in e, the magnetic charges Z^m in $10^{-2}\,\mu_B/\text{Å}$, the eigenvalues C in $\text{eV}\,\text{Å}^{-2}$, and the coupling tensors α^{latt} in $\text{ps}\,\text{m}^{-1}$.

Mode	LDA				LDA+U			
	Z^e	Z^m	C	α	Z^e	Z^m	C	α
${E_u}^1$	6.9	13.3	28	0.403	7.3	19.0	32	0.533
${E_u}^2$	3.3	22.7	17	0.530	3.0	27.8	21	0.471
${E_u}^3$	0.2	-4.4	16	-0.007	0.3	-4.2	17	-0.009
${E_u}^4$	1.1	-0.1	10	-0.001	0.5	-1.9	11	-0.010
All $\perp$				0.926				0.985
${A_{2u}}^1$	8.4	0.1	19	0.004	8.4	0.2	25	0.006
${A_{2u}}^2$	0.3	0.0	10	0.000	0.6	0.2	11	0.001
All $\parallel$				0.005				0.007

To isolate the actual effect of the functional, not their secondary effect via compressed or expanded cell volumes, LDA and LDA+U calculations were performed at the fixed experimental lattice constant of 5.36 Å with a rhombohedral angle of 55.1° (Table 3.2), leading to a heavily expanded (only slightly expanded) cell in the LDA (LDA+U) calculations. The choice of the cell volume has a noticeable effect on the overall coupling tensor: in the left panel of Table 3.19 we can see that the LDA value for $\alpha_\perp$ *quadruples* when the cell is kept at the experimental lattice parameters. The equilibrium LDA+U cell volume is close to the experimental value, resulting in similar values for α in both fixed- and relaxed-cell calculations.

Yet, taking a closer look, one sees that despite the similarities in the fixed-cell $\alpha_\perp^{\text{LDA}}$ and $\alpha_\perp^{\text{LDA+U}}$, their individual contributions vary, both comparing their microscopic influences and their mode contributions. As an example, the magnetic charges in the LDA+U description are often more than a factor of 2 larger than the LDA values. Due to cancellations between soft and hard modes and due to larger eigenvalues in the LDA+U calculations, the overall effects on α cancel each other out.

Table 3.20: Comparison of values for α^{latt} and α^{el} from the present work and literature. Brackets indicate whether the cell was allowed to relaxed or if the experimental values were fixed. α given in $\text{ps}\,\text{m}^{-1}$.

Details	$\alpha_{\perp}^{\text{latt}}$	$\alpha_{\perp}^{\text{el}}$	$\alpha_{\parallel}^{\text{latt}}$	$\alpha_{\parallel}^{\text{el}}$
LDA (Rel.)	0.272	0.553	0.006	0.000
LDA (Exp.)	0.926	0.522	0.005	0.000
LDA+U (Rel.)	0.918	0.323	0.005	0.000
LDA+U (Exp.)	0.985	0.313	0.007	0.000
PBE (Rel.)	0.618		0.004	
PBESol (Rel.)	0.460		0.007	
PBE (Rel.) [211]	0.633		0.0024	
PBE (Rel.) [197]	0.77	0.26	0.0026	0.0007
LDA+U (Exp.) [209]	1.11	0.34	0	0
LDA+U (Exp.) [164]	0.43		0.00	

Table 3.20 summarises and compares the key findings of the *xc*-functional study with literature and also includes the *electronic* part of α. The fixed-cell LDA and LDA+U values for α^{latt} are similar ($0.926\,\text{ps}\,\text{m}^{-1}$ and $0.985\,\text{ps}\,\text{m}^{-1}$ for $\alpha_{\perp}$ and $0.005\,\text{ps}\,\text{m}^{-1}$ and $0.007\,\text{ps}\,\text{m}^{-1}$ for $\alpha_{\parallel}$). The electronic coupling seems consistent within the functionals, regardless of the cell volume. All values are in excellent agreement with literature, particularly the ones of overlapping parameters.

Let us compare the effect of the electronic structure on the ME lattice response. Table 3.2 on page 104 shows the band gaps and magnetic moments for the LDA and LDA+U in fixed- and relaxed-cell calculations; Fig. 3.13 shows the density of states for LDA+U at its equilibrium lattice parameter, and for LDA at its equilibrium and the theoretical lattice parameter (*i.e.* under negative pressure). Comparing both LDA calculations, the band gap does not change as significantly as the lattice ME coupling ($0.272\,\text{ps}\,\text{m}^{-1}$ for relaxed- and $0.926\,\text{ps}\,\text{m}^{-1}$ for fixed-cell LDA calculations). We can also observe the effect of the *d*-bands shifting when changing to LDA+U, but comparing the

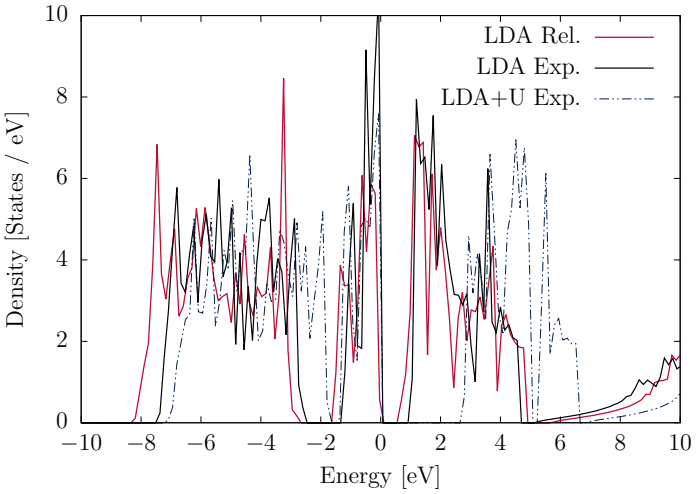


Figure 3.13: Electronic density of states around the Fermi energy at 0 eV for Cr_2O_3 for LDA+U (with relaxed cell parameters) and LDA calculations (for relaxed and fixed cell parameters). The choice of lattice parameters does no affect the band gap strongly. As expected, including the Hubbard U shifts the d-bands and widens the gap. However, because the LDA and LDA+U description predict almost identical ME lattice responses in the fixed-cell calculations on the basis of a fundamentally different electronic structure, we conclude that the latter does not substantially effect the lattice ME coupling. Our LDA+U DOS agrees well with the ones given in literature [220].

almost equal lattice responses for the experimental-cell LDA and LDA+U, we can conclude that the change in α^{latt} is not correlated with the size of the band gap.

With respect to the electronic contribution, including a U brings our results in perfect agreement with the LDA+U values reported in Ref. [210]. The influence of the cell seems negligible for both the LDA and LDA+U. Investigating the correlation between U, the band gap, and the electronic response leads to the fixed-cell results in Fig. 3.14: the band gap widens with increasing U, which is to be expected. As opposed to the lattice contribution, the band gap has an effect on the electronic coupling, which decreases with a larger gap.

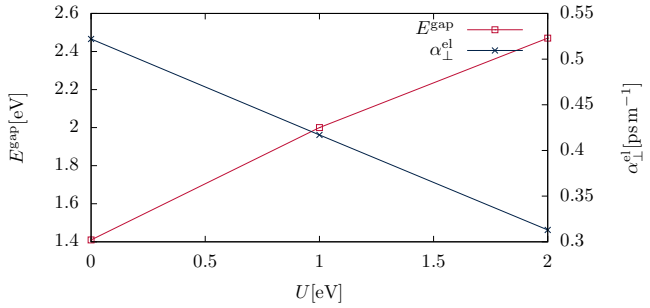


Figure 3.14: Effect of the Hubbard U on the band gap E^{gap} and the transverse electronic ME coupling α^{el} in calculations for the experimental cell. The value for U widens the band gap and thus decreases the electronic response.

3.4 Summary

In this chapter, the theoretical framework to determine the full magnetoelectric response in the equilibrium $\bar{3}'m'$ phase of Cr_2O_3 was explored. We derived the form of the atomic Born effective charges and magnetic charges, as well as the overall ME coupling tensor in a thorough group-theoretical analysis. We showed that the computational approach is capable of determining the ME response, first by reporting on the agreement with literature values for the Cr_2O_3 ground-state properties, as well as with the results obtained by different codes and exchange-correlation functionals. Secondly, we determined the different contributions to the ME tensor. With the implemented Zeeman magnetic field, we compared the "ingredients" for the lattice-mediated response, *viz.* the force-constant matrix, the Born effective charges, and the magnetic charges. The coupling was decomposed into the IR active phonon modes, and shown to be in perfect agreement with literature values. The analysis led to insights about the microscopic mechanisms for different predictions of the tensor properties. In addition, we reported the electronic ME part, which also compares well with literature. The results verify that the ME tensor is predicted well and that we can be confident with respect to further studies of hitherto unknown quantities.

A systematic study of the ME effect with respect to computational parameters showed that great care has to be taken in the choice of the modelled unit cell and the *xc*-functional. Some of the reasons for discrepancies in previously published studies were found: key findings include that the choice of the lattice parameter greatly influences the lattice response, whereas it leaves the electronic contribution unchanged. The relaxed-cell LDA result of the transverse α^{latt} was measured to be smaller than the experimental-cell value by a factor of 4, as the equilibrium cell volume was underestimated by almost 8 %. The mode decomposition showed that the smaller coupling is due to a stronger cancellation between modes, as well as magnetic charges, which were 3 times larger when the experimental cell was modelled.

The effect of a Hubbard U on the LDA functional was shown to have a noticeable effect on the electronic ME response; it turns out to be positively correlated with a decreasing band gap. The lattice coupling is largely unaffected when changing from LDA to LDA+U calculations.

Another correlation that became apparent when using different functionals is of fundamental nature: we found that in studies, where an accurate description of the magnetic moment is necessary, converging to small energy thresholds is crucial, as the magnetic moments often do not converge as quickly as the total energy. In turn, when small energy thresholds are reached, the correct implementation of the *xc*-functional needs to be guaranteed, which is not the case when the common GGA functionals are used with noncollinear magnetism. The convergence becomes slow and unstable. We also reported on higher-order coupling, which occurs for GGA and LDA+U calculations when magnetic fields of more than 50 T are applied. However, a decomposition of the GGA response showed that the nonlinear coupling is purely quadratic, only occurs for the element in α that should be zero by symmetry, and vanishes for low fields. The LDA+U behaviour is linear up to magnetic fields of 20 T.

A good understanding of the effects of the numerical parameters on the predicted ME response was established. By isolating the effect of the *xc*-functional when fixing the cell to its experimental value, we concluded that the cell volume (electronic structure) has large effects on the lattice mediated (electronic) ME response. Two new hypotheses can thus be raised: we firstly suggest that the lattice-mediated coupling can be tailored by external pressure, secondly that the electronic response exhibits discontinuities with a smaller and smaller band gap. Cr_2O_3 provides the possibility to answer these questions by studying the effect of pressure on the ME tensor—ambient conditions will provide trends; a predicted phase transition from its ground-state antiferromagnetic insulating phase to a paramagnetic metal serves as a model transition to study both the magnetic- and the electronic-structure effects on the ME tensor. These hypotheses will be the topic of the next section.

4 Pressure Dependence of the ME Effect

In the last chapter, the influence of the lattice parameter on the lattice-mediated ME response α^{latt} was shown, as well as the correlations between the Hubbard U (hence the band gap) and the electronic response α^{el}. The present chapter explores the possibilities to specifically tailor both the lattice and the electronic response by external pressure; modifying both the crystallographic and the electronic structure.

Cr_2O_3 is chosen as a model material for three reasons: firstly, is of general interest already "on its own" in single phases, because it exhibits room-temperature magnetoelectricity and is neither multiferroic nor piezomagnetic, making it the ideal material to study the fundamental mechanisms for ME. In addition, strain was already shown to result in large ME lattice responses in single-phase systems [209].

Secondly, it is often used in strained heterostructures, in exchange-bias devices, and nanoparticles [2, 37, 49]. Despite its relatively small coupling, its other properties are sought-after in these technological applications (Section 1.1) [227–230]. The giant ME effect was observed in strained heterostructures and nanorods [231, 232]. The origin of a ME response in Cr_2O_3 nanopar-

ticles that is 600 % larger than its bulk value [230] is still debated: charge accumulation at the interface, epitaxial strain, or the change in magnetic anisotropy by applying a voltage are posited causes [233]. Adjusting the ME response through epitaxial strain or interface coupling makes these structures ideal to tailor ME behaviour for technical applications.

Thirdly, a phase transition around 20 GPa to 35 GPa from its antiferromagnetic (AFM) insulating phase to a paramagnetic (PM) phase is reported. The nature of the phase transition is still debated—a transition to a metallic phase has, however, been suggested in literature, making Cr_2O_3 a suitable candidate to study the dependence of the electronic response on the band gap. It becomes clear that a systematic study of the pressure dependence of the ME coupling both at ambient pressures and at phase transitions is necessary and of current technological interest.

4.1 Preliminaries

We will start by reporting on previous studies of the effect of pressure on Cr_2O_3, followed by the computational parameters used in the present thesis to model the ME response in Cr_2O_3 under pressure.

4.1.1 Theoretical Background

The behaviour of Cr_2O_3 and other corundum-type structures under pressure has been the subject of numerous studies. Early studies focus on structural changes, such as compressibility behaviours, and on pressures that are below the critical pressure for a phase transition [234, 235]. The authors in Ref. [236] examine the magnetic structure and reveal a linear decrease of the Néel temperature under pressures up to 1.3 GPa in Cr_2O_3. The resulting phase diagram shows that at constant temperature, the AFM-PM phase transition can be achieved by pressure.

The nature of the phase transition is explored in more recent studies [94, 222, 237–239]. Ref. [222] investigates the interplay between magnetic and structural properties in Cr_2O_3 and reveals that the different magnetic phases in Cr_2O_3 have a noticeable effect on its structure. In the same way, the compression behaviours of Cr_2O_3 in its different magnetic phases differ—in agreement with the anomalies at the Néel temperature.[1] The AFM-PM phase transition is predicted around 15 GPa and is thought to be of structural nature; the authors raise the question if a transition into the ruby Rh_2O_3 (II) phase occurs. Additional bands occur in the Raman spectrum of Ref. [238] between pressures of 13 GPa to 38 GPa. X-ray diffraction results exclude a structural transition to the ruby structure, so that the authors give alternative reasons for the anomalies: the phase transition could be of magnetic nature or could be a "long-ranging" structural transition that is not completed until 38 GPa. Two recent studies conclude that the transition is indeed not into the ruby structure, but rather of "magnetic and electronic" nature [94, 239]. Ref. [94] reports the phase transition to be into the centrosymmetric $3m$ phase at 10 GPa.

4.1.2 First-Principles Formalism

To study the pressure dependence of the ME response, we employ density functional theory and determine the lattice-mediated and electronic response. The formalism of Chapter 3 is followed and α^{latt} computed according to Eq. 3.6, α^{el} according to Eq. 3.5. As already explored, the LDA provides a more stable implementation with noncollinear magnetism, so that we chose to model the pressure dependence with the LDA functional. The numerical specifications are similar, yet some parameters have to be chosen more tightly. As we approach the metal-insulator transition (MIT), an accurate sampling of the Brillouin zone becomes more important, and is sampled with a $6 \times 6 \times 6$

[1] Ref. [237] interprets the large expansion at T_N with the disappearance of magnetic ordering forces.

Monkhorst-Pack grid [144] centred around Γ. The plane-wave basis set is cut off for energies above 700 eV. Other parameters remain the same: the tetrahedron smearing method after Blöchl is employed with a broadening width of 0.05 eV, structural relaxation performed by residual minimization up to a maximum change in forces of 5×10^{-6} eV Å^{-2}. To model the effect of pressure, a range of homogeneous pressures of −10 GPa to 50 GPa is applied in 5 GPa steps[2] to the cells and volume relaxations performed. The relaxed cells are studied with respect to their ME coupling, where no symmetry constraints are used. A mode decomposition of the lattice response leads to further insights.

4.2 Results

4.2.1 Ground-State Properties

Fig. 4.1 shows the results for the Cr magnetic moment after ionic and electronic relaxations, as well as the band gap over pressure. The development of the ground-state properties already highlights three regimes of interest: an "adiabatic" region at ambient pressures up to ∼ 15 GPa, a phase transition spanning between the critical pressure of P_c = 18 GPa and 35 GPa, and a high-pressure phase where the AFM structure collapses and relaxes into the paramagnetic phase for pressure above ∼ 35 GPa. Our calculations reveal that at a pressure of ∼ 23 GPa, the PM phase becomes energetically more stable, whereas it is 0.6 eV per cell higher in energy at zero pressure.

To confirm that the non-magnetic phase at high pressures is a continuation of the paramagnetic phase at low pressures, we compare the AFM and PM compression behaviour. Fig. 4.2 shows the cell volume, lattice parameter, and cell angle for both phases; Fig. 4.3 summarises the relative changes. The

[2] Two additional pressures were simulated around the metal-insulator transition at 13 GPa and 18 GPa.

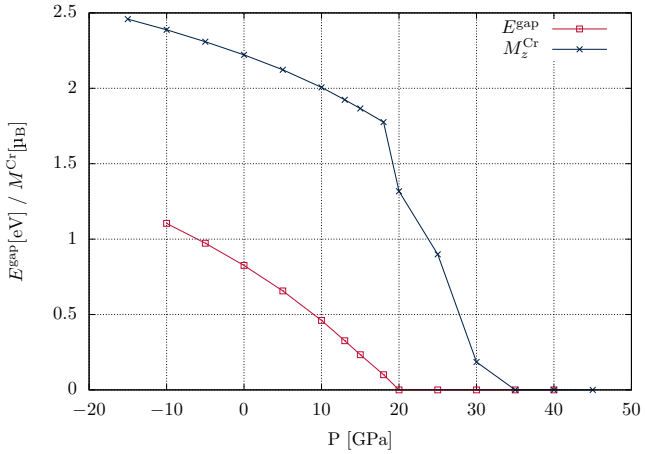


Figure 4.1: Pressure dependence of the band gap and the magnetic moment of the Cr atom in Cr_2O_3. At about $P_c = 20\,\mathrm{GPa}$, Cr_2O_3 undergoes a phase transition from the AFM insulating $\bar{3}'m'$ phase to the PM metallic phase.

structures confirm the previous distinction in adiabatic AFM regime up to P_c, a phase transition, and an adiabatic PM regime. The structural changes also compare well with literature; Ref. [234] highlights the decrease in cell angle for Cr_2O_3 (α^{cell} is almost constant in Fe_2O_3 and increases in Al_2O_3), which is reproduced well by our DFT simulations (Fig. 4.2c). The authors mention its unique compressibility behaviour over pressure: for Cr_2O_3, the compressibility increases, *i.e.* V/V_0 becomes flat at higher pressures. Fe_2O_3, on the other hand, shows a more negative slope at increasing pressures, whereas the compressibility of Al_2O_3 stays constant over pressure. The results from Ref. [235] reproduce the earlier study and yield a slightly increasing compressibility of Cr_2O_3 over pressure. This behaviour is also well matched by the present results: Fig. 4.3a shows the reported compression behaviour of $\bar{3}'m'$ Cr_2O_3 up to the phase transition. The equilibrium cell parameters of the PM phase given in Ref. [222] differ considerably from the AFM phase with a lattice parameter (rhombohedral angle) of $a^{\mathrm{lat}} = 5.69\,\text{Å}$ ($\alpha^{\mathrm{cell}} = 47.2°$) compared to the AFM values of $a^{\mathrm{lat}} = 5.37\,\text{Å}$ ($\alpha^{\mathrm{cell}} = 55.2°$). Our values agree perfectly with the cited literature (Fig. 4.2).

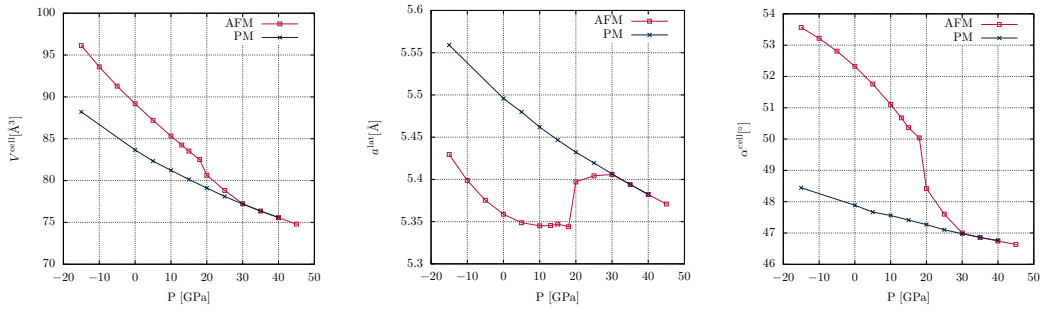


Figure 4.2: Pressure dependence of the structural properties in the AFM and PM phase of Cr_2O_3 in absolute values. (**a**) shows the compressibility behaviour of the volume, (**b**) the lattice constant over pressure, and (**c**) the pressure dependence of the rhombohedral angle. Comparing the AFM and PM trends gives another indication that the PM phase is modelled at high pressures.

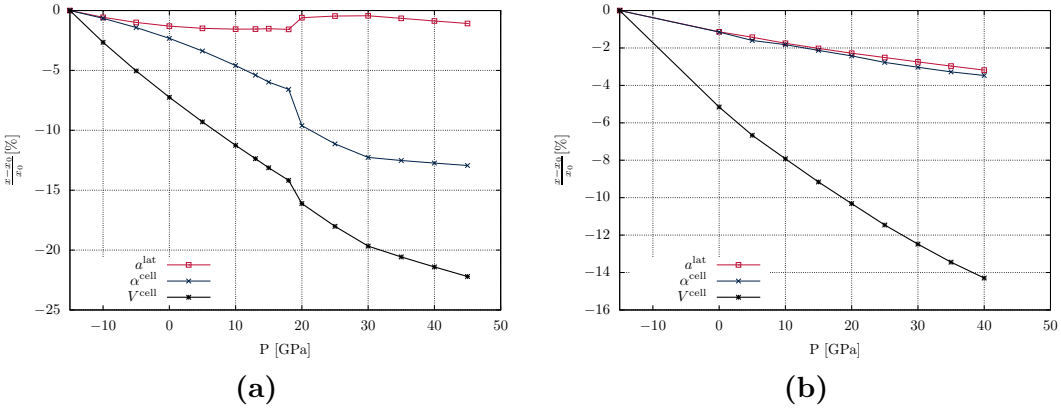


Figure 4.3: Pressure dependence of the structural properties in the (**a**) AFM and (**b**) PM phase of Cr_2O_3 in relative units. The phase transition from AFM to PM at P_c can be observed. Noticeable is also the distinct compression behaviours of the AFM and PM phases: where the compressibility of the AFM phase only slightly decreases (slope of $^{\Delta V}/_{V_0}$), the PM phase decreases in compressibility at lower pressures.

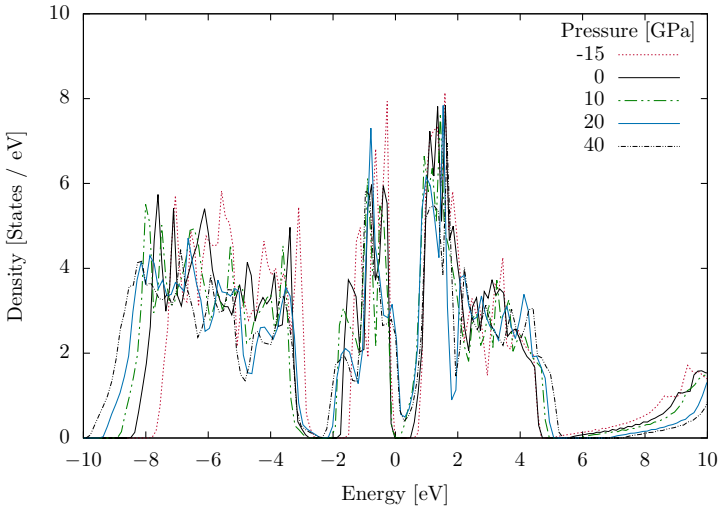
4.2.2 Electronic Properties

As reported in the LDA calculations in Ref. [222], the PM phase is metallic.[3] The nature of the electronic structure of Cr_2O_3 is in between a Mott-Hubbard and a charge transfer insulator [240].[4] Anomalies of the Young's modulus and the inverse susceptibility at the Néel temperature of Cr_2O_3 are observed [241], which also point to the structural and electronic change when reaching the phase transition.

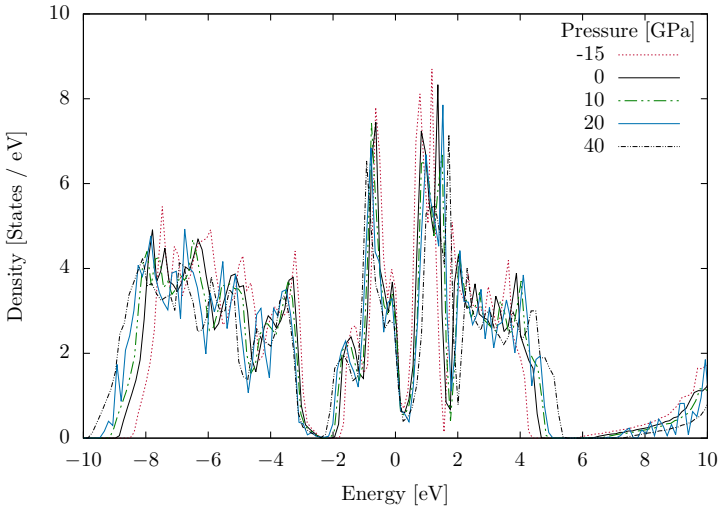
To get an insight into the metal-insulator transition in addition to the decreasing band gap in Fig. 4.1, we analyse the density of states (DOS) for the AFM and PM phase for different pressures (Fig. 4.4). The PM phase of Cr_2O_3 is known to be metallic [222], which is indicated by the DOS at zero pressure. The AFM results complement the magnetic and structural changes from the last section: at the transition pressure of $P_c = 20\,\mathrm{GPa}$, the system transforms into the PM phase and becomes metallic. All DOSs at pressures $\geq P_c$ yield the same results for both AFM and PM starting configurations. The results thus show that Cr_2O_3 does indeed exhibit an interesting behaviour under pressure—a long, adiabatic phase with decreasing cell volume, magnetic moment, and band gap; a phase transition around P_c; and a paramagnetic adiabatic phase for higher pressures.

[3] As shown in Section 2.2.3, we note that the LDA predicts Cr_2O_3 to be more metallic than experiments and, *e.g.* hybrid functionals or LDA+U, leading to a lower predicted pressure for the metal-insulator transition. Yet, the scope of this study is to predict *trends* rather than absolute values. We are interested in relative increases or decreases in the ME response over the band gap, magnetic moment, or cell volume, all of which are predicted equally between the functionals.

[4] In the series of corundum-type M_2O_3, with M belonging to the first-row transition metals Sc–Fe, the insulating character increases with the M atomic number and a transition from Mott-Hubbard to charge-transfer insulators takes place [240]. Fe_2O_3 belongs to the charge-transfer insulators and Cr lies in between.



(a)



(b)

Figure 4.4: Density of states relative to the Fermi energy in the (**a**) AFM and (**b**) PM phase of Cr_2O_3 under pressure. The PM phase is reported to be metallic [222], which is matched by our calculations. The AFM phase undergoes a phase transition into the PM phase at $P_c = 20\,\mathrm{GPa}$ (Fig. 4.1) and therefore yields the same DOS as the PM phase for $P \geq P_c$.

4.3 Analysis

4.3.1 Lattice Response

The pressure behaviours of the *components* of the lattice-mediated ME tensor (at zero pressure shown to be dominant), as well as the *mode decomposed* coupling, offer insights into the pressure behaviour of the overall ME coupling in Cr_2O_3.

To analyse α^{latt}, let us take a closer look at the ambient "adiabatic" regime, followed by the region at higher pressures close to the phase transition.

Ambient Pressures

Fig. 4.5 shows the eigenvalues of the IR active modes, and the Born effective charge (BEC) and magnetic-charge (MC) tensors in the basis of the modes. If we focus on the ambient pressure range, we see that the mode eigenvalues increase with higher pressure, which is to be expected, due to higher lattice stiffness and increasing frequencies. The BECs show a fairly constant behaviour over pressure. The inset of Fig. 4.5c shows a remarkable behaviour though: the two positively contributing E_u modes drop significantly in magnitude, whereas the two oppositely polarisable E_u modes and the two A_{2u} modes stay small and constant over ambient pressures.

Combining the terms leads to the overall lattice response given in Fig. 4.6. Again, let us first focus on the adiabatic change under pressure. We see indeed that the two positive transverse modes have the strongest effect on the overall transverse α^{latt} and the two negative ones remain constant and almost zero over the pressure range. The increase in value with negative pressure is significant: a pressure of $-15\,\text{GPa}$, corresponding to a strain of $1.4\,\%$, leads to an increase of three-fold in the value of $\alpha_{\perp}^{\text{latt}}$. The longitudinal element of α^{latt} remains

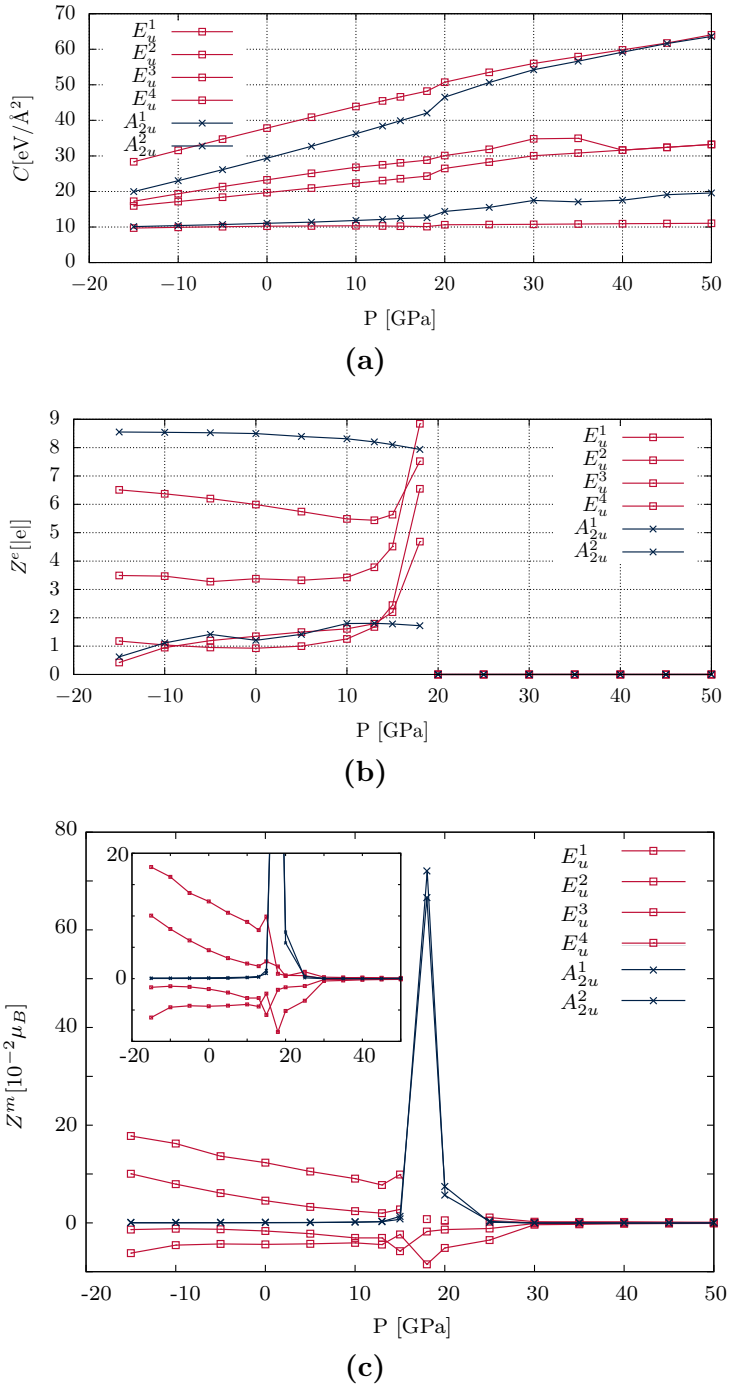


Figure 4.5: Behaviour of the mode-decomposed (**a**) eigenvalues C, (**b**) Born effective charges Z^e, and (**c**) magnetic charges Z^m of Cr_2O_3 under pressure. The inset in (**c**) shows a more detailed view of the magnetic charges. Above the phase transition at 20 GPa, the system is metallic, leading to zero Born effective charges. Beyond 35 GPa the system is centrosymmetric, leading to zero magnetic charges. Of interest are the behaviours at ambient pressures and around the phase transition.

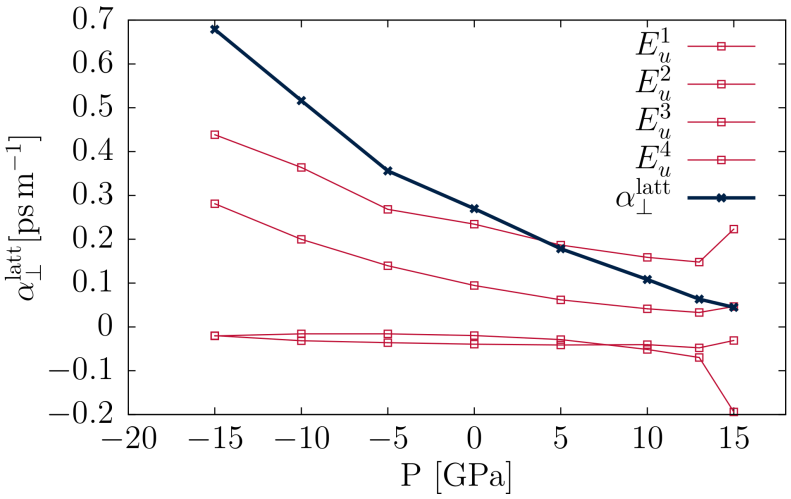
small (see inset of Fig. 4.6b). Between $-15\,\mathrm{GPa}$ and $5\,\mathrm{GPa}$, the value for $\alpha_{\parallel}^{\mathrm{latt}}$ stays between $0.005\,\mathrm{ps\,m^{-1}}$ and $0.006\,\mathrm{ps\,m^{-1}}$.

Magnetic Phase Transition

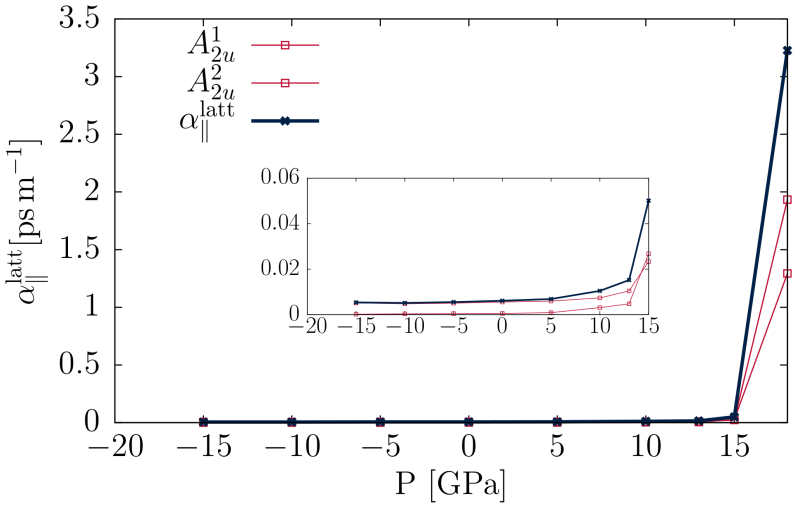
Considerably more interesting is the behaviour beyond the pressure of 15 GPa. Firstly, we note a discontinuity in the eigenvalues, which is attributed to the structural transition at that pressure. Secondly, we see a sudden increase of the BEC tensors, which follows from the closing band gap. Thirdly, the *longitudinal* contributions to the magnetic charges diverge to values of $\sim 70 \times 10^{-2}\,\mu_{\mathrm{B}}/\text{Å}$, up from $0.15 \times 10^{-2}\,\mu_{\mathrm{B}}/\text{Å}$ and $0.04 \times 10^{-2}\,\mu_{\mathrm{B}}/\text{Å}$ at zero pressure. The divergence is remarkable, particularly in comparison with the usually dominant transverse response. We define the phenomenon as "magnetic softness", in analogy to "structural softness" coined in Ref. [242]. Close to the *magnetic* phase transition, the magnetic moments can be influenced easily, and can in turn easily influence lattice modes, if one thinks of the alternative definition of the magnetic charges: $Z^m = {}^{\partial \mathbf{M}}/_{\partial \mathbf{u}}$.

The effect of the decreasing magnetic charges and increasing eigenvalues outweighs the increase in BECs for transverse modes, leading to a monotonic convergence of the overall lattice coupling to zero (Fig. 4.6a). The opposite is true for the longitudinal components, which enhance each other for the overall $\alpha_{\parallel}$: constant BECs, increasing eigenvalues, and diverging magnetic charges lead from the build up (inset of Fig. 4.6b) to a *giant* increase up to P_c: where $\alpha_{\parallel}^{\mathrm{latt}}(5\,\mathrm{GPa}) = 0.006\,\mathrm{ps\,m^{-1}}$, it reaches ten-fold that value at 15 GPa, and a value of $3.227\,\mathrm{ps\,m^{-1}}$ at 18 GPa, which encapsulates an increase to *650 times* its value at zero pressure, is one order of magnitude (two orders of magnitude) higher than the dominant transverse response at zero pressure (at P_c).

The magnetic softness leads to the zz-phonon instabilities at P_c, similar to the results of Ref. [209], where the ionic and electronic contribution to α



(a)



(b)

Figure 4.6: Behaviour of the (**a**) transverse and (**b**) longitudinal lattice-mediated ME responses α^{latt} of Cr_2O_3 under pressure up until the metal insulator transition at 20 GPa. All values are zero in the metallic phase. Results are given in the basis of the IR active modes in Cr_2O_3. The strong increase in $\alpha_\perp^{\text{latt}}$ when decreasing P is due to the increase in magnetic charges and decrease in lattice stiffness (*i.e.* decrease of phonon mode eigenvalues), as shown in Fig. 4.5. The divergence of $\alpha_\parallel^{\text{latt}}$ is due to magnetic softness due to the AFM-PM phase transition. The inset in (**b**) resolves the behaviour at ambient pressures in a more detailed fashion.

were determined over applied strain and towards a phase transition. In the case of Cr_2O_3, we move towards a MIT, leading to additional insights of a correlation between band gap and electronic response.

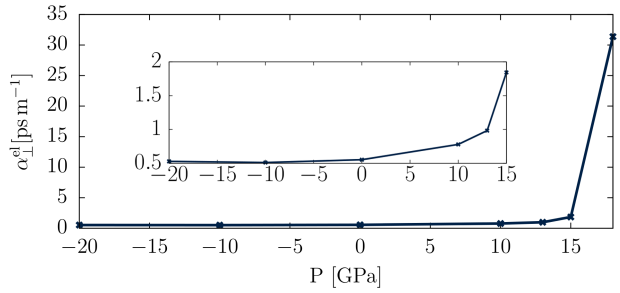
4.3.2 Electronic Response

The authors in Ref. [209] report a correspondence between the band gap and the electronic contribution to α, and suggest a divergence of α^{el} might be seen close to a MIT. The dependence of the ME coupling on an applied U is considered in Section 3.3.3, where we found that the band gap correlates indeed with α^{el}, whereas it leaves α^{latt} unchanged. The MIT seen in Cr_2O_3 in the present work provides a powerful way to investigate the behaviour of α^{el} over pressure.

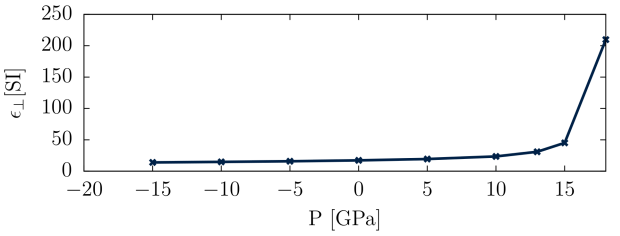
Ambient Pressures

The electronic response α^{el} of Cr_2O_3 over pressure is shown in Fig. 4.7a.[5] At zero pressure, the response is of $0.533\,\mathrm{ps\,m^{-1}}$, larger than the perpendicular lattice response with $0.273\,\mathrm{ps\,m^{-1}}$. This is due to the underprediction of α^{latt} in the smaller LDA unit cell (Section 3.3.3). The electronic response is, however, modelled close to literature values, as it is independent of the lattice volume. As expected, this behaviour is mirrored at ambient pressures: in the regime of $-20\,\mathrm{GPa}$ to $0\,\mathrm{GPa}$, the change is minimal ($0.528\,\mathrm{ps\,m^{-1}}$ to $0.533\,\mathrm{ps\,m^{-1}}$). We expect α^{el} to depend on the band gap. Even though the band gap becomes smaller with higher pressure (see the band gap in Fig. 4.1 and the DOS in Fig. 4.4), α^{el} does not change dramatically. Close to a MIT, we expect a discontinuity, as a transition from non-conducting to conducting or *vice versa* takes place.

[5] The longitudinal part of α^{el} is predicted to be zero for all pressures.



(a)



(b)

Figure 4.7: Behaviour of the (**a**) electronic ME response α^{el} and (**b**) static dielectric tensor ϵ of Cr_2O_3 under pressure up until the metal insulator transition at 20 GPa. All values are zero in the metallic phase. The divergence of $\alpha_\perp^{\mathrm{el}}$ is attributed to the transition from insulating to metallic, confirmed by the divergence of the static dielectric tensor $\epsilon_\perp$. The inset in (**b**) shows the region of pressures ≤ 15 GPa.

Metal Insulator Transition

The transition from the AFM insulating phase to the PM metal takes place at the critical pressure $P_c = 18$ GPa. Close to that pressure, the electronic ME coupling increases to a value of $1.844\,\mathrm{ps\,m^{-1}}$ at 15 GPa, about three-fold the zero-pressure value. However, the divergence at P_c, where the value reaches $31.373\,\mathrm{ps\,m^{-1}}$, is remarkable. This value is *60 times* larger than its already sizeable *zero-pressure value*, and is larger than the normally dominant lattice contribution by a factor of 70.

Formulation for α^{el}

This giant value is allowed due to the divergence of the dielectric permittivity. As described in Chapter 1, the upper bound for α is determined by the magnetic permeability μ and dielectric permittivity ϵ via $\alpha \leq \sqrt{\epsilon\mu}$. The diver-

gence of $\epsilon_\perp$ close to the MIT is shown in Fig. 4.7b. As suggested in Ref. [209], the generalised Lyddane-Sachs-Teller relationship needs to be expanded by a formulation for the spin contribution to α^{el} in order to arrive at a relation for α^{el}, ϵ, and μ. However, we do not pursue this here.

4.3.3 Discussion

The reported structural changes of Cr_2O_3 under ambient pressure agree well with literature, as well as the phase transition at P_c. Of interest for the magnetoelectric response are both the absolute value of the coupling achieved, and the relative behaviour compared to the zero-pressure values. The range of lattice-mediated ME responses over different pressures reported in the present chapter compares well with the ranges for different materials reported in literature. Particularly the behaviour of α^{latt} towards lattice instabilities is shown to diverge [209, 242]. Fig. 4.8 shows a summary of the previously reported maximum values for α,[6] where the three ME contributions of Cr_2O_3 from the present thesis are added. The value of $\alpha_\perp$ in Cr_2O_3 (red box) lies in between the other values. Despite the relative weakness of its ME response, Cr_2O_3 is of interest in current technology, mostly because of its room-temperature ME. The braces indicate materials, in which the effect of pressure or strain was investigated. $BiFeO_3$ is one such example [242], where "structural softness" close to a phase transition is responsible for the increase in coupling strength. $CaMnO_3$ exhibits the divergence of the aforementioned longitudinal response [209].

Four observations are worth noting: firstly, the values in Fig. 4.8 refer to the lattice values, since these are usually dominant. Not only is our value for α^{el} larger than α^{latt} in the ambient regime, it also exhibits the largest maximum response of the other values for Cr_2O_3. In addition, the value of

[6] Modified figure, courtesy of E. Bousquet.

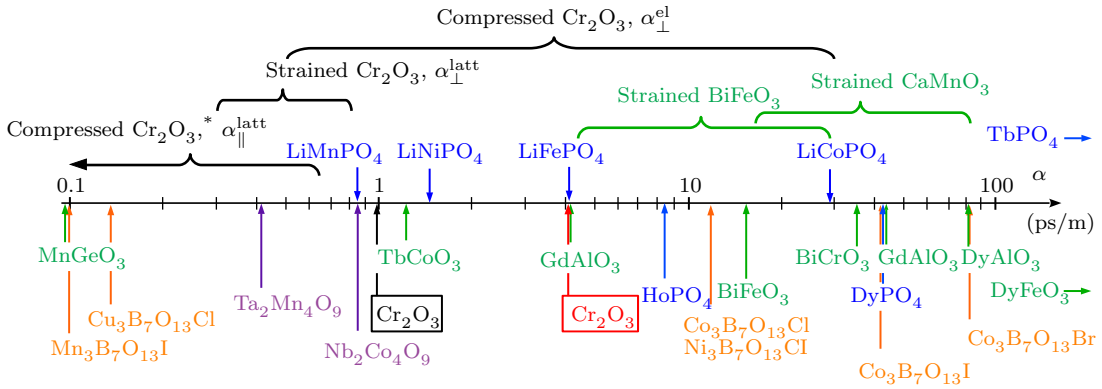


Figure 4.8: Comparison of strengths of the *largest* measured ME coupling tensor for different families of materials. The red box highlights the largest reported value for Cr_2O_3, measured at room temperature. Black labels describe the LDA coupling strengths reported in the present chapter. Both the span and the absolute values achieved in Cr_2O_3 are worth noting, particularly as Cr_2O_3 is a room-temperature magnetoelectric. * the value for $\alpha_\parallel^{latt}$ computed at 0 GPa is $0.005\,\mathrm{ps\,m^{-1}}$. Modified figure from an original provided by E. Bousquet.

$\alpha^{el} > 30\,\mathrm{ps\,m^{-1}}$ falls in the upper end of the diagram, exceeding the value for $BiFeO_3$ (strained and unstrained) and most phosphates—all of which need low temperatures to exhibit their ME.

Secondly, if we examine the *range* of values achieved, *i.e.* the ratio of α^{max}/α^{0}, the diverging values at the phase transitions lead to a high span of about two orders of magnitude for $\alpha_\parallel^{latt}$ and $\alpha_\perp^{el}$. Regardless of the material, this raises the question if one of the compounds with already large zero-pressure couplings could be engineered to show even higher absolute values.

Thirdly, as compared to the lattice response, which can be increased by structurally or magnetically destabilising the material, the electronic response is more easily tunable. The results from this chapter show that the band gap has a huge impact on α^{el}, which can be altered by pressure or, *e.g.* doping.

Fourthly, the results raise the question, if the divergence of the longitudinal lattice response can be reproduced at room temperature. Compared to its

zero-temperature value, it increases by an order of magnitude at 260 K [19], due to the non-relativistic exchange (Chapter 1). It is worth investigating if both behaviours can be combined to reach sizeable ME couplings at room temperature.

4.4 Summary

This chapter explores the effects of pressure on the ME coupling in Cr_2O_3 and sheds light on the nature of the phase transition at high pressures. The structural trends of the $\bar{3}'m'$ phase of Cr_2O_3 agree well with literature. The additional study of the magnetic and electronic properties reveal that Cr_2O_3 transitions from an antiferromagnetic insulator to a paramagnetic metal at around 18 GPa.

In the ambient pressure regime, the band gap, as well as the magnetic moment of the Cr atom decrease with increasing pressure. Higher lattice stiffness leads to larger eigenvalues of the force-constant matrix. In combination with fairly constant Born effective charges and decreasing magnetic polarisability of the hard transverse modes (which are responsible for the transverse ME lattice response $\alpha_{\perp}^{\text{latt}}$), the overall value for $\alpha_{\perp}^{\text{latt}}$ decreases steadily until it becomes zero in the paramagnetic phase. In the same way, negative pressures, leading to a tensile strain of 1.4 %, increase the usually dominant lattice response to three-fold of its zero-pressure value.

The behaviour of the *longitudinal* lattice response $\alpha_{\parallel}^{\text{latt}}$ shows a divergence at the phase transition, due to magnetic softness and the resulting destabilised phonon modes. At ambient pressures, its value is negligible, but becomes 650 times its value at 18 GPa, namely $3.227\,\text{ps}\,\text{m}^{-1}$. The *ratio* to its ground-state value is huge and the absolute value is also large for Cr_2O_3. This opens up the possibility to tailor the response at room temperature, where the longitudinal

response becomes more than 10 times its value at 0 K, so that high values at room temperature could be achieved.

The transition from non-conducting to conducting at P_c leads to another remarkable effect: the electronic transverse response, which is usually neglected at ambient pressures and is not influenced by structural changes, diverges when approaching the metal-insulator transition. The value of $31.373\,\mathrm{ps\,m^{-1}}$ is not only 60 times larger than its value at 0 GPa, but also large in absolute terms. The electronic response is of interest for engineering ME behaviour, as it is dependent on the band gap, which can be tailored by temperature, strain, or doping. The behaviour of the electronic response is in agreement with literature, where it was predicted to diverge with the dielectric permittivity. To the best of our knowledge, an actual observation of the diverging electronic part of the ME response was never reported before. It is an intriguing starting point to stimulate further research.

As we already mentioned, we expect the electronic ME response to be altered via changes in the electronic structure by doping. Substituting atoms might also break the symmetry of the studied material and in turn allow for more tensor elements to be finite. Additionally, the behaviour of the lattice response is of great interest in compounded systems: a study of the microscopic contributions to α^{latt} is intriguing and might point in new directions in the search for stronger ME responses. The following section studies the electronic and lattice-mediated magnetoelectric response of selected corundum-like compounds, explores the effects of substituting single Cr atoms in Cr_2O_3 for other *d*-metals (supported by group-theoretical analyses), and serves as a guidance for chemical trends in the ME behaviour.

5 Compounds Based on the Cr_2O_3 Corundum Phase

On the basis of the previous results and the ability to investigate the microscopic contributions to the magnetoelectric (ME) response, three questions can be raised: how do the single microscopic components of the lattice and electronic response depend on the chemistry of the studied material, how do atomic defects influence the lattice response, and how does the electronic structure affect the electronic ME response? In other words, how do defects influence the ME effect? Can we tailor the lattice response by introducing structural or magnetic softness via atomic substitutions, or tailor the electronic response through changes in the band structure, *e.g.* by doping? To answer these questions, we derive chemical trends along the Cr, Fe, and Ti 3*d*-elements that order in the corundum structure, while keeping the magnetic $\bar{3}'m'$ structure of ground-state Cr_2O_3. Doping with the aforementioned elements is simulated by substitutions on single or multiple Cr sites. The effect on the electronic contribution to the ME tensor is studied, as well as on the lattice contribution, with a particular focus on the behaviour of the magnetic charges, Born effective charges, and interatomic force-constant matrix.

This chapter is structured as follows: based on previous studies, the applications and properties of iron- and titanium oxide are explored, as well as their

role as defects in Cr_2O_3. The configurations studied in this chapter are examined from a symmetry perspective to support the analyses of the subsequent density functional theory (DFT) calculations. The results of the magnetoelectric properties are discussed with respect to their contributions: both the lattice and the electronic contribution to the ME tensor are determined; the former is in turn expanded into the microscopic contributions. As an exemplary mode decomposition of the ME contribution, we chose the limit of Fe_2O_3 in the $\uparrow\downarrow\uparrow\downarrow$ structure. Because it is isostructural to Cr_2O_3, we can interpret the differences between the ME response of the two structures by comparing each mode contribution.

5.1 Preliminaries

In the first part of this section, a background of Fe_2O_3 and Ti_2O_3 is given and previously reported studies on impurities in Cr_2O_3 are discussed. As the substitutions lower the symmetry of pure $\bar{3}'m'$ Cr_2O_3, the tensor forms of the Born effective charge (BEC) and magnetic charge (MC) tensors, as well as the ME coupling tensors need to be determined in a group-theoretical analysis. The computational parameters used are briefly discussed, before we report our results. In order to describe the order of dopants in the Cr_2O_3 matrix, we will specify all 4 metal sites in the 10-atomic unit cell explicitly in the notation (such as "$(CrCrCrM)_4O_6$" if the Cr_4 atom is substituted by a dopant, see Fig. 5.1 for a clarification).

5.1.1 The Impurity Atoms

Fe_2O_3 and Fe Impurities

Transition metal oxides are of great interest in current technology [243] and fundamental research. Fe_2O_3 is used as an active material in heterogeneous

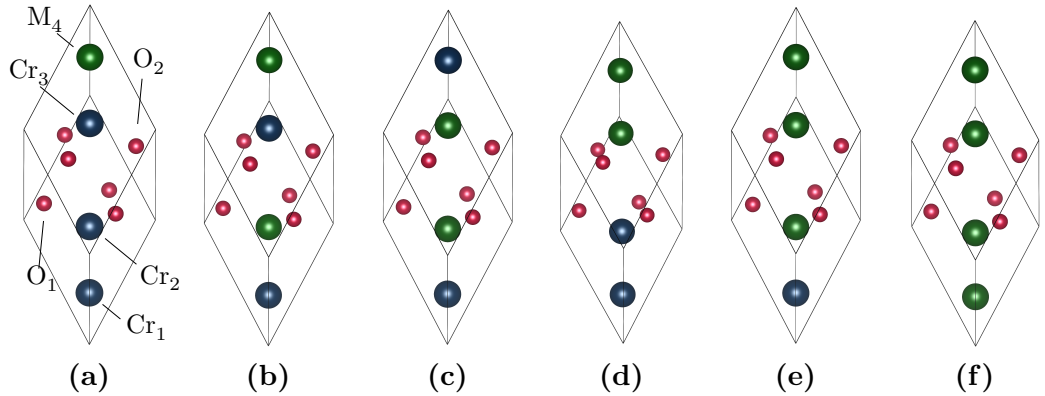


Figure 5.1: Relaxed structures of $(Cr_{1-x}Fe_x)_2O_3$ in the substituted $\bar{3}'m'$ corundum phase of Cr_2O_3; the magnetic $\uparrow\downarrow\uparrow\downarrow$ configuration of the Cr_2O_3 parent phase is retained. Labels in (**a**) define the notation used in the chapter, the dopant is therefore generalised by "M". (**a**) $(CrCrCrFe)_4O_6$ with the crystallographic (magnetic) point group 3 (3), (**b**) $(CrFeCrFe)_4O_6$ with $3m$ ($3m'$), (**c**) $(CrFeFeCr)_4O_6$ with $\bar{3}$ ($\bar{3}'$), (**d**) $(CrCrFeFe)_4O_6$ with the crystallographic and magnetic point group 32, (**e**) $(CrFeFeFe)_4O_6$ with the same symmetry as (**a**), and (**f**) Fe_2O_3 with the original crystallographic (magnetic) point group $\bar{3}m$ ($\bar{3}'m'$). Instead of Fe, Ti can be used in the same way as a dopant.

catalysis, is abundant in the Earth's crust, and is also the prototypical piezomagnetic and weakly ferromagnetic material. Analogous to Cr_2O_3, Fe_2O_3 was first predicted to be piezomagnetic based on its magnetic symmetry [244], which was later confirmed experimentally [245, 246]. Fe_2O_3 orders in the $\uparrow\uparrow\downarrow\downarrow$ magnetic configuration at room temperature with a Néel temperature of $T_N = 955\,\mathrm{K}$ [240, 247]. It is also an interesting material to study with respect to its lattice and electronic ME response in the $\uparrow\downarrow\uparrow\downarrow$ structure, both as a stand-alone compound and as a dopant in Cr_2O_3. It is a charge-transfer insulator (compared to the Mott-Hubbard/charge-transfer insulating nature of Cr_2O_3) with a smaller band gap than Cr_2O_3 and thus provides an ideal way to influence the electronic structure, hence the electronic ME response.

The magnetic and electronic properties of Fe_2O_3 have not been fully reproduced hitherto, as it "poses challenges to theory" due to the strongly correlated *d*-electrons of Fe [248]. Early Hartree-Fock studies report a band gap of $\sim 11\,\mathrm{eV}$ [240], compared to the experimental value of $2.0\,\mathrm{eV}$ [249]. A full DFT study by Rollmann *et al.* reports the $\uparrow\uparrow\downarrow\downarrow$ structure as energetically most

stable, followed by the ↑↓↑↓ (210 meV per Fe atom higher in energy), followed by the (actual ground-state configuration) ↑↓↓↑ (220 meV per Fe atom higher in energy than ↑↑↓↓). Subsequent studies re-confirmed, however, the ↑↓↓↑ structure as the ground state [218, 221].

A collapse of the Fe magnetic moments is reported under pressure in the GGA calculations of Ref. [248]. At volumes about 10 % lower than the equilibrium value, both the ↑↓↑↓ and ↑↓↓↑ magnetic structures stabilise in low-spin states with values of $M^{\mathrm{Fe}} = 1.0\,\mu_{\mathrm{B}}$ ($1.2\,\mu_{\mathrm{B}}$) compared to their high-spin values of $M^{\mathrm{Fe}} = 3.4\,\mu_{\mathrm{B}}$ ($3.5\,\mu_{\mathrm{B}}$), respectively. The volume reduction corresponds to pressures of $\sim$ 14 GPa and is shifted to higher pressures with increasing Hubbard U. The first-order phase transition is reported in literature, where Fe_2O_3 undergoes a Mott transition to a *metallic and nonmagnetic state*, between 50 GPa to 75 GPa [250, 251]. The Rh_2O_3-II phase is claimed to be the structure at high pressures. Ref. [252] shows that the transition to the metallic state is isostructural and that the structural change follows at higher pressures. This behaviour is surprisingly similar to the high-pressure behaviour of Cr_2O_3 (explored in Section 4) and provides an interesting outlook for what happens if Fe is substituted in a slightly denser matrix, such as Cr_2O_3, both from an electronic and a magnetic perspective.

Structural, magnetic, and electronic properties of Fe substitutions in Cr_2O_3 from DFT simulations with non-local Hartree-Fock exchange contributions are reported in Ref. [218]. It is shown that in all permutations, the ↑↓↑↓ and ↑↓↓↑ phases are close in energy. The former is the ground state for Cr_2O_3 and $(CrFeFeCr)_4O_6$, the latter for the other configurations. Employing GGA+U, the authors of Ref. [248] report a slightly lower energy for the ↑↑↓↓ structure of Fe_2O_3. We therefore conclude that even in those configurations, in which the ↑↓↑↓ structure of substituted Fe in Cr_2O_3 is not the ground state,

they are still close enough in energy that it is not unreasonable to study their chemical trends when doping Cr_2O_3.

Ti_2O_3 and Ti Impurities

Titanium oxide compounds, such as TiO_2 and Ti_2O_3, have been of technological interest for decades. In addition to their use in "low-cost, high-efficiency" photovoltaics [253] and photocatalysts [254], they seem promising for the use in resistive random access memories (RRAMs)[1] [255, 257, 258].

Ti_2O_3 orders paramagnetically in the corundum phase as a Mott-Hubbard insulator with an almost vanishing band gap of $\sim 0.1\,\mathrm{eV}$ [259]. It is of further interest, not only because of the fundamental mechanisms that occur in transition-metal oxides [243], but also because of the metal-insulator transition it undergoes between 400 K to 600 K [260, 261]. As for the case of Cr_2O_3 or Fe_2O_3, the transition from insulating to metallic correlates with fluctuations and instabilities of charge, spin, and orbital degrees of freedom [262]. The question of band-gap altering through Ti-doping in Cr_2O_3 therefore is raised, as well as the influence of the substitutions on the local magnetic structure.

The substitution of one Cr atom by Ti in an 80-atomic supercell of Cr_2O_3 is examined by GGA+U methods in Ref. [263]. The authors find that the formation enthalpy is positive with a value of 0.22 eV and that the Cr atoms move away from the impurity. The $\uparrow\downarrow\uparrow\downarrow$ magnetic state is the most favourable one. Neither the positive- or negative-spin sublattice is preferred by the impurity. Moreover, delocalised electron states occur at the bottom of the conduction band, due to the Cr 3*d*-states, leading to a metallic state. *n*-type electrical conductivity complies with experimental evidence. A net magnetic moment

[1] RRAMs are attractive non-charge-based alternatives for current charge-based memories, whose performance and storage capacity are limited and decrease over time [255]. RRAMs are based on materials that change resistance when a voltage is applied, the so-called "memristive switching"—which has also been observed in Cr_2O_3 [256].

of $\sim 2\,\mu_B$ for the cell is induced, which is attributed to the smaller magnetic moment of the Ti atom ($\pm 0.88\,\mu_B$, depending on the sublattice).

To investigate the influence of the dopants, the magnetic symmetries of the different configurations are determined, which is covered in the next section on the basis of group theory.

5.1.2 Group-Theory Analysis

In order to repeat the symmetrisation of the coupling tensor α from Section 1.2.3 for the configurations shown in Fig. 5.1, their magnetic point groups need to be determined. Substituting single atoms can only *lower* the symmetry of the parent structure. We will therefore use the initial Cr_2O_3 *crystallographic space group* $R\bar{3}c$ (in the Hermann-Mauguin notation) as a starting point and test which symmetry operations are valid in all compounds. The M_2O_3 structure is equal to the one of Cr_2O_3 ($\bar{3}'m'$) and we will focus on the low-symmetry structures. $(CrCrCrM)_4O_6$ and $(CrMMM)_4O_6$ also have similar structures, so symmetry considerations hold true for both.

As we only substitute atoms on the three-fold axis z, all compounds still obey the three-fold symmetry, whereas their inversion centre is removed for all (leading to $3 \parallel z$ as a generating element instead of $\bar{3}$) but the $(CrMMCr)_4O_6$ configuration (invariant under $\bar{3}$). The glide plane is only a generating element of the $(CrMCrM)_4O_6$ configuration (Fig. 5.1b); it reduces to the two-fold rotation symmetry in $(CrCrMM)_4O_6$. The crystallographic space groups are therefore $R3$, $R3c$, $R\bar{3}$, and $R32$ for (**a**), (**b**), (**c**), and (**d**) in Fig. 5.1, respectively. Only the mirror operation in the glide plane, as well as the inversion when acting upon $\bar{3}$, change the direction of the spins when including time reversal. These operations are therefore primed. In the same order, their *magnetic point groups* are thus 3, $3m'$, $\bar{3}'$, and 32.

Table 5.1: Transformation matrices T for the $3 \parallel z$, $m \perp x$, and $2 \parallel x$ operations, which are used to symmetrise α and the Born effective charge and magnetic-charge tensors in the substituted $(Cr_{1-x}M_x)_2O_3$ configurations.

$T(3 \parallel z)$	$T(m \perp x)$	$T(2 \parallel x)$
$\begin{pmatrix} -1/2 & \sqrt{3}/2 & 0 \\ -\sqrt{3}/2 & -1/2 & 0 \\ 0 & 0 & 1 \end{pmatrix}$	$\begin{pmatrix} -1 & 0 & 0 \\ 0 & 1 & 0 \\ 0 & 0 & 1 \end{pmatrix}$	$\begin{pmatrix} 1 & 0 & 0 \\ 0 & -1 & 0 \\ 0 & 0 & -1 \end{pmatrix}$

Coupling Tensor

The form of the linear ME tensor α_{ij} can be predicted by tensor symmetrisation. The transformation matrices T are summarised in Table 5.1. We symmetrise according to $\alpha'_{ij} = \pm\|T\|T_{ik}T_{jl}\alpha_{kl} \equiv \alpha_{ij}$ (Section 1.2.3) and solve the set of equations when setting $\alpha' \equiv \alpha$. Again, "$\pm$" represents time-reversal. Let us start by symmetrising under 3 and $\bar{3}'$. Because $T(\bar{3}) = -T(3)$, the sign changes for $\bar{3}'$ cancel each other out and the symmetrisation is equal to 3:

$$
\begin{aligned}
&\begin{pmatrix} \alpha'_{11} & \alpha'_{12} & \alpha'_{13} \\ \alpha'_{21} & \alpha'_{22} & \alpha'_{23} \\ \alpha'_{31} & \alpha'_{32} & \alpha'_{33} \end{pmatrix} \\
&= \begin{pmatrix} -1/2 & -\sqrt{3}/2 & 0 \\ \sqrt{3}/2 & -1/2 & 0 \\ 0 & 0 & -1 \end{pmatrix} \begin{pmatrix} \alpha_{11} & \alpha_{12} & \alpha_{13} \\ \alpha_{21} & \alpha_{22} & \alpha_{23} \\ \alpha_{31} & \alpha_{32} & \alpha_{33} \end{pmatrix} \begin{pmatrix} -1/2 & \sqrt{3}/2 & 0 \\ -\sqrt{3}/2 & -1/2 & 0 \\ 0 & 0 & 1 \end{pmatrix} \\
&= \begin{pmatrix} \frac{1}{4}\left(\alpha_{11} + 3\alpha_{22} + \alpha_{12}\sqrt{3} + \alpha_{21}\sqrt{3}\right) & \frac{1}{4}\left(\alpha_{12} - 3\alpha_{21} + \alpha_{11}\left(-\sqrt{3}\right) + \alpha_{22}\sqrt{3}\right) & \frac{1}{2}\left(-\alpha_{13} - \sqrt{3}\alpha_{23}\right) \\ \frac{1}{4}\left(-3\alpha_{12} + \alpha_{21} + \alpha_{11}\left(-\sqrt{3}\right) + \alpha_{22}\sqrt{3}\right) & \frac{1}{4}\left(3\alpha_{11} - \sqrt{3}\alpha_{12} - \sqrt{3}\alpha_{21} + \alpha_{22}\right) & \frac{1}{2}\left(\sqrt{3}\alpha_{13} - \alpha_{23}\right) \\ \frac{1}{2}\left(-\alpha_{31} - \sqrt{3}\alpha_{32}\right) & \frac{1}{2}\left(\sqrt{3}\alpha_{31} - \alpha_{32}\right) & \alpha_{33} \end{pmatrix} \\
&\equiv \begin{pmatrix} \alpha_{11} & \alpha_{12} & \alpha_{13} \\ \alpha_{21} & \alpha_{22} & \alpha_{23} \\ \alpha_{31} & \alpha_{32} & \alpha_{33} \end{pmatrix}, \qquad (5.1)
\end{aligned}
$$

which leads to the tensor forms for α in the 3 and $\bar{3}'$ magnetic point groups shown in the left panel of Fig. 5.2. Further symmetrisation under m' and 2 (same transformation matrices) results in

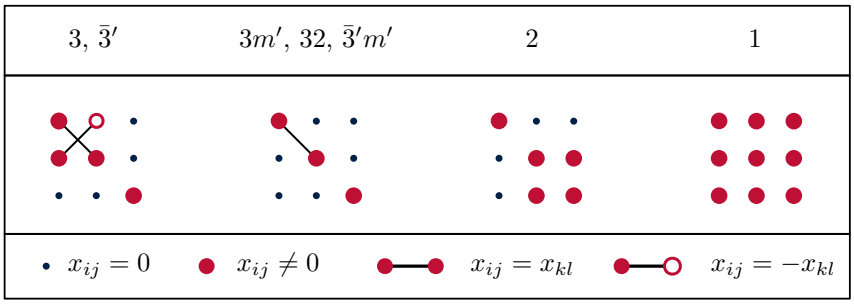


Figure 5.2: Tensor forms of atomistic and macroscopic tensor quantities in compounds of Cr_2O_3. The first row shows the symmetry operations under which the tensor is invariant.

$$
\begin{aligned}
&\begin{pmatrix} \alpha''_{11} & \alpha''_{12} & \alpha''_{13} \\ \alpha''_{21} & \alpha''_{22} & \alpha''_{23} \\ \alpha''_{31} & \alpha''_{32} & \alpha''_{33} \end{pmatrix} \\
&= (-1) \begin{pmatrix} -1 & 0 & 0 \\ 0 & 1 & 0 \\ 0 & 0 & 1 \end{pmatrix} \begin{pmatrix} \alpha_{11} & \alpha_{12} & 0 \\ -\alpha_{12} & \alpha_{11} & 0 \\ 0 & 0 & \alpha_{33} \end{pmatrix} \begin{pmatrix} -1 & 0 & 0 \\ 0 & 1 & 0 \\ 0 & 0 & 1 \end{pmatrix} \\
&= \begin{pmatrix} \alpha_{11} & -\alpha_{12} & 0 \\ \alpha_{12} & \alpha_{11} & 0 \\ 0 & 0 & \alpha_{33} \end{pmatrix} \equiv \begin{pmatrix} \alpha_{11} & \alpha_{12} & 0 \\ -\alpha_{12} & \alpha_{11} & 0 \\ 0 & 0 & \alpha_{33} \end{pmatrix},
\end{aligned}
\tag{5.2}
$$

making $\alpha_{12} = \alpha_{21} = 0$, shown in the second panel of Fig. 5.2. The forms agree with the ones given in Ref. [120].

The form of the BEC and MC tensors can be derived from their atomic site symmetry. The Wyckoff positions and their respective symmetry is shown in Table 5.2. Three distinct site symmetries are present: 3 (and $\bar{3}'$), 2, and 1, all of which have been symmetrised in Section 3 for the $\bar{3}'m'$ phase. A graphical depiction is given in Fig. 5.2.

5.1.3 First-Principles Formalism

Similar computational parameters are chosen to model the compound phases as for pure Cr_2O_3 (Chapter 3). However, the compounds exhibit smaller band

Table 5.2: Wyckoff positions (WPs) for the Cr and O atoms in the 3, $3m'$, and $32'$ magnetic point groups. The on-site symmetry is displayed in the second panels.

	$\bar{3}'m'$		3		$3m'$		32		$\bar{3}'$	
Atom	WP	Sym.	WP	Sym.	WP	Sym.	WP	Sym.	WP	Sym.
Cr	$4c$	$3 \parallel z$	$1a$	$3 \parallel z$	$2a$	$3 \parallel z$	$2c$	$3 \parallel z$	$1a$, $1b$	$\bar{3}' \parallel z$
O	$6e$	$2 \parallel x$	$3b$	1	$6b$	1	$3d$, $3e$	$2 \parallel x$	$3d$, $3e$	$\bar{1}'$

gaps, and are, in the case of Ti_2O_3, often predicted to be metallic when using standard functionals [260, 264]. The correct treatment of the electronic structure at small band gaps is of importance, as we emphasised in the previous Chapter 4. Therefore, the rotationally invariant LDA+U by Dudarev *et al.* is used [142] and the Brillouin zone is sampled with a Γ-centred $6 \times 6 \times 6$ k-point grid. We thus achieve convergence of the polarisation to $10^{-5}\,\mu C\,cm^{-2}$ per atom. The plane-wave cut-off energy is increased to 650 eV, in order to guarantee a numerical precision of 0.5 meV per atom. Other parameters remain equal: structural relaxations with a force threshold of $\Delta F \leq 5 \times 10^{-6}\,eV\,Å^{-2}$, collinear treatment for the computation of the BECs and the force-constant matrix, and noncollinear treatment for the computation of the magnetic charges.

The PAW data sets for Fe and Ti include the $4s$ and $3d$ electrons as valence. To select values for U_{eff} in Fe and Ti, the ↑↓↓↑ ground state of Fe_2O_3 and the paramagnetic (PM) ground state of Ti_2O_3 are modelled and compared to literature. We find that $U = 4.0$ eV for Fe and $U = 2.0$ eV for Ti predict band gaps similar to theoretical and experimental studies, and are in the range of values used in literature (see Table 5.3). The recommendation from Ref. [265] for $U(\text{Ti}) = 2.0$ eV based on formation enthalpies and structural parameters agrees well with our findings.

Achieving ionic and electronic convergence requires a careful choice of minimisation parameters, as the modelled magnetic structure is not the ground

state of either Fe_2O_3 or Ti_2O_3. To converge the ground state to 0.5 meV per atom, we used Gaussian smearing with a smearing width of 0.02 eV and the Kerker mixing scheme [266] with a linear electronic/magnetic mixing parameter of $2 \times 10^{-2}/8 \times 10^{-2}$. The number of non-self-consistent steps at the beginning of an electronic *scf* step is set to 20 (the default is 10), which increases the chance of finding the ground state, if the initial wave functions are not close to the ground state. In compounds with small band gaps, we experience difficulties in achieving the accurate force threshold of $\Delta F \leq 5 \times 10^{-6}\,\mathrm{eV\,\AA^{-2}}$ and observe the atoms to "hop" close to the ground state. In order to stabilise the ionic relaxations, we set the maximum weight for a band to be considered empty to zero, leading to slightly slower, but more stable calculations.[2] We also use the blocked Davidson scheme for the diagonalisation and decrease the steps in ionic relaxations to half of the default value.

5.2 Results

5.2.1 Ground-State Properties

Table 5.3 compares our predicted ground-state properties of Fe_2O_3 and Ti_2O_3 with literature values. The LDA+U value for Cr_2O_3 with two literature values serves as a comparison. An extensive comparison is given in Chapter 3. For Fe_2O_3, a wide range of predicted values is reported. Our values for a^{lat}, α^{cell}, and V^{cell} predict average values. Cell volume and band gap are at the upper end of the literature values. The Fe_2O_3 structure is only slightly larger than the one of Cr_2O_3, in agreement with Ref. [217], which reports similar values, and contrary to Ref. [218], which reports the Fe_2O_3 volume to be 3 % larger than the Cr_2O_3 volume. The results for the Ti_2O_3 ground-state properties are also in agreement with literature, except for its electronic structure: the

[2] This value is usually 0 in static calculations, whereas it is set to a default of 1×10^{-3} during relaxations.

Table 5.3: Structural, electronic, and magnetic properties of ↑↓↓↑ Fe_2O_3 and PM Ti_2O_3 benchmarked against literature values. The values for Cr_2O_3 from Chapter 3 are shown for comparison. Lattice parameter a^{lat}, cell angle α^{cell}, cell volume V^{cell}, magnetic moment of the M = Cr, Fe, and Ti atom M_M, and band gap E^{gap}. In the case of DFT+U calculations, the used U of the M atom is given. Missing cell volumes/cell angles from the literature are added for consistency.

Details	a^{lat} [Å]	α^{cell}[°]	V^{cell}[Å^3]	M_M [μ_B]	E^{gap} [eV]	U [eV]
			Cr_2O_3(↑↓↑↓)			
Our work	5.34	55.1	95.5	2.8	2.5	2.0
LDA+U [216]	5.37	54.3	95.0	2.8	2.8	3.2
Hybrid [221]	5.39	55.1	98.1	3.52	3.3	-
			Fe_2O_3 (↑↓↓↑)			
Our work	5.36	55.0	96.3	4.1	2.5	4.0
LDA+U [216]	5.42	54.1	96.9	4.1	1.9	4.3
Hybrid [218]	5.49	58.8	102.8	4.0	1.9	-
Exp. [249, 267][1]	5.43	50.2	86.9	-	2.0	-
GGA+U. [248]	5.49	57.7	101.3	3.5	2.0	4.0
Hybrid [221]	5.43	56.6	100.5	4.4	2.4	-
			Ti_2O_3 (PM)			
Our work	5.43	55.7	101.9	-	0.0	2.0
Exp. [259, 268, 269][2]	5.43	56.8	104.9	-	0.1	-
Hybrid [221]	5.43	56.6	104.3	-	0.2	-

[1] Structural parameters from Ref. [267], band gap from Ref. [249];
[2] Structural parameters from DFT from Ref. [268], band gap from Refs. [259, 269]

PM Ti_2O_3 phase is predicted to be metallic by our calculations, compared to narrow band gaps reported in literature.

Fe Substitution

Table 5.4 shows the ground-state parameters of the compound phases modelled in the present thesis. Let us start by discussing the case of Fe, shown in the first panel of the table. We notice an anomaly in the crystallographic and magnetic structures. Bearing in mind that the volumes of Cr_2O_3 and Fe_2O_3 in their ground states are 96.5 Å^3 and 96.3 Å^3, respectively (Table 5.3), the volumes

of the compound phases are all considerably smaller. We identify a potential reason for this behaviour to be the magnitude of the magnetic moments of the Fe atoms. Only the $(CrFeCrFe)_4O_6$ structure retains its Fe magnetic moments of 4.1 μ_B (highlighted in green in Table 5.4), whereas low-spin Fe moments of 0.9 μ_B to 1.0 μ_B are observed in all others (highlighted in blue in Table 5.4). The $(CrFeFeFe)_4O_6$ structure exhibits a "hybrid" behaviour, where one atom (on position M_2, closest to the Cr atom) shows a magnetic moment of 1.0 μ_B, the other two remain at 4.1 μ_B and 4.0 μ_B. Interestingly, that specific volume is also in between the volumes belonging to the low-spin and high-spin phases. As a guide, the volumes are coloured accordingly to their Fe magnetic moments, with the hybrid volume being black.

This observation is in accordance with Ref. [248] (Section 5.1.1), which illustrates the high-spin and low-spin phases of Fe_2O_3 in the $\uparrow\downarrow\uparrow\downarrow$ and $\uparrow\uparrow\downarrow\downarrow$ magnetic structures. This behaviour is consistent with the change in volume. The low-spin states were stabilised in smaller volumes, starting from $\sim 10\,\%$ lattice reduction. It is worth noting that the high-spin states in the present work did not converge to ionic forces smaller than the required threshold for the computation of magnetoelectric properties. Combining this observation with the behaviour of the magnetic moments leads to the conclusion that the high-spin states are possibly close in energy to the low-spin states and are in a shallow energetic minimum.

The electronic structure is largely independent of the high-spin or low-spin magnetic structure. However, the band gap depends on the distance between Cr atoms: for two or more neighbouring Cr atoms per unit cell, *i.e.* for the $(CrCrCrFe)_4O_6$, $(CrCrFeFe)_4O_6$, and $(CrFeFeCr)_4O_6$, the band gap remains at 2.4 μ_B to 2.5 μ_B, for less, it shrinks to 1.6 μ_B to 1.7 μ_B. Comparing the order of the spin arrangement in the limit of Fe_2O_3, the $\uparrow\downarrow\uparrow\downarrow$ structure from Table 5.4

Table 5.4: Structural, magnetic, and electronic properties of the Fe- and Ti-substituted Cr_2O_3 in the ↑↓↑↓ magnetic structure. Lattice parameter a^{lat}, cell angle α^{cell}, cell volume V^{cell}, magnetic moments of the four metal atoms M in the order shown in the left panel, and band gap E^{gap}. The compounds in bold are not considered for calculations of the ME tensors, as they cannot stabilise to the required precision or are predicted to be metallic. Coloured magnetic moments belong to the M dopants. Green (blue) highlights volumes and magnetic moments belonging to the high-spin (low-spin) phases.

Details	a^{lat} [Å]	α^{cell}[°]	V^{cell}[Å^3]	**M** [μ_B]	E^{gap} [eV]
$(CrCrCrFe)_4O_6$	5.27	55.3	92.23	$(2.9, -2.8, 2.9, -0.9)$	2.4
$(CrFeCrFe)_4O_6$	5.34	55.3	96.10	$(2.8, -4.1, 2.8, -4.1)$	1.7
$(CrCrFeFe)_4O_6$	5.21	55.5	89.59	$(2.8, -2.8, 1.0, -1.0)$	2.4
$(CrFeFeCr)_4O_6$	5.25	55.4	91.44	$(2.8, -1.0, 1.0, -2.8)$	2.5
$(CrFeFeFe)_4O_6$	5.30	53.5	93.38	$(2.9, -1.0, 4.1, -4.0)$	1.6
Fe_2O_3	5.09	55.7	84.03	$(1.0, -1.0, 1.0, -1.0)$	1.6
$(CrCrCrTi)_4O_6$	5.35	55.7	97.37[1]	$(2.8, -2.9, 2.8, -0.6)$	0.4
$(CrTiCrTi)_4O_6$	5.39	55.3	98.60	$(2.6, -0.6, 2.6, -0.6)$	0.0
$(CrCrTiTi)_4O_6$	5.36	56.2	99.40	$(2.8, -2.8, 0.5, -0.5)$	0.6
$(CrTiTiCr)_4O_6$	5.45	54.4	99.54	$(3.1, 0.0, 0.1, -3.1)$	0.2
$(CrTiTiTi)_4O_6$	5.42	55.4	100.53	$(2.8, -0.3, 0.0, -0.3)$	0.0
Ti_2O_3	5.44	55.6	102.26	$(0.5, -0.5, 0.5, -0.5)$	0.2

[1] This value lies within 1 ‰ of the reported 97.5 Å^3 in Ref. [263]

exhibits a smaller band gap, whereas the ground-state ↑↓↓↑ from Table 5.3 belongs to the wider-gap insulators.

Ti Substitution

The lattice parameter and volume for $(Cr_{1-x}Ti_x)_2O_3$ steadily increase with x. Comparing the overlap of Ti_2O_3 in its PM and ↑↓↑↓ phase (bottom panels of Tables 5.4 and 5.3, respectively), we see that the magnetic structure does not have a strong influence on the lattice. The magnetic moment of the added Ti atom is small and varies from $|M^{Ti}| = 0.0\,\mu_B$ to $0.6\,\mu_B$ (highlighted in green in Table 5.4). The band gap stays small: even substituting only one Ti atom

decreases the band gap from 2.5 eV in pure Cr_2O_3 to 0.4 eV in $(CrCrCrTi)_4O_6$. Besides $(CrCrTiTi)_4O_6$, the other structures have even smaller band gaps and are, in the case of $(CrTiCrTi)_4O_6$ and $(CrTiTiTi)_4O_6$, metallic. By comparing the effect of the spin arrangement in the Ti_2O_3 limit, we see that whilst the $\uparrow\downarrow\uparrow\downarrow$ structure from Table 5.4 is a narrow-gap insulator, the PM ground-state from Table 5.3 is predicted to be metallic.

Differential Electronic Charge Densities

To gain insight into the binding behaviour of the impurity atoms in the Cr_2O_3 matrix, the differences in charge densities are displayed in Fig. 5.3. In the case of one impurity, the data is determined via the difference of the final charge density and the "single" charge densities: $\Delta\rho = \rho((CrCrCrM)_4O_6) - \rho((CrCrCr)_4O_6) - \rho(M)$. For two Cr substitutions with M_1 and M_2, we compute $\Delta\rho = \rho((CrCrM_1M_2)_4O_6) - \rho((CrCr)_4O_6) - \rho(M_1) - \rho(M_2)$. The effect of the binding can thus be isolated. Differences between the single Fe and Ti impurities become apparent: where the former shows more of a covalent binding behaviour (Fig. 5.3a), the Ti behaviour is less pronounced and more ionic (Fig. 5.3c). For the "layered" compositions (Figs. 5.3b and 5.3d), the charge density becomes more similar: hybridisation occurs between the impurity atoms and the matrix elements, whereas no channels can be observed between the impurities themselves.

5.2.2 Magnetoelectric Response

As mentioned in the previous section, not all configurations converge to the accuracy required to perform ME-response calculations, due to the accurate energy- and force-threshold needed. The magnetoelectric properties are determined only for the compounds that stabilise accurately enough in the $\uparrow\downarrow\uparrow\downarrow$ magnetic structure. When substituting Fe in Cr_2O_3, the $(CrCrCrFe)_4O_6$,

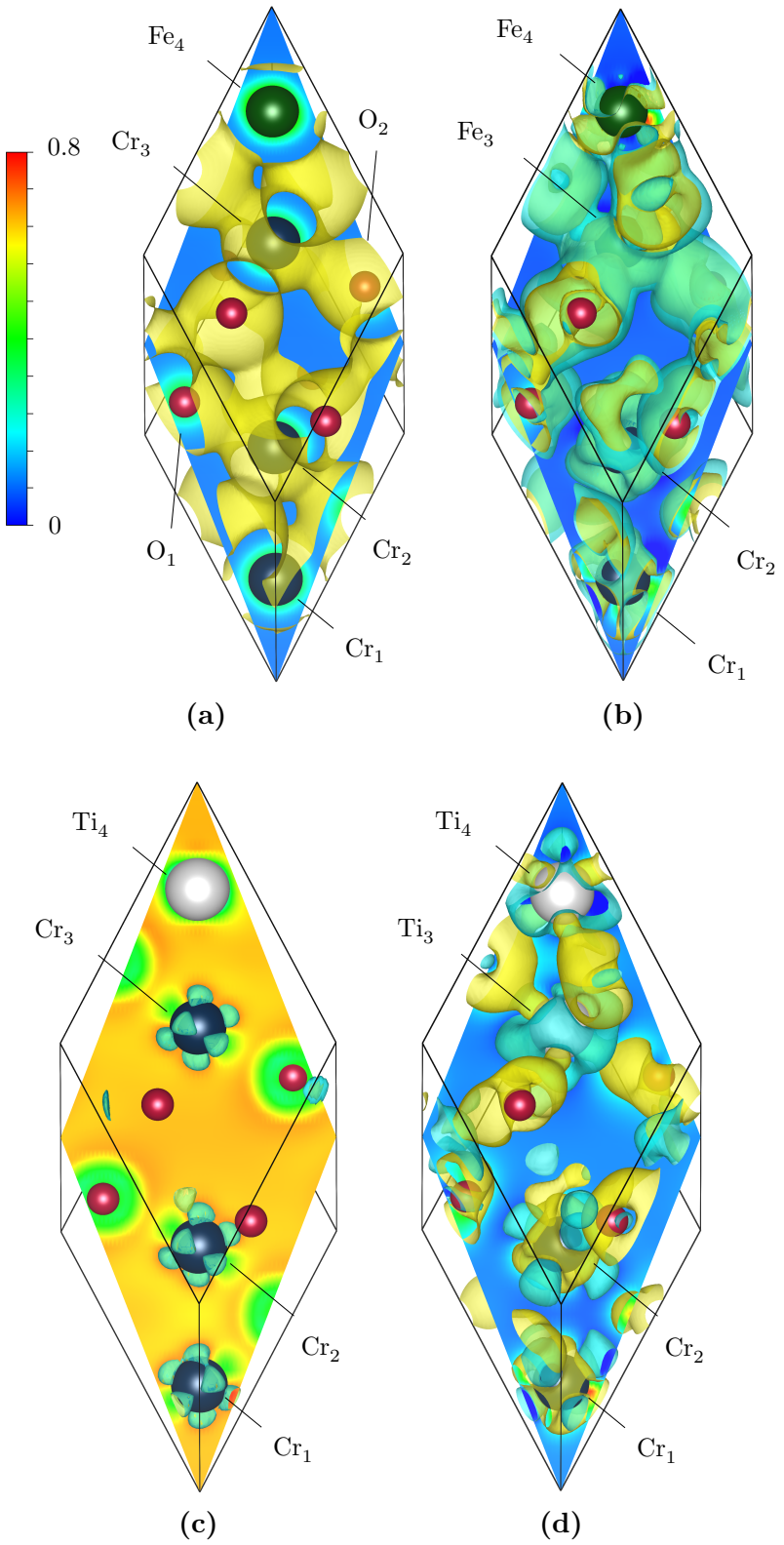


Figure 5.3: Differences in the charge density distributions of $(Cr_{1-x}M_x)_2O_3$ in the substituted $\bar{3}'m'$ corundum phase of Cr_2O_3. Yellow (cyan) isosurfaces describe positive (negative) charge differences at 10 % of the maximum value. The plane $\perp y$ shows the density difference with a maximum value of 80 %, the colour bar applies to all figures. (**a**) $(CrCrCrFe)_4O_6$ shows signs of hybridisation with more ionic character, (**b**) $(CrCrFeFe)_4O_6$ hybridises along the Fe-O channels. The charge density in (**c**) for $(CrCrCrTi)_4O_6$ is less pronounced, whereas $(CrCrTiTi)_4O_6$ in (**d**) shows similar channels as (**b**).

$(CrFeCrFe)_4O_6$, and $(CrCrFeFe)_4O_6$ structures are compared, as well as the limit of Fe_2O_3 in the $\bar{3}'m'$ phase. Because most configurations in the Ti substitution are metallic (or close to being metallic), the Berry phase polarisation could not be determined for any but the $(CrTiTiCr)_4O_6$ phase.

Born Effective Charges

The Born effective charges for the M atoms are shown in Table 5.5. The tables summarise the Wyckoff positions with their respective symmetries and number of inequivalent positions from Table 5.2. In $(CrCrCrFe)_4O_6$, all M positions are inequivalent. For better comparability, the corresponding BECs for the other compounds are given too, even though they can be obtained by symmetry operations of the group (highlighted in bold).

The BEC tensors obey the symmetry and similar elements are of similar magnitude (for example, the 11-elements vary from $2.1\,e$ to $4.6\,e$). Fe impurities do not affect the BEC tensors of the remaining Cr atoms much: the Cr tensors are similar to the ones in pure Cr_2O_3 (11-components between $2.9\,e$ to $3.1\,e$, 33-components 11-components between $3.0\,e$ to $3.2\,e$). The same holds true for Fe (11-components between $2.1\,e$ to $2.3\,e$, 33-components between $2.8\,e$ to $3.0\,e$). The Cr tensors in the $(CrCrTiTi)_4O_6$ compound, however, increase in value to a 11-value of $4.1\,e$, twice their standalone value, and similar in magnitude to the Ti BECs. The BECs for the O atoms, not reported here, are also similar to the values of Cr_2O_3.

Magnetic Charges

The compound phases have a remarkable effect on the magnetic charges. The tensors are shown in Table 5.6 for the Cr-positions, and in Table 5.7 for the O-positions. As a preliminary point, let us note that the magnetic contributions are much more pronounced compared to the Cr_2O_3 phase. The responses

Table 5.5: Born effective charges Z^e of the M atoms in M-substituted Cr_2O_3 (M=Fe/Ti/Cr), $(Cr_{1-x}M_x)_2O_3$. All tensors are given in e. Underneath the compound description, the atomic symmetry of the M position is given in parentheses, followed by the number of inequivalent M positions. In the case of $(CrCrCrFe)_4O_6$, all four M positions are inequivalent; for consistency, symmetry images are also shown for higher-symmetry point groups—tensors that can be obtained from M_1 by using the symmetry operations of the group are highlighted in bold.

Compound	M_1	M_2	M_3	M_4
Cr_2O_3 (3, 1)	$\begin{pmatrix} 3.0 & -0.2 & 0.0 \\ 0.2 & 3.0 & 0.0 \\ 0.0 & 0.0 & 3.2 \end{pmatrix}$	$\begin{pmatrix} \mathbf{3.0} & \mathbf{0.2} & \mathbf{0.0} \\ \mathbf{-0.2} & \mathbf{3.0} & \mathbf{0.0} \\ \mathbf{0.0} & \mathbf{0.0} & \mathbf{3.2} \end{pmatrix}$	$\begin{pmatrix} \mathbf{3.0} & \mathbf{0.2} & \mathbf{0.0} \\ \mathbf{-0.2} & \mathbf{3.0} & \mathbf{0.0} \\ \mathbf{0.0} & \mathbf{0.0} & \mathbf{3.2} \end{pmatrix}$	$\begin{pmatrix} \mathbf{3.0} & \mathbf{-0.2} & \mathbf{0.0} \\ \mathbf{0.2} & \mathbf{3.0} & \mathbf{0.0} \\ \mathbf{0.0} & \mathbf{0.0} & \mathbf{3.2} \end{pmatrix}$
$(CrCrCrFe)_4O_6$ (3, 4)	$\begin{pmatrix} 3.0 & -0.1 & 0.0 \\ 0.1 & 3.0 & 0.0 \\ 0.0 & 0.0 & 3.0 \end{pmatrix}$	$\begin{pmatrix} 3.0 & 0.4 & 0.0 \\ -0.4 & 3.0 & 0.0 \\ 0.0 & 0.0 & 3.2 \end{pmatrix}$	$\begin{pmatrix} 2.9 & 0.2 & 0.0 \\ -0.2 & 2.9 & 0.0 \\ 0.0 & 0.0 & 3.0 \end{pmatrix}$	$\begin{pmatrix} 2.3 & -0.3 & 0.0 \\ 0.3 & 2.3 & 0.0 \\ 0.0 & 0.0 & 3.0 \end{pmatrix}$
$(CrCrFeFe)_4O_6$ (3, 2)	$\begin{pmatrix} 3.1 & -0.2 & 0.0 \\ 0.2 & 3.1 & 0.0 \\ 0.0 & 0.0 & 3.1 \end{pmatrix}$	$\begin{pmatrix} \mathbf{3.1} & \mathbf{0.2} & \mathbf{0.0} \\ \mathbf{-0.2} & \mathbf{3.1} & \mathbf{0.0} \\ \mathbf{0.0} & \mathbf{0.0} & \mathbf{3.1} \end{pmatrix}$	$\begin{pmatrix} 2.2 & 0.4 & 0.0 \\ -0.4 & 2.1 & 0.0 \\ 0.0 & 0.0 & 2.8 \end{pmatrix}$	$\begin{pmatrix} \mathbf{2.2} & \mathbf{-0.4} & \mathbf{0.0} \\ \mathbf{0.4} & \mathbf{2.1} & \mathbf{0.0} \\ \mathbf{0.0} & \mathbf{0.0} & \mathbf{2.8} \end{pmatrix}$
Fe_2O_3 (3, 1)	$\begin{pmatrix} 2.1 & -0.4 & 0.0 \\ 0.4 & 2.1 & 0.0 \\ 0.0 & 0.0 & 2.8 \end{pmatrix}$	$\begin{pmatrix} \mathbf{2.1} & \mathbf{0.4} & \mathbf{0.0} \\ \mathbf{-0.4} & \mathbf{2.1} & \mathbf{0.0} \\ \mathbf{0.0} & \mathbf{0.0} & \mathbf{2.8} \end{pmatrix}$	$\begin{pmatrix} \mathbf{2.1} & \mathbf{0.4} & \mathbf{0.0} \\ \mathbf{-0.4} & \mathbf{2.1} & \mathbf{0.0} \\ \mathbf{0.0} & \mathbf{0.0} & \mathbf{2.8} \end{pmatrix}$	$\begin{pmatrix} \mathbf{2.1} & \mathbf{-0.4} & \mathbf{0.0} \\ \mathbf{0.4} & \mathbf{2.1} & \mathbf{0.0} \\ \mathbf{0.0} & \mathbf{0.0} & \mathbf{2.8} \end{pmatrix}$
$(CrCrTiTi)_4O_6$ (3, 2)	$\begin{pmatrix} 4.1 & 0.8 & 0.0 \\ -0.8 & 4.1 & 0.0 \\ 0.0 & 0.0 & 2.0 \end{pmatrix}$	$\begin{pmatrix} \mathbf{4.1} & \mathbf{-0.8} & \mathbf{0.0} \\ \mathbf{0.8} & \mathbf{4.1} & \mathbf{0.0} \\ \mathbf{0.0} & \mathbf{0.0} & \mathbf{2.0} \end{pmatrix}$	$\begin{pmatrix} 4.6 & 0.9 & 0.0 \\ -0.9 & 4.6 & 0.0 \\ 0.0 & 0.0 & 3.7 \end{pmatrix}$	$\begin{pmatrix} \mathbf{4.6} & \mathbf{-0.9} & \mathbf{0.0} \\ \mathbf{0.9} & \mathbf{4.6} & \mathbf{0.0} \\ \mathbf{0.0} & \mathbf{0.0} & \mathbf{3.7} \end{pmatrix}$

are still linear, though noisier. Slight deviations from the group-theoretically predicted forms of the MC tensors become apparent. We therefore stress that we do not guarantee a similar accuracy for the MCs as in the equilibrium structures. Moreover, the iz-responses for Fe-substituted Cr_2O_3 is for most M atoms too noisy to predict making the computation of the slope $\frac{\partial F_i}{\partial H_z}$ difficult, and are thus set to zero.

The magnitudes of the force responses are up to 10 times larger than in the Cr_2O_3 ground state. Huge values can be observed in the Cr MCs, even

Table 5.6: Magnetic charges Z^m of the M atoms in $(Cr_{1-x}M_x)_2O_3$ (M=Fe/Ti/Cr). All tensors are given in $10^{-2}\,\mu_B/Å$. Shown in parentheses are the symmetry of the M atom as well as the corresponding number of equivalent positions. Highlighted in bold are the tensors that can be obtained by symmetry operations of the tensor of M_1.

Compound	M_1	M_2	M_3	M_4
Cr_2O_3 (3, 1)	$\begin{pmatrix} 7.3 & -6.3 & 0.0 \\ 6.3 & 7.3 & 0.0 \\ 0.0 & 0.0 & 0.0 \end{pmatrix}$	$\begin{pmatrix} \mathbf{7.3} & \mathbf{6.3} & \mathbf{0.0} \\ \mathbf{-6.3} & \mathbf{7.3} & \mathbf{0.0} \\ \mathbf{0.0} & \mathbf{0.0} & \mathbf{0.0} \end{pmatrix}$	$\begin{pmatrix} \mathbf{7.3} & \mathbf{6.3} & \mathbf{0.0} \\ \mathbf{-6.3} & \mathbf{7.3} & \mathbf{0.0} \\ \mathbf{0.0} & \mathbf{0.0} & \mathbf{0.0} \end{pmatrix}$	$\begin{pmatrix} \mathbf{7.3} & \mathbf{-6.3} & \mathbf{0.0} \\ \mathbf{6.3} & \mathbf{7.3} & \mathbf{0.0} \\ \mathbf{0.0} & \mathbf{0.0} & \mathbf{0.0} \end{pmatrix}$
$(CrCrCrFe)_4O_6$ (3, 4)	$\begin{pmatrix} 0.0 & 86.2 & 0.0 \\ -86.0 & 0.0 & 0.0 \\ 0.0 & 0.0 & 0.0 \end{pmatrix}$	$\begin{pmatrix} 8.3 & 18.5 & 0.0 \\ -18.1 & 8.7 & 0.0 \\ 0.0 & 0.0 & 0.0 \end{pmatrix}$	$\begin{pmatrix} 22.0 & -21.4 & 0.0 \\ 20.6 & 22.7 & 0.0 \\ 0.0 & 0.0 & 0.0 \end{pmatrix}$	$\begin{pmatrix} 0.0 & -13.9 & 0.0 \\ 13.6 & 2.9 & 0.0 \\ 0.0 & 0.0 & -4.6 \end{pmatrix}$
$(CrCrFeFe)_4O_6$ (3, 2)	$\begin{pmatrix} 0.0 & 76.0 & 0.0 \\ -63.5 & 0.0 & 0.0 \\ 0.0 & 0.0 & 0.0 \end{pmatrix}$	$\begin{pmatrix} \mathbf{0.0} & \mathbf{-63.5} & \mathbf{0.0} \\ \mathbf{76.0} & \mathbf{0.0} & \mathbf{0.0} \\ \mathbf{0.0} & \mathbf{0.0} & \mathbf{0.0} \end{pmatrix}$	$\begin{pmatrix} 51.3 & 0.0 & 0.0 \\ 0.0 & 59.9 & 0.0 \\ 0.0 & 0.0 & 0.0 \end{pmatrix}$	$\begin{pmatrix} \mathbf{51.2} & \mathbf{0.0} & \mathbf{0.0} \\ \mathbf{0.0} & \mathbf{59.8} & \mathbf{0.0} \\ \mathbf{0.0} & \mathbf{0.0} & \mathbf{0.0} \end{pmatrix}$
Fe_2O_3 (3, 1)	$\begin{pmatrix} 31.0 & -32.5 & 0.0 \\ 28.9 & 29.8 & 0.0 \\ 0.0 & 0.0 & 0.0 \end{pmatrix}$	$\begin{pmatrix} \mathbf{31.0} & \mathbf{28.9} & \mathbf{0.0} \\ \mathbf{-32.5} & \mathbf{29.8} & \mathbf{0.0} \\ \mathbf{0.0} & \mathbf{0.0} & \mathbf{0.0} \end{pmatrix}$	$\begin{pmatrix} \mathbf{31.0} & \mathbf{28.9} & \mathbf{0.0} \\ \mathbf{-32.5} & \mathbf{29.8} & \mathbf{0.0} \\ \mathbf{0.0} & \mathbf{0.0} & \mathbf{0.0} \end{pmatrix}$	$\begin{pmatrix} \mathbf{31.0} & \mathbf{-32.5} & \mathbf{0.0} \\ \mathbf{28.9} & \mathbf{29.8} & \mathbf{0.0} \\ \mathbf{0.0} & \mathbf{0.0} & \mathbf{0.0} \end{pmatrix}$
$(CrCrTiTi)_4O_6$ (3, 2)	$\begin{pmatrix} 92.2 & -42.9 & 0.0 \\ 67.1 & 65.9 & 0.0 \\ 0.0 & 0.0 & -2.2 \end{pmatrix}$	$\begin{pmatrix} \mathbf{91.9} & \mathbf{44.8} & \mathbf{0.0} \\ \mathbf{-68.3} & \mathbf{64.9} & \mathbf{0.0} \\ \mathbf{0.0} & \mathbf{0.0} & \mathbf{1.7} \end{pmatrix}$	$\begin{pmatrix} -36.0 & -40.2 & 0.0 \\ 59.2 & -21.8 & 0.0 \\ 0.0 & 0.0 & 19.3 \end{pmatrix}$	$\begin{pmatrix} \mathbf{-36.3} & \mathbf{39.3} & \mathbf{0.0} \\ \mathbf{-58.7} & \mathbf{-22.8} & \mathbf{0.0} \\ \mathbf{0.0} & \mathbf{0.0} & \mathbf{19.2} \end{pmatrix}$

for only one Fe impurity. Interestingly, even the ↑↓↑↓ state of Fe_2O_3 exhibits values that are 4 times larger than in Cr_2O_3. Ti has the strongest effect on the MCs of all M atoms. The MCs of the O atoms presented in Table 5.7 are similarly accentuated. For the structures in which O_1 and O_2 are inequivalent, *i.e.* $(CrCrCrM)_4O_6$ and $(CrCrMM)_4O_6$, their respective MC tensors are fundamentally different, both on a symmetry level and on a quantitative level.

Table 5.7: Magnetic charges Z^m of the O atoms in $(Cr_{1-x}M_x)_2O_3$(M=Fe/Ti/Cr). All tensors are given in $10^{-2}\,\mu_B/Å$. Underneath the compound description, the atomic symmetry of the O position is given in parentheses, followed by the number of inequivalent O positions. In the case of Cr_2O_3 and Fe_2O_3, the tensors of all O atoms can be obtained by symmetry operations from O_1; for consistency, their Z^m are also shown for the O_2 atoms (highlighted in bold).

Compound	O_1	O_2
Cr_2O_3 (2, 1)	$\begin{pmatrix} -1.1 & 0.0 & 0.0 \\ 0.0 & -0.4 & 0.0 \\ 0.0 & -0.3 & 0.0 \end{pmatrix}$	$\begin{pmatrix} \mathbf{-1.1} & \mathbf{0.0} & \mathbf{0.0} \\ \mathbf{0.0} & \mathbf{-0.4} & \mathbf{0.0} \\ \mathbf{0.0} & \mathbf{-0.3} & \mathbf{0.0} \end{pmatrix}$
(CrCrCrFe) (1, 2)	$\begin{pmatrix} 0.0 & 0.0 & 50.5 \\ 0.0 & 50.0 & 9.4 \\ 3.2 & 0.6 & 1.5 \end{pmatrix}$	$\begin{pmatrix} -59.3 & 16.5 & 0.0 \\ 52.3 & -11.2 & -54.3 \\ 0.0 & -2.2 & 0.0 \end{pmatrix}$
(CrCrFeFe) (2, 2)	$\begin{pmatrix} 0.0 & 0.0 & 0.0 \\ 0.0 & 71.4 & 35.9 \\ 0.0 & 0.0 & 3.0 \end{pmatrix}$	$\begin{pmatrix} -87.3 & 0.0 & 0.0 \\ 0.0 & -41.5 & -97.8 \\ 0.0 & 0.0 & 0.0 \end{pmatrix}$
Fe_2O_3 (2, 1)	$\begin{pmatrix} -124.3 & 0.0 & 0.0 \\ 0.0 & 109.9 & -78.0 \\ 0.0 & -3.3 & -0.7 \end{pmatrix}$	$\begin{pmatrix} \mathbf{-124.3} & \mathbf{0.0} & \mathbf{0.0} \\ \mathbf{0.0} & \mathbf{109.9} & \mathbf{-78.0} \\ \mathbf{0.0} & \mathbf{-3.3} & \mathbf{-0.7} \end{pmatrix}$
(CrCrTiTi) (2, 2)	$\begin{pmatrix} -48.6 & 0.0 & 0.0 \\ 0.0 & 1.3 & -11.9 \\ 0.0 & -30.7 & 0.0 \end{pmatrix}$	$\begin{pmatrix} -6.4 & 0.0 & 0.0 \\ 0.0 & -1.2 & -11.9 \\ -35.5 & 0.0 & -12.7 \end{pmatrix}$

5.3 Analysis

5.3.1 Magnetoelectric Tensor

We can combine the previous results to compute the lattice-mediated ME response, as introduced in Section 3.1.3. In addition, the electronic response is computed via the Berry phase polarisation over the magnetic field. We arrive at the tensors given in Table 5.8. The total response is shown as the sum of the lattice and electronic contribution. Again, the LDA+U values for Cr_2O_3 from Chapter 3.3.3 are given as comparison. The tensor forms

agree with the shapes derived from symmetry analyses. The tensor elements that one expects to be zero by symmetry are well-described with a maximum value of $\alpha_{21}^{\text{latt}} = -0.062\,\text{ps}\,\text{m}^{-1}$ in the $(\text{CrCrTiTi})_4\text{O}_6$ compound. However, some pairs of elements, which should be equal (or equal and opposite sign), have a larger deviation from their symmetrical value (the largest difference being $\alpha_{11}^{\text{latt}}$ and $\alpha_{22}^{\text{latt}}$ in $\text{CrCrCrFe})_4\text{O}_6$ with values of $0.660\,\text{ps}\,\text{m}^{-1}$ and $0.397\,\text{ps}\,\text{m}^{-1}$, respectively). We note that the actual ME coupling tensors are quantitatively similar to each other and the Cr_2O_3 response, despite the fundamentally different magnetic charges. The largest element in the lattice-response of the Fe compounds is only 50 % larger than in Cr_2O_3 (α_{12} and α_{21} in $(\text{CrCrCrFe})_4\text{O}_6$). $(\text{CrCrTiTi})_4\text{O}_6$ exhibits larger transverse responses with up to $\alpha_{22}^{\text{latt}} \simeq 5.0\,\text{ps}\,\text{m}^{-1}$. The anomaly, however, is its longitudinal response: $\alpha_{\parallel}^{\text{latt}}$ reaches values almost *three orders of magnitude higher* than its Cr_2O_3 counterpart.

The electronic response is of the same order of magnitude as the lattice response. We note that the electronic tensors obey the symmetry constraints more strictly than the lattice tensors, the largest difference being α_{11} and α_{22} in Fe_2O_3 with a deviation of $< 6\,\%$. The electronic response is also of equal sign as the lattice response in all but the longitudinal contribution in $(\text{CrCrTiTi})_4\text{O}_6$, enhancing the ME response to values as large as $5.6\,\text{ps}\,\text{m}^{-1}$ in Fe_2O_3 and $9.6\,\text{ps}\,\text{m}^{-1}$ in $(\text{CrCrTiTi})_4\text{O}_6$. Again, $\alpha_{\parallel}$ in the Ti-based compound is anomalous: it is larger than its lattice-equivalent—but points in the opposite direction. The total longitudinal ME response is thus still large ($-2.3\,\text{ps}\,\text{m}^{-1}$), but negative.

5.3.2 Interpretation and Discussion

From a mode decomposition, we get further insights into the ionic mechanisms behind the ME coupling in the different compounds. Because the mixed com-

Table 5.8: Lattice-mediated, electronic, and total ME coupling tensors in M-substituted Cr_2O_3, $(Cr_{1-x}M_x)_2O_3$. All tensors are given in $ps\,m^{-1}$. The values for pure Cr_2O_3 are given for comparison. The numbers in parentheses underneath the compound labels are the magnetic point groups, followed by the band gaps.

Compound	α^{latt}	α^{el}	α^{tot}
Cr_2O_3 $(\bar{3}'m')$ 2.5 eV	$\begin{pmatrix} 0.918 & 0.000 & 0.000 \\ 0.000 & 0.918 & 0.000 \\ 0.000 & 0.000 & 0.005 \end{pmatrix}$	$\begin{pmatrix} 0.323 & 0.000 & 0.000 \\ 0.000 & 0.323 & 0.000 \\ 0.000 & 0.000 & 0.000 \end{pmatrix}$	$\begin{pmatrix} 1.241 & 0.000 & 0.000 \\ 0.000 & 1.241 & 0.000 \\ 0.000 & 0.000 & 0.005 \end{pmatrix}$
$(CrCrCrFe)_4O_6$ (3) 2.4 eV	$\begin{pmatrix} 0.660 & 1.455 & -0.001 \\ -1.440 & 0.397 & -0.021 \\ -0.001 & -0.011 & -0.098 \end{pmatrix}$	$\begin{pmatrix} 0.843 & 0.758 & 0.000 \\ -0.879 & 0.882 & 0.000 \\ 0.000 & 0.000 & 0.052 \end{pmatrix}$	$\begin{pmatrix} 1.503 & 2.213 & 0.000 \\ -2.334 & 1.279 & 0.000 \\ 0.000 & 0.000 & 0.150 \end{pmatrix}$
$(CrCrFeFe)_4O_6$ (32) 2.4 eV	$\begin{pmatrix} 1.177 & 0.015 & 0.000 \\ 0.014 & 1.268 & 0.000 \\ -0.001 & -0.001 & -0.096 \end{pmatrix}$	$\begin{pmatrix} 1.348 & 0.000 & 0.000 \\ 0.000 & 1.348 & 0.000 \\ 0.000 & 0.000 & 0.000 \end{pmatrix}$	$\begin{pmatrix} 2.412 & 0.000 & 0.000 \\ 0.000 & 2.434 & 0.000 \\ -0.001 & -0.001 & -0.096 \end{pmatrix}$
Fe_2O_3 $(\bar{3}'m')$ 1.6 eV	$\begin{pmatrix} 1.086 & 0.000 & 0.000 \\ 0.000 & 1.064 & 0.000 \\ 0.000 & 0.000 & -0.079 \end{pmatrix}$	$\begin{pmatrix} 4.475 & 0.000 & 0.000 \\ 0.000 & 4.189 & 0.000 \\ 0.000 & 0.015 & 0.005 \end{pmatrix}$	$\begin{pmatrix} 5.561 & 0.000 & 0.000 \\ 0.000 & 5.253 & 0.000 \\ 0.000 & 0.015 & -0.074 \end{pmatrix}$
$(CrCrTiTi)_4O_6$ (32) 0.6 eV	$\begin{pmatrix} 3.979 & 0.015 & 0.040 \\ -0.062 & 4.953 & 0.004 \\ -0.004 & -0.029 & 3.553 \end{pmatrix}$	$\begin{pmatrix} 4.434 & 0.000 & 0.000 \\ 0.000 & 4.659 & 0.000 \\ 0.000 & 0.000 & -5.874 \end{pmatrix}$	$\begin{pmatrix} 8.413 & 0.015 & 0.040 \\ -0.062 & 9.612 & 0.000 \\ -0.004 & -0.029 & -2.321 \end{pmatrix}$

pounds have different space groups than the $\bar{3}'m'$ phase, we take Fe_2O_3 as an example and compare the mode-decomposed responses to Cr_2O_3. The BECs and MCs are mapped onto the IR active modes $\Gamma^{\text{IR}} = 4E_u + 2A_{2u}$. Table 5.9 shows a comparison between the Cr_2O_3 and Fe_2O_3 mode-decomposed components of α. As to be expected from the atomic BECs, their mode-decomposed values are also similar in magnitude. All Fe_2O_3 modes have a higher frequency, but fall into the same regime as in Cr_2O_3.

The decomposition of the magnetic charges provides a powerful analysis of the ME behaviour. In particular, the cancellation that leads to the similar coupling tensors observed. We see that the E_u^2 mode, which exhibits a similarly strong magnetic response as the E_u^1 and E_u^3 modes, is magnetically active in the

Table 5.9: Comparison of the mode contribution for α^{latt} in Cr_2O_3 and Fe_2O_3. Acoustic modes were excluded. $U = 2.0\,\text{eV}$ in the case of Cr_2O_3, $U = 4.0\,\text{eV}$ for Fe_2O_3. The Born effective charges Z^e are given in e, the magnetic charges Z^m in $10^{-2}\,\mu_B/\text{Å}$, the eigenvalues C in $\text{eV}\,\text{Å}^{-2}$, and the coupling tensor α in $\text{ps}\,\text{m}^{-1}$.

Mode	Cr_2O_3				Fe_2O_3			
	Z^e	Z^m	C	α^{latt}	Z^e	Z^m	C	α^{latt}
${E_u}^1$	7.2	19.0	36	0.481	5.6	109.4	49	1.745
${E_u}^2$	3.1	29.6	24	0.464	1.4	-202.9	29	-1.380
${E_u}^3$	0.6	-5.1	18	-0.010	0.3	204.5	19	0.503
${E_u}^4$	0.3	-1.5	11	-0.006	0.6	31.7	13	0.189
All $\perp$				0.918				1.056
${A_{2u}}^1$	8.5	0.1	29	0.004	7.2	-1.0	31	-0.033
${A_{2u}}^2$	1.0	0.1	11	0.001	1.6	-3.3	12	-0.058
All $\parallel$				0.005				-0.091

opposite direction as the electric polarisability. The overall couplings cancel each other out and a value of $1.056\,\text{ps}\,\text{m}^{-1}$ remains for α^{latt}.

Let us discuss the connection of the electronic response to the band gap. As mentioned in the introduction, a hypothesis of this chapter was that by altering the band gap and bringing it close to zero, the electronic response might be increased. Underneath the compound labels and point groups in Table 5.8, a reminder of the band gaps from Table 5.3 is given. We do indeed see a correlation: the band gaps of the first three compounds are $\sim 2.5\,\text{eV}$ corresponding to values of $\alpha^{\text{el}} = 0.3\,\text{ps}\,\text{m}^{-1}$ to $1.3\,\text{ps}\,\text{m}^{-1}$. The band gap for the pure Fe_2O_3 configuration is 1.6 eV, with $\alpha^{\text{el}} = 4.5\,\text{ps}\,\text{m}^{-1}$; the band gap of the Ti-doped compound is 0.6 eV, with a transverse (longitudinal) $\alpha^{\text{el}} = 4.7\,\text{ps}\,\text{m}^{-1}$ ($\alpha^{\text{el}} = -5.9\,\text{ps}\,\text{m}^{-1}$).

In analogy with the diverging longitudinal response close to the magnetic phase transition in Cr_2O_3 at high pressures (Chapter 4), we speculate this is because the magnetic moments on the Ti impurities are close to zero for longitudinal modes (with the PM phase being the actual ground state of Ti_2O_3).

5.4 Summary

The full lattice- and electronic magnetoelectric tensors of M-substituted Cr in Cr_2O_3 (with M=Fe,Ti) in the ↑↓↑↓ magnetic structure are computed. A group-theoretical analysis provides the crystallographic and magnetic point groups of the compound structures, as well as the shape of their BEC, MC, and ME tensors.

Already the ground-state properties of the Fe-substituted Cr_2O_3 display an interesting behaviour; in agreement with literature [248], we find that the Fe atoms relax into high- or low-spin states, either as single impurities or in the limit of pure ↑↓↑↓ Fe_2O_3. The spin states correlate with the equilibrium volume, which is smaller (larger) for the low-spin (high-spin) configuration. Additionally, we find that the high-spin structures are unstable in the non-ground-state spin structure, hence they do not converge to the accuracy required for the computation of the ME response. In the case of Ti substitution, only the layered $(CrCrTiTi)_4O_6$ configuration stabilises *and* leads to a non-metallic ground state.

The analysis of the ME coupling tensors leads to interesting insights: the (atomic) magnetic charges exhibit elements that are about 10 times larger than the ones in Cr_2O_3. Investigating the (mode-decomposed) magnetic response shows that the large contributions map onto three transverse modes: two, which are polarisable in the same direction as the Born effective charges; one, which contributes negatively to the overall ME response. The effects cancel each other out and lead to a lattice-mediated response that is of the same order of magnitude as the one for Cr_2O_3.

The electronic response, however, is about one order of magnitude larger than the one for Cr_2O_3, when considering small-band-gap compounds. Fe_2O_3

and $(CrCrTiTi)_4O_6$ show band gaps of 1.6 eV and 0.6 eV, respectively, with a corresponding increase of the electronic response up to $5\,\mathrm{ps\,m^{-1}}$.

The present chapter is a first study and the number of data points to derive actual trends for doping needs to be expanded. A controlled study of the interplay of ME properties with the lattice, magnetic, and electronic structures in doped materials would build on the present work, which exemplifies results from previous chapters: the correlation of closing band gaps with the divergence of the electronic ME response and the divergence of the longitudinal lattice response close to a magnetic phase transition. To properly isolate the suggested effects, a more systematic doping study could shed light on the role of impurities in different parts of the response. We hope that these findings stimulate such research.

6 Spinflop Phase of Cr_2O_3

As already highlighted in the previous chapters, there is still a surprising amount of uncertainty surrounding the magnetoelectric (ME) effect in the prototypical ME material Cr_2O_3. In particular its behaviour throughout the T-H phase diagram is not well understood; in turn this hampers the systematic search for materials with a stronger ME response. The remarkable increase in parts of the ME response, which are usually overlooked, makes a more thorough understanding of the components of the response necessary, so that the magnitude of the response can be increased in a targeted way. By determining the microscopic contributions to the lattice response, further insight can be gained into the mechanisms behind the response. In this chapter, a set of density functional theory (DFT) calculations provides answers to the nature of the spinflop phase of Cr_2O_3—avoiding the problem of multiple domains that occur in experimental studies—and shows a novel chiral ME response, well-known in the multiferroics community, but not yet observed in pure MEs.

6.1 Preliminaries

6.1.1 Theoretical Background

At magnetic fields of 5.8 T in the rhombohedral [111]-direction, Cr_2O_3 undergoes a first-order phase transition into the so-called *spinflop* (SF) phase,

with spins ordered in the same G-type $\uparrow\downarrow\uparrow\downarrow$ pattern as the ground-state $\bar{3}'m'$ phase, but directed in the basal plane [270–273]. One possible spin orientation is shown in the middle panel of Fig. 6.1. Due to rotating the spins away from the z-axis into the plane, the three-fold symmetry around z is broken and the three oxygen atoms of one formula unit become inequivalent. We can define three equivalent coordinate systems, which are displayed in the right panel of Fig. 6.1 and lead to six equivalent 180° domains. The three possible directions of x_1, x_2, and x_3 are shown and the respective y_1, y_2, and y_3 complete the right-handed set with z directed along the rhombohedral [111] axis. The exact direction of the spins in the SF phase has not been clearly determined yet [274]: three possible orientations are along one of the surviving two-fold axes [90, 273], *i.e.* along one of the three oxygen atoms of the structural unit (shown in the middle panel of Fig. 6.1), perpendicular to the two-fold axis [275, 276], or in a generic direction. These configurations correspond to the magnetic structures $2'/m$, $2/m'$, and $\bar{1}'$, respectively. The authors of all aforementioned studies stress, however, that the measured responses are too small to give a definitive answer about the Cr magnetic-moment orientation.

Because the form of the magnetoelectric coupling tensor α depends on the magnetic point group of the crystal, ME experiments can be performed in order to clarify the magnetic structure of the SF phase. As opposed to the ME tensor form of the ground-state $\bar{3}'m'$ phase, the magnetic configurations in the SF cases allow for off-diagonal terms, which are indeed observed experimentally [277]. It was suggested in previous studies that the ME effect in the SF phase is associated with the appearance of a toroidal moment, as introduced in Section 1.2.2. The antisymmetric part of the ME coupling tensor, $\alpha_{ij} = -\alpha_{ji}$, *can* couple to the toroidal moment $\boldsymbol{T} = \sum_i \mathbf{r_i} \times \mathbf{S_i}$, where $\mathbf{S}_i$ are the spins of the ions at positions $\mathbf{r}_i$. Measurements of the ME response are therefore only an *indicator* for the appearance of a coupling to the toroidal

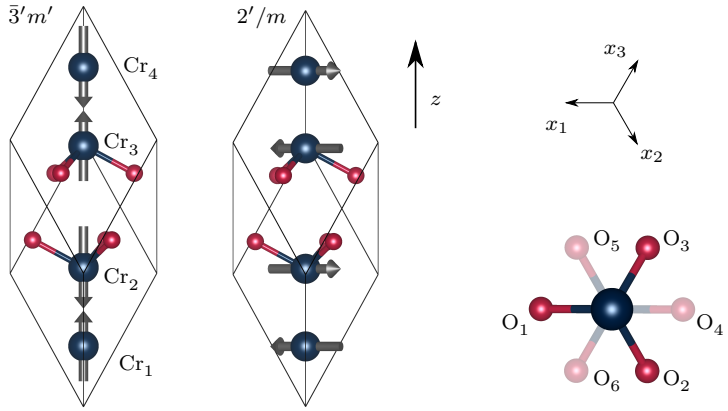


Figure 6.1: Structures of Cr_2O_3. Left panel: rhombohedral primitive cell of Cr_2O_3 with arrows indicating the AFM coupled Cr magnetic moments along z. The magnetic point group is $\bar{3}'m'$. Two 180° domains are possible, linked via time reversal symmetry. Middle panel: $2'/m$ phase, one of the spinflop phases, with spins aligned in the basal plane, thus breaking the 3-fold symmetry. Displayed here is the $2'/m$ configuration with spins along the x-axis. Right panel: view along z (the half-transparent O atoms belong to the "lower" structural unit). Due to the symmetry breaking, O_2 is no longer a symmetry image of O_1. However, when the spins are aligned along x, O_2 and O_3 can still be obtained by each other by rotating around x.

moment. However, antisymmetric tensor components do not uniquely result in a ferrotoroidic order [72]. In Ref. [277], antisymmetric contributions of α are observed and the author therefore (wrongly) concludes that the SF phase of Cr_2O_3 is toroidal.

6.1.2 Group-Theory Analysis

As introduced in Section 1.2.3, the form of the linear ME tensor α_{ij} can be predicted entirely by symmetry once the magnetic point group is known [90, 120]. The symmetrisation in Section 3.1.1 for the AFM equilibrium phase of Cr_2O_3 in low applied magnetic fields (LF phase) shows that α_{ij} is diagonal and α_{11} and α_{22} are equal (left panel of Fig. 6.3). What follows is the derivation of the *spinflop* tensor forms for the magnetic charges (MCs) Z^m and the overall ME coupling tensor based on a group-theoretical analysis.

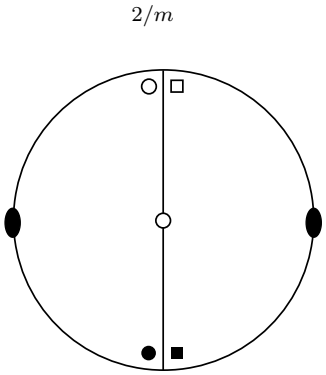


Figure 6.2: Stereographic projection of the crystallographic point group $2/m$, the spinflop phase of Cr_2O_3, modified from Refs. [57, 207]. The generating elements are $2 \parallel x$ and $m \perp x$.

We start by determining the crystallographic space and point groups of the SF phases. By rotating the Cr spins into the basal plane, the three-fold symmetry of the $R\bar{3}c$ phase is broken. The remaining symmetry elements are the two-fold rotation and the glide plane c, thus generating the crystallographic space (point) group $C2/c$ ($2/m$). The stereographic projection of $2/m$ is shown in Fig. 6.2. To determine the *magnetic* space group for the high-symmetry SF phases,[1] we start with the configuration where the spins are directed along x, *i.e.* the remaining two-fold axis. Rotating around the x axis at the origin maps one "up" spin to a "down" spin, so that 2 becomes $2'$. The spins point out of the glide plane, meaning that they stay unchanged when we apply c, leading to the overall magnetic space group $C2'/c$ for spins along x, which corresponds to the magnetic *point* group $2'/m$. In the second case (spins along y), let us imagine the spins in the basal plane perpendicular to the two-fold axis. Rotating around the origin preserves the handedness of the spins, thus keeping the unprimed 2 element. The spins lie, however, in the glide plane $\perp x$, leading to a handedness change when we act upon c, making it c'. The second SF space (point) group is therefore $C2/c'$ ($2/m'$).

Because the crystallographic symmetry remains during the phase transition (space group $R\bar{3}c$), quantities linked to the crystal rather than the mag-

[1] The generic $\bar{1}'$ configuration leads to a tensor in which all components are allowed by symmetry

Table 6.1: Wyckoff positions (WP) for the Cr and two O atoms in the $\bar{3}'m'$, the $2'/m$, and the $2/m'$ magnetic phases of Cr_2O_3. The corresponding on-site symmetry is displayed in the second panels.

	$\bar{3}'m'$		$2'/m$		$2/m'$	
Atom	WP	Symmetry	WP	Symmetry	WP	Symmetry
Cr	$4c$	$3 \parallel z$	$8f$	1	$8f$	1
O_1	$6e$	$2 \parallel x$	$4e$	$2' \parallel x$	$4e$	$2 \parallel x$
O_2	$6e$	$2 \parallel x$	$8f$	1	$8f$	1

netic phase obey the same symmetry requirements regardless of the magnetic configuration.[2] The Born effective charges (BECs) therefore have the same tensor forms as in the LF $\bar{3}'m'$ phase. The symmetry elements of the *magnetic* space group change and so do the Wyckoff positions hence the on-site symmetries when determining magnetic properties. The three inequivalent Wyckoff positions of the $C2'/c$ and $C2/c'$ space groups[3] are $8f$ for the Cr atoms, $4e$ for the O atoms on the two-fold axis, and $8f$ for the other O atoms. A summary of the Wyckoff positions including their respective symmetries is given in Table 6.1.

We can repeat the tensor symmetrisation of Chapter 3 to determine the tensor forms of the magnetic charges in the $2'/m$ and $2/m'$ phases. Because the Cr and O_2 atoms have the magnetic on-site symmetry 1 in both SF phases (Table 6.1), their MC tensors are not restricted and can take a general form. The O_1 atom obeys the two-fold symmetry—primed and unprimed in the $2'/m$ phase and the $2/m'$ phase, respectively. We symmetrise Z^m under $2 \parallel x$ with its transformation matrix $T_{ij}(2)$, which should leave Z^m (in the following again "Z") invariant:

$$Z'_{ij} = \|(T_{ij}(2)\| \underbrace{(\mp 1)}_{\text{Time inversion}} T_{ik}(2) Z_{jl} T_{kl}(2)$$

[2] The structural order parameter occurring as a second-order effect is negligible, as shown in the results Section 6.2.1.

[3] The unit cell in the monoclinic structures contains twice as many atoms as the rhombohedral one, so that the number of atomic positions add up to 20 instead of 10.

$$
\begin{aligned}
&= \mp \begin{pmatrix} 1 & 0 & 0 \\ 0 & -1 & 0 \\ 0 & 0 & -1 \end{pmatrix} \begin{pmatrix} Z_{11} & Z_{12} & Z_{13} \\ Z_{21} & Z_{22} & Z_{23} \\ Z_{31} & Z_{32} & Z_{33} \end{pmatrix} \begin{pmatrix} 1 & 0 & 0 \\ 0 & -1 & 0 \\ 0 & 0 & -1 \end{pmatrix} \\
&= \begin{cases} \begin{pmatrix} -Z_{11} & Z_{12} & Z_{13} \\ Z_{21} & -Z_{22} & -Z_{23} \\ Z_{31} & -Z_{32} & -Z_{33} \end{pmatrix} & \text{for } 2'/m \\ \begin{pmatrix} Z_{11} & -Z_{12} & -Z_{13} \\ -Z_{21} & Z_{22} & Z_{23} \\ -Z_{31} & Z_{32} & Z_{33} \end{pmatrix} & \text{for } 2/m' \end{cases} \\
&\equiv \begin{pmatrix} Z_{11} & Z_{12} & Z_{13} \\ Z_{21} & Z_{22} & Z_{23} \\ Z_{31} & Z_{32} & Z_{33} \end{pmatrix}, \qquad (6.1)
\end{aligned}
$$

which leads to two inverted tensor forms for each spinflop phase, Fig. 6.3.

In order to determine the symmetry of α, the point group symmetries have to be taken into account. If we compare the symmetry elements of the magnetic charges with the ones of the point group, we see that we can combine the symmetrisations: in addition to the on-site symmetry $2' \parallel x$ ($2 \parallel x$) in the $2'/m$ ($2/m'$) phase, the whole point group is generated if we add $m \perp x$ ($m' \perp x$). The respective transformation matrices are equal.[4] The tensor forms of α in both SF phases obey therefore the same symmetry requirements as their respective $Z^m(O_1)$ tensors. A summary of all possible tensor forms is given in Fig. 6.3.

[4] A mirror operation is a two-fold rotation followed by inversion, inversion being coupled to time reversal in the present point groups. In the case of $2'/m$, $2'$ is therefore followed by m (being $2\bar{1}'$) and in the case of $2/m'$, 2 is followed by m' (being $2'\bar{1}'$).

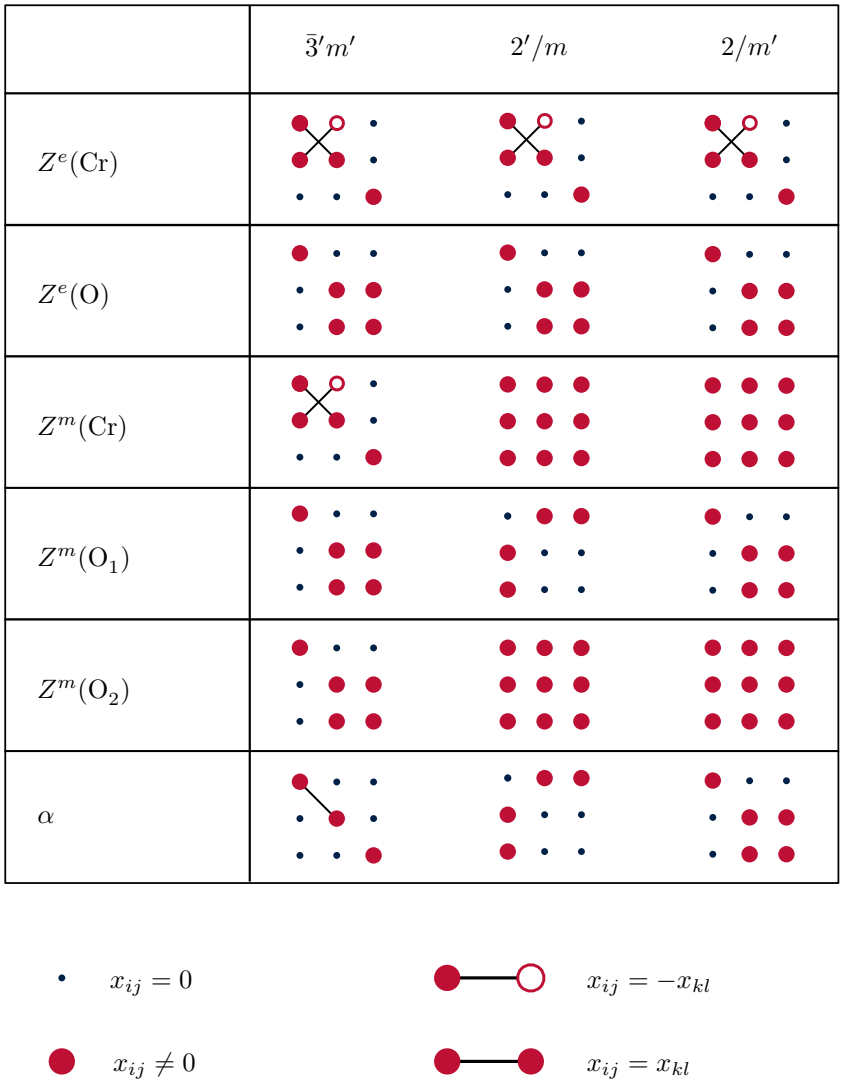


Figure 6.3: Tensor forms of the Born effective charges Z^e and magnetic charges Z^m (both based on the site symmetry of the atom) and of the overall ME coupling tensor α (based on the point group of the magnetic crystal class).

6.2 Results

6.2.1 Ground-State Properties

Similar computational parameters are chosen to model the spinflop phases as in the previous chapter: the LDA functional with a plane-wave cut-off energy of 550 eV, a $4 \times 4 \times 4$ Γ-centred Monkhorst-Pack k-point grid, and a tight convergence for the structural relaxation with a force-threshold of $\Delta F \leq 5 \times 10^{-6}\,\mathrm{eV\,Å^{-2}}$. Tetrahedron smearing is employed with a broadening width of 0.05 eV. Again, the BECs and the interatomic force-constant (IFC) matrix are calculated for the $\bar{3}'m'$ ground state treating spins collinearly and thus neglecting spin-orbit coupling (SOC). The argument is similar to the one given in Chapter 3, SOC is shown to have a negligible effect on the BECs and the IFC matrix. The effect of the spinflop case is, however, tested and results in a similarly small effect. This is also to be expected, as a coupling of the spins to the lattice is small in Cr_2O_3 (see next paragraph). For the computation of the magnetic charges, SOC is included, a Zeeman magnetic field is applied, and the Hellman-Feynman forces on each atom are computed. Using the same BECs and IFC matrix for all three magnetic phases leads to the positive side effect that we are able to isolate the influence of the magnetic charges on the overall magnetoelectric tensor, in turn allowing to gain further insight into the microscopic role of the recently defined "dynamical magnetic charges". The electronic ME contribution α^{el} is calculated "directly" from Eq. 3.5 via the change in Berry phase polarisation over H with fixed ionic positions [210].

To answer the question of the effect of the different spin configurations on the lattice properties of Cr_2O_3, the change in energy, lattice parameter, rhombohedral angle, cell volume, Cr_1-Cr_2, Cr_2-Cr_3, and Cr_2-O_1 bond lengths, and the angle of the oxygen triangle centred at Wyckoff position $4e$ are given in

Table 6.2: Absolute and relative *change* in ground-state properties when going from the $\bar{3}'m'$ to the SF phases (both SF phases lead to the same distortions). E_{tot}[meV], $a_{\mathrm{lat}}^{\mathrm{rhomb}}$[mÅ], $\alpha_{\mathrm{lat}}^{\mathrm{rhomb}}[10^{-3\circ}]$, $c_{\mathrm{lat}}^{\mathrm{hex}}$[mÅ], $V_{\mathrm{cell}}^{\mathrm{rhomb}}[10^{-3}\,\text{Å}^3]$, Δ[mÅ], and $\angle[10^{-3\circ}]$ denote the total energy, lattice parameter, rhombohedral angle, cell volume, bond lengths, and the angle in the oxygen triangle centred at Wyckoff position $4e$, respectively. Absolute changes given in the respective unit, relative values are divided by the $\bar{3}'m'$ value and given in dimensionless 10^{-4}.

	E_{tot}	$a_{\mathrm{lat}}^{\mathrm{rhomb}}$	$\alpha_{\mathrm{lat}}^{\mathrm{rhomb}}$	$c_{\mathrm{lat}}^{\mathrm{hex}}$	$V_{\mathrm{cell}}^{\mathrm{rhomb}}$	$\Delta(\mathrm{Cr_1\text{-}Cr_2})$	$\Delta(\mathrm{Cr_1\text{-}Cr_2})$	$\Delta(\mathrm{Cr_2\text{-}O_1})$	$\angle \mathrm{O_1O_2O_3}$
Abs.	0.5	0.1	-3.9	0.6	5.8	0.1	0.2	0.1	0.2
Rel.	5.0	0.2	-0.8	0.4	0.7	0.2	0.5	0.3	2.5

Table 6.2. All values were reproduced in the $2'/m$ phase and the $2/m'$ phase, as well as their respective 180° domains. The magnetic phases have indeed a measurable effect on the lattice properties. From $\angle \mathrm{O_1O_2O_3}$, we can see the breaking of the three-fold symmetry: in the $\bar{3}'m'$ phase, the oxygen triangle was perfectly equilateral; in the SF phases, the angle at $\mathrm{O_1}$—the oxygen atom on the two-fold axis—widened slightly to 60.0002°. Yet all changes are below 0.5 ‰, supporting the choice to use the collinear BECs and IFC matrix in the following analysis.

It is worth noting that our results agree with two studies on magnetostriction at the SF transition, which studied the change in hexagonal lattice parameter c and/or the change in volume V. The authors measured a discontinuity in c and V at the critical field when increasing the magnetic field along z. Ref. [278] reports a value of $\Delta c/c$ of 2.8×10^{-5}, Ref. [272] measured it to be $(3.5 \pm 0.4) \times 10^{-5}$ at 4.2 K, both of which are notably similar to the present result of 4×10^{-5}. Our value for $\Delta V/V = 7 \times 10^{-5}$ is also in good agreement with the 2.0×10^{-5} measured in Ref. [272].

6.2.2 Magnetoelectric Response

The results for the magnetic charges are given in Table 6.3. The $Z^m(\mathrm{O_2})$ in the LF phase are given for completeness; in the LF phase, $\mathrm{O_1}$ and $\mathrm{O_2}$ are

Table 6.3: Magnetic charges Z^m in the $\bar{3}'m'$, $2'/m$, and $2/m'$ magnetic phases of Cr_2O_3. All Z^m are given in $10^{-2}\,\mu_B$ /Å. The last row demonstrates how the three-fold symmetry is broken in the SF phases: $Z^m(O_2)$ is rotated by 120°, which, in the $\bar{3}'m'$ phase, leads to the exact same result as $Z^m(O_1)$. This is not the case for the SF phases, where C_3 is not a symmetry operation of the space groups anymore.

Phase	$\bar{3}'m'$	$2'/m$	$2/m'$
$Z^m(\mathrm{Cr})$	$\begin{pmatrix} 2.4 & 5.6 & 0.0 \\ -5.6 & 2.4 & 0.0 \\ 0.0 & 0.0 & 0.0 \end{pmatrix}$	$\begin{pmatrix} 0.0 & -0.1 & -2.3 \\ 0.0 & 0.0 & 5.6 \\ 0.1 & 18.9 & 0.0 \end{pmatrix}$	$\begin{pmatrix} -0.1 & 0.0 & -5.6 \\ 0.0 & 0.0 & -2.3 \\ -18.8 & 0.2 & 0.0 \end{pmatrix}$
$Z^m(\mathrm{O}_1)$	$\begin{pmatrix} -2.7 & 0.0 & 0.0 \\ 0.0 & -0.5 & 0.0 \\ 0.0 & -2.7 & 0.0 \end{pmatrix}$	$\begin{pmatrix} 0.0 & -1.5 & 3.0 \\ -0.3 & 0.0 & 0.0 \\ -0.1 & 0.0 & 0.0 \end{pmatrix}$	$\begin{pmatrix} 1.7 & 0.0 & 0.0 \\ 0.0 & -0.3 & 0.1 \\ 0.0 & -0.1 & 2.5 \end{pmatrix}$
$Z^m(\mathrm{O}_2)$	$\begin{pmatrix} -1.1 & 1.0 & 0.0 \\ 1.0 & -2.2 & 0.0 \\ 2.3 & 1.4 & 0.0 \end{pmatrix}$	$\begin{pmatrix} 0.3 & 0.8 & 0.8 \\ 0.2 & -1.4 & -1.2 \\ -0.1 & -0.1 & -2.2 \end{pmatrix}$	$\begin{pmatrix} -0.7 & 0.3 & -1.2 \\ 1.3 & 0.2 & 2.2 \\ -0.1 & -0.1 & -1.3 \end{pmatrix}$
$C_3 \cdot Z^m(\mathrm{O}_2)$	$\begin{pmatrix} -2.7 & 0.0 & 0.0 \\ 0.0 & -0.5 & 0.0 \\ 0.0 & -2.7 & 0.0 \end{pmatrix}$	$\begin{pmatrix} -1.4 & 0.8 & -1.4 \\ 0.2 & 0.3 & -0.1 \\ 0.0 & 0.1 & -2.2 \end{pmatrix}$	$\begin{pmatrix} -0.7 & -1.3 & 2.5 \\ -0.3 & 0.2 & -0.1 \\ 0.0 & 0.1 & -1.3 \end{pmatrix}$

symmetry images of each other and can thus be obtained from one another by the three-fold rotation, *i.e.* a 120° rotation around z. The MCs are in good agreement with our group-theoretical analysis from Fig. 6.3. We notice some similarities and differences in the MCs: firstly, one "large" transverse term of $18.9 \times 10^{-2}\,\mu_B$ /Å ($18.8 \times 10^{-2}\,\mu_B$ /Å) appears in the $2'/m$ ($2/m'$) phase, which is not present in the $\bar{3}'m'$ phase. Secondly, two values seem similar in all three phases: $2.4 \times 10^{-2}\,\mu_B$ /Å ($2.3 \times 10^{-2}\,\mu_B$ /Å) in the LF (SF) phases and $5.6 \times 10^{-2}\,\mu_B$ /Å in all three phases.

With the microscopic contributions, the lattice-mediated magnetoelectric coupling tensor can be determined for the low-field and spinflop phases. As shown in Chapter 3, the electronic contribution to α can be sizeable, particularly in comparison with the underestimated LDA lattice response. We therefore combine the lattice-mediated and electronic coupling tensor to compute the total coupling tensor α^{tot}. The results are shown in Table 6.4. Again, the

Table 6.4: Lattice-mediated, electronic, and total magnetoelectric coupling tensor, α^{latt}, α^{el}, and α^{tot}, respectively, in the $\bar{3}'m'$, $2'/m$, and $2/m'$ magnetic phases of Cr_2O_3. The ME tensors are given in $\text{ps}\,\text{m}^{-1}$. The underlined numbers highlight the transverse responses that occur in every configuration. Elements in italics are longitudinal responses, when the field is applied along x, y, or z in the $2'/m$, $2/m'$, and $\bar{3}'m'$ phase, respectively. Highlighted by bold fonts are transverse in-plane contributions, which are only present in the SF phases.

Phase	$\bar{3}'m'$	$2'/m$	$2/m'$
α^{latt}	$\begin{pmatrix} \underline{0.310} & 0.000 & -0.001 \\ 0.000 & \underline{0.310} & 0.000 \\ 0.000 & 0.000 & \textit{0.005} \end{pmatrix}$	$\begin{pmatrix} -0.001 & \mathbf{-0.012} & \underline{-0.309} \\ 0.001 & -0.001 & 0.000 \\ \textit{0.019} & 0.000 & 0.000 \end{pmatrix}$	$\begin{pmatrix} \mathbf{-0.012} & 0.000 & 0.000 \\ 0.000 & -0.002 & \underline{-0.309} \\ 0.000 & \textit{0.019} & 0.001 \end{pmatrix}$
α^{el}	$\begin{pmatrix} \underline{0.525} & 0.000 & 0.000 \\ 0.000 & \underline{0.525} & 0.000 \\ 0.000 & 0.000 & \textit{0.000} \end{pmatrix}$	$\begin{pmatrix} 0.000 & \mathbf{-0.028} & \underline{-0.518} \\ 0.000 & 0.000 & 0.000 \\ \textit{0.062} & 0.000 & 0.000 \end{pmatrix}$	$\begin{pmatrix} \mathbf{-0.028} & 0.000 & 0.000 \\ 0.000 & 0.000 & \underline{-0.518} \\ 0.000 & \textit{0.062} & 0.000 \end{pmatrix}$
α^{tot}	$\begin{pmatrix} \underline{0.835} & 0.000 & -0.001 \\ 0.000 & \underline{0.835} & 0.000 \\ 0.000 & 0.000 & \textit{0.005} \end{pmatrix}$	$\begin{pmatrix} -0.001 & \mathbf{-0.040} & \underline{-0.827} \\ 0.001 & -0.001 & 0.000 \\ \textit{0.081} & 0.000 & 0.000 \end{pmatrix}$	$\begin{pmatrix} \mathbf{-0.040} & 0.000 & 0.000 \\ 0.000 & -0.002 & \underline{-0.827} \\ 0.000 & \textit{0.081} & 0.001 \end{pmatrix}$

form of the tensors are as predicted to within $0.001\,\text{ps}\,\text{m}^{-1}$, which we take to be our computational uncertainty (bottom row of Fig. 6.3 and Table 6.4). Taking into account the change in numerical parameters, the coupling tensors of the $\bar{3}'m'$ phase are similar to those predicted in Chapter 3: the transverse electronic contribution $\alpha_{\perp}^{\text{el}} = 0.525\,\text{ps}\,\text{m}^{-1}$ is slightly larger than the lattice contribution of $\alpha_{\perp}^{\text{latt}} = 0.310\,\text{ps}\,\text{m}^{-1}$, whereas the longitudinal part is $\alpha_{\parallel}^{\text{latt}} = 0.005\,\text{ps}\,\text{m}^{-1}$ ($\alpha_{\parallel}^{\text{el}} = 0.000\,\text{ps}\,\text{m}^{-1}$) in the case of the lattice (electronic) contribution.

For a mode decomposition, let us consider the symmetry constraints of the MC and BEC tensors. Because in the $\bar{3}'m'$ phase all improper rotations are coupled to time-reversal symmetry, the MCs are of the same form as the BECs. Therefore, those phonon modes that couple to the electric field, *i.e.* the infrared (IR) active modes, are also the ones that couple to the magnetic field. As introduced in Chapter 3, the IR active phonon modes in the $R\bar{3}c$ crystallographic space group are

$$\Gamma^{\mathrm{IR}} = 4E_u + 2A_{2u}. \tag{6.2}$$

In the SF phases, when x and y are no longer equivalent, we observe changes in the magneto-active response from the mode decomposition of the BECs and the MCs. The degeneracy of the IR active E_u modes is removed for the magnetic response, and other modes become magneto-active in x, y, or z. We also find that the exceptionally large component in the Z^m(Cr) (the 32 and 31 component in the $2'/m$ and $2/m'$ phase, respectively) maps onto magneto-active modes that are mutually exclusive to the IR active ones. That value has therefore no effect on the coupling tensor. Even though the magnetic charge tensors are quite dissimilar, this leads to the surprising similarity of the coupling tensors.

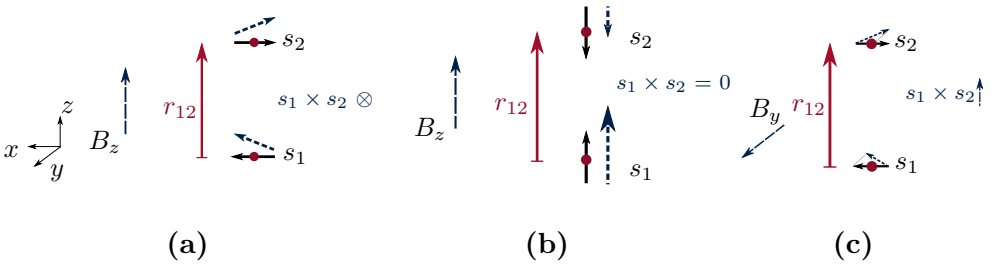
6.3 Analysis

The following analysis is a result of the collaboration with Prof. Paolo Radaelli, who derived the tensor forms of the phenomenological contributions to α in Section 6.3.1 and determined the Landau invariants in Section 6.3.2.

6.3.1 Microscopic Contributions

On the basis of the ME tensors, important observations can be made. Firstly, the ME tensor α is *not* what one would expect from a toroidal moment. There is clearly a toroidal (antisymmetric) component, but this is identical in magnitude to the traceless symmetric component. This should not be particularly surprising, since the toroidal mechanism $\mathbf{P} = \boldsymbol{T} \times \mathbf{H}$ does not capture the large difference between the longitudinal and transverse susceptibilities.

Secondly, the magnitudes of the "large" elements of the ME tensor ($0.835\,\mathrm{ps\,m^{-1}}$ and $0.827\,\mathrm{ps\,m^{-1}}$) are the same (within error) in the two SF



(a) **(b)** **(c)**

Figure 6.4: Mechanisms for the magnetisation response to an external magnetic field identifying the two (three) significant terms in α in the LF (SF) phase(s). (**a**) Antisymmetric DM response: a magnetic field is applied along z, transverse to the spin direction, making them cant in the xz-plane and form a part of a cycloid propagating around y. (**b**) Longitudinal response: the magnetic field is applied along the spin direction, modifying their magnetic-anisotropy field and therefore the value of their magnetic moment. (**c**) Chiral response: in the spinflop phases, a second transverse response is allowed. If the spins are aligned along x, a field along y makes them cant in the xy-plane and form part of a helix propagating around z.

phases *and* in the LF phase. In fact, all these large ME responses can be approximated by the following compact expression:

$$\alpha \approx 0.8\,\mathrm{ps\,m^{-1}} \begin{pmatrix} \hat{m}_z & 0 & -\hat{m}_x \\ 0 & \hat{m}_z & -\hat{m}_y \\ 0 & 0 & 0 \end{pmatrix}, \tag{6.3}$$

where $\hat{m}_x$, $\hat{m}_y$ and $\hat{m}_z$ are the components of a unit vector parallel to the spin on the Cr($4c$) atom at Wyckoff position 0.1590.

A clue as to the origin of this tensor form of "large" components is the fact that all of the components correspond to a *transverse* spin response in the plane containing both the spins and z, so that the rotated spins (under the action of the magnetic field) can be thought of as forming a segment of a cycloid. The schematic representation is shown in Fig. 6.4a for the example of a magnetic field along z in the $2'/m$ phase, which makes the spins rotate in the xz-plane; the same mechanism holds equally true for the LF or the other SF phase, *e.g.* H applied along x or y in the $\bar{3}'m'$ phase makes the spins form a cycloid rotating in the xz- or yz-plane.

We can show that the tensor form in Eq. 6.3 is exactly the one predicted from the spin current [66] or inverse Dzyaloshinskii-Moriya (DM) [64] mechanisms (Section 1.2.4), which are well known in the context of multiferroics. We write the transverse response of the magnetisation $\mathbf{m}_i$ on Cr site i as

$$\begin{aligned}\Delta\mathbf{m}_i &= \chi^{\perp}\frac{\mathbf{m}_i\times(\mathbf{H}\times\mathbf{m}_i)}{|\mathbf{m}_i|^2}\\ &= \chi^{\perp}\frac{\mathbf{H}(\mathbf{m}_i\cdot\mathbf{m}_i)-\mathbf{m}_i\,(\mathbf{H}\cdot\mathbf{m}_i)}{|\mathbf{m}_i|^2}\\ &= \chi^{\perp}\left(\mathbf{H}-\frac{\mathbf{m}_i\,(\mathbf{H}\cdot\mathbf{m}_i)}{|\mathbf{m}_i|^2}\right),\end{aligned} \tag{6.4}$$

$\chi^{\perp}$ being the transverse susceptibility. Using $\mathbf{m}_1=\mathbf{m}+\Delta\mathbf{m}$ and $\mathbf{m}_2=-\mathbf{m}+\Delta\mathbf{m}$, the inverse DM polarisation is

$$\begin{aligned}\mathbf{P} &= \mu\mathbf{r}_{12}\times(\mathbf{m}_1\times\mathbf{m}_2)\\ &= \mu\mathbf{r}_{12}\times\{(-\mathbf{m}\times\mathbf{m})+(\mathbf{m}\times\Delta\mathbf{m})-(\Delta\mathbf{m}\times\mathbf{m})+(\Delta\mathbf{m}\times\Delta\mathbf{m})\}\\ &= 2\mu\chi^{\perp}\mathbf{r}_{12}\times\left\{\mathbf{m}\times\left(\mathbf{H}-\frac{\mathbf{m}(\mathbf{H}\cdot\mathbf{m})}{|\mathbf{m}_i|^2}\right)\right\}\\ &= 2\mu\chi^{\perp}\mathbf{r}_{12}\times(\mathbf{m}\times\mathbf{H})\\ &= 2\mu\chi^{\perp}\left(\mathbf{m}\,(\mathbf{H}\cdot\mathbf{r}_{12})-\mathbf{H}\,(\mathbf{m}\cdot\mathbf{r}_{12})\right),\end{aligned} \tag{6.5}$$

μ being a coupling constant and, in the case of Cr_2O_3, $\mathbf{r}_{12}\parallel z$ connecting the Cr atoms. With this, the ME tensor takes the form:

$$\begin{aligned}\boldsymbol{\alpha}=\frac{\partial\mathbf{P}}{\partial\mathbf{H}} &= 2\mu\chi^{\perp}\left(\mathbf{m}\otimes\mathbf{r}_{12}-\mathbf{m}\cdot\mathbf{r}_{12}\mathbb{1}\right)\\ &= 2\mu\chi^{\perp}\left\{\begin{pmatrix}m_x\\m_y\\m_z\end{pmatrix}[0,0,1]-\left[\begin{pmatrix}m_x\\m_y\\m_z\end{pmatrix}\cdot\begin{pmatrix}0\\0\\1\end{pmatrix}\right]\mathbb{1}\right\}\\ &= 2\mu\chi^{\perp}\left\{\begin{pmatrix}0&0&m_x\\0&0&m_y\\0&0&m_z\end{pmatrix}-\begin{pmatrix}m_z&0&0\\0&m_z&0\\0&0&m_z\end{pmatrix}\right\}\end{aligned}$$

$$= -2\mu\chi^{\perp} \begin{pmatrix} m_z & 0 & -m_x \\ 0 & m_z & -m_y \\ 0 & 0 & 0 \end{pmatrix}, \tag{6.6}$$

where $\otimes$ is the outer (tensor) product and $\mathbb{1}$ is the unit tensor. Eq. 6.6 and Eq. 6.3 have exactly the same form, including the non-trivial sign of the tensor elements.

In all phases, the ME tensor α has a small longitudinal term (*i.e.* with the field H parallel to the spins) of magnitude $0.005\,\mathrm{ps\,m^{-1}}$ ($0.081\,\mathrm{ps\,m^{-1}}$) for the LF (SF) phase(s), which generates $P \parallel z$ in all cases:

$$\boldsymbol{\alpha} = \mu\chi^{\parallel} \begin{pmatrix} 0 & 0 & 0 \\ 0 & 0 & 0 \\ m_x & m_y & m_z \end{pmatrix}. \tag{6.7}$$

The mechanism is shown in Fig. 6.4b for the $\bar{3}'m'$ case, and can be equally applied to the SF phases. In the ground state, this is associated with a small longitudinal susceptibility of relativistic origin [76], while at finite temperatures, the symmetric Heisenberg exchange makes this term become the dominant contribution to α in the LF phase, as shown in Ref. [208]. Indeed, our calculations show that without SOC, all components in all phases go to zero.

Considerably more interesting is the additional *in-plane transverse* term of magnitude $-0.012\,\mathrm{ps\,m^{-1}}$, which is only present in the SF phases. Here, the field H lies in the xy-plane perpendicular to the spins and generates $P \parallel x$, *i.e.* parallel to the surviving 2-fold axis of the monoclinic structure. The mechanism is shown in Fig. 6.4c for the $2'/m$ phase, but holds true for both SF phases. Upon application of a magnetic field in the in-plane transverse direction, the rotated spins can be thought of as forming a segment of a helix propagating along and spiralling around z.

This small term is due to the breaking of axial symmetry upon SF magnetic ordering, coupled with the breaking of chiral symmetry upon application of a magnetic field in the in-plane transverse direction: as already mentioned, SF magnetic ordering breaks the 3-fold symmetry of the Cr_2O_3 parent phase. Consequently, the *crystallographic* symmetry is also lowered, due to coupling of the staggered magnetisation with a structural order parameter, which has the transformation properties of an axial vector $\mathbf{A} = A_x\hat{\mathbf{x}} + A_y\hat{\mathbf{y}} + A_z\hat{\mathbf{z}}$. Expanding the Landau free energy with respect to $\mathbf{A}$ leads to

$$F = -\kappa((m_x^2 - m_y^2)A_x - 2m_x m_y A_y) + \nu(A_x^2 + A_y^2), \tag{6.8}$$

when $\mathbf{m}$ is directed along x or y, and κ and ν are constants. Minimising F with respect to A_x and A_y leads to

$$\begin{aligned} \frac{\partial F}{\partial A_x} &= -\kappa(m_x^2 - m_y^2) + 2\epsilon A_x = 0 \\ \frac{\partial F}{\partial A_y} &= -2m_x m_y + 2\epsilon A_y = 0; \\ \Leftrightarrow \quad A_x &= \lambda(m_x^2 - m_y^2) \\ A_y &= -\lambda(m_x m_y) = 0; \end{aligned} \tag{6.9}$$

where $\lambda = \kappa/2\nu$ is a (small) magnetoelastic coupling constant. Because the two-fold axis is preserved during the SF transition, $\mathbf{A}$ is directed along x in both SF phases, which is exactly the result of Eq. 6.9 ($A_y = 0$). The form of A_x is easily understood, too: being axial, $\mathbf{A}$ and $\mathbf{M}$, the structural and magnetic order parameter, respectively, transform in the same way under a three-fold rotation. Due to their different time-reversal behaviour, $\mathbf{A} \propto \mathbf{M}^2$ from a simple symmetrisation of the trilinear coupling term. $\mathbf{A}$ must switch sign if $\mathbf{M}$ is rotated by 90° around z, *e.g.* from $\hat{\mathbf{x}}$ to $\hat{\mathbf{y}}$, leading to $A_x = \lambda(m_x^2 - m_y^2)$.[5]

[5]The full Landau analysis follows in Section 6.3.2.

To arrive at a description for the polarisation induced by a coupling to $\mathbf{A}$, let us consider the applied magnetic field. If a field is applied in the in-plane transverse direction, the aforementioned helix has the distinct chirality $\mathbf{r}_{12} \cdot (\mathbf{m}_1 \times \mathbf{m}_2)$. In analogy to the ferroaxial multiferroic mechanism [69, 118], which was introduced in Section 1.2.4, the following phenomenological polarisation can be derived:

$$\begin{aligned} \mathbf{P} &= \mu\sigma\mathbf{A} \\ \Leftrightarrow \quad P_x &= \mu\lambda(m_x^2 - m_y^2)\,\mathbf{r}_{12} \cdot (\mathbf{m}_1 \times \mathbf{m}_2) \\ &= 2\mu\chi^{\perp}\lambda(m_x^2 - m_y^2)\,\mathbf{r}_{12} \cdot (\mathbf{m} \times \mathbf{H}) \\ &= 2\mu\chi^{\perp}\lambda(m_x^2 - m_y^2)\;(\mathbf{r}_{12} \times \mathbf{m}) \cdot \mathbf{H}; \\ P_y &= 0, \end{aligned} \tag{6.10}$$

yielding

$$\begin{aligned} \boldsymbol{\alpha} = \frac{\partial \mathbf{P}}{\partial \mathbf{H}} &= 2\mu\chi^{\perp}\lambda(m_x^2 - m_y^2)\hat{\mathbf{x}} \otimes (\mathbf{r}_{12} \times \mathbf{m}) \\ &= 2\mu\chi^{\perp}\lambda(m_x^2 - m_y^2)\left\{\begin{pmatrix}1\\0\\0\end{pmatrix}[-m_y, m_x, 0]\right\} \\ &= 2\mu\chi^{\perp}\lambda\begin{pmatrix}(m_x^2 m_y - m_y^3) & (-m_x^3 + m_y^2 m_x) & 0\\ 0 & 0 & 0\\ 0 & 0 & 0\end{pmatrix} \\ &= -2\mu\chi^{\perp}\lambda m^2\begin{pmatrix}m_y & m_x & 0\\ 0 & 0 & 0\\ 0 & 0 & 0\end{pmatrix}. \end{aligned} \tag{6.11}$$

From Eq. 6.11, we see that the ME tensor has the desired form corresponding to the first-principle result. By comparing Eq. 6.11 with Eq. 6.6, one can understand why the former, containing the small parameter λ, is considerably smaller than the latter.

6.3.2 Landau Invariants

In the previous section, a derivation is obtained for the microscopic mechanism behind the transverse DM coupling, as well as for the novel ferroaxial coupling in Cr_2O_3. Moving from the atomistic description to a symmetry-based approach, the present section covers a purely phenomenological *ansatz* to see which terms are allowed by symmetry. Both the DM and the chiral term in the ME response can be derived on the basis on a Landau analysis.

The free energy is expanded in terms of the magnetic order parameter L, which is used instead of the magnetisation M, the magnetic field strength H, and the polarisation P. The order parameters have to be *totally symmetric* with respect to the symmetry operations of the parent phase, *i.e.* the paramagnetic space group $R\bar{3}c$. As time reversal is a symmetry element of $R\bar{3}c$ and only those terms that are linear in both H and P contribute to α, L can only occur in odd powers.

We therefore expand F in terms of 3^{rd} and 5^{th} order, *i.e.* linear in L, H, and P, and linear in L^3, H, and P, respectively. Table 6.5 shows the invariant polynomials classified into their irreducible representations of $R\bar{3}c$.

The resulting tensor forms are shown in Table 6.6. These forms are fully consistent with the tensor symmetry. There is more symmetry than what could be expected: as an example, the terms in β are identical in the first and second spinflop phase, as well as γ. The relation is confirmed by the calculations: for the longitudinal response γ we observe in Table 6.4 a total value of $0.081\,\text{ps}\,\text{m}^{-1}$. This additional symmetry would be eventually lost by summing enough terms in the expansion. The important terms α, β, and γ, which are discussed in Section 6.3.1 on the grounds of their microscopic background, are all of 3^{rd} order. Another 3^{rd}-order term (δ), a mixed transverse/longitudinal term, does not seem to play a role in Cr_2O_3.

Table 6.5: Invariant polynomials of the space group $R\bar{3}c$ up to 5^{th} order that give rise to terms in the ME tensor, ordered by their irreducible representations ("irreps"). The cs are arbitrary constants.

Tensor element	Irrep (LHP)	Invariant
α_{xy}	$\Gamma_1^-\Gamma_3^+\Gamma_3^-$	$(1+cL_z^2)L_z(H_xP_x+H_yP_y)$
α_z	$\Gamma_1^-\Gamma_2^+\Gamma_2^-$	$(1+cL_z^2)L_zH_zP_z$
β	$\Gamma_3^-\Gamma_2^+\Gamma_3^-$	$(1+c(L_x^2+L_y^2))(L_yH_zP_y+L_xH_zP_x)$
γ	$\Gamma_3^-\Gamma_3^+\Gamma_2^-$	$(1+c(L_x^2+L_y^2))(L_yH_yP_z+L_xH_xP_z)$
δ	$\Gamma_3^-\Gamma_3^+\Gamma_3^-$	$(1+c(L_x^2+L_y^2))(L_y(H_xP_x-H_yP_y)+L_x(H_xP_y+H_yP_x))$
ϵ	$\Gamma_3^-\Gamma_3^+\Gamma_3^-$	$L_y^3(H_xP_x+H_yP_y)-L_x^3(H_yP_x-H_xP_y)+3L_yL_x(L_y(H_yP_x-H_xP_y)-L_x(H_xP_x+H_yP_y))$
ζ	$\Gamma_3^-\Gamma_3^+\Gamma_3^-$	$L_y^2(L_yH_xP_x)+L_x^2(L_xH_yP_x)+L_xL_y(2L_yH_xP_y-L_yH_yP_x-L_xH_xP_x-2L_xH_yP_y)$
η	$\Gamma_3^-\Gamma_2^+\Gamma_2^-$	$(L_y^3-3L_yL_x^2)H_zP_z$

Table 6.6: Tensor forms of the ME tensor for Cr_2O_3 in its low-field and spinflop phases expressed in terms of invariant polynomials (Table 6.5), based on Landau theory.

$\bar{3}'m'$	$2'/m$	$2/m'$
$\begin{pmatrix} \alpha_{xy} & 0 & 0 \\ 0 & \alpha_{xy} & 0 \\ 0 & 0 & \alpha_z \end{pmatrix}$	$\begin{pmatrix} 0 & \delta-\epsilon+\zeta & \beta \\ \delta+\epsilon & 0 & 0 \\ \gamma & 0 & 0 \end{pmatrix}$	$\begin{pmatrix} \delta+\epsilon+\zeta & 0 & 0 \\ 0 & -\delta+\epsilon & \beta \\ 0 & \gamma & \eta \end{pmatrix}$

The "chiral" term we discussed is ζ, and is a purely transverse 5^{th}-order term that is zero if H and L are parallel. Note that the ζ term can be rewritten through the axial vector:

$$\mathbf{A} = -(\mathbf{T} \cdot \mathbf{H})\mathbf{P}, \tag{6.12}$$

where $\mathbf{T}$ is the magnetic order parameter (L_y, L_x), which transforms as a toroidal moment, and leads to

$$\mathbf{A} = -(L_y H_x - L_x H_y)\mathbf{P}. \tag{6.13}$$

Inserting ζ from Table 6.5 yields

$$\zeta = (L_x^2 - L_y^2)A_x - 2L_x L_y A_y. \tag{6.14}$$

As expected, the form of the coupling in Eq. 6.14 is identical to that of Eq. 6.9, which is the aforementioned chirality purely derived on the basis of Landau theory.

6.4 Summary

In the present chapter, the lattice-mediated magnetoelectric tensor of Cr_2O_3 in both low-field and high-field (spinflop) phases is computed by first-principles

calculations. We find that the $2'/m$ and $2/m'$ phase are close in energy, so that either configuration would be likely to occur. Structural changes show a breaking of the three-fold symmetry of the $\bar{3}'m'$ phase, the changes are, however, small. By determining the ME tensor for different *magnetic*, not *crystallographic* structures, insights are gained into the role of the recently defined magnetic charges. The fact that the largest elements in the magnetic charges of the spinflop phases are more than three times larger than the biggest elements in the low-field phase does not seem to have an effect on the overall coupling tensor. A group-theoretical analysis supports these findings, and shows that by breaking the three-fold symmetry when going from the low-field to the spinflop phase, the degeneracy of the transverse IR active E_u modes is removed. The large contributions in the spinflop magnetic charges map onto mutually exclusive magneto-active phonon modes and hence not contribute to the overall ME response.

Another finding from the DFT calculations is that the ME tensor is not primarily toroidal, as previously speculated. Instead, the origin and shape of the ME responses in the low-field and spinflop phases are analysed by a combination of group-theory and a phenomenological approach, in which the microscopic mechanisms behind the coupling are derived. We find that the approximate form of the ME tensor *in all spin configuration considered* can be well predicted phenomenologically using the spin-current model, which is well known in multiferroics as the inverse Dzyaloshinskii-Moriya interaction. There are two additional small components: the first is a longitudinal component known from previous studies of the low-field phase, while the second arises from a novel *chiral* mechanism, which is akin to the ferroaxial mechanisms in multiferroics. In addition, the Landau analysis shows that the "well-known" contributions, *i.e.* the longitudinal and DM component, are of 3^{rd} order, whereas the novel chiral component is of 5^{th} order.

The relevance of the findings manifests itself in four points: firstly, the spinflop phases of Cr_2O_3 were clarified on a structural and energetic level. Secondly, as research in ferrotoroidicity gained in importance over the last few years, it is fundamental to know that the ME response in the spinflop phases is not of purely toroidal nature. Thirdly, in addition to the quantitative results of the DFT simulations, we give a microscopic explanation for the dominant elements in the ME response both in the prototypical magnetoelectric Cr_2O_3 *and* its spinflop phases. Lastly, not only do we report values for an additional contribution in the spinflop phases, but we show that it can be attributed to a new type of mechanism in MEs. Particularly the latter finding might provide directions to look for magnetoelectricity in "new" configurations, and possibly find stronger chiral responses.

7 Conclusion and Perspective

7.1 Summary

The goal of this project was to gain insights into the microscopic mechanisms behind magnetoelectricity (ME) with state-of-the-art computational methods. Linear ME materials exhibit a coupling between electric and magnetic properties with the coupling constant α [15–17]:

$$\alpha_{ij} = \mu_0 \left(\frac{\partial M_j}{\partial E_i} \right) = \left(\frac{\partial P_i}{\partial H_j} \right), \tag{7.1}$$

where μ_0 is the vacuum permeability, M and P, H and E are the spontaneous magnetisation and polarisation, and the external magnetic and electric field, respectively. As explored in Chapter 1, there are vast possibilities for their applications: switching magnetic states with a voltage makes them useful for spintronics, magnetic storage devices, or the replacements of SQUIDs (Superconducting quantum interference devices). Magnetic states of exchange-bias systems [42–44][1] could be changed by a voltage when using magnetoelectric materials as one of the layers [38–41]. Moreover, renewed interest emerged in multiferroics, *i.e.* materials with a long-range magnetic and electric order (such as ferromagnetism and ferroelectricity) [7]. The prospect of finding mag-

[1] Exchange bias systems make use of *magnetic pinning* through a coupling of ferromagnetic and antiferromagnetic interfaces. Exchange-bias layers are already used in MRAMs (magnetoresistive random-access memories) and permanent magnets

netoelectric multiferroics, in which magnetic and electric properties not only co-exist, but also couple, led to a revival in the research of magnetoelectricity [9]. However, current MEs lack one or more of the crucial properties to make them of actual use in current technology: ambient operating temperatures, higher coupling constants, and moderate magnetic fields to keep the materials in their magnetoelectric state.

To understand the fundamental mechanisms behind ME, and thus open up new pathways in the search for stronger MEs, we employed density functional theory (DFT) for the computation of their properties. Chapter 2 introduced the existing first-principles framework, as well as the adaptations necessary to model the subtle ME response. We used Berry phases [172] to compute changes in polarisation [170, 171, 173], and implemented an external Zeeman magnetic field in VASP and Quantum Espresso according to Ref. [210]. The electronic contribution was determined via the polarisation change over the magnetic field, whereas the lattice response is expanded into three contributions: the Born effective charges (BECs), the magnetic charges (MCs), and the interatomic force-constant (IFC) matrix.

The methodology was applied to the prototypical ME material Cr_2O_3, an insulator with an antiferromagnetic $\uparrow\downarrow\uparrow\downarrow$ structure exhibiting ME at room temperature [18–20]. Chapter 3 outlined the *ansatz* used in the present work to determine the ME coupling tensor α. We illustrated how group theory is used to determine symmetry considerations for ME materials, and introduced the formalisms for the computation of the lattice-mediated and electronic response (α^{latt} and α^{el}, respectively) on the basis of Cr_2O_3. The *xc*-functional, the physical approximation in DFT for exchange and correlation effects, was shown to negatively influence the computational stability when using semi-local functionals in combination with noncollinear magnetism. It was also

shown that the quantitative prediction of the ME response depends on the choice of the *xc*-functional. Using the two most common descriptions for the functional, the local density approximation [128, 131–133] and the generalised gradient approximation [136, 137], the results differed by a factor of 3. We have shown that this is due to the secondary effect of the different predictions of cell volumes and band gaps modelled by different functionals, and we found that the former influenced the lattice-mediated ME response, whilst the latter altered the electronic response.

We examined the influence of pressure on both ME contributions in Cr_2O_3 in Chapter 4. This led us to an understanding of the interplay between structural properties and the lattice response, as well as between the band gap and the electronic response. Strain has recently been explored with respect to its effect on ME, where it was shown to lead to diverging ME lattice responses [209, 242]. Strained heterostructures exhibit giant ME effects [231, 232], and Cr_2O_3 nanoparticles have been reported to show 600 % larger ME responses than the bulk value [230].[2] Cr_2O_3 shows a phase transition from an antiferromagnetic insulator to a paramagnetic metal at a critical pressure of $P_c = 18\,\mathrm{GPa}$. To understand the mechanistic relationships for ME, we put a particular focus in Chapter 4 on two regimes: firstly, the adiabatic regime at ambient pressures, where we showed that already a tensile strain of 1.4 % led to an increase in the dominant transverse lattice response by a factor of 4. Secondly, the behaviour around the phase transition was analysed. We find that a collapse of the Cr magnetic moment and subsequent relaxation into the paramagnetic phase led to a divergence of the longitudinal lattice response. A phonon mode decomposition, for which we mapped the lattice, electronic, and magnetic properties of the system onto infrared active

[2] The nature of the giant response in the Cr_2O_3 nanoparticles is still debated: charge accumulation at the interfaces or strain effects [233]

phonon modes, led to further insights: we saw the magnetic charges, the analogue of the Born effective charges, diverging at the phase transition, and thus attributed the divergence of the overall lattice coupling to *magnetic softness*. The longitudinal lattice response rose to $3.2\,\mathrm{ps\,m^{-1}}$, a value *650 times larger* than its zero-pressure value. This effect is particularly interesting, as the longitudinal lattice response is negligible at 0 K, but becomes the dominant term at room temperature [19]. Moreover, we indeed observed a correlation between the closing band gap and the electronic ME response. Being of the same order of magnitude as the transverse lattice term and largely unaffected by the strain at ambient pressures, we found that the electronic response diverges close to P_c. Its largest value reached $31.4\,\mathrm{ps\,m^{-1}}$, which is remarkable in terms of relative and absolute effects. It is 60 times larger than its value at zero pressure, and falls into the upper end of the previously reported ME responses to date—many of which operate at low temperatures.

The idea to tailor both the electronic ME response by band-gap alterations and the lattice response by phonon instabilities raised the question how impurities affect the ME response. In Chapter 5, we studied the ME response when substituting Cr atoms in Cr_2O_3 with Fe and Ti, whose oxides order isostructurally to Cr_2O_3. Being placed in a non-equilibrium magnetic structure, the compounds showed an increase of the magnetic charges of up to 10 times the value of the ground-state Cr_2O_3. Their overall lattice response, however, was of the same order of magnitude as the parent structure. We discovered that in the case of Fe_2O_3, this behaviour is attributed to a transverse magneto-active mode, that contributes negatively to the overall tensor and cancels the large responses of two other transverse modes. Nevertheless, the doping influenced the electronic structure, and thus increased the electronic ME response to about ten times the value of Cr_2O_3.

In Chapter 6, we performed controlled first-principles calculations by expanding the lattice response into the BECs, IFC matrix, and MCs. We were thus able to isolate the sole effect of the magnetic configuration on the ME coupling. We modelled the "spinflop" phase of Cr_2O_3, which occurs at high magnetic fields along the rhombohedral [111] direction, in which the magnetic moments are rotated by π to lie in the basal plane [90, 273]. To date, the spinflop phase poses many interesting questions: because of different domains occurring in experimental settings, it is still unclear in which direction the magnetic moments point [274–276], whence difficulties to determine the unambiguous single-phase ME tensor arise. Two high-symmetry structures are possible, which were the subject of the present work. In addition, the nature of the spinflop phase, which was suggested to be of toroidal character [277], is still unclear. We conducted a group-theoretical analysis to determine the shape of all atomic and macroscopic quantities required. We then modelled the spinflop phase, altering only the magnetic charges and keeping the other parameters fixed, so that we were able to isolate the effect of the magnetic structure on the overall ME tensor. We combined the lattice and electronic contribution and thus determined the overall coupling for the low-field and two spinflop phases. Firstly, we showed that there clearly is a toroidal component, but that the ME response is by no means purely toroidal. Secondly, we found that the ME responses in the low-field and spinflop phases are the sum of the following distinct components: a longitudinal term, which becomes dominant at room temperature [64], occurs in all phases, as well as the transverse term, which is of relativistic nature and arises due to the inverse Dzyaloshinksii-Moriya (DM) interaction [66]. The two spinflop phases showed a third in-plane transverse response. We used Landau analysis to determine the invariants of the Cr_2O_3 space group and combined the findings with a phenomenological approach, which led to the result that the longitudinal and DM term are of 3^{rd} order,

whereas the novel chiral component is of 5^{th} order. We found the latter to be of chiral nature akin to the relativistic ferroaxial mechanism—well-known in the multiferroics community, but hitherto unknown in magnetoelectrics.

Summa summarum, we believe that we illustrated ways with which the ME response can be tailored to fit specific requirements or with which new coupling phenomena can be explored. We shed light into the microscopic mechanisms behind ME and hope that we opened up new pathways to search for (**a**) stronger ME lattice coupling through strain or magnetic softness; (**b**) larger electronic responses at insulator-metal transitions; and (**c**) new chiral magnetoelectrics.

7.2 Outlook

Both a qualitative and a quantitative understanding of the re-emerging field of magnetoelectrics is crucial for new developments. We have attempted to convey that investigating magnetoelectric phenomena with first-principles methods is a powerful way to gain insights into the relationships behind the coupling. The benefits of *ab initio* methods to treat ideal and single-phase systems, lead to an understanding that would be difficult, if not impossible, to achieve by experimental means. However, these methods come with their limitations: with restricted computational power, one needs to use approximations, small cells, and work in the zero-Kelvin limit. More accurate ways to treat the Brillouin zone are desired, particularly at transitions from metallic to insulating phases. One can also imagine larger supercells, in which doping is investigated in a more rigorous way. Both suggestions provide opportunities to analyse the diverging electronic ME response in more detail. Further work is also required with respect to doping and the altered lattice contribution. It might be a promising way to include lattice and magnetic softness and thus increase

the lattice-mediated response. Other dopants could be a good starting point for more controlled studies, and other compounds throughout the $3d$ transition metals oxides could be examined, *e.g.* with respect to the insulator-metal transition in V_2O_3. Choosing parent structures with a stronger ME response than Cr_2O_3 could take this study one step further and possibly away from hypothetical structures towards real configurations. The choice of more accurate parameters would make a study of the strain-mediated ME effect possible: in addition to the electronic (lattice-mediated) response, for which we determine the polarisation-change for fixed (relaxed) ions, we could let the cell size relax under the magnetic field, in turn resulting in the strain-mediated part to the ME coupling.[3]

Outside the computational field of magnetoelectric modelling, experimental work is required to complement recent findings and study the physics of more complex crystal structures. Experiments of doping would shed light on the interplay between the electronic ME response and band gaps, and between the lattice response and magnetic softness. Setups of pressure studies close to insulator-metal transitions would benefit the field. One could also think of the possibility to decouple the electronic and lattice response, which, so far, are distinguished based on DFT, by applying high- and low-frequency fields and thus coupling to the electrons and nuclei, respectively.

From a purely theoretical standpoint, one can also imagine the implementation of routines that predict the ME tensor in a perturbative manner by density functional perturbation theory. A formulation for the relationship between the dielectric tensor and the electronic contribution needs to be developed, as the current theory only accounts for the upper boundary of the ME response. This work could also raised the need towards developing more stable

[3]The strain-mediated ME tensor occurs, from a symmetry point of view, in piezoelectric piezomagnets, such as $BiFeO_3$ [279].

minimisers in connection with semi-local or non-local *xc*-functionals. We have reached a stage where the applicability of local functionals was explored and reached its limits, so that the ill-defined usage of gradient functional with non-collinear magnetism hampers quantitative predictions. With the use of stable *xc*-functionals away from local approximations and the growth of computational power, we can imagine highly-accurate *ab initio* studies, which can be routinely applied in a "high-throughput" manner.

We hope that the present project stimulates further research in both the computational side of materials modelling and the technological implementation side of magnetoelectrics.

Bibliography

[1] K. Momma and F. Izumi, Journal of Applied Crystallography **44**, 1272 (2011).

[2] M. Fiebig and N. A. Spaldin, The European Physical Journal B **71**, 293 (2009).

[3] S.-W. Cheong and M. Mostovoy, Nature Materials **6**, 13 (2007).

[4] C. Ederer and N. A. Spaldin, Current Opinion in Solid State and Materials Science **9** (2005).

[5] G. Meurant, *Solid State Physics, Volume 4*, edited by F. Seitz and D. Turnbull (Academic Press Inc., 1957).

[6] N. A. Spaldin and M. Fiebig, Science **309**, 391 (2005).

[7] H. Schmid, Ferroelectrics **162**, 317 (1994).

[8] J. F. Scott, Journal of Materials Chemistry **22**, 4567 (2012).

[9] W. Eerenstein, N. D. Mathur, and J. F. Scott, Nature **442**, 759 (2006).

[10] M. Bibes, J. E. Villegas, and A. Barthélémy, Advances in Physics **60**, 5 (2011).

[11] W. C. Röntgen, Annalen der Physik **271**, 264 (1888).

[12] P. Curie, Journal of Physics **3**, 393 (1894).

[13] J. Curie and P. Curie, Bulletin de la Société minéralogique de France **3**, 90 (1880).

[14] P. J. W. Debye, Zeitschrift für Physik **36** (1926).

[15] L. D. Landau and E. M. Lifshitz, *Electrodynamics of Continuous Media* (Oxford Pergamon Press, Oxford, 1960).

[16] I. Dzyaloshinsky, Journal of Physics and Chemistry of Solids **4**, 241 (1958).

[17] I. E. Dzyaloshinskii, Sov. Phys. JETP **10**, 628 (1960).

[18] D. N. Astrov, Sov. Phys. JETP **11**, 708 (1960).

[19] D. N. Astrov, Sov. Phys. JETP **13**, 729 (1961).

[20] V. J. Folen, G. T. Rado, and E. W. Stalder, Physical Review Letters **6**, 607 (1961).

[21] G. T. Rado, Physical Review **128**, 2546 (1962).

[22] G. T. Rado and V. J. Folen, Journal of Applied Physics **33**, 1126 (1962).

[23] W. Kleemann, Journal of Applied Physics **114**, 1 (2013).

[24] E. Bousquet and A. Cano, Journal of Physics: Condensed Matter **123001** (2016).

[25] M. Fiebig, Journal of Physics D: Applied Physics **38**, R123 (2005).

[26] J.-P. Rivera, The European Physical Journal B **71**, 299 (2009).

[27] W. F. Brown, R. M. Hornreich, and S. Shtrikman, Physical Review **168**, 574 (1968).

[28] M. Bibes, Nature **7**, 425 (2008).

[29] C. A. F. Vaz and U. Staub, Journal of Physics: Condensed Matter **27**, 500301 (2015).

[30] T. Jungwirth, X. Marti, P. Wadley, and J. Wunderlich, Nature Nanotechnology **11**, 231 (2016).

[31] T. Kimura, Y. Sekio, H. Nakamura, T. Siegrist, and a. P. Ramirez, Nature Materials **7**, 291 (2008).

[32] V. Scagnoli, U. Staub, Y. Bodenthin, R. A. de Souza, M. García-Fernández, M. Garganourakis, A. T. Boothroyd, D. Prabhakaran, and S. W. Lovesey, Science **332**, 696 (2011).

[33] Y. Kitagawa, Y. Hiraoka, T. Honda, T. Ishikura, H. Nakamura, and T. Kimura, Nature Materials **9**, 797 (2010).

[34] S. H. Chun, Y. S. Chai, Y. S. Oh, D. Jaiswal-Nagar, S. Y. Haam, I. Kim, B. Lee, D. H. Nam, K.-T. Ko, J.-H. Park, J.-H. Chung, and K. H. Kim, Physical Review Letters **104**, 037204 (2010).

[35] K. Taniguchi, N. Abe, S. Ohtani, H. Umetsu, and T. Arima, Applied Physics Express **1** (2008).

[36] S. Ishiwata, Y. Taguchi, H. Murakawa, Y. Onose, and Y. Tokura, Science (New York, N.Y.) **319**, 1643 (2008).

[37] P. Borisov, A. Hochstrat, V. V. Shvartsman, and W. Kleemann, The Review of Scientific Instruments **78**, 106105 (2007).

[38] M. Street, W. Echtenkamp, T. Komesu, S. Cao, P. A. Dowben, and C. Binek, Applied Physics Letters **104**, 222402 (2014).

[39] X. He, Y. Wang, N. Wu, A. N. Caruso, E. Vescovo, K. D. Belashchenko, P. a. Dowben, and C. Binek, Nature Materials **9**, 579 (2010).

[40] X. Chen, A. Hochstrat, P. Borisov, and W. Kleemann, Applied Physics Letters **89**, 202508 (2006).

[41] C. Binek and B. Doudin, Journal of Physics: Condensed Matter **17**, 39 (2005).

[42] P. van der Zaag, R. M. Wolf, A. R. Ball, C. Bordel, L. F. Feiner, and R. Jungblut, Journal of Magnetism and Magnetic Materials **148**, 346 (1995).

[43] W. C. Cain and M. H. Kryder, Journal of Applied Physics **67**, 5722 (1990).

[44] W. H. Meiklejohn and C. P. Bean, Physical Review **102**, 1413 (1956).

[45] J. Nogués and I. K. Schuller, Journal of Magnetism and Magnetic Materials **192**, 203 (1999).

[46] M. N. Baibich, J. M. Broto, A. Fert, F. Nguyen Van Dau, F. Petroff, P. Etienne, G. Creuzet, A. Friederich, and J. Chazelas, Physical Review Letters **61**, 2472 (1988).

[47] C. Chappert, A. Fert, and F. N. Van Dau, Nature Materials **6**, 813 (2007).

[48] M. Kiwi, Journal of Magnetism and Magnetic Materials **234**, 584 (2001).

[49] P. Borisov, A. Hochstrat, X. Chen, W. Kleemann, and C. Binek, Physical Review Letters **94**, 117203 (2005).

[50] P. Borisov and W. Kleemann, Journal of Applied Physics **110**, 033917 (2011).

[51] Y. Shiratsuchi, T. Nakatani, S.-I. Kawahara, and R. Nakatani, Journal of Applied Physics **106**, 033903 (2009).

[52] T. Ashida, Y. Sato, T. Nozaki, and M. Sahashi, Journal of Applied Physics **113**, 17D711 (2013).

[53] C. Binek, Physics **6**, 13 (2013).

[54] T. Hahn, *International Tables for Crystallography Volume A: Space-group symmetry* (Springer Netherlands, 2002).

[55] H. K. D. H. Bhadeshia, "C6: Crystallography," (2015).

[56] "Wulffman Documentation," (2002).

[57] T. Kimura, *Graduate School of Engineering Science, Osaka University*, Tech. Rep. (Ascona, 2011).

[58] A. Authier, in *International Tables for Crystallography*, Vol. D (Springer Netherlands, 2013) pp. 3–33.

[59] D. B. Litvin, *Magnetic Group Tables* (International Union of Crystallography, Chester, England, 2013).

[60] R. E. Newnham, *Properties of Materials: Anisotropy, Symmetry, Structure* (Oxford University Press, Oxford, 2005).

[61] A. Authier, in *International Tables for Crystallography* (Springer Netherlands, 2003) Chap. Tensorial, pp. 136–139.

[62] L. D. Landau and E. M. Lifshitz, *Statistical Physics Part 1*, 3rd ed. (Pergamon Press, Oxford, 1980).

[63] J.-C. Tolédano and P. Tolédano, *The Landau Theory of Phase Transitions: Application To Structural, Incommensurate, Magnetic And Liquid Crystal Systems* (WSPC, 1987).

[64] M. Mostovoy, Physical Review Letters **96**, 067601 (2006).

[65] I. Sosnowska and A. K. Zvezdin, Journal of Magnetism and Magnetic Materials **140-144**, 167 (1995).

[66] H. Katsura, N. Nagaosa, and A. V. Balatsky, Physical Review Letters **95**, 057205 (2005).

[67] T. Moriya, Physical Review **120**, 91 (1960).

[68] N. Benedek and C. Fennie, Physical Review Letters **106**, 107204 (2011).

[69] R. D. Johnson, S. Nair, L. C. Chapon, A. Bombardi, C. Vecchini, D. Prabhakaran, A. T. Boothroyd, and P. G. Radaelli, Physical Review Letters **107**, 2 (2011).

[70] Y. Yang, J. Íñiguez, A.-J. Mao, and L. Bellaiche, Physical Review Letters **112**, 057202 (2014).

[71] C. Ederer and N. A. Spaldin, Physical Review B **76**, 214404 (2007).

[72] N. A. Spaldin, M. Fiebig, and M. Mostovoy, Journal of Physics: Condensed Matter **20**, 434203 (2008).

[73] C. Ederer, European Physical Journal B **71**, 349 (2009).

[74] F. Thöle, M. Fechner, and N. A. Spaldin, Phys. Rev. B **93**, 195167 (2016).

[75] G. A. Gehring, Ferroelectrics **161**, 275 (1994).

[76] O. de Alcantara Bonfim and G. Gehring, Advances in Physics **29**, 731 (1980).

[77] N. A. Hill, The Journal of Physical Chemistry B **104**, 6694 (2000).

[78] N. A. Hill, A. Filippetti, N. A. Hill, and A. Filippetti, Journal of Magnetism and Magnetic Materials **242-245**, 976 (2002).

[79] K. F. Wang, J.-M. Liu, and Z. F. Ren, Advances in Physics **58**, 321 (2009).

[80] T. Kimura, Annual Review of Materials Research **37**, 387 (2007).

[81] S. Picozzi and A. Stroppa, The European Physical Journal B **85** (2012).

[82] I. A. Sergienko and E. Dagotto, Physical Review B - Condensed Matter and Materials Physics **73**, 1 (2006).

[83] P. W. Anderson, Physical Review **115**, 2 (1959).

[84] S.-W. Cheong, J. D. Thompson, and Z. Fisk, Physical Review B **39**, 4395 (1989).

[85] H. Schmid, Physica Status Solidi **37**, 209 (1970).

[86] T. H. O'Dell, *The electrodynamics of magneto-electric media* (North-Holland Pub. Co., 1970).

[87] G. T. Rado, Physical Review Letters **6**, 609 (1961).

[88] R. Hornreich and S. Shtrikman, Physical Review **161**, 506 (1967).

[89] H. Yatom and R. Englman, Physical Review **188**, 793 (1969).

[90] H. Wiegelmann, A. G. M. Jansen, P. Wyder, J.-P. Rivera, and H. Schmid, Ferroelectrics **162**, 141 (1994).

[91] E. Kita, K. Siratori, and A. Tasaki, Journal of Applied Physics **50**, 7748 (1979).

[92] M. Stękiel, R. Przeniosło, I. Sosnowska, A. Fitch, J. B. Jasiński, J. a. Lussier, and M. Bieringer, Acta Crystallographica Section B Structural Science, Crystal Engineering and Materials **71**, 203 (2015).

[93] T. R. McGuire and F. H. Grannis, Physical Review **102**, 1000 (1956).

[94] L. Bayarjargal and B. Winkler, Applied Physics Letters **102**, 182403 (2013).

[95] J. R. Teague, R. Gerson, and W. J. James, Solid State Communications **8**, 1073 (1970).

[96] I. Sosnowska, T. Peterlin-Neumaier, and E. Steichele, Journal of Physics C: Solid State Physics **15**, 4835 (1982).

[97] J. Wang, J. B. Neaton, H. Zheng, V. Nagarajan, S. B. Ogale, B. Liu, D. Viehland, V. Vaithyanathan, D. G. Schlom, U. V. Waghmare, N. A. Spaldin, K. M. Rabe, M. Wuttig, and R. Ramesh, Science (New York, N.Y.) **299**, 1719 (2003).

[98] T. Kimura, S. Kawamoto, I. Yamada, M. Azuma, M. Takano, and Y. Tokura, Physical Review B **67**, 180401 (2003).

[99] S. Picozzi and C. Ederer, Journal of Physics: Condensed Matter **21**, 303201 (2009).

[100] A. Kimel, R. Pisarev, F. Bentivegna, and T. Rasing, Physical Review B **64**, 201103 (2001).

[101] T. Hoffmann, P. Thielen, P. Becker, L. Bohatý, and M. Fiebig, Physical Review B **84**, 184404 (2011).

[102] S. Picozzi, K. Yamauchi, B. Sanyal, I. Sergienko, and E. Dagotto, Physical Review Letters **99**, 1 (2007).

[103] A. Muñoz, M. T. Casáis, J. A. Alonso, M. J. Martínez-Lope, J. L. Martínez, and M. T. Fernández-Díaz, Inorganic Chemistry **40**, 1020 (2001).

[104] N. Hur, S. Park, P. A. Sharma, J. S. Ahn, S. Guha, and S.-W. Cheong, Nature **429**, 392 (2004).

[105] G. Blake, L. Chapon, P. Radaelli, S. Park, N. Hur, S.-W. Cheong, and J. Rodríguez-Carvajal, Physical Review B **71**, 214402 (2005).

[106] C. Vecchini, L. Chapon, P. Brown, T. Chatterji, S. Park, S.-W. Cheong, and P. Radaelli, Physical Review B **77**, 134434 (2008).

[107] Y. Noda, H. Kimura, M. Fukunaga, S. Kobayashi, I. Kagomiya, and K. Kohn, Journal of Physics: Condensed Matter **20**, 434206 (2008).

[108] C. Fang and J. Hu, Europhysics Letters (EPL) **82**, 57005 (2008).

[109] T. Tyson, Z. Chen, M. DeLeon, S. Yoong, and S.-W. Cheong, Journal of Magnetism and Magnetic Materials **321**, 1714 (2009).

[110] V. V. Men'shenin, V. V. Nikolaev, and a. V. Dmitriev, The Physics of Metals and Metallography **112**, 25 (2011).

[111] T. Katsufuji, S. Mori, M. Masaki, Y. Moritomo, N. Yamamoto, and H. Takagi, Physical Review B **64**, 104419 (2001).

[112] K. Siratori, J. Akimitsu, E. Kita, and M. Nishi, J. Phys. Soc. Jpn. **48**, 1111 (1980).

[113] E. Ascher, Philosophical Magazine **17**, 149 (1968).

[114] S. L. Hou and N. Bloembergen, Physical Review **138**, A1218 (1965).

[115] T. H. O'Dell, Philosophical Magazine **16**, 487 (1967).

[116] K. Siratori and E. Kita, J. Phys. Soc. Jpn. **48**, 1443 (1980).

[117] R. Johnson, N. Terada, and P. Radaelli, Physical Review Letters **108**, 219701 (2012).

[118] R. D. Johnson, L. C. Chapon, D. D. Khalyavin, P. Manuel, P. G. Radaelli, and C. Martin, Physical Review Letters **108**, 2 (2012).

[119] S. H. Chun, Y. S. Chai, Y. S. Oh, D. Jaiswal-Nagar, S. Y. Haam, I. Kim,

B. Lee, D. H. Nam, K.-T. Ko, J.-H. Park, J.-H. Chung, and K. H. Kim, Physical Review Letters **104**, 049901 (2010).

[120] A. S. Borovnik-Romanov and H. Grimmer, in *International Tables for Crystallography*, Vol. D (John Wiley and Sons, Inc, 2006) Chap. 1.5, pp. 105–149.

[121] R. M. Martin, *Electronic Structure: Basic Theory and Practical Methods* (Cambridge University Press, 2008).

[122] P. C. W. Davies and D. S. Betts, *Quantum Mechanics*, 2nd ed. (CRC Press, 1994).

[123] P. W. Atkins and R. Friedman, *Molecular Quantum Mechanics*, 5th ed. (Oxford University Press, Oxford, 2010).

[124] M. Born and R. Oppenheimer, Annalen der Physik **20**, 457 (1927).

[125] P. Hohenberg and W. Kohn, Physical Review **136**, 864 (1964).

[126] R. G. Parr and W. Yang, *Density-Functional Theory of Atoms and Molecules* (Oxford University Press, 1989).

[127] R. G. Parr and W. Yang, *Density-Functional Theory of Atoms and Molecules* (Oxford University Press, 1994).

[128] W. Kohn and L. J. Sham, Physical Review **140**, A1133 (1965).

[129] K. Burke, *The ABC of DFT*, Tech. Rep. (Department of Chemistry, University of California, Irvine, Irvine, 2007).

[130] E. Kaxiras, *Atomic and Electronic Structure of Solids* (Cambridge University Press, 2003).

[131] D. M. Ceperley and B. J. Alder, Physical Review Letters **45**, 566 (1980).

[132] J. P. Perdew and A. Zunger, Physical Review B **23** (1981).

[133] S. H. Vosko, L. Wilk, and M. Nusair, Canadian Journal of Physics **58**, 1200 (1980).

[134] F. Favot, A. Dal Corso, and A. Baldereschi, The Journal of Chemical Physics **114**, 483 (2001).

[135] J. P. Perdew and Y. Wang, Physical Review B **45**, 244 (1992).

[136] J. Perdew, K. Burke, and M. Ernzerhof, Physical Review Letters **77**, 3865 (1996).

[137] J. P. Perdew, Physical Review Letters **55**, 1665 (1985).

[138] J. P. Perdew, AIP Conference Proceedings **577**, 1 (2001).

[139] C. Tuma, A. Daniel Boese, and N. C. Handy, Physical Chemistry Chemical Physics **1**, 3939 (1999).

[140] B. Himmetoglu, A. Floris, S. De Gironcoli, and M. Cococcioni, International Journal of Quantum Chemistry **114**, 14 (2014).

[141] A. I. Liechtenstein, V. I. Anisimov, and J. Zaanen, Physical Review B **52**, 5467 (1995).

[142] S. L. Dudarev, S. Y. Savrasov, C. J. Humphreys, and A. P. Sutton, Physical Review B **57**, 1505 (1998).

[143] N. W. Ashcroft and N. Mermin, *Solid State Physics* (Brooks/Cole, 1976).

[144] H. J. Monkhorst and J. D. Pack, Physical Review B **13**, 5188 (1976).

[145] J. C. Slater, Physical Review **51**, 846 (1937).

[146] D. J. Singh and L. Nordström, *Planewaves, pseudopotentials, and the LAPW method* (Birkhäuser, 2006).

[147] O. K. Andersen, Physical Review B **12**, 3060 (1975).

[148] J. Lin, A. Qteish, M. Payne, and V. Heine, Physical Review B **47**, 4174 (1993).

[149] N. Troullier and J. L. Martins, Physical Review B **43**, 1993 (1993).

[150] D. Vanderbilt, Physical Review B **41**, 7892 (1990).

[151] C. Lee, D. Vanderbilt, K. Laasonen, R. Car, and M. Parrinello, Physical Review B **47**, 4863 (1993).

[152] S. J. Clark, M. D. Segall, C. J. Pickard, P. J. Hasnip, M. I. J. Probert, K. Refson, and M. C. Payne, Zeitschrift für Kristallographie **220**, 567 (2005).

[153] P. E. Blöchl, Physical Review B **50**, 17953 (1994).

[154] G. Kresse and J. Hafner, Journal of Physics: Condensed Matter **6**, 8245 (1994).

[155] P. E. Blöchl, C. J. Först, and J. Schimpl, Bulletin of Materials Science **26**, 33 (2003).

[156] G. Kresse and D. Joubert, Physical Review B **59**, 1758 (1999).

[157] S. Baroni, S. D. Gironcoli, A. D. Corso, and P. Giannozzi, Reviews of Modern Physics **73**, 515 (2001).

[158] X. Gonze and C. Lee, Physical Review B **55**, 10355 (1997).

[159] H. Hellmann, *Einführung in die Quantenchemie*, edited by D. Andrae (Springer Spektrum, Berlin-Heidelberg, 1937).

[160] R. P. Feynman, Physical Review **56**, 340 (1939).

[161] G. J. Ackland, M. C. Warren, and S. J. Clark, Journal of Physics: Condensed Matter **9**, 7861 (1997).

[162] S. Baroni and R. Resta, Physical Review B **33**, 7017 (1986).

[163] X. Gonze, Physical Review A **52**, 1096 (1995).

[164] J. Íñiguez, Physical Review Letters **101**, 12 (2008).

[165] R. Resta and D. Vanderbilt, Topics in Applied Physics **105**, 31 (2007).

[166] N. A. Spaldin, Journal of Solid State Chemistry **195**, 2 (2012).

[167] O. F. Mossotti, Memorie di Matematica e die Fisica della Societa Italiana delle Scienze Residente in Modena **24**, 49 (1850).

[168] R. Clausius, *Die mechanische Wärmetheorie* (Braunschweig, Friedrich Vieweg und Sohn, 1876).

[169] I. Souza, J. Íñiguez, and D. Vanderbilt, Physical Review Letters **89**, 117602 (2002).

[170] R. D. King-Smith and D. Vanderbilt, Physical Review B **47**, 1651 (1993).

[171] R. Resta, Journal of Physics: Condensed Matter **14**, R625 (2002).

[172] M. V. Berry, Proceedings of the Royal Society A **392**, 45 (1984).

[173] D. Vanderbilt, Journal of Physics and Chemistry of Solids **61**, 147 (1999).

[174] P. Umari and A. Pasquarello, Physical Review Letters **89**, 157602 (2002).

[175] T. Oda, A. Pasquarello, and R. Car, Physical Review Letters **80**, 3622 (1998).

[176] D. Hobbs and J. Hafner, Annals of the Marie Curie Fellowship Association **4**, 1 (2006).

[177] J. Kübler, K.-H. Höck, J. Sticht, and A. R. Williams, Journal of Applied Physics **63**, 3482 (1988).

[178] R. Lorenz, J. Hafner, S. S. Jaswal, and D. J. Sellmyer, Physical Review Letters **74**, 3688 (1995).

[179] L. Nordström and D. Singh, Physical Review Letters **76**, 4420 (1996).

[180] D. Hobbs and J. Hafner, Journal of Physics: Condensed Matter **13**, 681 (2001).

[181] D. Hobbs, G. Kresse, and J. Hafner, Physical Review B **62**, 11556 (2000).

[182] D. Hobbs, G. Kresse, and J. Hafner, *Fully unconstrained noncollinear magnetism within the projector augmented-wave method* (Psi-K Scientific Highlight of the Month).

[183] D. Hobbs, J. Hafner, and D. Spišák, Physical Review B **68**, 014407 (2003).

[184] E. Sjöstedt and L. Nordström, Physical Review B **66**, 14447 (2002).

[185] S. Sharma, J. K. Dewhurst, C. Ambrosch-Draxl, S. Kurth, N. Helbig, S. Pittalis, S. Shallcross, L. Nordström, and E. K. U. Gross, Physical Review Letters **98**, 1 (2007).

[186] K. Capelle, G. Vignale, and B. L. Györffy, Physical Review Letters **87**, 206403 (2001).

[187] G. Scalmani and M. J. Frisch, Journal of Chemical Theory and Computation Letter **8**, 2193 (2012).

[188] I. W. Bulik, G. Scalmani, M. J. Frisch, and G. E. Scuseria, Physical Review B - Condensed Matter and Materials Physics **87**, 1 (2013).

[189] A. Malashevich, I. Souza, S. Coh, and D. Vanderbilt, New Journal of Physics **12**, 053032 (2010).

[190] D. Xiao, J. Shi, and Q. Niu, Physical Review Letters **95**, 137204 (2005).

[191] T. Thonhauser, D. Ceresoli, D. Vanderbilt, and R. Resta, Physical Review Letters **95**, 137205 (2005).

[192] D. Ceresoli, T. Thonhauser, D. Vanderbilt, and R. Resta, Physical Review B **74**, 024408 (2006).

[193] J. Shi, G. Vignale, D. Xiao, and Q. Niu, Physical Review Letters **99**, 197202 (2007).

[194] X.-L. Qi, T. L. Hughes, and S.-C. Zhang, Physical Review B **78**, 195424 (2008).

[195] A. Essin, J. Moore, and D. Vanderbilt, Physical Review Letters **102**, 146805 (2009).

[196] S. Coh, D. Vanderbilt, A. Malashevich, and I. Souza, Physical Review B **83**, 85108 (2011).

[197] A. Malashevich, S. Coh, I. Souza, and D. Vanderbilt, Physical Review B **86**, 1 (2012).

[198] K. Yamauchi and S. Picozzi, Physical Review B **85**, 85131 (2012).

[199] A. Scaramucci, E. Bousquet, M. Fechner, M. Mostovoy, and N. A. Spaldin, Physical Review Letters **109**, 197203 (2012).

[200] E. Pyykkö, Chemical Review **88**, 563 (1988).

[201] L. Kleinman, Physical Review B **21**, 2630 (1980).

[202] G. B. Bachelet and M. A. Schlüter, Physical Review B **25**, 2103 (1982).

[203] A. Dal Corso, Physical Review B **82**, 075116 (2010).

[204] A. Dal Corso, Physical Review B **81**, 075123 (2010).

[205] L. A. Hemstreet, C. Y. Fong, and J. S. Nelson, Physical Review B **47**, 4238 (1993).

[206] G. Theurich and N. Hill, Physical Review B **64**, 073106 (2001).

[207] J. K. Cockcroft, P. Barnes, and M. P. Attfield, "Point Group Diagrams," (2006).

[208] M. Mostovoy, A. Scaramucci, N. A. Spaldin, and K. Delaney, Physical Review Letters **105**, 087202 (2010).

[209] E. Bousquet and N. A. Spaldin, Physical Review Letters **107**, 1 (2011).

[210] E. Bousquet, N. A. Spaldin, and K. Delaney, Physical Review Letters **106**, 1 (2011).

[211] M. Ye and D. Vanderbilt, Physical Review B **89**, 064301 (2014).

[212] G. Kresse and J. Furthmüller, Physical Review B - Condensed Matter and Materials Physics B, Condensed matter **54**, 11169 (1996).

[213] P. Giannozzi, S. Baroni, N. Bonini, M. Calandra, R. Car, C. Cavazzoni, D. Ceresoli, G. L. Chiarotti, M. Cococcioni, I. Dabo, A. Dal Corso, S. de Gironcoli, S. Fabris, G. Fratesi, R. Gebauer, U. Gerstmann, C. Gougoussis, A. Kokalj, M. Lazzeri, L. Martin-Samos, N. Marzari, F. Mauri, R. Mazzarello, S. Paolini, A. Pasquarello, L. Paulatto, C. Sbraccia, S. Scandolo, G. Sclauzero, A. P. Seitsonen, A. Smogunov, P. Umari, and R. M. Wentzcovitch, Journal of Physics: Condensed Matter **21**, 395502 (2009).

[214] K. Dewhurst, S. Sharma, L. Nordström, F. Cricchio, F. Bultmark, and H. Gross, *Elk Code* (http://elk.sourceforge.net/).

[215] P. Pulay, Chemical Physics Letters **73**, 393 (1980).

[216] N. J. Mosey, P. Liao, and E. A. Carter, The Journal of chemical physics **129**, 014103 (2008).

[217] A. Rohrbach, J. Hafner, and G. Kresse, Physical Review B **70**, 125426 (2004).

[218] E. A. Moore, Physical Review B **76**, 195107 (2007).

[219] Y. Wang, H. Fang, C. L. Zacherl, Z. Mei, S. Shang, L.-Q. Chen, P. D. Jablonski, and Z.-K. Liu, Surface Science **606**, 1422 (2012).

[220] F. Maldonado, R. Rivera, and A. Stashans, Physica B: Condensed Matter **407**, 1262 (2012).

[221] Y. Guo, S. J. Clark, and J. Robertson, Journal of Physics: Condensed Matter **24**, 325504, 1 (2012).

[222] A. Y. Dobin, W. Duan, and R. M. Wentzcovitch, Physical Review B **62**, 11997 (2000).

[223] L. M. Corliss, J. M. Hastings, R. Nathans, and G. Shirane, Journal of Applied Physics **36**, 1099 (1965).

[224] A. H. Hill, A. Harrison, C. Dickinson, W. Zhou, and W. Kockelmann, Microporous and Mesoporous Materials **130**, 280 (2010).

[225] X. Wu, D. Vanderbilt, and D. Hamann, Physical Review B **72**, 035105 (2005).

[226] A. van de Walle and G. Ceder, Physical Review B **59**, 14992 (1999).

[227] S. Sahoo and C. Binek, Philosophical Magazine Letters **87**, 259 (2007).

[228] J. Ma, J. Hu, Z. Li, and C.-W. Nan, Advanced Materials **23**, 1062 (2011).

[229] R. Ramesh and N. A. Spaldin, Nature Materials **6**, 21 (2007).

[230] D. Halley, N. Najjari, H. Majjad, L. Joly, P. Ohresser, F. Scheurer, C. Ulhaq-Bouillet, S. Berciaud, B. Doudin, and Y. Henry, Nature Communications **5**, 3167 (2014).

[231] P.-E. Janolin, N. a. Pertsev, D. Sichuga, and L. Bellaiche, Physical Review B **85**, 140401 (2012).

[232] M. D. Glinchuk, E. A. Eliseev, A. N. Morozovska, and R. Blinc, Physical Review B - Condensed Matter and Materials Physics **77**, 1 (2008).

[233] D. Halley, N. Najjari, F. Godel, M. Hamieh, B. Doudin, and Y. Henry, Physical Review B **91**, 214408 (2015).

[234] G. K. Lewis and H. Drickamer, The Journal of Chemical Physics **44**, 181 (1966).

[235] Y. Sato and S.-I. Akimoto, Journal of Applied Physics **50**, 5285 (1979).

[236] T. G. Worlton, R. M. Brugger, and R. B. Bennion, Journal of Physics and Chemistry of Solids **29**, 435 (1968).

[237] S. Rekhi, L. S. Dubrovinsky, R. Ahuja, S. K. Saxena, and B. Johansson, Journal of Alloys and Compounds **302**, 16 (2000).

[238] J. Mougin, T. Le Bihan, and G. Lucazeau, Journal of Physics and Chemistry of Solids **62**, 553 (2001).

[239] P. Dera, B. Lavina, Y. Meng, and V. B. Prakapenka, Journal of Solid State Chemistry **184**, 3040 (2011).

[240] M. Catti, G. Sandrone, G. Valerio, and R. Dovesi, Journal of Physics and Chemistry of Solids **57**, 1735 (1996).

[241] R. Street and B. Lewis, Philosophical Magazine **1**, 663 (1956).

[242] J. C. Wojdeł and J. Íñiguez, Physical Review Letters **105**, 1 (2010).

[243] C. H. Ahn, J.-M. Triscone, and J. Mannhart, Nature **424**, 1015 (2003).

[244] I. Dzyaloshinskii, Sov. Phys. JETP **6**, 621 (1957).

[245] R. L. Townsend Jr, T. G. Phillips, and R. L. White, Solid State Communications **6**, 603 (1968).

[246] T. G. Phillips, R. L. Townsend Jr, and R. L. White, Physical Review **162** (1959).

[247] C. W. Searle and G. W. Dean, Physical Review B **1**, 4337 (1970).

[248] G. Rollmann, A. Rohrbach, P. Entel, and J. Hafner, Physical Review B - Condensed Matter and Materials Physics **69**, 1 (2004).

[249] S. Mochizuki, Physica Status Solidi (A) **41**, 591 (1977).

[250] M. P. Pasternak, G. K. Rozenberg, G. Machavariani, O. Naaman, R. D. Taylor, and R. Jeanloz, Physical Review Letters **82**, 4663 (1999).

[251] G. K. Rozenberg, L. S. Dubrovinsky, M. P. Pasternak, O. Naaman, T. Le Bihan, and R. Ahuja, Physical Review B **65**, 1 (2002).

[252] J. Badro, G. Fiquet, V. V. Struzhkin, M. Somayazulu, H.-k. Mao, G. Shen, and T. Le Bihan, Physical Review Letters **89**, 205504 (2002).

[253] B. O'Regan and M. Grätzel, Nature **353**, 737 (1991).

[254] K. Hashimoto, H. Irie, and A. Fujishima, Japanese Journal of Applied Physics **44**, 8269 (2005).

[255] D.-H. Kwon, K. M. Kim, J. H. Jang, J. M. Jeon, M. H. Lee, G. H. Kim, X.-S. Li, G.-S. Park, B. Lee, S. Han, M. Kim, and C. S. Hwang, Nature nanotechnology **5**, 148 (2010).

[256] S.-C. Chen, T.-C. Chang, S.-Y. Chen, H.-W. Li, Y.-T. Tsai, C.-W. Chen, S. M. Sze, F.-S. Yeh(Huang), and Y.-H. Tai, Electrochemical and Solid-State Letters **14**, 103 (2011).

[257] D. S. Jeong, R. Thomas, R. S. Katiyar, J. F. Scott, H. Kohlstedt, A. Pe-

traru, and C. S. Hwang, Reports on Progress in Physics **75**, 076502 (2012).

[258] D. B. Strukov, G. S. Snider, D. R. Stewart, and R. S. Williams, Nature **453**, 80 (2008).

[259] K. Smith and V. Henrich, Physical Review B **38**, 5965 (1988).

[260] H. J. Zeiger, Physical Review B **11**, 5132 (1975).

[261] V. Eyert, U. Schwingenschlögl, and U. Eckern, Europhysics Letters (EPL) **70**, 782 (2005).

[262] M. Imada, A. Fujimori, and Y. Tokura, Reviews of Modern Physics **70**, 1039 (1998).

[263] F. Maldonado, C. Novillo, and A. Stashans, Chemical Physics **393**, 148 (2012).

[264] L. F. Mattheiss, Journal of Physics: Condensed Matter **8**, 5987 (1996).

[265] S. Lutfalla, V. Shapovalov, and A. T. Bell, Journal of Chemical Theory and Computation **7**, 2218 (2011).

[266] G. P. Kerker, Physical Review B **23**, 3082 (1981).

[267] J. M. D. Coey and G. a. Sawatzky, Journal of Physics C: Solid State Physics **4**, 2386 (1971).

[268] X. Zhong, I. Rungger, P. Zapol, and O. Heinonen, Physical Review B - Condensed Matter and Materials Physics **91**, 1 (2015).

[269] J. M. Honig and T. B. Reed, Physical Review **174**, 1020 (1968).

[270] S. Foner, Physical Review **130**, 183 (1963).

[271] Y. Shapira, Physical Review **187**, 734 (1969).

[272] R. D. Yacovitch and Y. Shapira, Physica **86-88B**, 1126 (1977).

[273] J. Ohtani and K. Kohn, J. Phys. Soc. Jpn. **53**, 3744 (1984).

[274] M. Fiebig, D. Fröhlich, and H. Thiele, Physical Review B **54**, R12681 (1996).

[275] Y. F. Popov, Z. A. Kazei, and A. M. Kadomtseva, Zh. Eksp. Teor. Fiz. **55**, 238 (1992).

[276] D. V. Belov, G. P. Vorob'ev, A. M. Kadomtseva, Y. F. Popov, and A. K. Zvezdin, JETP Letters **58**, 579 (1993).

[277] Y. F. Popov, A. M. Kadomtseva, D. V. Belov, and G. P. Vorob, Journal of Experimental and Theoretical Physics Letters **69**, 330 (1999).

[278] K. L. Dudko, V. V. Eremenko, and L. M. Semenenko, Physica Status Solidi (B) **43**, 471 (1971).

[279] J. C. Wojdeł and J. Íñiguez, Physical Review Letters **103**, 267205 (2009).